

**MOLECULAR DESIGN AND SYNTHESIS
OF DIPHENYLAMINE BASED
METAL-FREE CHROMOPHORES FOR
DYE SENSITIZED SOLAR CELLS
(DSSCs)**

Thesis

Submitted in partial fulfillment of the requirements for the
degree of

DOCTOR OF PHILOSOPHY

by

RAJALAKSHMI K.



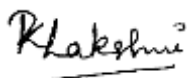
DEPARTMENT OF CHEMISTRY
NATIONAL INSTITUTE OF TECHNOLOGY KARNATAKA
SURATHKAL, MANGALORE - 575 025

September, 2020

DECLARATION

By the Ph.D. Research Scholar

I hereby declare that the Research Thesis entitled “**Molecular design and synthesis of diphenylamine based metal-free organic chromophores for dye sensitized solar cells (DSSCs)**” which is being submitted to the **National Institute of Technology Karnataka, Surathkal** in partial fulfillment of the requirements for the award of the Degree of **Doctor of Philosophy in Chemistry** is a *bonafide report of the research work carried out by me*. The material contained in this Research Thesis has not been submitted to any University or Institution for the award of any degree.



Rajalakshmi K.

Reg. No. 148041CY14F05

Department of Chemistry

Place: NITK - Surathkal

Date: 18-9-2020

CERTIFICATE

This is to certify that the Research Thesis entitled “**Molecular design and synthesis of diphenylamine based metal-free chromophores for dye sensitized solar cells (DSSCs)**” submitted by Mrs. Rajalakshmi K. (Register Number: **148041CY14F05**) as the record of the research work carried out by her *is accepted as the Research Thesis submission* in partial fulfillment of the requirements for the award of degree of Doctor of Philosophy.

Prof. A. Vasudeva Adhikari

Research Guide

Date:

Chairman - DRPC

Date:

ACKNOWLEDGEMENTS

I would like to express my deep sense of gratitude to my research supervisor **Dr. Airody Vasudeva Adhikari**, Professor HAG, Department of Chemistry. His invaluable guidance and support were always with me despite his busy schedule, without which I would not have completed this endeavor successfully. The directions he gave and the knowledge he shared in each and every single step of this work made it all possible. I am extremely thankful to him for all his support during my research work.

I sincerely thank Prof. K. Umamaheshwar Rao, Director, NITK and Prof. Swapan Bhattacharya, former Director, NITK for providing necessary facilities to carry out this research work. I express my earnest thanks to the RPAC members, Prof. A. Chitharanjan Hegde, Chemistry Department and Prof. Anandhan Srinivasan, Department of Metallurgical and Materials Engineering for insightful comments and constructive criticism towards the improvement of research quality.

My special thanks to Prof. Ahmed El-Shafei, Dr. Islam Abdellah and Mr. Fathy M Attia, Department of Textile Engineering, Chemistry and Science at NC State University, USA for providing fabrication facility for our molecules. I also thank Dr. Surya Prakash Singh, Senior Scientist, Polymers and Functional Materials, Indian Institute of Chemical Technology (IICT), Hyderabad. I am grateful to Dr. P. Anees, Materials Physics Division, Indira Gandhi Centre for Atomic Research, Kalpakkam, Tamil Nadu, India for helping with computational studies.

I am thankful to Prof. A. M. Isloor, HOD, Department of Chemistry for helping to complete my PhD. I am also thankful to Prof. A. N. Shetty, Prof. B. R. Bhat, Prof. D. K. Bhat, Dr. Udaya Kumar D, Dr. D. R. Trivedi, Dr. S. S. Mal, Dr. P. B. Beneesh, Dr. S. Dutta and Dr. Debashree, Department of Chemistry for their constant support and encouragement. I also wish to extend my gratitude to all non-teaching staff of the Department of Chemistry.

I thank Indian Institute of Chemical Technology (IICT), Hyderabad and Manipal Institute of Technology (MIT), Manipal, Cochin University of Science and Technology (CUSAT), Kerala for providing NMR and Mass Spectral facilities.

I also thank my colleagues Dr. Dickson D. Babu, Dr. Praveen Naik, Dr. Vinayakumara D. R., Mr. Naveen Chandra P., Ms. Kavya S. Keremane, Mr. Madhukara

Acharya, Ms Sruthi H, Ms. Vishrutha and Mr. S S. Sudhanva Prasad for their constant support, encouragement and company.

I am grateful to my dear friends Dr. Aranganathan V., Dr. Venkatadri T., Mr. Suraj Babbar, Dr. Shwetha Gayappu and Mr. Ramanjaneyulu S. for their help during the course of this work. Also, I am indebted to my friends Ms. Anuma Saroja and Mrs. Reethu Haridas for their support and help during my research work. I extend my sincere thanks to all the research scholars in the Department of Chemistry for their constant help and support.

Mere words are not enough to express my gratitude to my family, father Mr. Kesavan P., mother Dr. Chitra G., husband Dr. Sunil Kumar N., brothers Mr. Praveen K. and Dr. Arun K., sister in-laws Dr. Sreeranjini K. S., Mrs. Anamika S. and my in-laws for their constant support, encouragement and prayers. Finally, I thank the God almighty for strengthening me during hardships to successfully complete this endeavor.

RAJALAKSHMI K.

ABSTRACT

Dye-sensitized solar cell (DSSC), which belongs to third generation solar cells has emerged as an attractive and promising low-cost solar device for harvesting solar energy. Grätzel and O'Brian invented DSSC in the year 1991, from that onwards it has been a promising technology attracted by both academic and industrial clad. Sensitizer is one of the vital components of DSSCs. It absorbs solar energy effectively to inject electrons into the TiO₂ layer thereby producing electric energy. Here, sensitizer (dye) plays a crucial role in achieving high injection rate, thereby increasing the efficiency of the cell. Among the metal-free sensitizers *n*- type organic chromophores are of great importance. Even though, there are lots of studies on-going in this field, there is an ample scope for investigation of efficient sensitizers as they affect directly on PCE. Also, development of novel co-sensitizers for DSSCs sensitized with metal-based dyes, is an equally important area of research study. In this context, it was planned to design, synthesize and investigate the photovoltaic performance of new organic dyes based on *diphenylamine* as *n*-type sensitizers/co-sensitizers for DSSCs.

Based on the detailed literature survey, twenty seven new *n*-type organic diphenylamine based sensitizers/co-sensitizers were designed using various molecular engineering strategies. They were successfully synthesized following appropriate synthetic protocols. Further, they were well-characterized by (FTIR, NMR and MS) spectral, optical and electrochemical analyses. The results revealed that, all the new dyes displayed the λ_{abs} and λ_{emi} in the range of 350-560 nm and 430-690 nm, respectively. Their band gaps were calculated to be in order of 1.90-3.09 eV. DFT study has been employed to optimize the molecular geometries and to apprehend the effect of structures of organic sensitizers/co-sensitizers on their photovoltaic performances in devices. Also, TD-DFT simulations were carried out for the selected dyes. Finally, the synthesized dyes were subjected to the photovoltaic studies as sensitizers/co-sensitizers in DSSCs. Among newly synthesized organic sensitizers, the cell fabricated with **D₂₂** carrying cyanoacetic acid as an anchoring unit displayed the optimum *PCE* of **5.909** %. Whereas, the co-sensitization studies indicated that, under the same conditions, the device co-sensitized using **D₂₆** with **HD-2** sensitizer showcased upheld *PCE* of **10.55** % showing an increment of 3.18 %. To sum up, by appropriately optimizing the molecular structures of organic chromophores, it is possible to further ameliorate the photovoltaic performance of the cells.

Keywords: Diphenylamine; dye; *n*-type sensitizer; co-sensitizer; DFT; DSSC; **HD-2**

CONTENTS

AN OVERVIEW OF DYE-SENSITIZED SOLAR CELLS (DSSCs).....	1
1.1 INTRODUCTION TO SOLAR CELLS	1
1.1.1 Solar cell and its present scenario	2
1.2.1 Solar spectrum	3
1.3.1 Solar cell terminologies	4
1.1.3.1 Short circuit current (I_{sc})	5
1.1.3.2 Open circuit voltage (V_{oc})	5
1.1.3.3 Series resistance (R_s)	6
1.1.3.4 Shunt resistance (R_{sh})	6
1.1.3.5 Fill factor (FF)	7
1.1.3.6 Efficiency (η)	7
1.1.3.7 Incident-Photo-Current Conversion Efficiency (IPCE)	8
1.2 BRIEF HISTORY OF DSSC	8
1.3 KEY COMPONENTS OF DSSC	9
1.3.1 Transparent conductive substrate.....	9
1.3.2 Mesoporous semiconductor	10
1.3.3 Sensitizer.....	11
1.3.3.1 Metal-based dyes.....	11
1.3.3.2 Metal-free organic dyes.....	12
1.3.3.2.1 Organic chromophores for DSSC.....	13
1.3.4 Counter electrode	14
1.3.5 Electrolyte	15
1.4 WORKING PRINCIPLE OF DSSC	15
1.4.1 <i>n</i> -Type DSSC	17
1.5 ADVANTAGES OF DSSC OVER OTHER PHOTOVOLTAICS	18
1.6 CHALLENGES IN THE FIELD OF DSSC	19
1.7 CO-SENSITIZATION	20
1.8 INSPIRATION FOR PRESENT WORK	21
1.9 STRUCTURAL DESIGN OF SENSITIZERS	22
1.10 CHARACTERIZATION TECHNIQUES	24
1.11 BROAD OBJECTIVES OF THE PRESENT WORK.....	24
1.12 THESIS STRUCTURE	25

LITERATURE REVIEW, SCOPE, OBJECTIVES AND DESIGN OF NEW SENSITIZERS/CO-SENSITIZERS	27
2.1 INTRODUCTION.....	27
2.2 LITERATURE REVIEW.....	28
2.2.1 Diphenylamine based sensitizers	29
2.2.2 Different spacer units and anchoring groups used in <i>n</i> -type sensitizers.....	31
2.2.3 Co-sensitizers for Ru (II) based DSSCs.....	35
2.3 SALIENT FEATURES OF THE LITERATURE REVIEW	40
2.4 SCOPE AND OBJECTIVES	41
2.5 MOLECULAR DESIGN OF NEW <i>n</i> -TYPE SENSITIZERS/CO-SENSITIZERS ..	43
2.5.1 Design of chromophores D₁₋₃ (Series-1)	43
2.5.2 Design of chromophores D₄₋₇ (Series-2)	44
2.5.3 Design of chromophores D₈₋₁₁ (Series-3)	45
2.5.4 Design of chromophores D₁₂₋₁₇ (Series-4)	46
2.5.5 Design of chromophores D₁₈₋₂₁ (Series-5)	47
2.5.6 Design of chromophores D₂₂₋₂₃ (Series- 6)	47
2.5.7 Design of chromophores D₂₄₋₂₇ (Series-7)	48
SYNTHESIS AND STRUCTURAL CHARACTERIZATION.....	51
3.1 INTRODUCTION.....	51
3.2 EXPERIMENTAL	51
3.2.1 Materials and methods	52
3.2.2 Synthesis of chromogens D₁₋₂₇ (Series 1-7)	52
3.2.2.1 Synthesis of chromophores D₁₋₃ (Series-1)	52
3.2.2.2 Synthesis of chromophores D₄₋₇ (Series-2)	57
3.2.2.3 Synthesis of chromophores D₈₋₁₁ (Series-3)	61
3.2.2.4 Synthesis of chromophores D₁₂₋₁₇ (Series-4)	66
3.2.2.5 Synthesis of chromophores D₁₈₋₂₁ (Series-5)	71
3.2.2.6 Synthesis of chromophores D₂₂₋₂₃ (Series- 6)	76
3.2.2.7 Synthesis of chromophores D₂₄₋₂₇ (Series-7)	80
3.2.3 Results and discussion	83
3.2.3.1 Chromophores D₁₋₃ (Series-1)	84
3.2.3.2 Chromophores D₄₋₇ (Series-2)	86
3.2.3.3 Chromophores D₈₋₁₁ (Series-3)	88
3.2.3.4 Chromophores D₁₂₋₁₇ (Series-4)	91
3.2.3.5 Chromophores D₁₈₋₂₁ (Series-5)	93

3.2.3.6	Chromophores D₂₂₋₂₃ (Series-6)	95
3.2.3.7	Chromophores D₂₄₋₂₇ (Series-7)	98
3.3	CONCLUSIONS	100
PHOTOPHYSICAL, ELECTROCHEMICAL AND THEORETICAL INVESTIGATIONS		101
4.1	PHOTOPHYSICAL INVESTIGATION	101
4.1.1	Materials and methods	101
4.1.2	Experimental	102
4.1.3	Results and discussion	102
4.2.3.1	Photophysical studies of chromophores D₁₋₃ (Series-1)	102
4.2.3.2	Photophysical studies of chromophores D₄₋₇ (Series-2)	105
4.2.3.3	Photophysical studies of chromophores D₈₋₁₁ (Series-3)	107
4.2.3.4	Photophysical studies of chromophores D₁₂₋₁₇ (Series-4)	109
4.2.3.5	Photophysical studies of chromophores D₁₈₋₂₁ (Series-5)	112
4.2.3.6	Photophysical studies of chromophores D₂₂₋₂₃ (Series-6)	114
4.2.3.7	Photophysical studies of chromophores D₂₄₋₂₇ (Series-7)	115
4.2	ELECTROCHEMICAL STUDIES.....	117
4.2.1	Materials and methods	118
4.2.2	Experimental	118
4.2.3	Results and discussion	118
4.2.3.1	Electrochemical studies of chromophores D₁₋₃ (Series-1)	119
4.2.3.2	Electrochemical studies of chromophores D₄₋₇ (Series-2)	121
4.2.3.3	Electrochemical studies of chromophores D₈₋₁₁ (Series-3)	123
4.2.3.4	Electrochemical studies of chromophores D₁₂₋₁₇ (Series-4)	124
4.2.3.5	Electrochemical studies of chromophores D₁₈₋₂₁ (Series-5)	126
4.2.3.6	Electrochemical studies of chromophores D₂₂₋₂₃ (Series-6)	127
4.2.3.7	Electrochemical studies of chromophores D₂₄₋₂₇ (Series-7)	129
4.3	THEORETICAL INVESTIGATION	130
4.3.1	DFT/TD-DFT simulations	130
4.3.2	Results and discussion	131
4.3.2.1	Theoretical studies of dyes D₁₋₃ (Series-1)	131
4.3.2.2	Theoretical studies of dyes D₄₋₇ (Series-2)	133
4.3.2.3	Theoretical studies of dyes D₈₋₁₁ (Series-3)	138
4.3.2.4	Theoretical studies of dyes D₁₂₋₁₇ (Series-4)	139
4.3.2.5	Theoretical studies of dyes D₁₈₋₂₁ (Series-5)	141

4.3.2.6	Theoretical studies of dyes D₂₂₋₂₃ (Series-6)	143
4.3.2.7	Theoretical studies of dyes D₂₄₋₂₇ (Series-7)	144
4.3.3	TD-DFT studies	145
4.4	CONCLUSIONS	146
PHOTOVOLTAIC AND ELECTROCHEMICAL IMPEDANCE STUDIES		149
5.1	PHOTOVOLTAIC INVESTIGATION	149
5.1.1	Introduction	149
5.1.2	Materials and methods	150
5.1.3	Experimental	150
5.1.3.1	Fabrication of DSSCs sensitized with D₁₋₂₇ (Series-1 to 7)	150
5.1.3.2	Fabrication of DSSCs co-sensitized with D₁₋₂₇ (Series-1 to 7)	151
5.1.4	Results and discussion	152
5.1.4.1	Photovoltaic performance of devices sensitized/co-sensitized with D₁₋₃ (Series-1)	152
5.1.4.2	Photovoltaic performance of devices sensitized/co-sensitized with D₄₋₇ (Series-2)	155
5.1.4.3	Photovoltaic performance of devices sensitized/co-sensitized with D₈₋₁₁ (Series-3)	159
5.1.4.4	Photovoltaic performance of devices sensitized/co-sensitized with D₁₂₋₁₇ (Series-4)	161
5.1.4.5	Photovoltaic performance of devices sensitized/co-sensitized with D₁₈₋₂₁ (Series-5)	164
5.1.4.6	Photovoltaic performance of devices sensitized/co-sensitized with D₂₂₋₂₃ (Series-6)	167
5.1.4.7	Photovoltaic performance of devices sensitized/co-sensitized with D₂₄₋₂₇ (Series-7)	169
5.2	ELECTROCHEMICAL IMPEDANCE SPECTROSCOPY STUDIES.....	172
5.2.1	Material and methods.....	173
5.2.2	Experimental	173
5.2.3	Results and discussion	173
5.2.3.1	Electrochemical impedance studies of devices sensitized/co-sensitized with D₁₋₃ (Series-1)	174
5.2.3.2	Electrochemical impedance studies of devices sensitized/co-sensitized with D₄₋₇ (Series-2)	177
5.2.3.3	Electrochemical impedance studies of devices sensitized/co-sensitized with D₈₋₁₁ (Series-3)	180
5.2.3.4	Electrochemical impedance studies of devices sensitized/co-sensitized with D₁₂₋₁₇ (Series-4)	183

5.2.3.5 Electrochemical impedance studies of devices sensitized/co-sensitized with D₁₈₋₂₁ (Series-5)	185
5.2.3.6 Electrochemical impedance studies of devices sensitized/co-sensitized with D₂₂₋₂₃ (Series-6)	188
5.2.3.7 Electrochemical impedance studies of devices sensitized/co-sensitized with D₂₄₋₂₇ (Series-7)	190
5.3 FTIR ANALYSIS: ANCHORING STUDIES OF THE DYES ON TiO ₂	192
5.4 CONCLUSIONS	195
SUMMARY AND CONCLUSIONS	197
6.1 SUMMARY	197
6.2 CONCLUSIONS	198
6.3 SCOPE FOR FUTURE WORK.....	200
REFERENCES	201
LIST OF PUBLICATIONS	219
BIO-DATA	223

LIST OF FIGURES

Fig 1.1	Schematic representation of potential for renewable energy sources	1
Fig 1.2	Various types of solar cell technologies and current trends of development	3
Fig 1.3	Solar irradiance spectrum at AM0	4
Fig 1.4	Solar cell equivalent circuit: I_L is photo generated current (A), I_D is diode current (A) and I_{SH} is shunt current (A)	5
Fig 1.5	I-V curve	7
Fig 1.6	(a) Structure of diphenyl amine; (b) its electrostatic potential map	14
Fig 1.7	Schematic representation of working in <i>n</i> -type DSSC	18
Fig 1.8	Schematic representation of a D- π -A structure on TiO ₂	23
Fig 2.1	Design of chromophores D ₁₋₃	44
Fig 2.2	Design of chromophores D ₄₋₇	45
Fig 2.3	Design of chromophores D ₈₋₁₁	46
Fig 2.4	Design of chromophores D ₁₂₋₁₇	46
Fig 2.5	Design of chromophores D ₁₈₋₂₁	47
Fig 2.6	Design of chromophores D ₂₂₋₂₃	48
Fig 2.7	Design of chromophores D ₂₄₋₂₇	48
Fig 3.1	¹ H NMR spectrum of D ₁ recorded in CDCl ₃	84
Fig 3.2	¹³ C NMR spectrum of D ₁ recorded in CDCl ₃	85
Fig 3.3	FTIR spectrum of D ₁	85
Fig 3.4	Mass spectrum of D ₁	86
Fig 3.5	¹ H NMR spectrum of D ₄ recorded in DMSO- <i>d</i> ₆	87
Fig 3.6	¹³ C NMR spectrum of D ₄ recorded in DMSO- <i>d</i> ₆	87
Fig 3.7	FTIR spectrum of D ₄	88
Fig 3.8	Mass spectrum of D ₄	88
Fig 3.9	¹ H NMR spectrum of D ₁₀ recorded in CDCl ₃	89
Fig 3.10	¹³ C NMR spectra of D ₁₀ recorded in CDCl ₃	90
Fig 3.11	FTIR spectrum of D ₁₀	90
Fig 3.12	Mass spectrum of D ₁₀	91

Fig 3.13	¹ H NMR spectrum of D₁₄ recorded in in CDCl ₃	92
Fig 3.14	¹³ C NMR spectrum of D₁₄ recorded in in CDCl ₃	92
Fig 3.15	FTIR spectrum of D₁₄	93
Fig 3.16	Mass spectrum of D₁₄	93
Fig 3.17	¹ H NMR spectrum of D₂₁ recorded in CDCl ₃	94
Fig 3.18	¹³ C NMR spectrum of D₂₁ recorded in CDCl ₃	95
Fig 3.19	FTIR spectrum of D₂₁	95
Fig 3.20	¹ H NMR spectrum of D₂₃ recorded in DMSO- <i>d</i> ₆	96
Fig 3.21	¹³ C NMR spectrum of D₂₃ recorded in DMSO- <i>d</i> ₆	97
Fig 3.22	FTIR spectrum of D₂₃	97
Fig 3.23	¹ H NMR spectrum of D₂₆ recorded in CDCl ₃	98
Fig 3.24	¹³ C NMR spectrum of D₂₆ recorded in DMSO- <i>d</i> ₆	99
Fig 3.25	FTIR spectrum of D₂₆	99
Fig 3.26	Mass spectrum of D₂₆	100
Fig 4.1	(a) Normalized absorption spectra of D₁₋₃ ; (b) their emission spectra in CHCl ₃ (3×10 ⁻⁵ M)	104
Fig 4.2	Absorption spectra of (a) D₁₋₃ adsorbed on TiO ₂ ; (b) D₁ in acidic and basic medium	104
Fig 4.3	(a) Normalized absorption spectra of D₄₋₇ ; (b) their emission spectra in CHCl ₃ (3×10 ⁻⁵ M)	105
Fig 4.4	Absorption spectra of D₄₋₇ adsorbed on TiO ₂ surface.	107
Fig 4.5	(a) Normalized absorption spectra of D₈₋₁₁ ; (b) their emission spectra in CHCl ₃ (3×10 ⁻⁵ M)	108
Fig 4.6	Absorption spectra of D₈₋₁₁ adsorbed on TiO ₂ surface.	109
Fig 4.7	(a) Normalized absorption spectra of D₁₂₋₁₇ ; (b) their emission spectra in CHCl ₃ (3×10 ⁻⁵ M)	110
Fig 4.8	Absorption spectra of D₁₈₋₂₁ with HD-2 adsorbed on TiO ₂ surface	111
Fig 4.9	(a) Normalized absorption spectra of D₁₈₋₂₁ ; (b) their emission spectra in DMF(3×10 ⁻⁵ M)	112
Fig 4.10	Absorption spectra of D₁₈₋₂₁ adsorbed on TiO ₂ surface	113
Fig 4.11	(a) Normalized absorption spectra of D₂₂₋₂₃ ; (b) their emission spectra in DMF(3×10 ⁻⁵ M)	114

Fig 4.12	Absorption spectra of D22-23 adsorbed on TiO ₂ surface	115
Fig 4.13	(a) Normalized absorption spectra of D24-27 ; (b) their emission spectra in CHCl ₃ (3×10 ⁻⁵ M)	116
Fig 4.14	Absorption spectra of D24-27 along with HD-2 adsorbed on TiO ₂ surface	117
Fig 4.15	(a) Cyclic Voltammograms of D1-3 ; (b) Schematic representation of HOMO and LUMO levels as well as calculated band gaps of the dyes	120
Fig 4.16	(a) Cyclic Voltammograms of D4-7 ; (b) Schematic representation of HOMO and LUMO levels as well as calculated band gaps of the dyes	122
Fig 4.17	(a) Cyclic Voltammograms of D8-11 ; (b) Schematic representation of HOMO and LUMO levels as well as calculated band gaps of the dyes	124
Fig 4.18	(a) Cyclic Voltammograms of D12-17 ; (b) Schematic representation of HOMO and LUMO levels as well as calculated band gaps of the dyes	125
Fig 4.19	(a) Cyclic Voltammograms of D18-21 ; (b) Schematic representation of HOMO and LUMO levels as well as calculated band gaps of the dyes	127
Fig 4.20	(a) Cyclic Voltammograms of D22-23 ; (b) Schematic representation of HOMO and LUMO levels as well as calculated band gaps of the dyes	128
Fig 4.21	(a) Cyclic Voltammograms of D24-27 ; (b) Schematic representation of HOMO and LUMO levels as well as calculated band gaps of the dyes	129
Fig 4.22	HOMO and LUMO levels of dyes D1-3	132
Fig 4.23	Molecular Electrostatic Potential (ESP) maps on the iso-surface of D1-3	133
Fig 4.24	HOMO and LUMO levels of dyes D4-7	135
Fig 4.25	(a) HOMO and (b) LUMO levels of dye-TiO ₂ (101) adduct	137
Fig 4.26	Molecular Electrostatic Potential (ESP) maps on the iso-surface of D4-7	137
Fig 4.27	HOMO and LUMO levels of dyes D8-11	139
Fig 4.28	Molecular Electrostatic Potential (ESP) maps on iso density of D8-11	139
Fig 4.29	HOMO and LUMO levels of dyes D12-17	140
Fig 4.30	Molecular Electrostatic Potential (ESP) maps on the iso density of D12-17	140
Fig 4.31	HOMO and LUMO levels of dyes D18-21	142
Fig 4.32	Molecular Electrostatic Potential (ESP) maps on the iso density of D18-21	142
Fig 4.33	HOMO/LUMO levels of dyes D22-23	143
Fig 4.34	Molecular Electrostatic Potential (ESP) maps on the iso density of D22-23	144
Fig 4.35	HOMO/LUMO levels of dyes D24-27	144

Fig 4.36	Molecular Electrostatic Potential (ESP) mapping on iso density of D24-27	145
Fig 4.37	Simulated absorption spectrum of D24 and (b) spectrum of D25	146
Fig 4.38	a-d Simulated vibrational spectra of D24 , D25 , D26 and D27 , respectively	146
Fig 5.1	(a) Photocurrent density vs. voltage; (b) IPCE characteristics for devices sensitized with D1-3 under illumination of simulated solar light (AM 1.5, 100 mW/cm ²)	153
Fig 5.2	(a) Photocurrent density vs. voltage; (b) IPCE spectra for N3 based devices co-sensitized with D1-3 under illumination of simulated solar light (AM 1.5, 100 mW/cm ²)	155
Fig 5.3	(a) Photocurrent density vs. voltage; (b) IPCE characteristics for devices sensitized with D4-7 under illumination of simulated solar light (AM 1.5, 100 mW/cm ²)	156
Fig 5.4	(a) Photocurrent density vs. voltage; (b) IPCE spectra for HD-2 based devices co-sensitized with D4-7 under illumination of simulated solar light (AM 1.5, 100 mW/cm ²)	158
Fig 5.5	(a) Photocurrent density vs. voltage; (b) IPCE characteristics for devices sensitized with D8-11 under illumination of simulated solar light (AM 1.5, 100 mW/cm ²)	160
Fig 5.6	(a) Photocurrent density vs. voltage; (b) IPCE spectra for HD-2 based devices co-sensitized with D8-11 under illumination of simulated solar light (AM 1.5, 100 mW/cm ²)	161
Fig 5.7	(a) Photocurrent density vs. voltage; (b) IPCE characteristics for devices sensitized with D12-17 under illumination of simulated solar light (AM 1.5, 100 mW/cm ²)	162
Fig 5.8	(a) Photocurrent density vs. voltage; (b) IPCE spectra for HD-2 based devices co-sensitized with D12-17 under illumination of simulated solar light (AM 1.5, 100 mW/cm ²)	163
Fig 5.9	(a) Photocurrent density vs. voltage; (b) IPCE characteristics for devices sensitized with D18-21 under illumination of simulated solar light (AM 1.5, 100 mW/cm ²)	165
Fig 5.10	(a) Photocurrent density vs. voltage; (b) IPCE spectra for HD-2 based devices co-sensitized with D18-21 under illumination of simulated solar light (AM 1.5, 100 mW/cm ²)	166
Fig 5.11	(a) Photocurrent density vs. voltage; (b) IPCE characteristics for devices sensitized with D22-23 under illumination of simulated solar light (AM 1.5, 100 mW/cm ²)	168
Fig 5.12	(a) Photocurrent density vs. voltage; (b) IPCE spectra for HD-2 based devices co-sensitized with D22-23 under illumination of simulated solar	169

	light (AM 1.5, 100 mW/cm ²)	
Fig 5.13	(a) Photocurrent density vs. voltage; (b) IPCE characteristics for devices sensitized with D₂₄₋₂₇ under illumination of simulated solar light (AM 1.5, 100 mW/cm ²)	170
Fig 5.14	(a) Photocurrent density vs. voltage; (b) IPCE spectra for HD-2 based devices co-sensitized with D₂₄₋₂₇ under illumination of simulated solar light (AM 1.5, 100 mW/cm ²)	171
Fig 5.15	Equivalent circuit diagram	173
Fig 5.16	(a) Nyquist plots and (b) Bode plots of devices sensitized with D₁₋₃	175
Fig 5.17	(a) Nyquist plots and (b) Bode plots for N3 based devices co-sensitized with D₁₋₃	177
Fig 5.18	(a) Nyquist plots and (b) Bode plots of devices sensitized with D₄₋₇	178
Fig 5.19	(a) Nyquist plots and (b) Bode plots for HD-2 based devices co-sensitized with D₄₋₇	180
Fig 5.20	(a) Nyquist plots and (b) Bode plots of devices sensitized with D₈₋₁₁	181
Fig 5.21	(a) Nyquist plots and (b) Bode plots for HD-2 based devices co-sensitized with D₈₋₁₁	182
Fig 5.22	(a) Nyquist plots and (b) Bode plots of devices sensitized with D₁₂₋₁₇	184
Fig 5.23	(a) Nyquist plots and (b) Bode plots for HD-2 based devices co-sensitized with D₁₂₋₁₇	185
Fig 5.24	(a) Nyquist plots and (b) Bode plots of devices sensitized with D₁₈₋₂₁	186
Fig 5.25	(a) Nyquist plots and (b) Bode plots for HD-2 based devices co-sensitized with D₁₈₋₂₁	187
Fig 5.26	(a) Nyquist plots and (b) Bode plots of devices sensitized with D₂₂₋₂₃	189
Fig 5.27	(a) Nyquist plots and (b) Bode plots for HD-2 based devices co-sensitized with D₂₂₋₂₃	189
Fig 5.28	(a) Nyquist plots and (b) Bode plots of devices sensitized with D₂₄₋₂₇	191
Fig 5.29	(a) Nyquist plots and (b) Bode plots for HD-2 based devices co-sensitized with D₂₄₋₂₇	192
Fig 5.30	FTIR spectrum of D₁ adsorbed on TiO ₂ surface	194
Fig 5.31	FTIR spectrum of D₂ adsorbed on TiO ₂ surface	194
Fig 5.32	FTIR spectrum of D₃ adsorbed on TiO ₂ surface	194

LIST OF TABLES

Table 2.1	Reported diphenylamine based dyes and their photovoltaic parameters	30
Table 2.2	Dyes carrying varied donor, spacer, anchoring units, with cell performance data	33
Table 2.3	Reported organic co-sensitizers with cell performance data	38
Table 4.1	Photophysical properties of D1-3	105
Table 4.2	Photophysical properties of D4-7	106
Table 4.3	Photophysical properties of D8-11	109
Table 4.4	Photophysical properties of D12-17	112
Table 4.5	Photophysical properties of D18-21	113
Table 4.6	Photophysical properties of D22-23	115
Table 4.7	Photophysical properties of D24-27	117
Table 4.8	Electrochemical data of D1-3	121
Table 4.9	Electrochemical data of D4-7	122
Table 4.10	Electrochemical data of D8-11	124
Table 4.11	Electrochemical data of D12-17	126
Table 4.12	Electrochemical data of D18-21	127
Table 4.13	Electrochemical data of D22-23	128
Table 4.14	Electrochemical data of D24-27	130
Table 5.1	Photovoltaic performance data of devices sensitized with D1-3	153
Table 5.2	Photovoltaic performance data of devices co-sensitized with D1-3	155
Table 5.3	Photovoltaic performance data of devices sensitized with D4-7	157
Table 5.4	Photovoltaic performance data of devices co-sensitized with D4-7	158
Table 5.5	Photovoltaic performance data of devices sensitized with D8-11	160
Table 5.6	Photovoltaic performance data of devices co-sensitized with D8-11	161
Table 5.7	Photovoltaic performance data of devices sensitized with D12-17	162
Table 5.8	Photovoltaic performance data of devices co-sensitized with D12-17	164
Table 5.9	Photovoltaic performance data of devices sensitized with D18-21	165
Table 5.10	Photovoltaic performance data of devices co-sensitized with D18-21	167

Table 5.11	Photovoltaic performance data of devices sensitized with D₂₂₋₂₃	168
Table 5.12	Photovoltaic performance data of devices co-sensitized with D₂₂₋₂₃	169
Table 5.13	Photovoltaic performance data of devices sensitized with D₂₄₋₂₇	170
Table 5.14	Photovoltaic performance data of devices co-sensitized with D₂₄₋₂₇	172
Table 5.15	EIS parameters of devices sensitized and co-sensitized using D₁₋₃ dyes	177
Table 5.16	EIS parameters of devices sensitized and co-sensitized using D₄₋₇ dyes	179
Table 5.17	EIS parameters of devices sensitized and co-sensitized using D₈₋₁₁ dyes	182
Table 5.18	EIS parameters of devices sensitized and co-sensitized using D₁₂₋₁₇ dyes	185
Table 5.19	EIS parameters of devices sensitized and co-sensitized using D₁₈₋₂₁ dyes	188
Table 5.20	EIS parameters of devices sensitized and co-sensitized using D₂₂₋₂₃ dyes	190
Table 5.21	EIS parameters of devices sensitized and co-sensitized using D₂₄₋₂₇ dyes	192

ABBREVIATIONS:

AM	Air mass
CB	Conduction band
CE	Counter Electrode
D- π -A	Donor- π -acceptor
DFT	Density functional theory
DSSC	Dye sensitized solar cells
D₁₋₃	Diphenylamine based sensitizers/co-sensitizers with D- π -A configuration
D₄₋₇	Diphenylamine based sensitizers/co-sensitizers with A-D- π -A configuration
D₈₋₁₁	Diphenylamine based sensitizers/co-sensitizers with D- π -A/D- π - π -A configuration
D₁₂₋₁₇	Diphenylamine based sensitizers/co-sensitizers with D-A/D- π -A configuration
D₁₈₋₂₁	Diphenylamine based sensitizers/co-sensitizers with D-D-A configuration
D₂₂₋₂₃	Diphenylamine based sensitizers/co-sensitizers with A-D- π -D-A configuration
D₂₄₋₂₇	Diphenylamine based sensitizers/co-sensitizers with D-A configuration
e ⁻	Electrons
ESOP	Excited state oxidation potential
ESP	Electrostatic potential
Eq	Equation
EW	Electron withdrawing
E ₀₋₀	Optical band gap
E _g	Electrochemical band gap
FF	Fill factor
Fs	Femtosecond
FTIR	Fourier-transform infra-red
FTO	Fluorine-doped tin oxide
GSOP	Ground state oxidation potential
ΔG_{inj}	Driving force for injection processes.
ΔG_{reg}	Driving force for regeneration processes.

ΔG_{rec}	Driving force for recombination processes.
GC	Glassy carbon
HOMO	Highest occupied molecular orbital
ICT	Intra-molecular charge transfer
I_{sc}	Short circuit current
IPCE	Incident-photo-current conversion efficiency
LUMO	Lowest unoccupied molecular orbital
λ_{abs}	Maximum absorbance wavelength
λ_{emi}	Maximum emission wavelength
J_{sc}	Short-circuit photocurrent density
LHE	Light harvesting efficiency
LUMO	Lowest unoccupied molecular orbital
MP	Melting Point
ms	Millisecond
mM	Millimole
η	Efficiency
<i>n</i> - Type DSSC	<i>n</i> - Type dye sensitized solar cell
<i>n</i> -SC	<i>n</i> -Type semiconductor
NHE	Normal hydrogen electrode
NMR	Nuclear magnetic resonance
PCE	Photon conversion efficiency
<i>p</i> - Type DSSC	<i>p</i> - Type dye sensitized solar cell
PV	Photovoltaic
ppm	Parts per million
RT	Room temperature
Ru (II)	Ruthenium (II)
S	Sensitizer
SC	Semiconductor

TD-DFT	Time-dependent density functional theory
TiO ₂	Titanium dioxide
TCO	Transparent conducting oxide
VB	Valence band
V _{OC}	Open circuit voltage
WE	Working electrode

AN OVERVIEW OF DYE SENSITIZED SOLAR CELLS (DSSCs)

Abstract:

This chapter includes an introduction to solar cells followed by a brief account on dye-sensitized solar cells (DSSCs). It also covers the different components, working principles, and photovoltaic parameters of DSSCs. Further, it comprises broad objectives of the present research work along with outline of the thesis structure.

1.1 INTRODUCTION TO SOLAR CELLS

Escalating the demand for energy coupled with the raising awareness of environmental issues make nations and public to reconsider the importance of exploring renewable energy resources. As already known, solar energy is the most abundant, inexhaustible and clean of all available renewable energy sources. Further, solar energy is the most viable long-term solution for the existing energy crisis. It is interesting to note that, the intercepted power of sun on earth is about 1.8×10^{11} MW which is far more than the present day energy consumption. According to International Energy Agency (IEA), the development in solar energy conversion may provide 5% of global electricity consumption in 2030 and about 11% by 2050 that can attribute to a largely decarbonized energy system. **Fig 1.1** shows the potential for each renewable energy source based on today's technology.

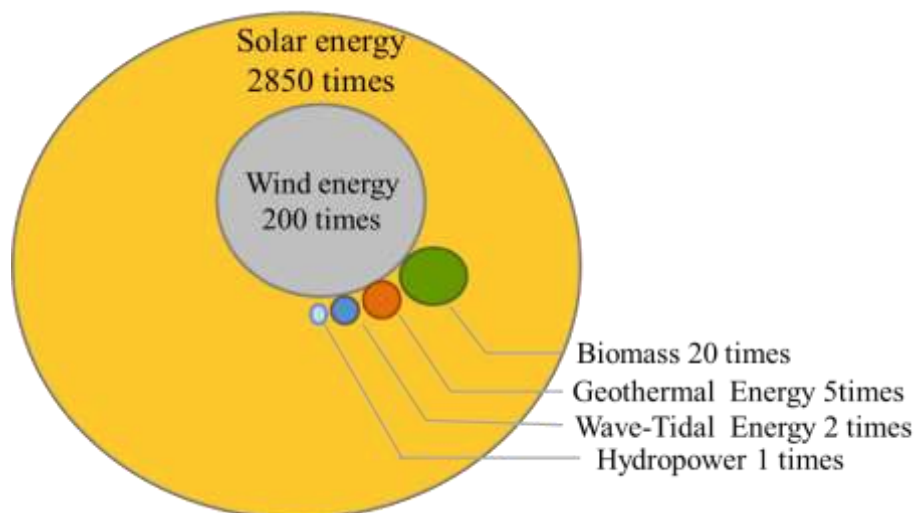


Fig 1.1 Schematic representation of potential for renewable energy sources

Solar energy can be harvested either by deriving directly from sunlight or by indirect methods and one of the finest ways to harness solar energy is the solar cell or

photovoltaic cells. In early 1870's Willoughby Smith serendipitously discovered that electricity traveled through selenium when it was exposed to light. Later, two American scientists William Adams and Richard Day invented that, solar energy creates a flow of electricity in selenium. Followed by this discovery, in early 1880's Charles Fritt invented the first PV cell with a layer of selenium on a metal plate and coating it with gold leaf. He reported an efficiency of about 1% in the device. The photovoltaic effect in silicon (Si) diode was discovered at Bell Lab by Chapin et al. in 1954 which marked the beginning of modern photovoltaic technology (Chapin et al. 1954).

1.1.1 Solar cell and its present scenario

Solar energy harvesting and its conversion to usable forms like electricity or chemical fuel remain a huge challenge. One of the promising ways of converting incident photon energy of the solar radiation into electrical energy is by photovoltaic cells (PV). Every solar cell requires a light absorbing material within it in order to absorb photons and generate free electrons *via* the photovoltaic effect. In a PV, the interface between the *n* and *p* semiconductors is considered as the heart of the device. One of the photons with sufficient energy only can throw out an electron which travels through '*n*' semiconductor to metal contacts on the surface and hole in the other hand travels in the direction to meet the '*p*' semiconductor. An electron at the metal contact flows through an external circuit and does work in the process to meet up with a hole at the rear contact. The energy required to transport electron from the semiconductor atom to a conduction site is fixed. A photon with short wavelength may have surplus energy after promoting an electron that excess energy is dissipated as heat. These two factors combine to produce a theoretical upper limit to PV efficiency of around 31% (Shockley and Queisser 1961) .

Solar cells are categorized into three generations based on their performance, and cost effectiveness and the classification is comprised in **Fig 1.2**. The first generation of solar cells has relatively higher efficiency with expensive production cost. This *p-n* junction with doped semiconductor is dominated in the commercial market and silicon-based solar cells are the major examples of this kind. The second generation includes the thin film solar cells based on CdTe or CuInGaSe. Even though

they have lower efficiency, they are much cheaper to produce and involve less tedious fabrication process. Third generation solar cells include any cell that is not grouped in first and second types. These category employs variety of different technologies. For a better future, these category should be commercialized and this requires tremendous research activities. Further, DSSC is a promising candidate of third generation solar cells.

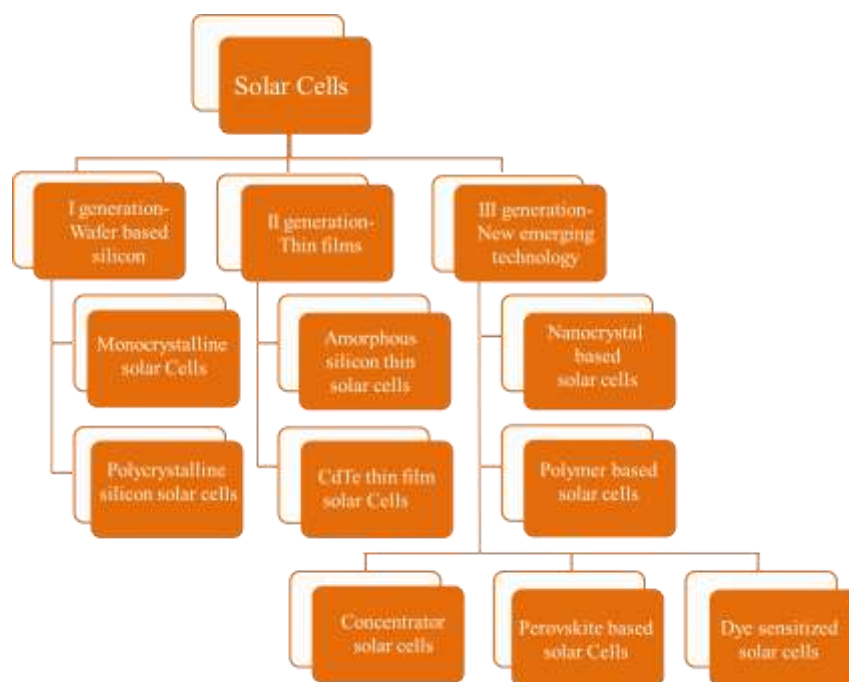


Fig 1.2 Various types of solar cell technologies and current trends of development (Sharma et al. 2015)

1.2.1 Solar spectrum

The Sun emits light in a range of wavelengths from the ultraviolet and visible to the infrared region. From the spectrum (**Fig 1.3**) it is very clear that, the maximum energy in the solar spectrum exists in the infra-red region (~55%), followed by the visible region (42%) and very little within the UV region (3%); which means that for better efficiency the solar cells must strive to absorb in the visible and IR region of the solar spectrum. This spectrum resembles the emission from a blackbody at a temperature of 5760 K. Generally, the emission is influenced by both the atmospheric absorption and the position of the Sun. To certify consistent test conditions, the American Society for Testing and Materials (ASTM) has set forth some parameters for solar irradiance. These include zero airmass (AM0), which is the solar irradiance

outside the earth's atmosphere, AM1.5, the standard solar spectrum and the black body spectrum. The values for these are $I_{AM0} = 1366.1 \text{ Wm}^{-2}$, $I_{AM1.5} = 1000.4 \text{ Wm}^{-2}$. The irradiance varies depending on the position of the Sun, orientation of the earth and sky conditions. There are two modes of irradiance, *i.e.* direct manner and diffuse light mode. The direct component can be concentrated, which increases the solar cell efficiency by increasing cell voltage output, whereas diffuse light arises by scattering of the sunlight in the atmosphere. Materials with rough surfaces such as DSSCs are relatively better suited for diffuse light than perfectly flat surfaces and they are less sensitive to movements of the Sun.

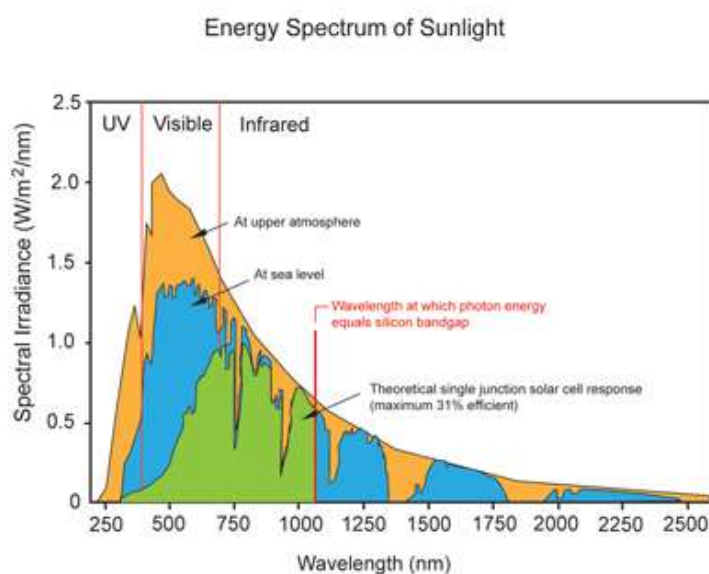


Fig 1.3 Solar irradiance spectrum at AM0

1.3.1 Solar cell terminologies

Fig 1.4 gives an equivalent circuit for an ideal solar cell consists of a current source in parallel with a forward biased diode. The performance of a solar cell mainly depends on a number of parameters like incident-photo-current conversion efficiency (IPCE), photocurrent (J_{SC}), photovoltage (V_{OC}), fill factor (FF), overall solar energy to electricity conversion efficiency (η). These photovoltaic parameters are discussed in the following section.

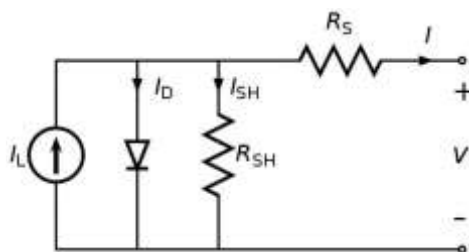


Fig 1.4 Solar cell equivalent circuit showing I_L (photo generated current in A), I_D (diode current in A and I_{SH} (shunt current in A)

1.1.3.1 Short circuit current (I_{SC})

The short circuit current is defined as the current from the cell when the load resistance is zero. Usually, solar cell current is represented as current density, J_{SC} value which is photocurrent per unit area (mAcm^{-2}) when a DSSC under irradiation is short-circuited. The equation 1.1 shows this relation.

$$J_{SC} = \frac{I_{SC}}{A} \quad (1.1)$$

where A is the effective area of the solar cell. It is a function of the solar illumination, optical properties and charge transfer probability of the cell.

J_{SC} value is related to IPCE spectra by the equation 1.2, where $I_s(\lambda)$ is the photo flux at wavelength λ under standard AM1.5 simulated sunlight. Thus, in order to obtain a high J_{SC} value, ideal molecular designs of sensitizer should feature the two major characteristics, *viz.* intense and broad sunlight-harvesting capability along with strong interactions between dye sensitizers and TiO_2 surface.

$$J_{SC} = e \int \text{IPCE}(\lambda) I_s(\lambda) d\lambda \quad (1.2)$$

1.1.3.2 Open circuit voltage (V_{OC})

The open circuit voltage (V_{OC}) can be defined as the difference in electrical potential between two terminals of a cell under illumination when the circuit is open. It is expressed by equation 1.3.

$$V_{OC} = \frac{k_B T}{e} \ln \left(\frac{J_{SC}}{J_0} + 1 \right) \quad (1.3)$$

where e is the elementary charge, k_B is the Boltzmann constant, T is the absolute temperature and J_0 is constant. In case of DSSC, the equation slightly modifies and it takes the form of equation **1.4**.

$$V_{OC} = \frac{E_{CB}}{e} + \frac{k_B T}{e} \ln\left(\frac{n}{N_{CB}}\right) - \frac{E_{redox}}{q} \quad (1.4)$$

Here n is the number of the electrons in semiconductor, N_{CB} is the effective density of states, and E_{redox} is the redox potential of the redox couple. Thus, the maximum V_{OC} value is calculated from the difference between the energy level (E_{CB}) of the conduction band of semiconductor and the redox potential of the electrolyte (I_3^-/Γ). Usually, experimental V_{OC} values will be lower than the theoretical value due to the undesired recombination process where the injected electrons recombine with I_3^- ions in the electrolyte and with dye cations.

1.1.3.3 Series resistance (R_S)

Series resistance abbreviated as R_S is a resultant of contact resistance and charge transfer resistance in the semiconductor material and its approximate value can be obtained from the slope of the I-V curve at the open circuit voltage point. The high value of R_S reduces the J_{SC} as well as FF, which further affects the maximum power output. In contrary, R_S value is unaffected by V_{OC} as the total current flow in this condition is zero.

1.1.3.4 Shunt resistance (R_{SH})

Normally a shunt allows electric current to pass around another point in the circuit by creating a low resistance path and the low resistance offered by it is called shunt resistance. Generally, low resistance may allow the photogenerated current to alternatively pass through, leading to significant power loss. Shunt resistance plays an important role in the performance of solar cell. Low shunt resistance results in the reduced Fill Factor and lower open circuit voltage there by decreasing the maximum power output. An approximation of the shunt resistance can be obtained from the slope of I-V curve (**Fig 1.5**) at the short circuit current point.

1.1.3.5 Fill factor (FF)

Fill factor is the ratio of maximum output power and the product of J_{SC} and V_{OC} values. FF reflects the extent of various electrical and electrochemical losses. Further, the betterment of FF can be obtained by an improvement in R_{SH} and decrement of the R_s values. The FF can be mathematically given by the equation 1.5.

$$FF = \frac{V_m \times I_m}{V_{OC} \times J_{SC}} \quad (1.5)$$

where, V_m and I_m are the voltage and current at maximum power point. Basically, the Fill factor is the measure of the square-ness of the I-V curve. When the value of FF , is closer to 1 the solar panel can provide more power.

Fig 1.5 is a typical I-V curve which shows the current and voltage characteristics of a particular photovoltaic cell or module which gives a detailed description of solar conversion ability and efficiency.

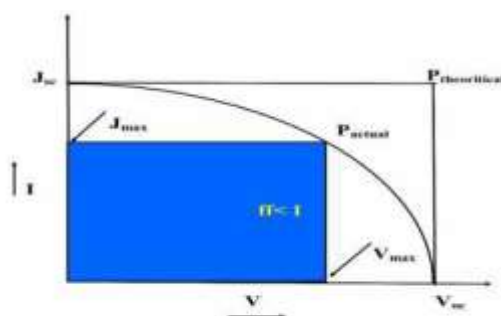


Fig 1.5 A typical I-V curve

1.1.3.6 Efficiency (η)

The efficiency (η) of solar cell is defined as the ratio of maximum electrical energy output to the energy input from the Sun. Mathematically, it is calculated by the equation 1.6.

$$\eta = \left(\frac{V_{OC} \times J_{SC} \times FF}{P_{in}} \right) \quad (1.6)$$

where P_{in} is the power input from the sunlight.

Besides the solar cell performance, the value of ‘ η ’ depends on certain factors such as the IPCE and intensity of incident light as well as operating temperature. In order to obtain a higher η , optimization of the V_{OC} , J_{SC} , FF values of the cell is essential.

1.1.3.7 Incident-Photo-Current Conversion Efficiency (IPCE)

Incident photon to current conversion efficiency or Quantum efficiency is a measure of efficiency of a solar cell in producing photo generated charge at a given wavelength of light. In other words it can be given as the ratio of the number of incident photon to the number of charge carriers generated and it is a function of the excitation wavelength as per equation 1.7.

$$IPCE(\lambda) = 1240 \times \frac{J_{SC}}{\lambda \times \phi} \quad (1.7)$$

where, J_{SC} is the short circuit current (mA/cm^2), λ is the wavelength (nm) and Φ is the incident radiative light flux (W/m^2).

For DSSC, the IPCE can be expressed as the product of light harvesting efficiency ($LHE(\lambda) = 1-10^{-10}$) at wavelength λ , quantum yield of electron injection (ϕ_{inj}) from the excited sensitizer into the conduction band of the TiO_2 electrode, and the efficiency of collection of the injected electron (η_{coll}) at the FTO glass. The mathematical equation is given below.

$$IPCE(\lambda) = LHE(\lambda) \times \phi_{inj} \times \eta_{coll} \quad (1.8)$$

Thus the IPCE of DSSC is directly related to the amount of adsorbed dyes on the TiO_2 surface (or LHE), electron injection efficiency into the conduction band of the TiO_2 , and electron collection efficiency in the external circuit under monochromatic illumination of the cell.

1.2 BRIEF HISTORY OF DSSC

Till date, photovoltaic market is dominated by traditional silicon solar cells. In spite of cost dropping over past decades, it is still expensive to compete with conventional sources of electricity. In this context, the concept of organic cell has been initiated as an alternative to the conventional silicon solar cells. Among the organic solar cells, DSSC does a prominent role. Although, the capability of organic

chromophores to generate electricity has been known from 1960s, the first attempt to generate electricity in DSSC was carried out in early 1970s. It was using ZnO sensitized with chlorophyll. This is the reason for referring DSSC as an ‘Artificial Photosynthesis’. The first embodiment of modern day DSSC dates back to late 1980s. Works by Gratzel and O’Regan in 1991, was a dawn to modern DSSC. They proved that DSSC can be feasible as an alternative energy source. Because of this, DSSCs are sometimes referred as Gratzel cell (Nazeeruddin et al. 1993; O’regan and Grätzel 1991). Since the invention of DSSC by O’Regan and Gratzel in 1991, it has been intensively studied for improvement. The fascinating features like low fabrication cost and relatively high efficiency have attracted the researcher’s interest towards it. The highest efficiency for DSSC with conventional ruthenium-based dyes is around 11.5% with iodine electrolyte. An efficiency of 28.9% has been reached for DSSC under indoor lighting by combining two dyes with cobalt electrolyte (Freitag et al. 2017).

1.3 KEY COMPONENTS OF DSSC

Generally, DSSCs consists of five main components, viz. transparent conductive substrate, mesoporous semiconductor, sensitizer, an electrolyte and a counter electrode.

1.3.1 Transparent conductive substrate

In a DSSC, transparent conductive material is made into a sheet which provides as a substrate for the deposition of the semiconductor, as well as acts as a current collector. For a DSSC to have a better efficiency, the transparency factor should be greater than 80% to allow the passage of maximum sunlight to the active area of the cell. The electrical conductivity of the transparent conductive substrate should be very high for efficient charge transfer and to minimize energy loss. FTO (fluorine tin oxide, $\text{SnO}_2:\text{F}$) and ITO (indium tin oxide, $\text{In}_2\text{O}_3:\text{Sn}$) are the majorly used transparent conductive substrates. Studies show that DSSCs with FTO substrates give better performance than that of ITO carrying devices as the resistance of FTO is independent of temperature. Thus, FTO is highly recommended for DSSCs due to its low-temperature stability. Further, polymers can also be used as an alternative to glass substrates and metals such as stainless steel, tungsten, and titanium also form a conducting layer and used as substrates.

1.3.2 Mesoporous semiconductor

Mesoporous semiconductor is an important component in a DSSC. Some of the desirable properties of these materials are higher light harvesting ability, electron injection, collection as well as low undesirable recombination capability. In any semiconducting material the electron transport rate highly depends on its crystallinity, morphology and the surface area. These properties affect largely on the efficiency of DSSCs. Despite of having good stability under irradiation in solution state, they cannot absorb visible light as they have relatively wide band gaps. Sensitization of wide band gap oxide with photosensitizers helps in absorbing radiation in visible range. The mesoporous semiconductor material coated on conducting material along with the sensitizer works as a working electrode. Examples of semiconductor materials used are titanium oxide (TiO_2), zinc oxide (ZnO), and stannic oxide (SnO_2). Experiments have shown that DSSCs based on ZnO and SnO_2 yield a lower efficiency in comparison to those based on nanocrystalline TiO_2 .

An ideal working electrode is made from a nanoporous semiconducting oxide layer which facilitates a high specific surface area for dye adsorption and good interconnection in between nanoparticles. In addition to dye adsorption, this mesoporous TiO_2 act as a sink for the transport of the photogenerated electrons. The mesoporous morphology of it gives a high specific area as well as a network of charge recombination sites. The properties of TiO_2 such as high refractive index, a good chemical stability, amphoteric surface and a low production cost make it widely acceptable. The nanocrystalline particle size of TiO_2 also matters in the DSSC. Normally, it is around 20 nm. To achieve this, the colloidal TiO_2 dispersion is applied to FTO substrate. Widely used techniques for deposition of TiO_2 layer on FTO are ‘Screen Printing’ and ‘Doctor Blading’ methods. The coating is followed by the annealing of TiO_2 film at 450-550 °C which removes the organic additives and helps in forming the good interconnection between the TiO_2 particles. When compared to the flat electrode, mesoporous electrodes are having 1000 times better surface area. The porous nature helps to fill the pore with an electrolyte which in turn assists to boost up the contact between dye molecule and electrolyte. Thus mesoporous TiO_2 acts as an excellent candidate for *n*-type semiconducting material for photo anodes.

1.3.3 Sensitizer

Among the various components of DSSC, the sensitizer which harvests solar energy and injects electrons into the semiconductor layer plays a crucial role in achieving high injection rate, thereby increasing the efficiency of the cell. An ideal sensitizer should possess some distinct properties. Firstly, it should have a broad and intense absorption band in highest photon flux region in order to harvest a good amount of light. Secondly, it should ensure the effective injection of a charge carrier to semiconductor for which anchoring group such as carboxylate or phosphate is required to graft the dye itself to a semiconductor which aids the injection of electron from excited dye to semiconductor. Thirdly, the molecular orbital levels of dyes should be placed in a way as to facilitate the injection of charge carrier to the valence/conduction band of semiconductor and should also match with the redox couple so as to regenerate the oxidized dye. The molar extinction coefficient of dye depends on the absorbance of light. Higher the molar extinction coefficient, better its absorbance capacity with a thinner semiconductor film. Last but not the least; the dye should have good stability, *i.e.* photoactive property at least 20 years of throughout current generation cycle under illumination. Based on the types of sensitizers used, DSSC can be broadly classified into metal-based DSSC (generally Ruthenium-based dyes) and metal-free DSSC.

1.3.3.1 Metal-based dyes

Most comprehensively studied metal-based dyes are ruthenium-based complexes. Several other heavy metals that are capable of producing triplet excited states have been deployed as central metal, replacing ruthenium. Metals like copper, osmium, iron and platinum have also been studied. However, in most cases the photocurrent extracted were very poor due to the poor injection and dye regeneration efficiencies. Ruthenium (Ru) metal complexes have shown very good photovoltaic performances comparing to all the rest. Ruthenium (II) complexes have been studied heavily since Grätzel and O'Regan had reported an efficient DSSC system with poly pyridyl ruthenium (II) complex dyes adsorbed on a crystalline *n*-type TiO₂ in 1991. Ruthenium complex dyes show some characteristic properties like broad absorption spectra through metal to ligand charge transfer (MLCT), the longer excitation lifetime

and chemical stability. Ru complexes with carboxylated bipyridine ligands were first used for sensitization of TiO₂ single crystals in 1979. De Silvestro and his coworkers reported a dye with three carboxylated bipyridine ligands to obtain an *IPCE* of 44%. A breakthrough finding by O'Regan and Gratzel was the discovery of a new dye with a trinuclear Ru complex on a mesoporous TiO₂ electrode with an efficiency (η) of 7.1-7.9%. Followed by this, in 1993 they designed a series of dyes. Among these dyes, the thiocyanate derivative *cis*(SCN)₂ *bis*(2,2'-bipyridyl-4,4'-dicarboxylate)-ruthenium(II) (coded **N3**) had shown an excellent efficiency of 10% for the first time. Later, Grätzel and co-workers had designed the 'black dye' coded as **N749** with ruthenium center containing one terpyridine and three carboxyl groups and three thiocyanate ligands. **Black dye** exhibited a broad spectrum near to IR region of 920 nm and yielded a conversion efficiency (η) = 10.4%, $J_{SC} = 20 \text{ mAcm}^{-2}$, $V_{OC} = 720 \text{ mV}$, $FF = 0.7$ under AM1.5 μ . In the year of 2014, Cheema et al. reported two heterolyptic Ru (II) bipyridyl complexes, *viz.* **HD-2** and **HD-2** mono, displaying enhanced efficiency, when compared to the basic dye **N719**.

1.3.3.2 Metal-free organic dyes

In recent years, as an alternative for ruthenium sensitizers, organic metal free dyes have been investigated. Metal-free dyes have some edge over to metal-based dyes. The key points are mentioned below.

- Diverse forms of organic dyes are available and it can be easily designed and synthesized.
- Metal-free dyes are superior to metal-based dyes concerning the environmental friendliness.
- It is cost effective as it allows fabrication of foldable and flexible large area devices.
- Normally, molar extinction coefficient of organic dyes is much higher than Ru complexes.

As described in the literature, general design of DSSC involves incorporation of an electron donor (D), π -conjugated spacer and an electron acceptor (A) moieties. Among these, the heavily explored configuration is D- π -A system. Considerable work

have been performed by changing different parts of organic dyes to optimize DSSC performance.

Based on the design and variation in the working principle, metal-free dyes are classified as *n*-type and *p*-type.

1.3.3.2.1 Organic chromophores for DSSC

The chromophore is a region in a molecule that absorbs light of certain wavelength of visible region and transmits or reflects others which imparts color to the molecule. Thus, visible light that hits the chromophores can thus be absorbed by exciting an electron from its ground state into an excited state. In the class of organic chromophores, heterocyclic compounds play prominent role and they constitute two-third of known organic compounds. These compounds have a vital significance in organic chemistry because of their varied configuration with regard to carbon rings and differences from each other. Majorly, heterocyclic compounds possess important applications as dyestuffs, fluorescent sensors, brightening agents, information storage, plastics, and analytical reagents. Heterocyclic compounds are intensively studied in the field of dyes; in fact numerous dyes found in nature are heterocyclic compounds. Some of the examples include an important vat dye indigo, which contains two indole units, and then another example is Tyrian dye obtained from species of snails. The photophysical properties of heterocyclic systems make them good candidates for photosensitizer application. Aryl amines are another group of aromatic chromophores which find a greater application in the field of DSSC. They possess simple structures and can easily be derivatized to achieve the desired properties in them.

Diphenylamine

Diphenylamine (DPA) is a derivative of aniline with the formula $C_{12}H_{11}N$, consisting of an amine bounded to two phenyl groups. As discussed in previous sections, aryl amines are promising donors for metal-free DSSC as sensitizers. The bulky phenyl groups in diphenyl amines are electron rich scaffold, this electron richness is one of the essential features for efficient dyes. The geometry of diphenylamine is quite interesting to study. DPA is having a pyramidal geometry in the ground state and planar geometry in the first excited state. It changes from this pyramidal geometry around the N-atom with unequal torsional angles of the phenyl

groups to the planar geometry. The two major features which play an important role in the intra-molecular dynamics and in the chemical behavior of the molecules are (i) the equilibrium orientation of the phenyl rings (twist angle, Φ) of the phenyl group around the C-N groups relative to the C-N-C plane (ii) the frequencies of the corresponding torsional motions. **Fig 1.6** shows the structure and electrostatic map of diphenylamine. The figure also depicts the torsional angles $\Phi(a)$ and $\Phi'(a')$ of the phenyl groups around the C-N bonds and the C-N-C bond angle $\theta(b)$. These interesting properties of diphenylamine make it a favorite candidate for metal-free sensitizer.

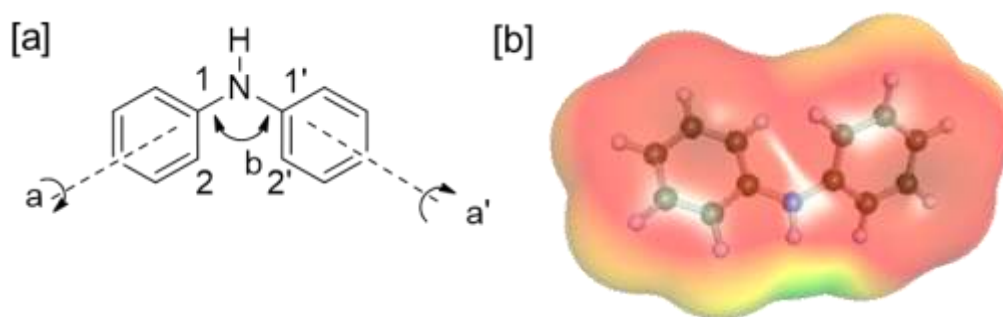


Fig 1.6 (a) Structure of diphenyl amine; (b) its electrostatic potential map

1.3.4 Counter electrode

Generally, the counter electrode acts as a interface where the oxidised electrolyte gets reduced. Platinum coated on FTO is a majorly used counter electrode (CE) in DSSC. During functioning of DSSC, the oxidized electrolyte diffuses towards the counter electrode where it accepts electrons from the external circuit. The platinum in counter electrode acts as a catalyst to accelerate the reduction reaction. Platinum is a preferred catalyst because of its high exchange current density, good catalytic activity, and transparency. Due to scarce and expensive nature of platinum, other materials such as graphite, carbon black, carbon nanotubes and activated carbon coated on FTO may be used as CE. Good electronic conduction, as well as catalytic activity, was observed for a mixture of graphite and carbon. Further, organic ion doped conducting polymer, *i.e.* poly(3,4-ethylene dioxythiophene) (PEDOT) on both ITO and glass have been proposed as CE.

1.3.5 Electrolyte

The last key component of dye sensitized solar cells is an electrolyte. The bench marks for an efficient electrolyte are (i) the photoexcited dye has to lose an electron before it reacts with the electrolyte, (ii) the oxidized dye molecule has to be reduced by the electrolyte rather than recombined with the electrons from the neighboring dye molecule, (iii) the reduced electrolyte has to react slowly with electrons in both TiO₂ and transparent conducting oxide (TCO) layers and (iv) the reduction rate of the oxidized ion at the cathode is to be rapid.

An important constituent of liquid electrolyte is the redox couple. Since the first work reported on DSSC, I⁻/I₃⁻ system is extensively used as redox couple in this field. Redox couple works as a charge carrier where it collects electrons at cathode and transports them back to the dye molecules. Organic solvents are being used as electrolytes which act as a neutral sink of I⁻ and I₃⁻ maintaining the redox potential in the bulk of the electrolyte *via* the fast redox reaction of the I⁻/I₃⁻ pair. A study reveals that I⁻/I₃⁻ in acetonitrile have given a good efficiency (η) of 11%. Studies have also been carried out in Br₂/Br⁻ based redox couple. Liquid electrolytes have many advantages like high ionic conductivity and good interfacial contact property whereas its volatile nature of solvent and leaking property leads to difficulty in dealing with it. To overcome this, room temperature ionic liquids (RTIL), quasi-solid state and solid state liquids have been studied. Ionic liquids were shown to be an alternative for the organic solvents as they possess very low vapor pressure and high ionic conductivity. However, their high corrosion rate and toxicity make them less acceptable. Recently, studies have been carried out on cobalt (Co^(II/III))poly pyridyl complexes as redox couple in combination with ruthenium dyes. They showed an impressive efficiency of over 8% at a low light intensity under full sunlight illumination. In Co^(II/III)-bipyridine redox electrolyte with zinc porphyrin has given an efficiency of 12.3%.

1.4 WORKING PRINCIPLE OF DSSC

Basic operating principle for all solar cells consists of three major processes, *viz.* absorption, separation and collection. Better efficiency is obtained by the optimization of these processes. Working principle of DSSC is no different but in this case separate mediums are used for light absorption or carrier generation (dye) and

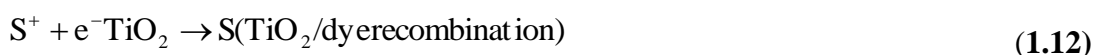
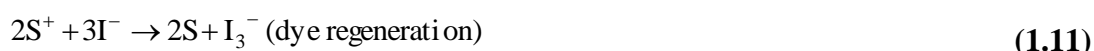
carrier transfer (semiconductor nanoparticles) unlike other solar cells, where a single medium is used for both the functions. In conventional silicon cell also, silicon acts as both source of photo electrons as well as providing the electric field to separate the charge and create a current. Unlike these silicon-based dyes, DSSC makes use of semiconductor solely for charge transport and a photosensitive dye to provide photoelectrons.

The general operating principle of DSSC includes excitation of the sensitizer by absorbing a photon. It follows the injection of the charge carrier from the excited sensitizer to the semiconductor. The charge is then transported through the semiconductor to the reach the CE through the external load. On the other hand, the oxidized sensitizer combines with an electron from the redox mediator and regenerates rapidly to the ground. In total, it can be said that, this cycle completes in a regenerative and stable photovoltaic energy conversion system as no net reaction occurs. Thus, the overall efficiency of the device is determined by the optimization of each of these processes, *i.e.* charge injection, charge recombination and dye regeneration. Among these three processes, charge injection triggers the operation cycle. Certain parameters should be satisfied for an efficient ultrafast injection processes in order to obtain a higher efficiency. Firstly, a strong overlap of acceptor units of dye should be there with the acceptor state of metal oxide electrode. Secondly, an optimized distance should be there between the dye and the acceptor metal oxide. Finally, the dye should not be aggregated. In DSSC, an undesirable process which leads to decrease of efficiency is the recombination. An optimized molecular structure of sensitizer is required to suppress the recombination process which further leads to dark current. Fast dye regeneration is a prerequisite for an efficient DSSC. The reduced form of redox mediator in the liquid electrolyte regenerates the dye in ground state prior to the back electron transfer. Ideally, this redox mediator should not absorb light for avoiding the photon-to-current-efficiency losses.

Based on the working principle metal-free sensitizers can be further divided into *n*-type sensitizers and *p*-type sensitizers.

1.4.1 *n*-Type DSSC

n-Type DSSC comprises of dye molecule which is coated on a semiconductor generally TiO₂, an electrolyte and a counter electrode. In this case, TiO₂ coated plate acts a photoanode. The operating principle is summarized in the equations **1.9-1.13**.



When exposed to sunlight, the dye molecule goes to an electronic state change from the ground (S) to the excited state (S*) whose lifetime is in order of few nanoseconds (**1.9**). By irradiation, the dye molecule adsorbed on the typically TiO₂, gets excited and then transfers an electron to the CB of the TiO₂ (**1.10**). The efficient electron injection is carried out when the Lowest Unoccupied Molecular Orbital (LUMO) level of dye is higher than the CB of TiO₂. The injection rate constant is in femtosecond range for singlet state.

The nonporous TiO₂ film consists of spherical anatase particles of diameter approximately of 20 nm. In the lattice, oxygen vacancies are there which make it a weakly *n* doped as the small particle size of TiO₂ restricts it from building the electric field. The circuit is completed as the electron travels through the external load and reaches the backside of CE and reduces the iodine in the electrolyte. The iodine reduction can also occur with the excited dye molecules causing recombination of the photo generated electron which is called dark current (**1.13**). The rate of iodine reduction at the CE has to be faster than that of the process of recombination at the TiO₂/electrolyte interface for an efficient charge transfer. The reduced iodide ion combines with the Highest Occupied Molecular Orbital (HOMO) of the dye to regenerate in the original form and makes it ready for electron generation (**1.11**). The HOMO level should be lower than the iodine to facilitate the effective regeneration. Photo anode reaction prevents the accumulation of the S*, which can lead to the

recombination of electrons in CB of TiO_2 with that of dye molecules (1.12). The working principle is summarized in Fig 1.7.

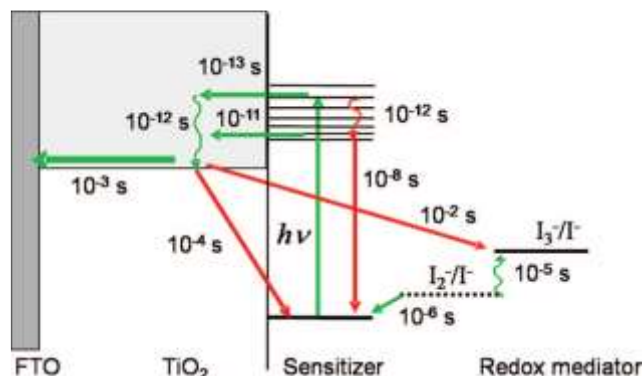


Fig 1.7 Schematic representation of working in *n*-type DSSC (Hagfeldt et al. 2010).

1.5 ADVANTAGES OF DSSC OVER OTHER PHOTOVOLTAICS

In the earlier sections, three generations of solar cells have been discussed. Among them, the first generation solar cells are dominating in the commercial scale at present. Solar cells of second generation is also having a better efficiency. Even though the power conversion of DSSCs (III generation) is not comparable to either I or II generation solar cells, it has an edge over in some points. These points are as follows.

- DSSC is one of the promising III generation photovoltaics. The power conversion efficiency has even crossed 13% with co-sensitization, which is comparable to both I (5-13%) and II generation solar cells (12-15%).
- In DSSC, the role of the semiconductor is solely of charge transporting, charge being supplied by dye, whereas, in silicon solar cell, it acts as both source of electron and electric field provider. Thus, optimizing is a much easier task in DSSC.
- Only low cost and abundantly available materials are required for DSSC which makes it cost effective.
- It does not demand high energy, costly high vacuum and materials for purification steps for the production of I and II generation cells.
- One of the major advantages of DSSC is that, it efficiently works even in low light conditions. This makes it popular in cloudy weather condition or non-direct sunlight where silicon-based cells fail to work efficiently. As the cutoff

light in DSSC is so low, they have been proposed for indoor usage to collect energy for small devices from the lights in the house.

- DSSCs are fabricated in a way which enhances efficiency. It uses a thin layer of conductive plastic on the front side to allow radiation of heat much easily and quickly. Therefore it operates at low internal temperature, whereas traditional solar cells are encased in glass with a metal at the back for increasing its strength which decreases its efficiency as the cells heat up internally.
- In the temperature range of 25-65°C DSSC efficiency is nearly temperature independent. But, the efficiency of silicon cells declines by 20% in this range.
- The DSSC technology can be expanded up to terawatt scale without facing material supply problem unlike I and II generation solar cells, which make use of highly toxic materials of small natural abundance.
- DSSCs have decorative effects when used in window panels of buildings, constructions and fancy materials.

1.6 CHALLENGES IN THE FIELD OF DSSC

The researches in the field of DSSC have gone in a rocket-up scale in the past few decades. However, many factors are to be tackled to compete with silicon solar cells in a commercial scale, for which it requires further optimization with regard to photovoltaic parameters. Unlike single material based semiconductor, DSSC has several key points which allow numerous innovative approaches. There is much scope for active research on various components of DSSC, which include mainly sensitizers, semiconductors, electrolyte, counter electrode and transparent conductive substrate. Several studies have been carried out in each component to achieve a better performance. The total performance of DSSC largely depends upon the photovoltaic parameters, *i.e.* J_{SC} , V_{OC} , and FF values. One has to improve these parameters to achieve a better efficiency which is a difficult task to fulfill. Among the key components, sensitizers have a pivotal role. As it is the medium to absorb light and inject the charge carrier to the semiconductor, its improvement will attribute to the overall cell-efficiency. Thus, designing of an efficient dye as a sensitizer comes into picture which further contributes to the overall performance of the cell. It is

challenging task to design a dye considering all the criteria. The general designing strategy for sensitizers has been discussed in detail under section 1.11. One of the major challenges in designing of sensitizer is to attain absorption of wide range of solar spectrum from the UV to IR region, which effectively contributes for improvement in the photocurrent. Ideally, a sensitizer should absorb solar light from the UV to IR region. The researchers have found out solutions for this problem. One of them includes co-sensitization technique.

1.7 CO-SENSITIZATION

Dye-sensitized solar cells are promising tools for harvesting solar energy. To achieve high efficiencies, it is vital to synergistically improve the J_{SC} and the V_{OC} . This can be conveniently achieved by the extension of conjugation frame work for sensitizers and co-sensitization methods. Co-sensitization can be considered as a technique involving sensitization of a semi conductor (metal oxide) electrode with two or more different dyes. The major contribution of co-sensitization is that it helps to enhance the light harvesting capability of dye by expansion of the light absorption range. Co-sensitization has been mainly carried out by two different approaches, a “stepwise sensitization” and a “dye-cocktail” method. In stepwise sensitization approach, TiO_2 electrode is dipped sequentially into each dye solution. In this method, dyes are adsorbed by turn onto the vacant spaces of the TiO_2 surface, where the previous dyes are not adsorbed completely. Therefore, the vacant spaces can be effectively filled in, and as a result, competitive adsorption does not occur. However, a cumbersome optimization such as relative dye concentration, dipping time, dipping order, and other conditions for each dye solution is required to achieve the highest efficiency. In contrast, the dye-cocktail method involves making use of a dye-mixture solution. Here, the factors like the extent of dye adsorption, dye mixing ratio play an important role in determining the overall efficiency of the cell. However, a decrease in the dye loading amount of the base-dye is expected because of competitive adsorption. Therefore, each method possesses certain merits as well as drawbacks, which finally affect the performance of the cell. For achieving high photovoltaic performance, certain structural and electronic criteria of co-sensitizers as well as base-dye should be fulfilled. From the view point of electronic structure, they should

possess two major requirements, *viz.* (i) matching of absorption characteristic of base-dye and co-sensitizer to enable a wide coverage of the solar light spectrum (ii) appropriate HOMO and LUMO energy levels for both the dyes. Also, the structural requirement must include the suppression of unfavorable dye aggregation, for which introduction of bulky substituents or long alkyl chains are most essential. Further, co-sensitizers should possess small size in order to effectively fill the vacant spaces between the molecules of base-dye, on the surface of semiconductor.

1.8 INSPIRATION FOR PRESENT WORK

One of the greatest challenges ahead of human kind is to replace the fossil fuel with a clean and cheap source which is indeed the Sun. Harnessing the power of the Sun with photovoltaic technologies appears to be the only reasonable large-scale answer to energy challenges. As the inorganic-based photovoltaics require high cost and high energy consuming methods for purification and fabrication, research on organic photovoltaics gains strength. As the inorganic-based photovoltaics require high cost and high energy consuming methods for purification and fabrication, research on organic photovoltaics gains strength and importance. However, developing organic photovoltaic devices with good light harvesting ability and optimum carrier transporting characteristic is a difficult task. In this context, DSSC, an example of organic photovoltaics is gaining much prominence. As discussed earlier, DSSC consists of two separate components for light harvesting and carrier transporting. Here, the charge generation occurs at the semiconductor-dye interface and the charge transport is facilitated by the semiconductor and the electrolyte. The major component of DSSC is the sensitizer whose structure and properties play a significant role in enhancing the performance of DSSCs. Obviously, an efficient harvesting of light energy can be achieved by the use of appropriate sensitizer, engineered by suitable structural design. Further, the carrier transport properties can be improved by optimizing the properties of the semiconductor as well as the electrolyte.

From all the factors discussed above, it can be concluded that, the designing strategy of dye affects the efficiency of DSSC. While designing, selection of suitable donor, π -spacer and acceptor/anchoring group is an important criterion for better

efficiency. Thus, there is an ample of scope for development of new sensitizers for DSSC.

1.9 STRUCTURAL DESIGN OF SENSITIZERS

As sensitizer is a key element for light harvesting and electron injection, it plays a vital role in developing an efficient DSSC. Dye design strategy plays a crucial part in the ongoing optimization of DSSC and it requires complete study of structural features of sensitizer. As already mentioned in earlier sections, an ideal dye should have two major characteristics. Firstly, sensitizers should have a broad and intense absorption band in the visible and near-IR region. Secondly, the dye must ensure an effective injection of charge into the semiconductor surface. Also, it should have improved opto-electronic properties. So far, the most comprehensively studied dyes are metal-based ruthenium complex dyes, which induce high PCE. Among the ruthenium based dyes, **N719** is considered to be the benchmark, simply because of its broad range of absorption, high efficiency of electron injection and slow rate of recombination. **N3** and **N749** (Black dye) are also best known among ruthenium-based dyes. The efficiency of DSSC is reflected in its photovoltaic parameters. One of the parameters, *i.e.* V_{OC} largely depends on interfacial charge recombination kinetics in the cell. In fact, the theoretical V_{OC} is considered to be the difference between the quasi-Fermi level of the semiconducting oxide and the redox potential of the redox mediator. Another parameter, FF is proportionally related to the total device resistance. Further, the J_{SC} value is related to extent of adsorption of the sensitizer, in turn IPCE values.

However, these ruthenium complexes suffer from disadvantages such as high cost and the need for sophisticated preparation techniques. Metal-free dye is an attractive alternative with substantial enhancements over the organometallic counterparts. It possesses several merits such as low cost of production, high molar extinction coefficient, ease of synthesis and environmental friendliness due to absence of metal ions.

Designing of sensitizers plays a vital role in obtaining an effective dye. With the help of theoretical methods a series of organic sensitizers based on different configurations like D- π -A, D- π -A- π -D, D- π -(A)_n, (D)_n- π -A, D- π -A- π -D, D-(π -A)_n

where $n = 1-4$, were designed by (Tseng et al. 2014). Most studied metal-free dyes consist of an electron donor (D), and an electron acceptor (A) at two ends which are connected by a π -spacer. **Fig 1.8** shows the schematic representation of a dye attached to a TiO_2 . All the three aforesaid parts have been shown to possess inevitable role in the designing of dye. The donor should have enough electron cloud to push onto the spacer which then propagates through conjugation, that is then pulled by the acceptor system. Finally the electrons are injected onto the conduction band of TiO_2 . The HOMO level of dye should be sufficiently positive than the electrolyte system to generate the dye molecule and also the LUMO level should be more negative than the conduction band edge of TiO_2 indicating that the electron can be energetically injected into the TiO_2 conduction band. Further, the literature reports reveal that the introduction of bulky groups, long hydrophobic alkyl and alkoxy chains on the donor (D) moiety or/and π -bridges, effectively blocks the approach of hydrophilic I_3^- ions to the metal oxide surface, and thus, suppress charge recombination. This phenomenon further results in an increase in the electron lifetime and V_{OC} value. The introduction of hindered substituents also suppresses the dye aggregation owing to a disturbance in the intermolecular π - π stacking. The accepting property of acceptor group is directly related to the electron affinity. So while designing, one has to concentrate to have a higher V_{OC} , J_{SC} , IPCE, molar extinction co-efficient and FF for enhanced efficiency of the cell. Different configurations (Tseng et al. 2014) other than conventional D- π -A systems were also shown to possess an improved photovoltaic performance. Thus, exploring new designing strategies would lead to development of new effective sensitizers for DSSCs.

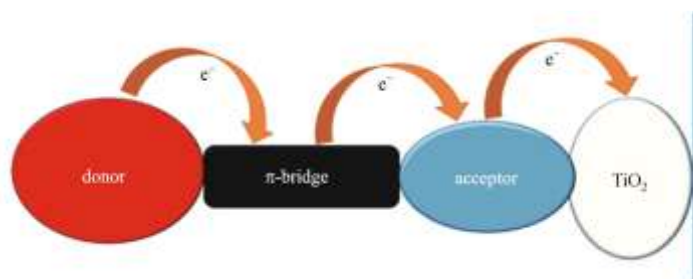


Fig 1.8 Schematic representation of a D- π -A configuration on TiO_2

1.10 CHARACTERIZATION TECHNIQUES

Generally, in the field of DSSCs, several characterization techniques are available for structural, photophysical, electrochemical and photoelectrochemical studies of sensitizers. Among them, structural characterization of new sensitizer is an important stage. Normally, a host of various methods like FTIR, NMR and Mass spectroscopic techniques are used for elucidating the structure of newly synthesized molecules. Further, in order to evaluate the photophysical properties, *viz.* λ_{abs} , λ_{emi} , E_{0-0} and ϵ , UV-Visible as well as Fluorescence spectroscopy is employed both in film and solution states of sample. Furthermore, cyclic voltammeter is utilized for determining various parameters such as E_{ox} , E_{ox}^* , E_{g} , ΔG_{inj} , ΔG_{rec} , ΔG_{reg} , *etc.* of the dyes. Most of the physical parameters including optimization of geometry are assessed by theoretical studies using Turbomole 7.2V software. Normally, performances of DSSCs are evaluated by the parameters such as V_{OC} , J_{SC} and η which are determined using the Oriel SOL3A solar simulator connected to Keithley 2400 source meter. Also, the IPCE is determined using QEX10 PV measurement system. In addition, EIS studies of devices are generally carried out in order to determine the charge dynamics with the help of Nyquist and Bode plots using Biologic SP-150 potentiostat.

1.11 BROAD OBJECTIVES OF THE PRESENT WORK

In the literature, several new organic chromophores with different structural configurations were reported as effective sensitizers as well as co-sensitizers for DSSCs. Also, their structure and photovoltaic parameters were correlated to throw light upon new design strategy used. In the next chapter, a detailed account of the literature survey on different types of organic chromophores as effective sensitizers/co-sensitizers has been included. Based on the literature reports, it was thought of designing several new *n*-type diphenylamine based metal-free chromophores, using different designing-strategies, as effective sensitizers/co-sensitizers for DSSC application. Further, it has been planned to synthesize newly designed molecules using standard synthetic protocols. Finally, it has been intended to fabricate DSSCs using new chromophores as sensitizers/co-sensitizers, keeping semiconductor and electrolyte unchanged in the cell. It has been also contemplated to

study the effect of structure of chromophores on device performance. It is hoped that new sensitizers/co-sensitizers would lead to improved efficiency and give valuable information about structural dependence on DSSC device parameters.

1.12 THESIS STRUCTURE

The entire thesis has been divided into six chapters. **Chapter 1** outlines a brief introduction to solar cells giving an emphasis on the dye-sensitized solar cells. Further, it covers description on *n*-type DSSCs including areas like different components, working principle, characterization techniques and design strategies for new sensitizers. It also involves the broad objectives of the work. **Chapter 2** includes a review of literature reported on design and synthesis of diphenylamine based dyes consisting of different auxiliary electron donors, π -spacers and acceptor units. This chapter extends with scope and objectives of the present research work, arrived at on the basis of detailed literature survey. Finally, it describes the design of seven new series comprising twenty seven *n*-type dyes as sensitizers/co-sensitizers for DSSC application. The experimental protocols leading to the synthesis of twenty-seven new organic sensitizers have been elaborated in **Chapter 3**. In addition, their structural characterization has been discussed in detail. **Chapter 4** describes a detailed account of investigation of optical and electrochemical properties of newly synthesized dyes. It also comprises their theoretical investigations using DFT simulations. **Chapter 5** consists of a detailed DSSC fabrication studies using the newly synthesized dyes as sensitizers/co-sensitizers. Also, results of their photovoltaic performance have been discussed in this chapter. Further, it covers estimation of electron lifetime as well as charge transport phenomenon of fabricated devices by EIS studies. Finally, **Chapter 6** includes the summary of the entire work and important conclusions as well as the outcome of the research work.

LITERATURE REVIEW, SCOPE, OBJECTIVES AND DESIGN OF NEW SENSITIZERS/CO-SENSITIZERS

Abstract:

Chapter 2 includes a detailed literature survey on different n-type diphenylamine based organic dyes as sensitizers/co-sensitizers for DSSC application. Further, it covers the scope and objectives of the present research work, derived from the literature survey carried out. In the end, design of seven new series of diphenyl amine based n-type dyes with various structural configurations has been incorporated.

2.1 INTRODUCTION

One of the biggest challenges of mankind is to replace the fossil fuel with a more cleanly renewable source keeping pace with the worldwide increasing thirst for energy. Therefore, it is high time to start looking for alternative sources of energy. The best alternative source is solar energy. Harvest of solar energy has always been one of the biggest endeavours of mankind. Up to now, commercially available photovoltaic technologies are based on inorganic materials, which require high costs and highly energy consuming preparation methods. An alternative for these issues is DSSC technique, but their efficiencies are still a long way behind the inorganic based silicon photovoltaic technologies. Thus, optimization of DSSC is required to achieve a ‘business-as-usual’ scenario. In DSSC, sensitizer is a major component which acts as a harvester of light energy. Based on literature reports, it is evident that enhancement of solar cell efficiency can be achieved by improving the property of sensitizer. Particularly, its geometry and electronic structure play a vital role on overall performance of the cell. Lots of literatures are available on different metal-free sensitizers based on various organic entities.

From the past few years, the reports of n-type organic co-sensitizers employed along with interesting Ru (II) based sensitizers, such as **N719**, **NCSU**, **HD-2**, *etc.*, are gaining much interest. Since the co-sensitization can improve the light harvesting ability of the cell, this concept has gained considerable importance.

Keeping all these in view, a detailed literature survey on organic sensitizers as well as co-sensitizers has been carried out and accordingly the major objectives of the

present research work have been identified. Various aspects like design concepts, structure-performance correlation, importance of geometry and electronic structure of reported organic based sensitizers/co-sensitizers have been discussed in the following section.

2.2 LITERATURE REVIEW

Even though enormous number *n*-type sensitizers have been reported, the quest for highly efficient sensitizer is still in progress. Generally, an ideal sensitizer should possess favorable electronic structure to acquire requisite spectral, electrochemical and photoelectrochemical properties in it. In the literature, a wide range of design strategies have been reported for the development of effective organic sensitizers. Amongst them, push-pull approach, *i.e.* D- π -A strategy, wherein an electron rich donating and electron deficient withdrawing scaffolds connected through a π -spacer unit, is considered to be one of the most promising and successful architectures to improve the photovoltaic performance of DSSCs. In such dyes, photo-induced ICT (Intra-molecular charge transfer) phenomenon can easily be controlled and their photophysical properties can be tuned by varying donor, spacer and the acceptor moieties in the structure. For instance, extension of the π -electron delocalization in the dye molecule improves its molar absorptivity coefficient. Moreover, it leads to an efficient charge separation and easy movement of electron from donor to the acceptor moieties in the dye. Several organic dyes derived from electron rich triphenylamine, diphenyl amine, aniline derivatives and fused heteroaromatic compounds such as carbazole, indole, phenothiazine, phenoxazine, perylene and cyanine systems have been reported as good sensitizers with improved photon conversion efficiency when used in DSSCs. The relation between different architectures and their photovoltaic parameters were studied in detail.

In the following section, reports on various design strategies relevant to electron rich diphenylamine based dyes carrying different spacer units and anchor/acceptor functionalities, and their effect on device performance as sensitizers, have been highlighted. Also, interesting aromatic/heteroaromatic dyes showing good co-sensitization behavior along with the most popular metal bound sensitizers have been discussed briefly.

2.2.1 Diphenylamine based sensitizers

Aromatic amine derivatives are being used immensely as donor moieties owing to their electron availability and richness. Among amine derivatives, diphenyl amine is one of the interesting and potential donor systems because of its easy derivatization. In the literature, few references are available on synthesis and investigation of device performance of new diphenyl amine based dyes carrying different anchoring groups with various spacer units.

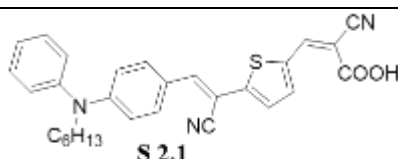
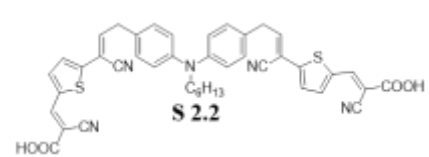
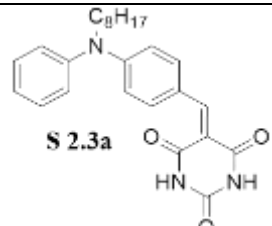
Hong et al. 2011 reported synthesis of a new series of dyes carrying *N*-substituted diphenylamine and carbazole as donor units. These dyes were used as sensitizers in DSSCs and their photoelectrochemical parameters were investigated. Among the reported sensitizers, diphenylamine dye (**S 2.1**) with thiophene acetonitrile and cyanoacetic acid as spacer unit and anchoring group, respectively displayed a PCE of 3.80%. This simple dye showed better absorption spectra when compared to its counterpart containing carbazole as donor system.

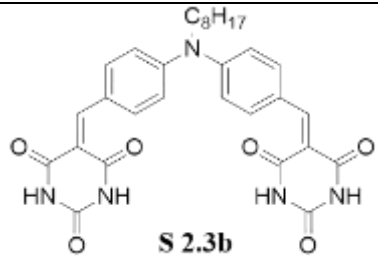
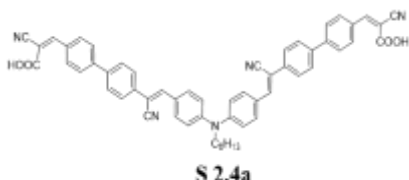
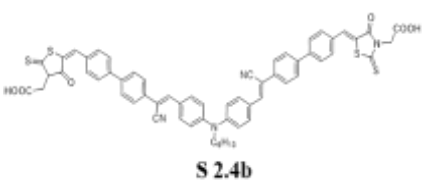
In the year of 2013, Ramkumar S. and Anandan S. synthesized a bi-anchored metal-free organic dye with diphenylamine (**S 2.2**) as a donor, thiophene acetonitrile unit as a π -bridge and cyanoacrylic acid group as an electron acceptor/anchor. They also studied the device performance using newly synthesized dye as sensitizer. It showed a maximum current conversion efficiency of 3.16%. In addition, it exhibited λ_{abs} and λ_{emi} at 458 and 582 nm, respectively and good adsorption to TiO₂ semiconductor film.

Later, in 2015, Hosseinzadeha and his group studied a series of novel sensitizers with diphenylamine (**S 2.3a-b**) as donor moiety. They synthesized and characterized bi-anchoring donor- π -acceptor architected dyes carrying barbituric acid and thiobarbituric acid as the acceptor/anchor moieties. Among the fabricated DSSCs, dye with structurally simple diphenylamine donor, and barbituric acceptor (**S 2.3a**) exhibited a high power conversion efficiency of 1.53% with a short circuit current density of 3.71 mAcm⁻², an open-circuit photo voltage of 550 mV and a fill factor of 0.75% under AM1.5 illumination (85 mWcm⁻²). Interestingly, they displayed intense absorption and emission behaviour due to their D- π -A architecture.

Again, in 2015 Ramkumar along with co-workers reported D-(π -A)₂ type diphenylamine based chromogens for DSSC application as sensitizers. In the newly designed sensitizers, conjugated cyano vinyl biphenyl system acts as the π -spacer. These dyes contain cyano acetic acid (**S 2.4a**) and rhodanine acetic acid (**S 2.4b**) as anchoring groups. They showed strong absorption and emission characteristics due to their favourable structural features. Further, the DFT studies indicated a good charge separation in HOMO and LUMO levels of both the molecules. This charge separation effectively contributes to the electron injection from LUMO to the CB of TiO₂. The authors observed an efficiency of 1.02 % for the sensitizer **S 2.4a**. **Table 2.1** summarizes the structures and reported photovoltaic parameters of newly synthesized diphenyl amine based dyes.

Table 2.1: Reported diphenylamine based dyes and their photovoltaic parameters

Reference	Sensitizer	J _{sc} (mAcm ⁻²)	V _{oc} (V)	FF%	η %
Hong et al. (2011)	 S 2.1	8.20	0.655	71.0	3.80
Ramkumar S. and AnandanS. (2013)	 S 2.2	7.01	0.612	62.7	3.16
Hosseinza- eha et al. (2015)	 S 2.3a	3.71	0.550	75.0	1.53

Hosseinzadeha et al. (2015)	 <p style="text-align: center;">S 2.3b</p>	2.63	0.510	75.0	1.00
Ramkumar et al. (2015)	 <p style="text-align: center;">S 2.4a</p>	1.67	0.832	62.2	1.02
Ramkumar et al. (2015)	 <p style="text-align: center;">S 2.4b</p>	2.15	0.545	40.9	0.56

2.2.2 Different spacer units and anchoring groups used in *n*-type sensitizers

Spacer units in a sensitizer generally provides an extended conjugation, thereby facilitating the movement of electrons across the dye molecule, finally leading to improved light harvesting ability as well as enhancing the cell efficiency. As effective spacers, different rigid and linear aromatic/heteroaromatic systems were studied in the literature. The most common heterocyclic systems include thiophene, furan, phenothiazine, indole, quinoline *etc.*, which augment extended conjugation for easy movement of electrons in the structure. Amongst the various heterocyclic systems, thiophene is the most studied aromatic spacer, because it provides an extra stability for the sensitizer and enhanced absorption. Similarly, furan is also considered to be a good spacer.

Presence of a good anchoring group is an important requisite for an effective sensitizer. Indeed, understanding the structure-performance relationship of anchoring group is a critical development for efficient DSSCs. Obviously, it has a prime role of binding with semiconductor as well as showing strong electron affinity.

Kim et al. in the year 2011 reported phenothiazine based chromophores, having various conjugated linkers, viz. thiophene, furan and 3,4-ethylenedioxythiophene, as effective sensitizers. The authors reported that the chromophores carrying furan as spacer **S 2.5** showed a maximum efficiency of 6.58%. It was also observed that it displayed the highest J_{SC} value owing to its flatter structure and lower resonance energy, which helps to transfer the electrons easily from phenothiazine donor system to CB of TiO_2 .

Later, in 2014 He and his co-workers synthesized four carbazole based D-D- π -A organic chromophores containing furan (**S 2.6**) and thiophene units as the spacer units. In these molecules, triphenylamine acts as an auxiliary electron-donating group and cyanoarylic acid acts as an electron acceptor/anchoring unit. Among the two reported chromophores, **S 2.6** carrying furan as π -conjugator showed the highest performance of 6.68%.

Thiophene based spacers were studied thoroughly because of their good conjugation ability. Babu et al. (2015) reported D- π -A configured indole based chromogens containing thiophene acetonitrile, as the π -spacer (**S 2.7a-c**) with various anchoring units such as cyanoacetic acid, rhodanine acetic acid and 4-amino benzoic acid. In the newly designed sensitizer, thiophene acetonitrile facilitates the electrons to move easily and enhances its λ_{abs} .

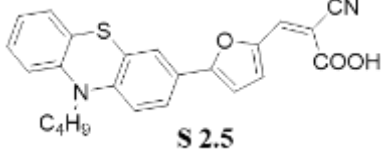
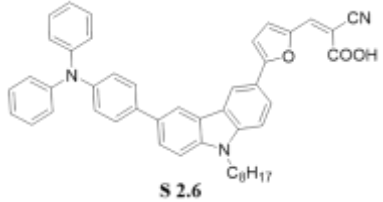
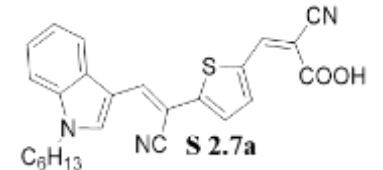
Gupta and co-workers (2015) reported design and synthesis of two D- π - π -A architected dyes with 4-(cyanomethyl)benzoic acid as an anchoring moiety with aryl amine as donor and thiophene as π -spacer units. The newly synthesized dyes with anchoring group 4-(cyanomethyl)benzoic acid (**S 2.8**) showed a significantly improved photovoltaic performance when compared to the sensitizer carrying cyanoacrylic acid anchor.

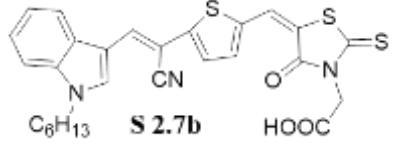
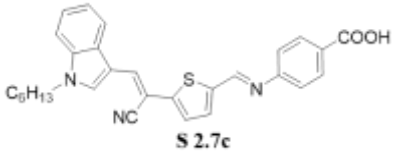
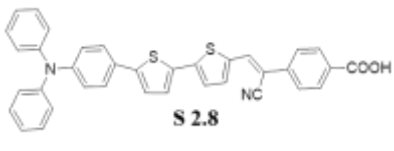
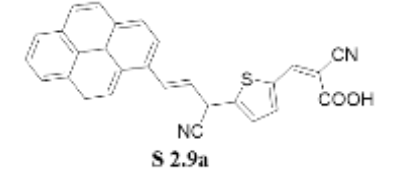
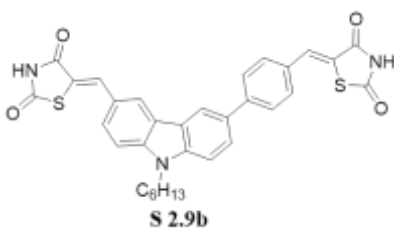
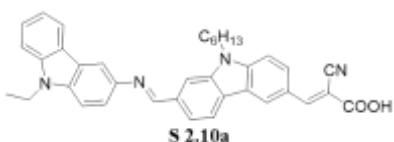
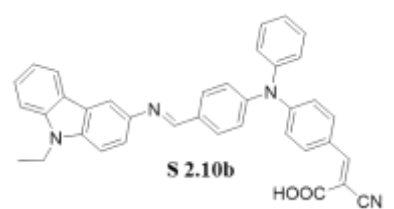
In 2016, two new pyrene based organic sensitizers (**S 2.9a-b**) were designed, synthesized and well characterized by Saritha et al. The reported D- π -A configured sensitizers comprised of thiophene-2-acetonitrile as spacer unit and cyano acetic acid or rhodanine-3-acetic acid as electron acceptor as well as anchoring unit. Both the dyes showed almost same efficiencies. Later in 2017, the same group reported two

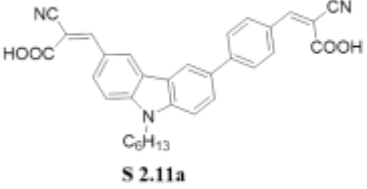
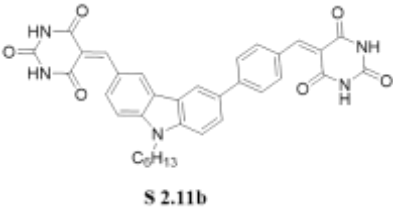
new D-D- π -A architected carbazole-based dyes (**S 2.10a-b**) with improved efficiency. In the design strategy, *N*-hexyl carbazole acts as donor and triphenylamine serves as donor as well as a π -spacer units. Here, *N*-ethyl carbazole works as an auxiliary donor and cyanoacetic acid functions as an anchoring group. These dyes displayed optimum efficiency of 3.12 % and 2.12 %, respectively.

Naik et al. (2018) reported design and synthesis of two new dual anchoring carbazole based dyes with A- π -D- π -A configuration (**S 2.11a-b**). Their device studies were also carried out. According to authors, the sensitizer bearing cyanoacetic acid (**S 2.11a**) showed maximum PCE of 2.38 % with J_{SC} = 6.36 mAcm^{-2} , V_{OC} = 0.599 V and IPCE = 57%. The details of structures **S 2.5-S 2.11** and their device performance parameters along with corresponding references are summarized in **Table 2.2**.

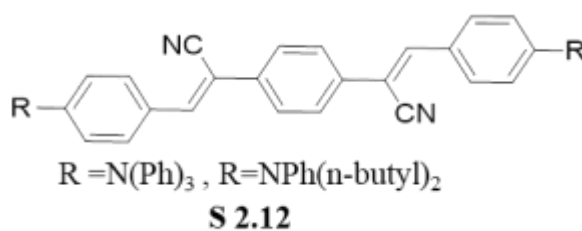
Table 2.2: Dyes carrying varied donor, spacer, anchoring units, with cell performance data

Reference	Sensitizer/dye	J_{SC} (mAcm^{-2})	V_{OC} (V)	FF%	$\eta\%$
Kim et al. (2011)	 S 2.5	12.18	0.771	70.02	6.58
He et al. (2014)	 S 2.6	13.26	0.724	66.10	6.68
Babu et al. (2015)	 S 2.7a	2.89	0.577	53.0	1.04

Babu et al. (2015)	 C ₆ H ₁₃ S 2.7b HOOC	1.24	0.509	47.6	0.35
Babu et al. (2015)	 C ₆ H ₁₃ S 2.7c	4.24	0.641	36.0	1.18
Gupta and co-workers (2015)	 S 2.8	8.21	0.673	76.0	4.20
Saritha et al. (2016)	 S 2.9a	4.51	0.584	56.8	1.76
Saritha et al. (2016)	 C ₆ H ₁₃ S 2.9b	3.66	0.520	53.0	1.18
Saritha et al. (2017)	 C ₆ H ₁₃ S 2.10a	8.09	0.656	50.0	3.12
Saritha et al. (2017)	 S 2.10b HOOC CN	7.76	0.580	50.0	2.63

Naik et al. (2018)	 <p style="text-align: center;">S 2.11a</p>	5.22	0.623	67.7	2.20
Naik et al. (2018)	 <p style="text-align: center;">S 2.11b</p>	1.748	0.548	65.0	0.62

It is worth noting that, presence of a strong acceptor unit along with good donor system normally enhances the optical and electrical properties of the molecule. Pond et al. in 2002, designed and synthesized three D-A-D configured dyes (**S 2.12**), carrying distyryl benzene with di-*n*-butyl/ diphenylamino group as a donor moiety and cyano group as an acceptor unit. The authors observed that, the presence of cyano group enhances the optical properties of the dye marginally. These dyes were studied in detail for their applications in OLEDs and NLO devices.

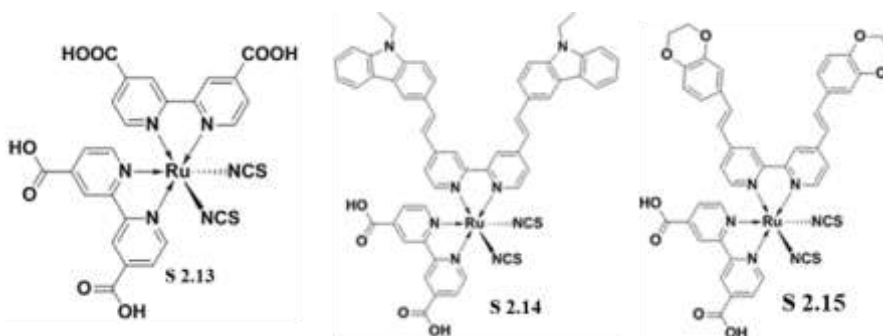


2.2.3 Co-sensitizers for Ru (II) based DSSCs

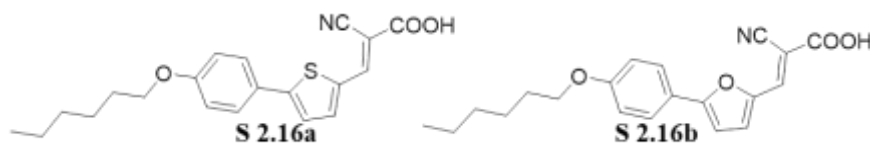
Co-sensitization is one of the techniques involving addition of a dye along with a metal-based sensitizer for further improvement of the performance of a DSSC. It enhances the overall efficiency of the cell by extending the light absorption spectrum. Accordingly, use of small organic dyes carrying interesting scaffolds like diphenylamine, carbazole, indole, phenothiazine *etc.* as co-sensitizers along with metal-based sensitizer has proven to be an effective method to enhance the overall performance of the cell. They have an important role in extending the π -conjugation

of the molecules and thereby enhancing their molar absorptivity (Hagfeldt et al. 2010; Mishra et al. 2009; Wu and Zhu 2013).

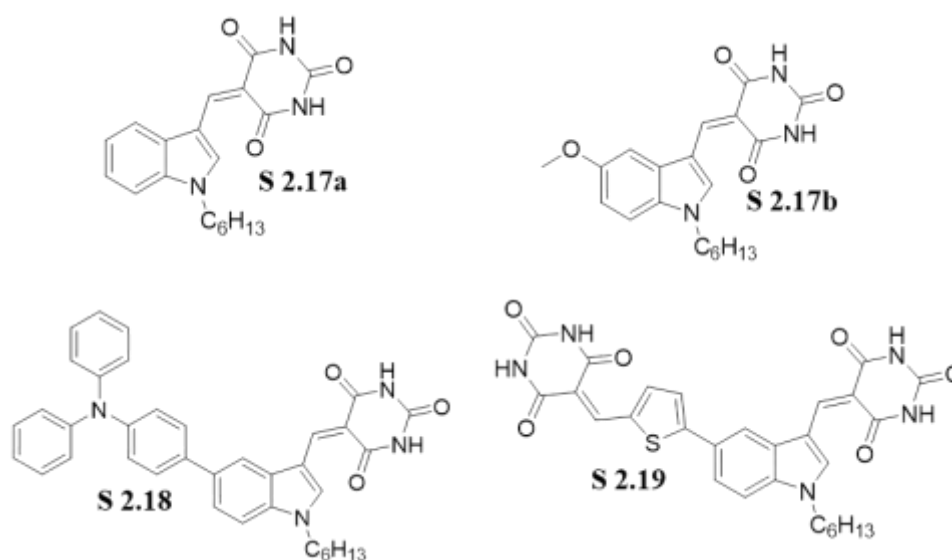
Fig 2.1 depicts structures of three ruthenium based complexes being used as efficient sensitizers in DSSCs. In the year 1993, Nazeeruddin and his group reported systematic study of the luminescence, visible light absorption, electrochemical, and photo redox properties of Ru (II) complexes (Nazeeruddin et al. 1993). Typically, the newly synthesized quadri anchoring dye, popularly known as **N3 (S 2.13)** showed an outstanding performance of 11.03%, when employed in the device as sensitizer. Further, in order to attain a better understanding of the role of anchoring group, a dianchoring Ru (II) dye **N719** was reported and the device sensitized with **N719** exhibited an enhanced performance. Furthermore, a newly synthesized Ru (II) complex, *i.e.* **NCSU-10 (S 2.14)**, was employed as a sensitizer in DSSC, which yielded a good performance of 10.19 % (Cheema et al. 2014a). Later, the same group reported another ruthenium (II) complex, *viz.* **HD-2 dye (S 2.15)** with PCE of 9.50%.



In the literature, many co-sensitizers were reported for Ru-complex sensitized DSSCs. **Table 2.4** summarizes some of the important references pertaining to organic co-sensitization studies along with reported photovoltaic parameters. In 2016, Luo and his coworkers designed and synthesized two new simple D- π -A configured organic dyes as effective co-sensitizers for **N719**-based DSSCs. The design includes the hexyloxy-substituted phenyl ring as an electron donor and cyanoacetic acid functions as an electron acceptor/anchoring unit. The authors incorporated two different π -spacers, *viz.* thiophene (**S 2.16a**) and furan (**S 2.16b**) in their structures. The studies indicated that, both co-sensitizers showcased higher photovoltaic performance than the cell fabricated with **N719** dye alone.



Babu et. al (2016), in search of new co-sensitizers, designed and synthesized two indole based dyes bearing barbituric acid as an anchor with different auxiliary donor groups (**S 2.17a-b**). They incorporated two different auxiliary donors, *viz.* methoxy (**S 2.17b**) or 4-methoxyphenyl to the dye **S 2.17a**. For co-sensitization studies, the authors used Ru-based **NCSU-10** sensitizer (**S 2.14**) as a base dye. In the study, **S 2.17a** showed the maximum enhancement with PCE of 10.12%, which might be due to efficient suppression of undesirable charge recombination process and, thereby resulting in longer electron lifetime. Later, same authors reported two organic co-absorbers with D-D-A architecture. Among the two dyes, the dye **S 2.18** carrying barbituric acid showed an enhanced performance along with **HD-2** (**S 2.15**) sensitizer. It gave efficiency (PCE) of 8.06%, while **HD-2** alone displayed 7.6 %. In 2017, they reported a new asymmetric co-sensitizer, **S 2.19** carrying indole moiety as donor system, thiophene as a spacer unit and barbituric acid as an anchoring group. This co-sensitizer along with **NCSU-10** (**S 2.14**) showed an enhanced efficiency of 10.68%.



Saritha et al. in 2017 investigated two new D-D- π -A configured carbazole-based dyes, *viz.* **S 2.10a-b** as effective co-sensitizers for **N719** based DSSCs. The

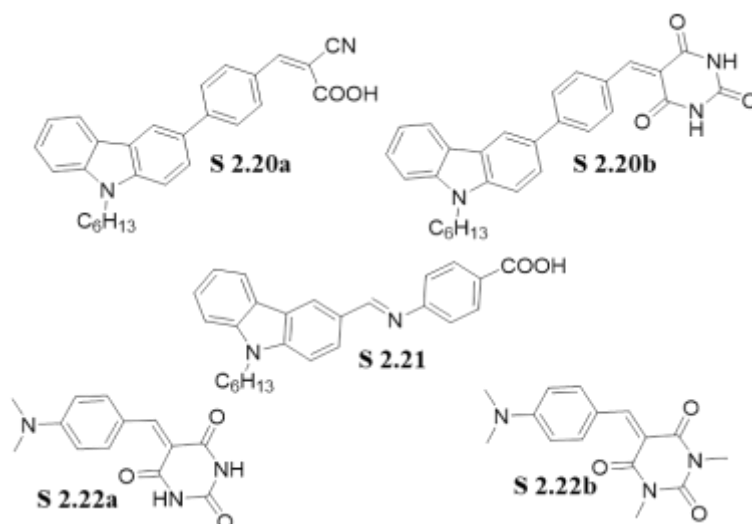
newly synthesized dye, **S 2.10a** displayed improved PCE of 8.01% with higher J_{sc} value of 19.33 mAcm^{-2} than that of **N-719** alone.

Table 2.3: Reported organic co-sensitizers with cell performance data

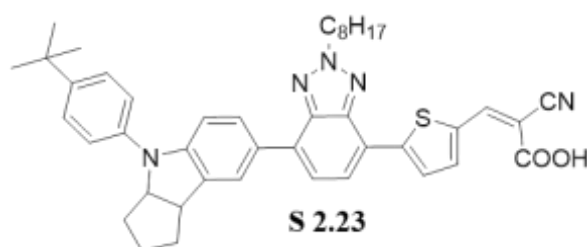
Reference	Co-sensitizer	Sensitizer	J_{sc} (mA.cm^{-2})	V_{oc} (V)	FF	PCE (%)
Luo et al. (2016)	S 2.16a	N719	17.673	0.736	0.66	8.60
Luo et al. (2016)	S 2.16b	N719	17.628	0.758	0.67	8.95
Babu et al. (2016)	S 2.17a	NCSU-10	22.69	0.715	62.4	10.12
Babu et al. (2016)	S 2.17b	NCSU-10	20.49	0.687	65.4	9.20
Babu et al. (2016)	S 2.18	HD-2	16.54	0.732	66.50	8.06
Babu et al. (2017)	S 2.19	NCSU-10	25.14	0.695	61.2	10.68
Saritha et al. (2017)	S 2.10a	N719	19.33	0.74	0.47	8.01
Naik et al. (2018)	S 2.20a	NCSU-10	21.19	0.658	65.85	9.19
Naik et al. (2018)	S 2.20b	NCSU-10	22.22	0.671	58.63	8.75

Naik et al. (2018)	S 2.21	NCSU-10	22.85	0.672	62.20	9.55
Naik et al. (2018)	S 2.22a	N3	15.49	0.641	64.65	6.43
Naik et al. (2018)	S 2.22b	N3	15.27	0.671	68.47	7.02

Naik et al. (2018) demonstrated a series of carbazole based dyes, bearing cyanoacetic acid (**S 2.20a**) and barbituric acid (**S 2.20b**) as effective co-sensitizers with Ru based **NCSU-10** and **N3** sensitizers. Among the newly synthesized co-sensitizers, **S 2.20a** showed the highest PCE of 9.19 % along with **NCSU-10** dye alone. In another article (2018), the same group of authors reported the synthesis of four new D-A type carbazole based co-sensitizers and investigation of their co-sensitization properties with **NCSU-10** sensitizer. Among them, carbazole carrying 4-amino benzoic acid (**S 2.21**) showed the highest PCE of 9.55 %. Recently (2018), the same research group designed and synthesized a series of simple D-A configured dimethyl aniline based dyes as co-sensitizers with **N3** dye. Interestingly, all the new dyes showed enhanced PCE values. Among the tested dyes, **S 2.22b** bearing methyl barbituric acid as an anchor displayed a quite good incremental result with PCE of 7.02 % at 0.3 mM concentration.



Most recently, Zheng and co-authors (2019) synthesized an interesting co-sensitizer bearing electron withdrawing N-substituted benzotriazole (**2.23**) for DSSCs sensitized with two porphyrin based dyes, *viz.* **XW40** and **XW41**. It was noticed that, the rigid benzotriazole containing dye acted as an efficient co-sensitizer, showing an enhanced PCE of 10.6 and 10.2 % when employed with the sensitizers **XW40** and **XW41**, respectively.



All the above references revealed that, the co-sensitizer effectively increases the cell efficiency either by reducing competitive adsorption through filling the vacant spaces or by minimizing dye-aggregation. In the present study, **N3** and **HD-2** sensitized DSSCs were used for co-sensitization studies of newly synthesized diphenylamine based organic chromogens.

2.3 SALIENT FEATURES OF THE LITERATURE REVIEW

Based on the detailed literature review pertaining to various sensitizers/co-sensitizers bearing different donors, π -spacers and anchoring systems, the following inferences can be drawn:

- Sensitizer should possess broad absorption band and high molar extinction coefficient in order to absorb more light energy.
- The dye should bear at least one anchoring group in order to adsorb on TiO₂ surface.
- The HOMO-LUMO levels of the dyes should match with redox and CB of TiO₂, respectively.
- There is a good scope for optimizing the design strategy and also varying different constituent in the molecular structure of a dye.
- Widely used design architecture for a sensitizer for the DSSC application is D- π -A approach. This architecture results in an intra-molecular charge separation upon excitation, which facilitates increase in absorption ability of the dye.
- Diphenylamine has been reported to be a good donor system
- Thiophene and phenylene derivatives are active conjugated spacers because of their efficient charge separation.
- Co-sensitization of interesting dyes with Ru (II) based sensitizer has enhanced the PCE of the devices considerably.

2.4 SCOPE AND OBJECTIVES

Even though, major breakthroughs have been made in the field of DSSCs by the introduction of metal-free sensitizers, there is still ample of scope to continue research on investigation of organic sensitizers which can enhance the efficiency of the cell to a large extent. The increase of interest in this field is evident from the number of publications coming out every year. Still lots of research need to be carried out to look into various aspects such as efficient light harvesting ability throughout the entire solar spectrum, tuning of the band-gap, charge generation and separation, molecular interactions, anchoring efficiency, dye aggregation, study of the effect of different functional groups on device performance *etc.* Also, there exists a plenty of opportunity for developing simple co-sensitizers to enhance the overall efficiency of Ru (II) based DSSCs. The search for effective organic co-sensitizers is in progress.

From the literature reports, it is clear that there are number of factors influencing the performance of a DSSC. Since DSSC technology is an area with more expectation, it requires vigorous research on various components of it. From the point

of view of a material scientist, the development of suitable materials for sensitizers, semiconductor, electrodes and electrolyte is playing much importance. In this field, design and development of an efficient sensitizer have significant role for achieving highly efficient DSSCs. At the molecular level, the geometry and electronic structure of the sensitizer contribute effectively to tailor the required properties in it. Therefore, it is an immediate challenge and requirement to design and synthesize optically stable and effective chromophores with good optical absorption behaviour, for DSSC application as sensitizers. As discussed in earlier section, effective co-sensitizers must possess characteristic properties like complementary absorption range, matching band gap, appropriate size, optical stability *etc.* There is a need for development of new co-sensitizers for the improvement in performance of devices sensitized with Ru complexes.

Based on the above facts and the detailed literature survey, the following main objectives have been intended in the present research work.

- 1) To design new push-pull configured *n*-type metal-free organic sensitizers/co-sensitizers based on diphenyl amine donor system employing various design strategies such as D- π -A (**Series-1**), A-D- π -A (**Series-2**), D- π - π -A (**Series-3**), D- π -A with nitro anchoring group (**Series-4**), D-D-A (**Series-5**), A-D- π -D-A (**Series-6**) and D-A (**Series-7**) architectures
- 2) To study the electron density distributions in HOMO-LUMO levels and electrostatic maps using Turbomole 7.2V software package at the def -TZVpp level
- 3) To synthesize newly designed *n*-type sensitizers/co-sensitizers using standard protocols and optimize the reaction parameters
- 4) To characterize the newly synthesized intermediates and target dyes by FTIR, $^1\text{H-NMR}$, $^{13}\text{C-NMR}$ and Mass spectroscopy techniques
- 5) To evaluate their photophysical parameters using UV-visible absorption and fluorescence emission spectroscopy
- 6) To study their electrochemical properties and charge carrying properties using cyclic voltammetry (CV)

- 7) To fabricate DSSC devices and quantify the performance of the newly synthesized sensitizers/co-sensitizers with respect to parameters such as incident photon to current efficiency (IPCE), short-circuit photocurrent (J_{sc}), open circuit photovoltage (V_{oc}), fill factor (FF) and the photon conversion efficiency (PCE)
- 8) Finally, to study the structure-performance relationship of dyes as sensitizers/co-sensitizers

2.5 MOLECULAR DESIGN OF NEW *n*-TYPE SENSITIZERS/CO-SENSITIZERS

It has been observed that, several new organic dyes with various design strategies, *e.g.* D-A, D- π -A, D- π - π -A, D-D-A and A-D- π -D-A were developed as effective sensitizers/co-sensitizers for improvement of efficiency in DSSCs. Further, it is interesting to note that, these sensitizers were derived from simple organic compounds such as diphenylamine, triphenylamine, carbazole, indole, phenothiazine *etc.* that are potential electron donating systems. Among the aforementioned donors, diphenylamine was selected for the present study owing to its good electron donating and easy derivatization property. Accordingly, the present research work has been aimed at design of new organic photosensitizers/co-sensitizers bearing diphenylamine (**Series-1** to **Series-7**) as donor system. Also, it has been planned to use 2-(thiophene-2-yl)-acetonitrile, 4-phenylacetonitrile, 1,4-phenylene-diacetonitrile *etc.* as spacer units. In addition, it was contemplated to use well-known electron withdrawing cyanoacetic acid, barbituric acid, rhodanine acetic acid *etc.* as acceptor/anchoring moieties.

2.5.1 Design of chromophores **D**₁₋₃ (**Series-1**)

As per literature reports, the anchoring group has a vital role in deciding the overall efficiency as it contributes significantly towards the charge injection from molecular orbital of the dye to the semiconductor. It has been established that, diphenylamine based D- π -A systems with different heterocyclic systems as π -spacers and various strong anchoring moieties are potential sensitizers/co-sensitizers, since they are quite stable and function as good chromophores. Keeping this in view, dyes of first series were designed with D- π -A strategy. Here, diphenylamine is selected as a

donor system because of its favorable properties as discussed earlier. Incorporation of hexyl chain to *N* atom of diphenyl amine reduces the dye aggregation and increases solubility of the resulting dye. Literature reports clearly state that, the introduction of cyano vinylene group in molecular core brings about the reduction of band gap and as a result an increase in λ_{abs} value is observed. In view of this, 2-(thiophene-2-yl)-acetonitrile was selected as a π -conjugate spacer. These molecules were expected to act as good sensitizers in devices. Further, in the new design, anchoring units, *i.e.* 4-aminobenzoic acid, barbituric acid and 2,4-nitrophenylacetonitrile were selected. These anchoring motifs were selected owing to strong anchoring property of carboxylic acid group, low recombination rate of barbituric acid and nitro group.

Also, they may function as good co-sensitizers for **N3** based DSSC, since they are structurally similar to the sensitizer **N3**. The design strategy for dyes, **D1-3** (**Series-1**) is summarized in **Fig 2.1**.

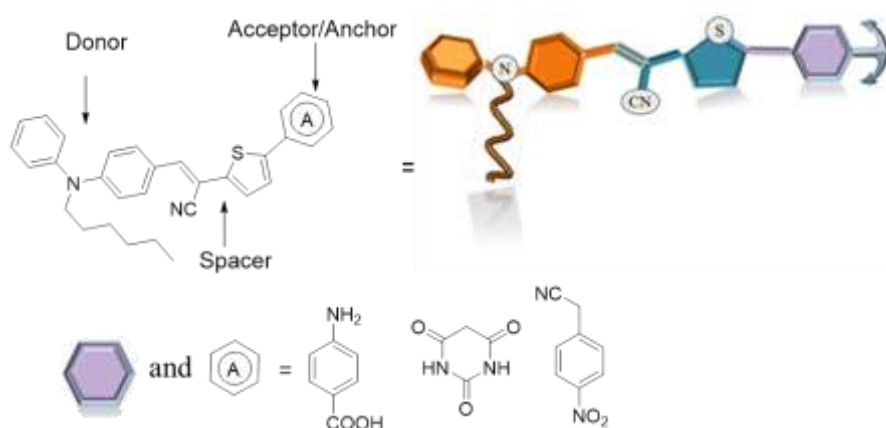


Fig 2.1 Design of chromophores **D1-3** (**Series-1**)

2.5.2 Design of chromophores **D4-7** (**Series-2**)

While designing the diphenyl based chromophores **D4-7** of **Series-2**, 2-(thiophene-2-yl)-acetonitrile was incorporated as a π -spacer unit mainly due to its good conjugation, high polarizability, thermal stability and an excellent charge transporting capability. In addition, cyanoacetic acid (**D4**), rhodanine acetic acid (**D5**), hydrazine benzoic acid (**D6**) and barbituric acid (**D7**) were introduced as electron acceptor as well as anchoring units. The special feature of these dyes lies in the fact that, these di-anchoring molecules possess several advantages over mono-anchoring

sensitizers, like multi-binding ability with TiO₂, panchromatic response due to extended conjugation, good electron extraction channel and enhanced stability. Also, they would exhibit higher charge recombination property when compared to mono-anchoring sensitizer. Consequently, they are anticipated to show increased device efficiency. In addition, they were expected to display good co-sensitization behaviour because of favourable structural features. The design strategy used for dyes **D**₄₋₇ has been summarized in **Fig 2.2**.

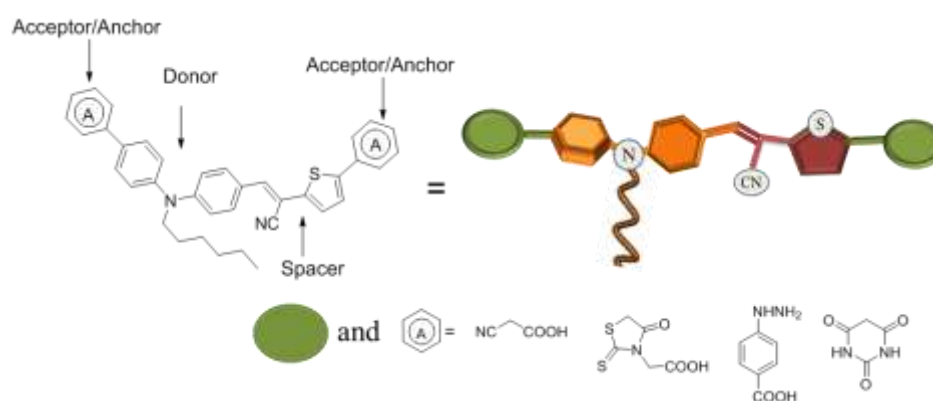


Fig 2.2 Design of chromophores **D**₄₋₇ (**Series-2**)

2.5.3 Design of chromophores **D**₈₋₁₁ (**Series-3**)

It has been well-established that, incorporation of π -conjugative spacer unit/s broadens the light harvesting spectrum of the resulting chromophores. Keeping this in view, in the design of chromophores, **D**_{8,9} having D- π -A configuration, 4-phenylacetonitrile system was used as spacer unit, while in case of **D**₁₀₋₁₁ with D- π - π -A architecture, an additional 2-(thiophene-2-yl)-acetonitrile group was employed as spacer unit. In all the dyes, diphenyl amine acts as an efficient donor moiety. Further, they carry cyanoacetic acid and barbituric acid as anchoring units. It has been hoped that, these organic chromogens would show good photosensitization. Also, they are supposed to possess attractive co-sensitization characteristics. **Fig 2.3** illustrates the design strategy used for **D**₈₋₁₁ dyes.

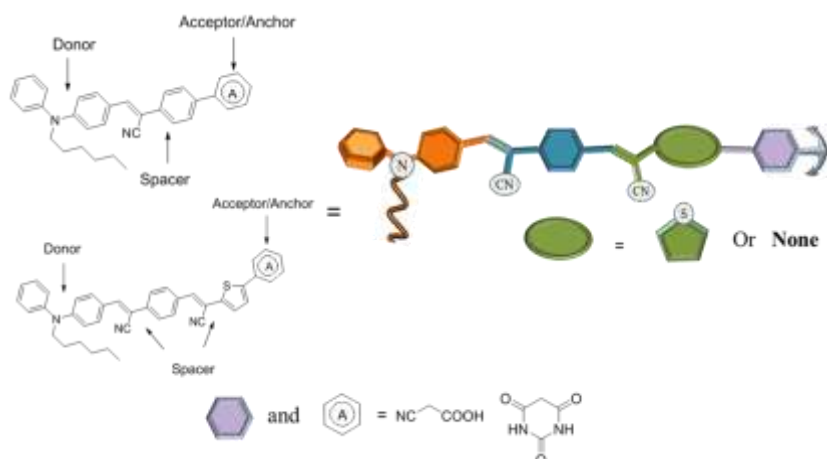


Fig 2.3 Design of chromophores **D8-11** (Series-3)

2.5.4 Design of chromophores **D12-17** (Series-4)

Hydrazone based organic dyes are popular in the commercial scene. They find many applications. These dyes possess several merits such as easy synthesis, rapid charge transporting ability and extra stability. It is well-known that NO_2 group is a powerful electron withdrawing functionality and hence, it has been explored as a strong anchoring group. Keeping these facts in view, new chromophores, **D12-17** except **D15** were designed, wherein diphenyl amine acts as a donor, different aromatic nitro compounds function as anchoring/accepting systems. While **D15** bearing no NO_2 group, with carboxylic acid group has been designed as a reference dye for the studies. Different spacer units, *viz.* 4-phenylacetonitrile, furan, *etc.* were incorporated in order to study the effect of conjugation length on their properties. The new chromophores can act as good sensitizers as well as co-sensitizers. The designing strategy for chromophores **D12-17** is shown in **Fig 2.4**.

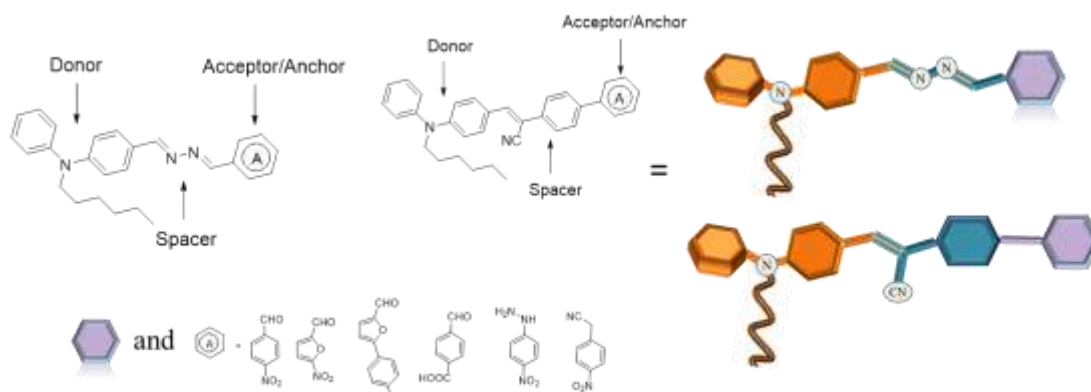


Fig 2.4 Design of chromophores **D12-17** (Series-4)

2.5.5 Design of chromophores D₁₈₋₂₁ (Series-5)

Four new organic sensitizers/co-sensitizers, *i.e.* D₁₈₋₂₁ with D-D-A configuration were designed and the designs are shown in Fig 2.5. These *N*-substituted diphenylamine based molecules consist of auxiliary donor units, *viz.* 5-amino-2,4-di-*tert*-butylphenol (D₁₈), 3,5-bis(dodecyloxy)aniline (D₁₉), pyren-1-amine (D₂₀) and benzo[d]thiazol-2-amine (D₂₁). Here, auxiliary donor systems enhance electron pushing capability of the principal donor, *i.e.* *N*-substituted diphenyl amine scaffold. Further, cyanoacetic acid unit was selected as electron acceptor/anchoring unit in all the molecules. As these chromophores hold required structural features, they are expected to display good sensitization as well co-sensitization property.

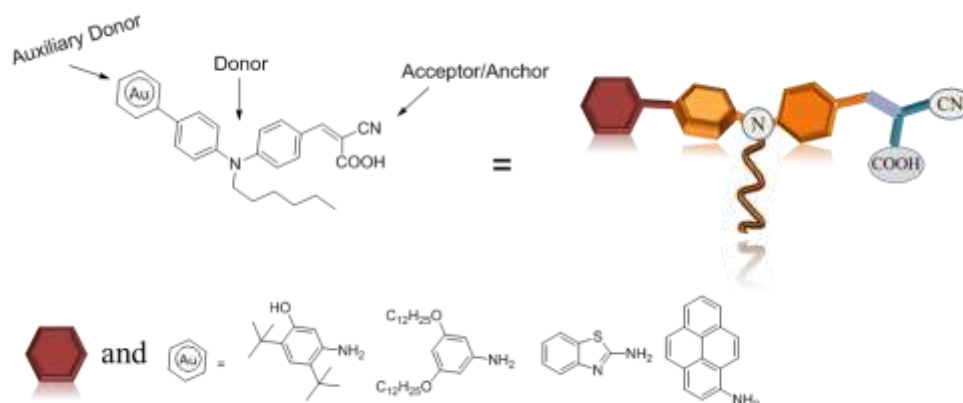


Fig 2.5 Design of chromophores D₁₈₋₂₁ (Series-5)

2.5.6 Design of chromophores D₂₂₋₂₃ (Series- 6)

Two conceptually new symmetric di-anchoring sensitizers/co-sensitizers with A-D- π -D-A configuration, *i.e.* D₂₂₋₂₃ were designed as shown in Fig 2.6. In these *N*-substituted diphenylamine donor based chromophores, electron withdrawing, (1,4-phenylene) diacetonitrile group was selected as a π -spacer unit, while cyanoacetic acid (D₂₂) and rhodanine acetic acid (D₂₃) were chosen as electron acceptor/anchoring units. These chromogens are predicted to possess all the advantages of bi-anchoring sensitizers as well as co-sensitizers.

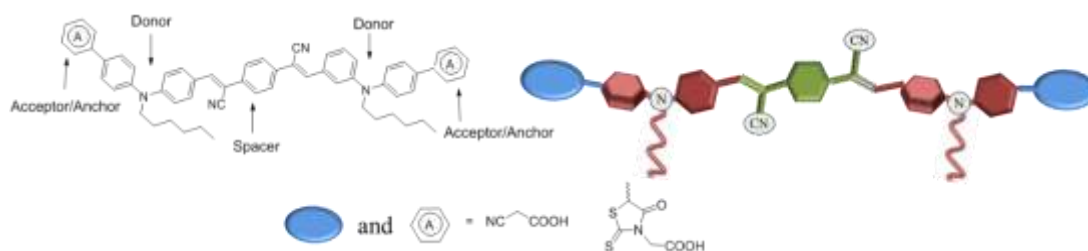


Fig 2.6 Design of chromophores **D₂₂₋₂₃** (**Series-6**)

2.5.7 Design of chromophores **D₂₄₋₂₇** (**Series-7**)

In **series-7**, four simple D-A type chromogens, *viz.* **D₂₄₋₂₇** were designed, where *N*-substituted diphenylamine moiety acts as a donor and various electron-pulling systems, *viz.* cyanoacetic acid (**D₂₄**), rhodanine acetic acid (**D₂₅**), hydrazine benzoic acid (**D₂₆**) and maleimide (**D₂₇**) function as anchoring/acceptor units. **Fig 2.7** illustrates the design strategy used for the dyes. These molecules are anticipated to act as good sensitizers as they fulfill the required criteria in their structure. Because of their smaller size, structural similarity to sensitizer and simple design, they are predicted to perform better in devices as co-sensitizers.

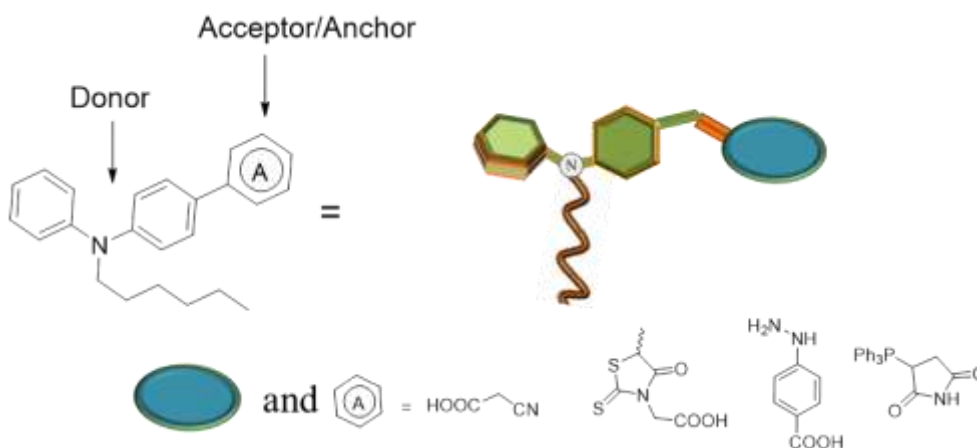


Fig 2.7 Design of chromophores **D₂₄₋₂₇** (**Series-7**)

From the literature reports on molecular design for sensitizers, it is evident that the incorporation of certain structural units in the dye molecule as donor/ π -spacer/anchor would alter the properties of the chromophores and hence the performance of the photovoltaic device. More precisely, the introduction of an extra donor, π -spacer or acceptor unit can lead to a bathochromic shift in the absorption

range, thereby increasing the overall performance of the dye in the device. Conclusively, keeping in view of all these points, seven new series of *N*-substituted diphenylamine based metal-free organic dyes, **D1-27**, *i.e.* (i) D- π -A, **D1-3 (Series-1)** (ii) A-D- π -A **D4-7 (Series-2)** (iii) D- π -A/D- π - π -A **D8-11 (Series-3)** (iv) D- π -A with nitro anchoring group, **D12-17 (Series-4)** (v) D-D-A, **D18-21 (Series-5)** (vi) A-D- π -D-A, **D22-23 (Series-6)** and (vii) D-A, **D24-27 (Series-7)**, have been designed as sensitizers/co-sensitizers for DSSC applications.

The details of design strategies used for new dyes are summarized in **Figs 2.5-2.11**. Using the well-established synthetic protocols, the designed chromophores were synthesized and the reaction conditions have been optimized to get the maximum yield (**Schemes 3.1 to 3.7**). Further, purification methods have been developed and the purified compounds have been characterized by various spectroscopy techniques such as FTIR, NMR and mass spectroscopy techniques. In order to evaluate the photophysical properties, *viz.* λ_{abs} , λ_{emi} , E_{0-0} and ϵ , UV-Visible as well as Fluorescence spectroscopy is employed at solution states of sample. Additionally, cyclic voltammetric studies were carried out to determine the electrochemical properties, such as E_{ox} , E_{ox}^* , E_{g} , ΔG_{inj} , ΔG_{rec} , ΔG_{reg} , *etc.* of the dyes. Furthermore, theoretical geometric optimizations and HOMO-LUMO calculations of dyes were performed by employing Turbomole 7.2v software. Also, ESP maps were generated using DFT calculations and theoretical spectral data were simulated with the help of TD-DFT studies. Finally, performances of DSSCs sensitized as well as co-sensitized with the new chromophores were studied by evaluating the parameters such as V_{OC} , J_{SC} and η . Also, the IPCE parameters of the dyes were also determined. In addition, EIS studies of devices were carried out in order to determine the charge dynamics from their Nyquist and Bode plots.

The synthetic strategies, procedures and structural characterization data of newly synthesized dyes have been included in **Chapter 3**. Further, the details of photophysical, electrochemical, and theoretical studies of chromophores are given in **Chapters 4**. Finally **Chapter 5** discusses the photoelectrochemical performance and impedance data of fabricated DSSCs using dyes **D1-27** as sensitizers as well as co-sensitizers.

SYNTHESIS AND STRUCTURAL CHARACTERIZATION

Abstract:

This chapter includes optimized synthetic protocols and purification techniques used for newly designed sensitizers/co-sensitizers, D₁₋₂₇. Further, it comprises structural characterization of new intermediates as well as target dyes using FTIR, ¹H NMR, ¹³C NMR, and mass spectroscopy studies. Also, a relevant discussion has been included in it.

3.1 INTRODUCTION

In the previous chapter, design of seven new series of *N*-substituted diphenylamine based dyes (D₁₋₂₇) with various push-pull configurations, such as D- π -A, A-D- π -A, D- π -A/D- π - π -A, A-D- π -D-A and D-A, has been discussed in detail. All the new chromophores were synthesized starting from the simple diphenylamine. In all the series of dyes other than **Series-5**, the diphenylamine core was first alkylated using bromohexane and then it was formylated with the help of Vilsmeier-Haack reaction to form 4-(hexyl (phenyl)amino)benzaldehyde as an intermediate. While in **Series-5**, alkylated diphenyl amine was di-formylated to yield 4,4'-(hexylazanediyl)dibenzaldehyde as an intermediate. These intermediates carrying formyl group/s were converted to final compounds through multistep reaction sequence in **Series-1** to **7**, as outlined in **Schemes 3.1-3.7**. Thus, after first two steps, the remaining reaction pathways are dissimilar for different series of dyes. All the reactions were carried out in nitrogen/argon atmosphere. Further, the synthesized dyes were purified using standard methods. Finally, all the unknown molecules were well-characterized by different spectroscopy tools.

3.2 EXPERIMENTAL

The materials used and the description on optimized synthetic as well as purification methods followed for the newly designed dyes are given in this section. Further, discussion on their structural characterization based on obtained spectroscopic data is included.

3.2.1 Materials and methods

All the starting materials and reagents were procured from Sigma Aldrich, Alfa-Aesar and Spectrochem companies. They were used without purifying further. All the solvents were dried prior to use. The reaction progress was monitored by TLC technique. The target molecules and intermediates were purified by column chromatography or recrystallization technique. All column chromatographic separations were carried out using Merck silica gel as adsorbate. ^1H and ^{13}C -NMR spectra were run on a BRUKER spectrometer in deuterated chloroform or dimethyl sulfoxide solution at 298 K. Chemical shifts (δ values) were recorded in units of ppm relative to tetramethylsilane (TMS) as an internal standard. Mass spectra were recorded on Shimadzu model LCMS-2010EV system that was equipped with electrospray ionization (ESI) probe. ATR-FTIR spectra were obtained from Bruker Alpha instrument equipped with a Silicon Carbide as IR source and the data acquisition was done on an attenuated total reflectance accessory made up of Zinc selenide crystal.

3.2.2 Synthesis of chromogens D_{1-27} (Series 1-7)

Synthetic protocols used for all the intermediates as well as target dyes and their purification methods including their characterization data are elaborated in the following section.

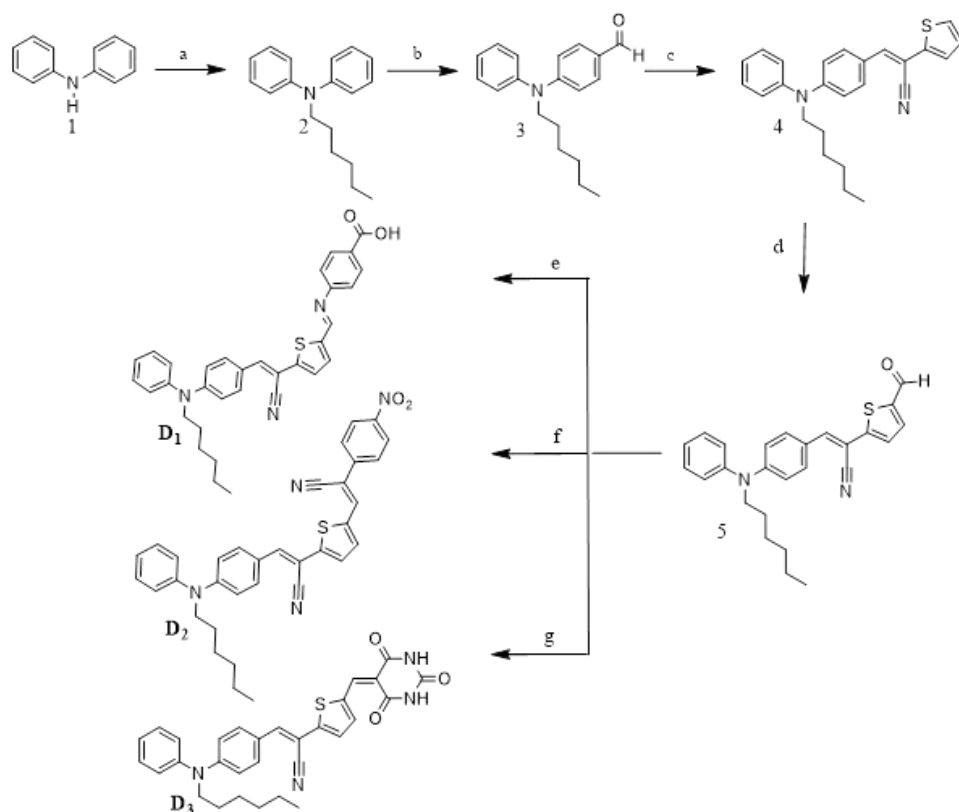
3.2.2.1 Synthesis of chromophores D_{1-3} (Series-1)

Scheme 3.1 outlines the synthetic routes of the newly designed dyes D_{1-3} . The necessary intermediates from *N*-hexyl-*N*-phenylaniline (**2**) to an aldehyde **5** were synthesized from well-documented procedures with slight modifications and the details were furnished herein. Firstly, Vilsmeier-Haack reaction protocol was used to obtain required 4-(hexyl(phenyl)amino)benzaldehyde (**3**). Secondly, Knoevenagel reaction was followed to prepare (*E*)-2-(5-formylthiophene-2-yl)-3-(4-(hexyl(phenyl)amino)phenyl)acrylonitrile (**4**). The final compounds D_{1-3} were obtained by subjecting the intermediate **5** to various condensation reactions including Knoevenagel reaction. The crude products were purified either by recrystallization or

column chromatography technique. The synthetic procedures for the intermediates **2** to **5** and final dyes **D**₁₋₃ are given in the following section.

N-Hexyl -*N*-phenylaniline (**2**)

A mixture of 1-bromohexane (1.47 g, 7.09 mM), diphenylamine (1 g, 5.9 mM), and sodium hydride (0.43 g, 18 mM) in DMF (15 mL) solvent was stirred at room temperature for 10 hours. The reaction mass was then neutralized with dil. HCl and the product was extracted using ethyl acetate (3×50 mL). The organic phase was dried using anhydrous sodium sulphate. The solvent was removed under reduced pressure and the crude product obtained was further purified by column chromatography on silica gel (100-200 mesh) using hexane as an eluent. The product was a colourless liquid. Yield: 95%.



Scheme 3.1. Synthetic routes for target dyes: (a) 1-Bromohexane, NaH, DMF, RT, 10 hours (b) POCl₃, DMF, RT, 12 hours (c) 2-(Thiophene-2-yl)-acetonitrile, NaOMe, CH₃OH, RT, 6 hours (d) POCl₃, DMF, RT, 15 hours (e) 4-Aminobenzoic acid, methanol, glacial acetic acid, 60 °C, 3 hours (f) 2-(4-Nitrophenyl)acetonitrile, piperidine, ethanol, 60 °C, 3 hours (g) Barbituric, methanol, reflux, 10 hours

4-(Hexyl (phenyl)amino benzaldehyde (3)

A dry round bottomed flask was charged with freshly distilled DMF (0.92 mL, 12 mM) and POCl₃ was added to it drop-wise (1.1 mL, 12 mM) at 0 °C under nitrogen atmosphere. The mixture was stirred for 30 min at 0 °C and to this *N*-hexyl-*N*-phenylaniline (**2**) (1.0 g, 3.95 mM) dissolved in dichloroethane (5 mL) was added while stirring and stirring was continued at room temperature for 12 hours. The reaction mass was then poured into ice cold water and subsequently basified using 5 M NaOH solution. The product was extracted using ethyl acetate (3×50 mL). The organic phase was dried using anhydrous sodium sulphate. The solvent was removed under reduced pressure and the crude oily product obtained was further purified by column chromatography on silica gel (100-200 mesh) using ethyl acetate/hexane (1%) as mobile phase to give light brown coloured liquid. Yield: 90%.

(E)-3-(4-(Hexyl (phenyl) amino) phenyl)-2-(thiophen-2-yl) acrylonitrile (4)

To a freshly prepared solution of sodium methoxide (0.1 g, 10 mM of sodium in 10 mL of methanol), 4-(hexyl (phenyl) aminobenzaldehyde (**3**, 1g, 3.5 mM) was added slowly while stirring. Thiophene-2-acetonitrile (0.48 g, 4.27 mM) was then added to the reaction mass and stirring was continued for 6 hours at room temperature. The product was extracted with ethyl acetate (3×50 mL). The organic phase was dried using anhydrous sodium sulphate. The solvent was removed under reduced pressure and the crude oily product obtained was further purified by column chromatography on silica gel (100-200 mesh) using hexane/ethyl acetate (1%) as an eluent yielded yellow liquid as the product. Yield: 80%.

(E)-2-(5-Formylthiophene-2-yl)-3-(4-(hexyl(phenyl)amino)phenyl)acrylonitrile (5)

Freshly distilled DMF (0.8 mL, 10.33 mM) was taken in a two necked round bottomed flask to which POCl₃ was added drop-wise (0.96 mL, 10.33 mM) at 0 °C under nitrogen. The reaction mixture was stirred for 30 minutes and to this compound **4** (4.1 g, 2.5 mM) dissolved in dichloroethane (5 mL) was added while stirring which was allowed to stir at room temperature for 15 hours. The reaction mass was then poured into ice cold water and subsequently basified using 5 M NaOH solution. The product was extracted using ethyl acetate (3×50 mL). The organic phase was dried

using anhydrous sodium sulphate. The solvent was removed under reduced pressure and the crude product obtained was further purified by column chromatography on silica gel (100-200 mesh) using *n*-hexane as an eluent yielded a bright red viscous liquid as the product. Yield: 80%. **¹H NMR** (CDCl₃, 400 MHz, δ ppm): 9.82 (1H, s), 7.88-7.86 (2H, d (J=8 Hz)), 7.76-7.73 (2H, d (J=12 Hz)), 7.38-7.37 (1H, d (J=4 Hz)), 7.34 (1H, s), 7.31-7.29 (1H, d (J=8 Hz)), 7.23-7.21 (2H, d (J=8 Hz)), 7.09-7.07 (1H, t (J=4 Hz)), 7.01-6.98 (2H, d (J=12 Hz)), 3.83-3.79 (2H, t (J=8 Hz)), 1.74-1.67 (2H, p), 1.32-1.24 (6H, m), 0.90-0.87 (3H, t (J=4 Hz)). **FTIR (ATR)**, ν cm⁻¹: 3072-2733 (C-H), 2212 (C≡N), 1665 (C=O), 1567 (C=C); **Mass (m/z)**: 414.00; Obtained (M+H): 415.00.

4-(((E)-(5-(E)-1-Cyano-2-(4-(hexyl(phenyl)amino)phenyl)vinyl)thiophen-2-yl)methylene-amino)benzoic acid (D₁)

A mixture of compound **5** (0.5 g, 1.2 mM) and 4-aminobenzoic acid (0.18 g, 1.3 mM) was heated to reflux in absolute methanol (10 mL) for 3 hrs. The separated solid was filtered at room temperature and recrystallized from methanol to obtain bright red colour solid. Yield 77%. MP: 155 °C **¹H NMR** (CDCl₃, 400 MHz, δ ppm): 8.50 (1H, s), 8.14-8.12 (2H, d(J=8 Hz)), 7.76-7.75 (2H, d (J=4 Hz)), 7.45-7.41 (3H, m), 7.37 (1H, s), 7.30-7.27 (3H, m), 7.25 (1H, s), 7.22 (1H, s), 7.21 (1H,s), 6.74-6.72 (2H, d (J=8 Hz)), 3.74-3.71 (2H, t (J=8 Hz)), 1.73-1.67 (2H, p), 1.36-1.30 (6H, m), 0.90-0.87 (3H, t (J=8Hz)). **¹³C NMR** (CDCl₃, 100 MHz, δ ppm): 162.01, 149.92, 149.32, 145.65, 140.38, 139.91, 137.43, 136.17, 130.36, 126.51, 125.69, 125.12, 123.29, 121.78, 120.97, 120.55,116.99, 116.30, 112.64, 109.21, 92.83, 46.76, 26.07, 21.97, 20.95, 17.13, 8.92. **FTIR (ATR)**, ν cm⁻¹: 3467 (O-H), 3026 (C-H), 2211 (C≡N), 1677 (C=O), 1602 (C=C), 1569 (C=N); **Mass (m/z)**: 533.21; Obtained (M+H): 534.00.

(Z)-3-(5-((E)-1-cyano-2-(4-(hexyl(phenyl)amino)phenyl)vinyl)thiophen-2-yl)-2-(4-nitro-phenyl)acrylonitrile (D₂)

A few drops of piperidine was added to the mixture of 4-nitrophenylacetonitrile (0.2 g, 1.233 mM) and compound **5** (0.5 g, 1.2 mM) in dry ethanol (15 mL) under nitrogen atmosphere. The reaction mixture was refluxed for about 3 hours. The reaction mass allowed to cool to room temperature and the product

was extracted using ethyl acetate (3×50 mL). Organic phase was dried using anhydrous sodium sulphate. The solvent was then removed under reduced pressure and the crude product obtained was further purified by column chromatography on silica gel using hexanes to yield the red solid. Yield 80%. MP: 130 °C. **¹H NMR** (CDCl₃, 400 MHz, δ ppm): 8.26-8.24 (2H, d (J=8 Hz)), 7.83-7.76 (4H, dd (J=16 Hz)), 7.52 (1H, s), 7.46-7.43 (2H, t (J=8Hz)), 7.30-7.22 (4H, m), 6.75-6.73 (2H, d (J=8 Hz)), 3.75-3.72 (2H, t (J=4 Hz)), 1.72-1.68 (2H, p), 1.35-1.31 (6H, m), 0.90-0.87 (3H, t (J=4 Hz)). **¹³C NMR** (CDCl₃, 100 MHz, δppm):151.36, 146.91, 145.13, 145.71, 141.95, 132.02, 130.09, 127.33, 126.34, 125.78, 124.29, 122.0, 118.62, 114.03, 102.25, 52.67, 31.60, 27.35, 26.67, 22.66, 14.04. **FTIR (ATR)**, ν cm⁻¹: 2915, 2848 (C-H), 2200 (C≡N), 1567, (C=C), 1503 (N=O), 1178 (C=N). **Mass (m/z)**: 558.21; Obtained (M+H): 559.12.

(E)-3-(4-(hexyl(phenyl)amino)phenyl)-2-(5-((2,4,6-trioxotetrahydropyrimidin-5(2H)-ylidene) methyl)thiophen-2-yl)acrylonitrile (D₃)

To a dry 100 mL RB flask, a mixture of compound **5** (0.5 g, 1.2 mM) and barbituric acid (0.160 g, 1.25 mM) was added. This mixture was dissolved in 20 mL of absolute methanol and then refluxed for 10 hours under argon atmosphere. The reaction completion was monitored by TLC technique. After reaction completion, the content was cooled down to room temperature; the solid obtained was collected by filtration and dried. The crude product was recrystallized from methanol to yield the pure compound. Yield 85%. MP: 180 °C. **¹H NMR** (DMSO-*d*₆, 400 MHz, δ ppm): 11.32, (1H, s), 11.22 (1H, s), 11.09 (1H, s), 8.38-8.36 (1H, d (J=8 Hz)), 8.18 (1H, s), 8.01-7.99 (1H, d (J=8 Hz)), 7.92-7.88 (1H, t (J=8 Hz)), 7.80 (1H, s), 7.70-7.69 (1H, J=4 Hz)), 7.51-7.42 (2H, m), 7.33-7.29 (1H, t (J=8 Hz)), 7.21-7.19 (1H, t (J=4 Hz)), 6.97-6.95 (1H, d (J=8 Hz)), 6.81-6.78 (1H, d (12 Hz)), 3.92-3.88 (2H, t (J=8 Hz)), 1.64-1.59 (2H, p (J=4 Hz)), 1.36-1.25 (6H, m), 0.86-0.83 (3H, t (J=4 Hz)); **¹³C NMR** (DMSO-*d*₆, 100 MHz, δppm): 164.74, 162.87, 155.24, 150.74, 150.68, 139.09, 138.48, 135.66, 132.50, 131.23, 130.59, 128.94, 128.11, 127.44, 126.98, 125.61, 123.72, 115.96, 114.39, 103.99, 97.63, 52.23-52.10, 31.46-31.43, 27.56-27.35, 26.33-26.29, 22.52, 14.31; **FTIR (ATR)**, ν cm⁻¹: 3171 (N-H stretch), 2918, 2845 (C-H

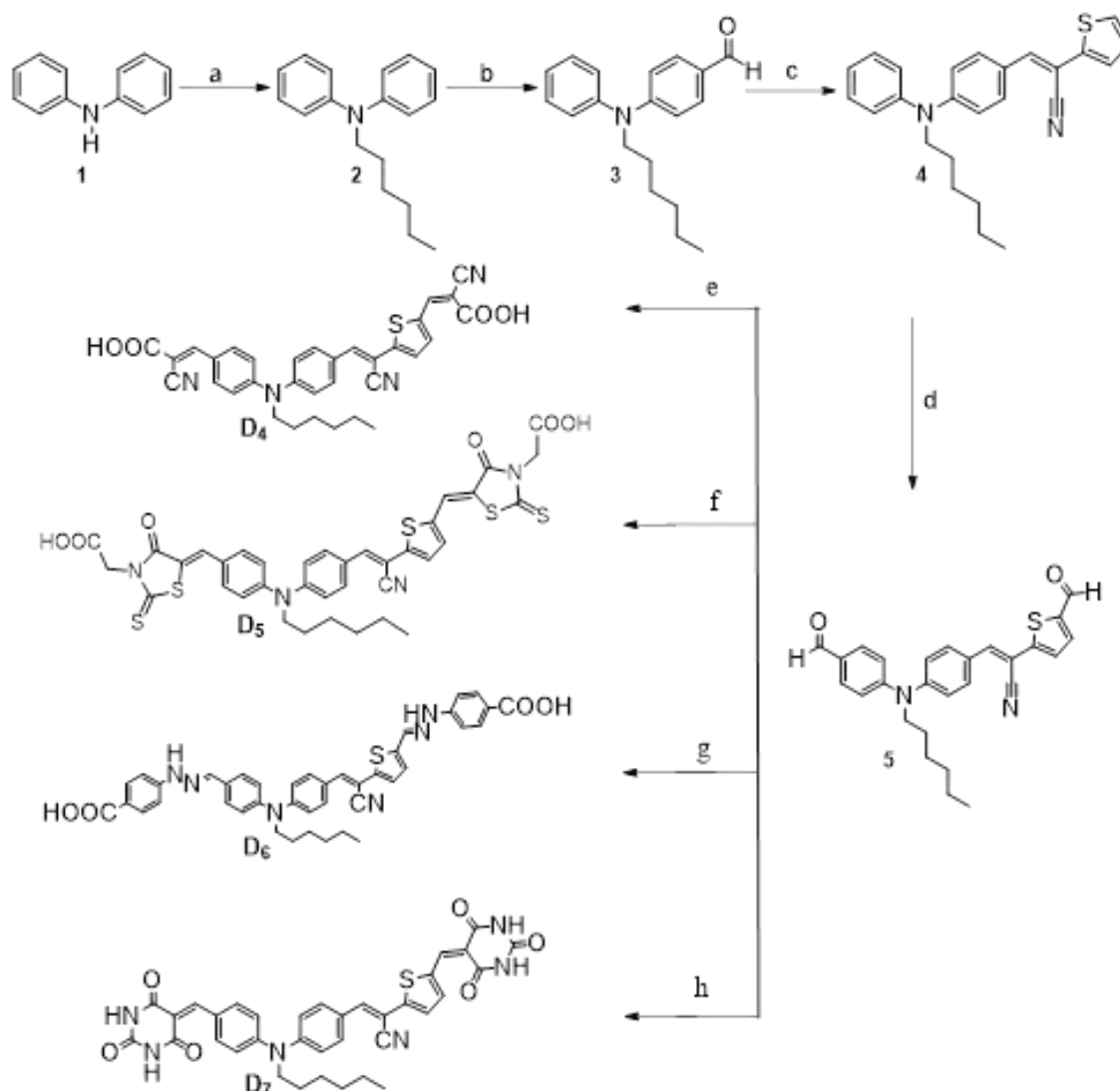
Stretch), 2211 (C≡N Stretch), 1690, 1658 (C=O stretch), 1605 (C=C), 1174 (C-N stretch); **Mass (m/z)**: 524.12; Obtained (M+H): 525.12.

3.2.2.2 Synthesis of chromophores D₄₋₇ (Series-2)

Series 2 (D₄₋₇) chromogens were synthesized by the pathway documented in **Scheme 3.2**. The necessary intermediates from **2** to **4** were synthesized using the same procedures followed in **Series-1**. The final **D₄₋₇** compounds were obtained by subjecting the intermediate **5** to various well-known reactions including Knoevenagel/Schiff condensation reactions. Recrystallization or column chromatography techniques were used to purify the synthesized crude dyes. Procedures adopted for the preparation of intermediate **5**, and target molecules **D₄₋₇** are given in the following section.

(E)-3-(4-((4-formylphenyl)(hexyl)amino)phenyl)-2-(5-formylthiophen-2-yl)acrylonitrile (**5**)

A 3.97 mL (0.025 mM) of freshly distilled POCl₃ was added drop-wise to the 1.9 mL (0.025 mM) of stirred solution of anhydrous DMF at 0 °C under nitrogen till the white coloured Vilsmeier salt was formed. The mixture was stirred for 30 min and to this *(E)*-3-(4-(hexyl(phenyl)amino)phenyl)-2-(thiophen-2-yl)acrylonitrile (**4**, 1 g, 2.5 mM) dissolved in dichloroethane (5 mL) was added while stirring and stirring was continued for some time. Then, the reaction mixture was heated at 90 °C for 12 hours. The reaction mass was allowed to cool down and was poured into ice cold water and subsequently basified using 5 M NaOH solution. The product was extracted using ethyl acetate (50×3 mL). The organic phase was dried using anhydrous sodium sulphate. The solvent was removed under reduced pressure and the crude product obtained was further purified by column chromatography on silica gel (100-200 mesh) using hexane as an eluent yielded a bright red viscous liquid as the product. Yield: 80%. **¹H NMR** (CDCl₃, 400 MHz, δ ppm): 9.89 (1H, s), 9.87 (1H, s), 7.91-7.89 (2H, d (J=8Hz)), 7.81-7.79 (2H, d (J=8Hz)), 7.73-7.72 (1H, d (J=4Hz)), 7.49 (1H, s), 7.44-7.43 (1H, d (J=4Hz)), 7.18-7.17 (2H, d (J=4Hz)), 7.14-7.12 (2H, d (J=8Hz)), 3.86-3.83 (2H, t (J=4Hz & 8Hz)), 1.74-1.68 (2H, q (J=4Hz & 8Hz)), 1.38-1.31 (6H, m), 0.90-0.88 (3H, t (J=4Hz)).



Scheme 3.2. Synthetic routes for target dyes: (a) 1-Bromohexane, NaH, DMF, RT, 10 hours (b) POCl₃, DMF, RT, 12 hours (c) 2-(Thiophene-2-yl)-acetonitrile, NaOMe, CH₃OH, RT, 6 hours (d) POCl₃, DMF, 90 °C, 12 hours (e) Cyanoacetic acid, ammonium acetate, glacial acetic acid, 110 °C, 10 hours (f) Rhodanine acetic acid, ammonium acetate, glacial acetic acid, 110 °C, 10 hours (g) 4-Hydrazinylbenzoic acid, methanol, glacial acetic acid, reflux, 3 hours (h) Barbituric acid, methanol, reflux, 12 hours

(Z)-3-(5-((*E*)-2-(4-((4-((*E*)-2-carboxy-2-cyanovinyl)phenyl)(hexyl)amino)phenyl)-1-cyanovinyl)thiophen-2-yl)-2-cyanoacrylic acid (**D₄**)

A mixture of (*E*)-3-(4-((4-formylphenyl)(hexyl)amino)phenyl)-2-(5-formylthiophen-2-yl)acrylonitrile (**5**, 0.5 g, 1.1 mM), ammonium acetate (3.04 g, 22 mM) and cyano acetic acid (0.2 g, 2.3 mM) was heated in glacial acetic acid for 10

hours. The separated solid was filtered at room temperature and recrystallized from methanol to obtain bright red coloured solid. Yield 77%.MP: 100 °C. **¹H NMR** (DMSO-*d*₆, 400 MHz, δ ppm): 8.34 (1H, s), 8.09 (1H, s), 7.96-7.94 (3H, d (J=8Hz)), 7.89 (2H, s), 7.53 (1H, s), 7.26-7.24 (3H, d (J=8Hz)), 7.15-7.12 (2H, d (J=12Hz)), 3.84 (2H, s), 1.28 (2H, s), 1.20 (4H, s), 0.79 (3H, s). **¹³C NMR** (CDCl₃, 100 MHz, δ ppm): 159.12, 158.36, 147.24, 145.11, 143.49, 141.41, 139.24, 137.55, 134.45, 130.91, 127.76, 126.53, 122.21, 121.39, 119.29, 117.00, 114.45, 112.51, 112.18, 112.03, 95.99, 46.56, 26.05, 22.15, 20.91, 17.16, 8.95. **FTIR (ATR)**, ν cm⁻¹: 3220 (O-H stretch), 2883, 2830 (C-H stretch), 2212 (C≡N stretch), 1702 (C=O), 1566, 1501 (C=C stretch). **Mass (m/z)**: 576.67; Obtained (M-H): 575.

2-((Z)-5-((5-((E)-2-(4-((4-((Z)-3-(carboxymethyl)-4-oxo-2-thioxothiazolidin-5-ylidene) methyl)phenyl)(hexyl)amino)phenyl)-1-cyanovinyl)thiophen-2-yl)methylene)-4-oxo-2-thioxothiazolidin-3-yl)acetic acid (D₅)

(*E*)-3-(4-((4-Formylphenyl)(hexyl)amino)phenyl)-2-(5-formylthiophen-2-yl)acrylonitrile (**5**, 0.5 g, 1.2 mM) was dissolved in glacial acetic acid (14 mL). To this ammonium acetate (3.04 g, 22 mM) was added and it was stirred. After 5 minutes of stirring, rhodanine acetic acid (0.46 g, 2.3 mM) was added to the mixture and it was heated to 110 °C in glacial acetic acid for 10 hours under nitrogen atmosphere. After cooling the mixture, the separated solid was filtered to yield the red solid. It was purified by recrystallization from methanol. Yield 80%. MP: 120 °C. **¹H NMR**: (DMSO-*d*₆, 400 MHz, δ ppm) : 8.08 (1H, s), 7.93 (1H, s), 7.88 (1H, s), 7.75 (2H, s), 7.57-7.56 (2H, d (J=4Hz)), 7.49 (1H, s), 7.20 (5H,s), 4.64 (4H, s), 3.84 (2H, s), 1.57 (2H, s), 1.28 (2H, s), 1.21 (4H, s), 0.80 (3H, s). **¹³C NMR** (CDCl₃, 100 MHz, δ ppm): ¹³C, DMSO-*d*₆, 100 MHz, δppm: 187.83, 186.66, 161.53, 161.03, 143.61, 142.29, 136.78, 132.35, 132.13, 128.61, 127.85, 126.42, 122.36, 121.68, 120.87, 116.09, 115.70, 114.96, 113.19, 111.88, 95.59, 46.54, 40.60, 26.03, 22.17, 20.93, 17.14, 8.92. **FTIR (ATR)**, ν cm⁻¹: 2917, (C-H stretch), 2211 (C≡N stretch), 1703 (C=O stretch), 1570 (C=C stretch), 1503 (C=S stretch). **Mass (m/z)**: 788.09; Obtained (M-H): 786.93.

4-(2-((E)-(5-((E)-2-(4-((4-((E)-(2-(4-Carboxyphenyl)hydrazono)methyl)phenyl)(hexyl)amino)phenyl)-1-cyanovinyl)thiophen-2-yl)methylene)hydrazinyl)benzoic acid (D₆)

A mixture of (*E*)-3-(4-((4-formylphenyl)(hexyl)amino)phenyl)-2-(5-formylthiophen-2-yl)acrylonitrile (**5**, 0.5 g, 1.1 mM) and 4-hydrazinyl benzoic acid (0.38g, 2.3 mM) was heated under reflux in absolute methanol for 3 hours. The separated solid was filtered and recrystallized from methanol to obtain bright red color solid. Yield 90%. MP: 105 °C. ¹H NMR (DMSO-*d*₆, 400 MHz, δ ppm): 10.91-10.90 (1H, d (J=4 Hz)), 10.77-10.72 (1H, d (J=20 Hz)), 8.06-8.04 (1H, d (J=8 Hz)), 7.92 (1H, s), 7.87 (1H, s), 7.79-7.75 (4H, t (J=8 Hz)), 7.69-7.67 (1H, d (J=8 Hz)), 7.63-7.61 (1H, d (J=8 Hz)), 7.58 (1H, s), 7.45 (1H, s), 7.27-7.16 (4H, m), 7.08-7.06 (1H, d (J=8 Hz)), 7.02-7.00 (2H, d (J=8 Hz)), 6.97-6.95 (1H, d (J=8Hz)), 6.90-6.88 (1H, d (J=8 Hz)), 6.76-6.73 (1H, d (J=12 Hz)), 3.71-3.68 (2H, t (J=8 Hz)), 1.56-1.52 (2H, t (J=8 Hz)), 0.80-0.73 (3H, t(J=8 Hz)). ¹³C NMR (DMSO-*d*₆, δ ppm): 162.33, 144.65, 143.88, 143.23, 140.97, 140.87, 135.15, 133.59, 126.60, 126.26, 125.96, 123.63, 122.54, 120.19, 120.01, 115.78, 115.28, 111.01, 110.78, 106.22, 94.28, 46.54, 26.05, 22.06, 20.96, 17.11, 8.90. FTIR (ATR), ν cm⁻¹: 3401 (-O-H, -N-H stretch), 2886, 2870 (C-H stretch), 2211 (C≡N stretch), 1671 (C=O stretch), 1597 (C=N stretch), 1505 (C=C stretch); Mass (m/z): 710.2; Obtained (M-H): 709.02.

(E)-3-(4-(hexyl(4-((2,4,6-trioxotetrahydropyrimidin-5(2H)-ylidene)methyl)phenyl)amino)phenyl)-2-(5-((2,4,6-trioxotetrahydropyrimidin-5(2H)-ylidene)methyl)thiophen-2-yl)acrylo nitrile (D₇)

A mixture of (*E*)-2-(5-formylthiophene-2-yl)-3-(4-(hexyl(phenyl) amino)phenyl) acrylonitrile (0.5 g, 1.1 mM) and barbituric acid (0.32 g, 2.3 mM) was taken in a dry 100 mL RB flask. The mixture was dissolved in 20 mL of absolute methanol and then refluxed for 12 hours under argon atmosphere. The reaction completion was monitored by TLC technique. After reaction completion, the content was allowed to cool; the solid obtained was collected by filtration and dried. The product was recrystallized from methanol to yield the pure compound. Yield 85%. MP: 130 °C. ¹H NMR (DMSO-*d*₆, 400 MHz, δ ppm): 11.29 (2H, s), 11.19 (1H, s), 11.06 (1H, s), 8.34 (1H, s), 8.32-8.30 (2H, d (J=8 Hz)), 8.14-8.11 (2H, d (J=8 Hz)), 8.01-7.95 (3H, m), 7.79-7.77 (1H, d (J=8Hz)), 7.61 (1H, s), 7.34-7.32 (1H, d (J=8Hz)), (7.23-7.16 (1H,

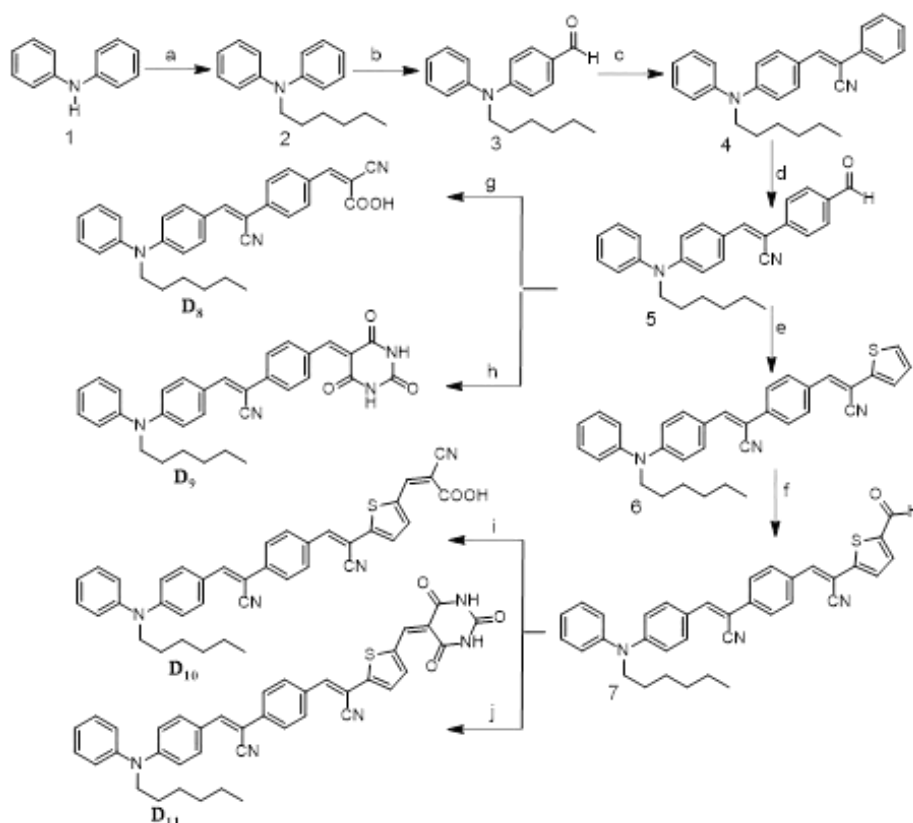
dd (J=8Hz & 12 Hz), 7.02-7.00 (1H, s), 3.85 (2H, s), 1.56 (2H, s), 1.28 (2H, s), 1.20 (4H, s), 0.79 (3H, s). ^{13}C NMR (DMSO- d_6 , δ ppm): 159.18, 158.32, 158.14, 157.34, 149.59, 147.10, 145.95, 145.29, 141.53, 139.95, 132.66, 131.34, 126.65, 126.43, 123.27, 119.57, 118.41, 112.40, 108.85, 106.81, 97.02, 46.65, 26.03, 22.23, 20.90, 17.12, 8.91. FTIR (ATR), ν cm^{-1} : 3188 (N-H stretch), 2882, 2815 (C-H stretch), 2213 (C \equiv N stretch), 1737, 1697 (C=O stretch), 1591, 1491 (C=C stretch); Mass (m/z): 662.70; Obtained (M+H): 663.20.

3.2.2.3 Synthesis of chromophores D_{8-11} (Series-3)

Scheme 3.3 depicts the synthetic pathway of the newly designed dyes D_{8-11} . The requisite intermediates from **2** to **7** were synthesized from well documented procedures with slight modifications. The intermediate **5** was transformed into D_{8-9} and compound **7** were converted to D_{10-11} following Knoevenagel reaction or Schiff base reactions. Required *N*-hexyl diphenyl amine (**2**) and 4-(hexyl (phenyl)aminobenzaldehyde (**3**) were synthesized using the same procedures followed for the dyes of the Series-1. The procedures for the synthesis of intermediates **4** to **7** and dyes D_{8-11} are given in the following section.

(*E*)-3-(4-(Hexyl (phenyl) amino) phenyl)-2-(thiophen-2-yl) acrylonitrile (**4**)

To a freshly prepared solution of sodium methoxide (0.12 g, 5.3 mM) of sodium in 10 mL of methanol), aldehyde **3** (0.5 g, 1.78 mM) was added slowly while stirring. 2-(4-formylphenyl)acetonitrile (2.26 g, 2.14 mM) was then added to the reaction mass and stirring was continued for 6 hours at room temperature. The product was extracted with ethyl acetate (3 \times 50 mL). The organic phase was dried using anhydrous sodium sulphate. The solvent was removed under reduced pressure and the crude oily product obtained was further purified by column chromatography on silica gel (100-200 mesh) using hexane/ethyl acetate (1%) as an eluent to yield light yellow liquid as the product. Yield: 80%.



Scheme 3.3. Synthetic routes for target dyes: (a) 1-Bromohexane, NaH, DMF, RT, 10 hours (b) POCl₃, DMF, RT, 12 hours (c) 2-(4-Formylphenyl)acetonitrile, NaOMe, CH₃OH, RT, 6 hours (d) POCl₃, DMF, RT, 12 hours (e) 2-(Thiophene-2-yl)acetonitrile, NaOMe, CH₃OH, RT, 6 hours (f) POCl₃, DMF, RT, 12 hours (g & i) Cyanoacetic acid, ammonium acetate, glacial acetic acid, 110 °C, 10 hours (h & j) Barbituric, Methanol, Reflux, 12 hours

(Z)-2-(4-Formylphenyl)-3-(4-hexyl(phenyl)amino)phenyl acrylonitrile (**5**)

In a dry two necked round bottom flask, freshly distilled DMF (0.41 mL, 5.26 mM) was taken and to this POCl₃ was added drop-wise (0.5 mL, 5.26 mM) at 0 °C under nitrogen atmosphere. The obtained mixture was allowed to stir for 30 min at 0 °C and to this compound **4** (0.5 g, 1.32 mM) dissolved in dichloroethane (5 mL) was added. The reaction mixture was stirred continuously for 12 hours at room temperature. The completion of reaction was monitored by TLC. After the completion of reaction, the reaction mass was poured into ice cold water and subsequently basified using 5 M NaOH solution. The product was extracted with ethyl acetate (50 mL×3). The organic phase was dried using anhydrous sodium sulphate. The solvent was removed under reduced pressure and the crude oily product obtained was further

purified by column chromatography on silica gel (100-200 mesh) using ethyl acetate/hexanes (1%) as mobile phase to give bright yellow coloured liquid. Yield: 90%.

(E)-3-(4-((*Z*)-1-Cyano-2-(4-(hexyl(phenyl)amino)phenyl)vinyl)phenyl)-2-(thiophen-2-yl) acrylonitrile (**6**)

In a single neck round bottom flask, compound **5** (0.5g g, 1.22 mM) was added slowly to freshly prepared solution of sodium methoxide (0.084 g, 3.67 mM of sodium in 10 mL of methanol) while stirring. 2-(thiophene-2-yl)-acetonitrile (0.18 g, 1.47 mM) was then added to reaction mass slowly. Stirring was continued for 6 hours at room temperature and the product was extracted using ethyl acetate/water (50 mL×3). Organic phase was dried using sodium sulfate. The solvent was removed under reduced pressure and the crude product obtained was further purified by column chromatography on silica gel using hexane. The product obtained was red coloured viscous liquid. Yield: 85%.

(Z) -2-(4-Formylphenyl)-3-(4-(hexyl(phenyl)amino)phenyl)acrylonitrile (**7**)

Distilled DMF (0.23 mL, 2.9 mM) was taken in a two necked dry round bottomed flask and to this POCl₃ (0.27 mL, 2.9 mM) was added cautiously in a drop-wise fashion at 0 °C under nitrogen. The mixture was stirred for 30 min and to this compound **6** (0.5 g, 0.97 mM) dissolved in dichloroethane (5 mL) was added while stirring and stirring was continued at room temperature for 12 hours. The reaction mass was then poured into ice cold water and subsequently basified by using 5 M NaOH solution. The product was extracted using ethyl acetate/water (50 mL×3). Organic phase was dried using sodium sulfate. The solvent was removed under reduced pressure and the crude product obtained was further purified by column chromatography on silica gel using ethyl acetate/hexanes (2%). The product obtained was bright red coloured sticky liquid. Yield: 85%.

(Z)-2-Cyano-3-(4-((*Z*)-1-cyano-2-(4-(hexyl(phenyl)amino)phenyl)vinyl)phenyl)acrylic acid (**D₈**)

A mixture of compound **5** (0.5 g, 1.2 mM), ammonium acetate (1.13 g, 14.6 mM) and cyano acetic acid (0.11 g, 1.48 mM) taken in a single necked round bottom flask was heated in glacial acetic acid at 110 °C for 10 hours. The separated solid was filtered at

room temperature and recrystallized from methanol to obtain bright red coloured solid. Yield 85%. MP: 120 °C. ¹H NMR (CDCl₃, 400 MHz, δ ppm): 9.74-9.71 (1H, d (J=12 Hz)), 7.96-7.94 (2H, d (J=8 Hz)), 7.72-7.65 (3H, m), 7.46-7.37 (4H, m), 7.29-7.27 (2H, d (J=8 Hz)), 7.16-7.14 (1H, d (J=8 Hz)), 7.02-7.00 (1H, d (J=8 Hz)), 6.93-6.91 (1H, d (J=8 Hz)), 3.79-3.78 & 3.68-3.67 (2H, t), 1.55-1.46 (2H, t), 1.29-1.15 (6H, m), 0.76 (3H, s). ¹³C NMR (CDCl₃, 100 MHz, δ ppm): 185.44, 146.96, 142.69, 136.98, 129.12, 126.57, 126.45, 126.01, 124.50, 124.20, 123.56, 120.66, 118.79, 118.38, 112.28, 103.28, 46.61, 26.05, 22.04, 20.95, 17.13, 8.89. FTIR (ATR), vcm⁻¹: 3057 (O-H stretch), 2921, 2850 (C-H stretch), 2212 (C≡N stretch), 1681 (C=O stretch), 1564, 1498 (C=C stretch). Mass (m/z): 475.22, M+H observed: 476.13

(Z)-3-(4-(Hexyl(phenyl)amino)phenyl)-2-(4-((2,4,6-trioxotetrahydropyrimidin-5(2H)-ylidene)methyl)phenyl)acrylonitrile (D₉)

A dry single neck 100 mL round bottom flask was charged with compound **5** (0.5 g, 1.22 mM) and barbituric acid (0.19 g, 1.46 mM). The mixture was dissolved in 20ml of absolute methanol and then was refluxed for 12 hours under argon atmosphere. The reaction completion was monitored by TLC technique. When the reaction has completed, the content was allowed to attain room temperature, the separated solid was collected by filtration and dried. The product was recrystallized from methanol. Yield 75%. MP: 145 °C. ¹H NMR (DMSO-*d*₆, 400 MHz, δ ppm): 11.32 (1H, s), 11.22 (1H, s), 11.09 (1H, s), 8.46 (1H, s), 8.38-8.36 (1H, d (J=8 Hz)), 8.18 (1H, s), 8.01-7.99 (1H, d (J=8Hz)), 7.92-7.88 (1H, t (J=8Hz)), 7.80 (1H, s), 7.70-7.69 (1H, d (J=4 Hz)), 7.59-7.58 (1H, d (J=4 Hz)), 7.52-7.42 (3H, m), 7.31-7.29 (1H, d (J=8 Hz)), 7.21-7.19 (1H, t (J=4 Hz)), 3.92-3.89 (2H, t (J=8 Hz)), 1.65-1.57 (2H, p), 1.36-1.25 (6H, m), 0.86-0.83 (3H, t (J=4 Hz)). ¹³C NMR (DMSO-*d*₆, 100 MHz, δ ppm): 168.20, 164.76, 162.89, 155.25, 152.11, 150.68, 147.33, 142.40, 138.53, 134.42, 132.02, 131.45, 130.79, 129.97, 129.68, 128.99, 1256.17, 125.80, 125.55, 123.60, 115.78, 113.13, 109.46, 52.13, 31.44, 27.56, 26.29, 22.51, 14.32. FTIR (ATR), vcm⁻¹: 3160, 3080 (N-H Stretch), 2920, 2845 (C-H stretch), 2206 (C≡N Stretch), 1692 (C=O stretch), 1651 (N-H bending), 1594 (C=C). Mass (m/z): 518.62, M+H observed: 519.47.

(Z)-2-Cyano-3-(5-((*E*)-1-cyano-2-(4-((*Z*)-1-cyano-2-(4-(hexyl(phenyl)amino)phenyl)vinyl)phenyl)vinyl)thiophen-2-yl)acrylic acid (**D10**)

Compound **7** (0.5 g, 0.923 mM), ammonium acetate (0.86 g, 11.09 mM) and cyano acetic acid (0.09 g, 1.11 mM) were taken together in a single necked 100 mL round bottom flask and were dissolved in glacial acetic acid (10 mL). This mixture was heated for 10 hours at 110 °C. The separated solid was filtered at room temperature and recrystallized from methanol to obtain bright red colour solid. **¹H NMR** (DMSO-*d*₆, 400 MHz, δ ppm): 8.42 (1H, s), 8.09 (1H, s), 7.93 (4H, s), 7.70 (3H, s), 7.52-7.29 (6H, m), 7.16 (1H, s), 7.08 (1H, s), 6.99 (1H, s), 3.82 (2H, s), 1.56 (2H, s), 1.19 (6H, s), 0.79 (3H, s). **¹³C NMR** (DMSO-*d*₆, 100 MHz, δ ppm): 159.29, 158.46, 148.23, 146.07, 144.66, 143.02, 142.71, 142.27, 140.68, 138.23, 137.05, 135.52, 130.04, 129.18, 128.12, 126.73, 126.00, 124.22, 123.59, 120.63, 119.67, 119.40, 117.99, 113.38, 112.29, 111.99, 102.85, 94.11, 46.62, 26.05, 24.09, 22.17, 20.95, 17.14, 8.91. **FTIR (ATR)**, vcm^{-1} : 2961, 2923, 2853 (C-H stretch), 2209 (C≡N stretch), 1686 (C=O stretch), 1561, 1501 (C=C stretch). **Mass (m/z)**: 608.22, M-H observed: 606.97.

(Hexyl(phenyl)amino)phenylvinylphenyl-2-(5-((2,4,6-trioxotetrahydropyrimidin-5(2H)-ylidene)methyl)thiophen-2-yl)acrylonitrile (**D11**)

A mixture of compound **7** (0.5g, 0.923 mM) and barbituric acid (0.14 g, 1.11 mM) was dissolved in absolute methanol taken in a dry 100 mL round bottom flask. The mixture was then refluxed for 12 hours under argon atmosphere. The reaction completion was monitored using TLC technique. The contents were allowed to cool down to room temperature, the separated solid was filtered and dried. The product was recrystallized from methanol. Yield 75%. **¹H NMR** (DMSO-*d*₆, 400 MHz, δ ppm): 11.28 (2H, s), 8.41 (1H, s), 8.10-8.09 (1H, d (J=4 Hz)), 7.96-7.90 (5H, m), 7.72-7.70 (2H, d (J=8 Hz)), 7.56-7.55 (1H, d (J=4 Hz)), 7.47-7.47 (2H, d (J=8 Hz)), 7.40-7.39 (2H, d (J=4 Hz)), 7.30-7.28 (2H, d (J=8 Hz)), 7.07-7.05 (2H, d (J=8 Hz)), 3.82 (2H, s), 1.57 (2H, s), 1.28 (2H, s), 1.20 (4H, s), 0.79 (3H, s). **¹³C NMR** (DMSO-*d*₆, 100 MHz, δ ppm): 158.38, 158.22, 148.14, 145.31, 144.75, 142.65, 141.75, 140.02, 138.38, 137.05, 130.76, 129.16, 126.85, 126.00, 124.24, 120.64, 120.53, 119.69, 118.16, 113.25, 112.33, 106.24, 102.94, 94.42, 46.57, 26.05, 22.17, 20.95,

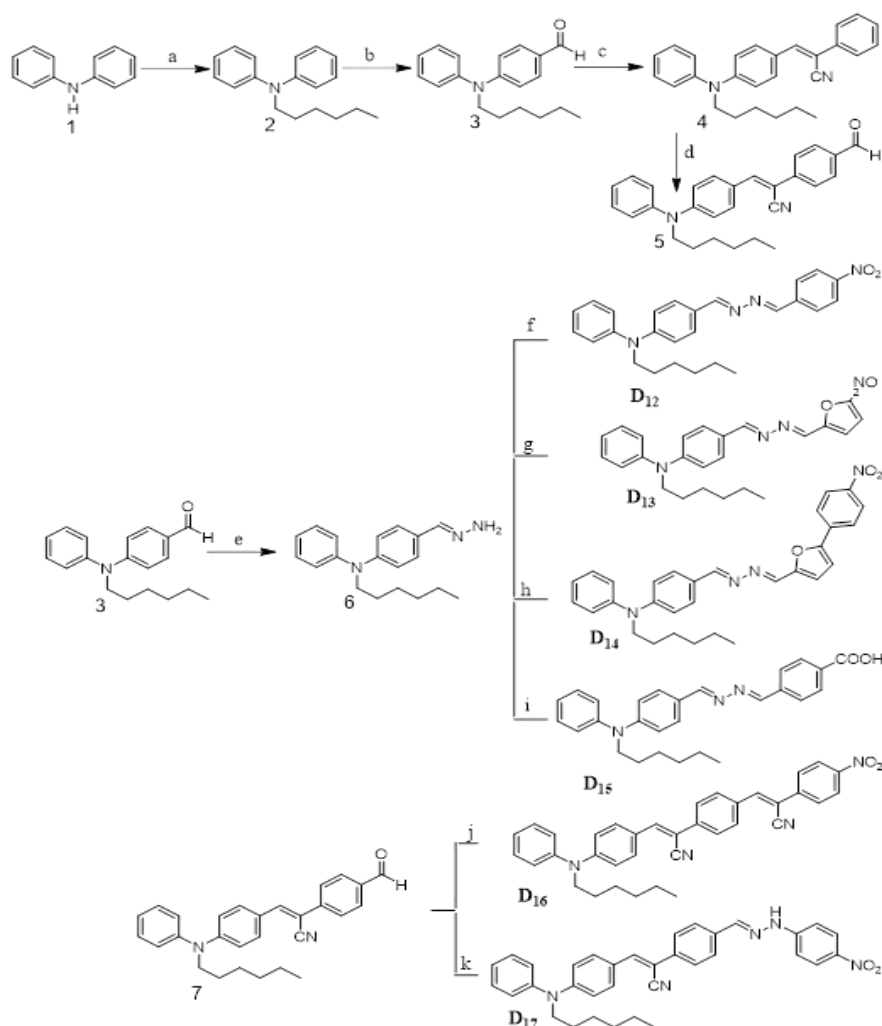
17.14, 8.92. **FTIR (ATR)**, ν cm^{-1} : 3384 (N-H), 2205 ($\text{C}\equiv\text{N}$), 1726, 1700 ($\text{C}=\text{O}$), 1661 ($\text{C}=\text{O}$), 1542 ($\text{C}=\text{C}$). **Mass (m/z)**: 651.23, M-H observed: 649.99.

3.2.2.4 Synthesis of chromophores D_{12-17} (Series-4)

The synthetic pathway followed for the dyes D_{12-17} is sketched in **Scheme 3.4**. All the required intermediates **2**, **3**, **4**, **5** and **6** were synthesized from the well-documented procedures incorporating slight modifications. The synthetic procedures followed for the compounds **1** to **3** have been given under **Series-1**, whereas the procedures for synthesis of intermediates **4** and **5** were documented under synthesis of **Series-3**. Here, aldehyde derivative **3** was condensed with hydrazine monohydrate to yield a penultimate product, (E)-N-hexyl-4-(hydrazonomethyl)-N-phenylaniline (**6**). This hydrazone was treated with different substituted aromatic aldehydes, viz. 4-nitrobenzaldehyde, 5-nitro-2-furaldehyde, 5-(4-nitrophenyl)furan-2-carbaldehyde), 4-formylbenzoic acid to yield the target dyes D_{12} , D_{13} , D_{14} and D_{15} , respectively. Another penultimate intermediate **5** was reacted with 4-nitrophenylacetonitrile in presence of catalyst, piperidine to yield D_{16} , whereas the compound **5** was treated with (4-nitrophenyl)hydrazine in presence of catalytic amount of glacial acetic acid to form D_{17} . Procedures followed for the synthesis of intermediate **6** and final dyes D_{12-17} are as follows.

(E)-N-Hexyl-4-(hydrazonomethyl)-N-phenylaniline (**6**)

4-(Hexyl(phenyl)aminobenzaldehyde (**3**, 1 g, 3.55 mM)) was dissolved in methanol (10 mL) in a single neck 100 mL round bottom flask. The solution was stirred for 10 minutes at room temperature. Hydrazine monohydrate (1.63 g, 35.5 mM) was added to the solution drop-wise and was refluxed for 5 hours. After the completion of reaction, 10 mL of distilled water was added and the product was extracted using DCM (50 mL \times 3). Organic phase was dried using sodium sulphate. The solvent was removed under pressure and the crude product was purified using recrystallization in methanol. The obtained product was a yellow solid. Yield 95%. MP: 120 °C.



Scheme 3.4. Synthetic routes for target dyes: (a) 1-Bromohexane, NaH, DMF, RT, 10 hours (b) POCl₃, DMF, RT, 12 hours (c) 2-(4-Formylphenyl)acetonitrile, NaOMe, CH₃OH, RT, 6 hours (d) POCl₃, DMF, RT, 12 hours (e) Hydrazine monohydrate, CH₃OH, heating, 5 hours (f) 4-Nitrobenzaldehyde (g) 5-Nitro-2-furaldehyde (h) 5-(4-Nitrophenyl)furan-2-carbaldehyde) (i) 4-Formylbenzoic acid (k) 4-Nitrophenylacetonitrile, piperidine, ethanol, reflux (j) (4-Nitrophenyl)hydrazine, methanol, glacial acetic acid, reflux, 7 hours

N-Hexyl-4-((*E*)-(((*E*)-4-nitrobenzylidene)hydrazono)methyl)-*N*-phenylaniline (**D₁₂**)

(*E*)-*N*-Hexyl-4-(hydrazonomethyl)-*N*-phenylaniline (**6**, 0.25 g, 0.85 mM) was taken in absolute methanol (10 mL) and to this solution, 4-nitrobenzaldehyde (0.15 g, 1.02 mM) was added while stirring, followed by two drops of glacial acetic acid as a catalyst. It was refluxed for 6-7 hours. Upon completion of reaction, the reaction mass was allowed to cool to room temperature. The separated solid was filtered and washed with methanol. The pure product was obtained by recrystallization from methanol as

orange red solid. Yield 75%. MP: 140 °C. ¹H NMR (CDCl₃, 400 MHz, δ ppm): 8.67 (1H, s), 8.60 (1H, s), 8.29-8.27 (2H, d (J=8 Hz)), 7.98-7.97 (2H, d (J=4 Hz)), 7.67-7.65 (2H, d (J=8 Hz)), 7.43-7.40 (2H, t (J=8 Hz)), 7.24-7.20 (3H, m), 6.78-6.76 (2H, d (J=8 Hz)), 3.74-3.71 (2H, t (J=4 Hz)), 1.72-1.67 (2H, q), 1.36-1.30 (6H, m), 0.89-0.87 (3H, t (J=4 Hz)). ¹³C NMR (CDCl₃, 100 MHz, δ ppm): 164.28, 157.64, 151.50, 148.82, 146.34, 140.62, 130.50, 129.92, 128.79, 126.76, 125.55, 124.01, 114.73, 52.60, 31.62, 27.35, 26.70, 22.66, 14.05. FTIR (ATR), ν cm⁻¹: 2925, 2854 (C-H stretch), 1589 (C=C), 1512 (C=N), 1492 (N=O). Mass (m/z): 428.54, M+H observed: 429.52.

N-Hexyl-4-((E)-(5-nitrofuranyl)methylene)hydrazono)methyl-N-phenylaniline (D13)

5-Nitro-2-furaldehyde (0.14 g, 1.02 mM) was added to compound **6** (0.25 g, 0.85 mM) dissolved in methanol (10 mL) and was stirred at room temperature for 10 min. Then, the reaction mass was refluxed for 6-7 hours in the presence of two drops of acetic acid as a catalyst. After the completion of reaction, the reaction mass was allowed to cool to room temperature. The solid precipitated was filtered and washed with methanol. The pure product was obtained by recrystallization from methanol as red solid. Yield 70%. MP: 105 °C. ¹H NMR (DMSO-*d*₆, 400 MHz, δ ppm): 8.65 (1H, s), 8.58 (1H, s), 7.82-7.81 (1H, d (J=4 Hz)), 7.69-7.67 (2H, d (J=8 Hz)), 7.48-7.44 (2H, t (J=8 Hz)), 7.33-7.32 (1H, d (J=4 Hz)), 7.26-7.24 (3H, d (J=8 Hz)), 6.80-6.78 (2H, d (J=8 Hz)), 3.76-3.73 (2H, t (J=4 Hz)), 1.63-1.55 (2H, p), 1.33-1.24 (6H, m), 0.86-0.82 (3H, t (J=8 Hz)). ¹³C NMR (CDCl₃, 100 MHz, δ ppm): 164.26, 152.26, 151.34, 151.16, 147.70, 145.63, 130.56, 129.99, 126.38, 125.51, 122.14, 117.46, 114.40, 51.61, 30.95, 26.80, 25.85, 22.00, 13.81. FTIR (ATR), ν cm⁻¹: 2950, 2922, 2850 (C-H stretch), 1605 (C=C stretch), 1510 (C=N stretch), 1495 (N=O stretch). Mass (m/z): 418.2; Obtained (M+H): 419.21.

N-Hexyl-4-((E)-(5-(4-nitrophenyl)furan-2-yl)methylene)hydrazono)methyl-N-phenylaniline (D14)

(*E*)-*N*-Hexyl-4-(hydrazonomethyl)-*N*-phenylaniline (**6**, 0.25 g, 0.85 mM) and 5-(4-nitrophenyl)furan-2-carbaldehyde (0.22 g, 1.02 mM) were dissolved in

methanol (15 mL) and it was refluxed for 6-7 hours with two drops of glacial acetic acid as a catalyst. The completed reaction mass was allowed to cool to room temperature. The solid precipitated was filtered and washed with methanol. The pure product was obtained by recrystallization from methanol as red solid. Yield 88%. MP: 160 °C. **¹H NMR** (CDCl₃, 400 MHz, δ ppm): 8.62 (1H, s), 8.52 (1H, s), 8.29-8.27 (2H, d (J=8 Hz)), 7.94-7.92 (2H, d (J=8 Hz)), 7.66-7.65 (2H, d (J=8 Hz)), 7.42-7.39 (2H, t (J=8 Hz)), 7.21-7.20 (3H, d (J=4 Hz)), 7.00 (2H, s), 6.79-6.77 (2H, d (J=8 Hz)), 3.74-3.71 (2H, t (J=4 Hz)), 1.72-1.66 (2H, p), 1.34-1.29 (6H, m), 0.90-0.87 (3H, t (J=8 Hz)). **¹³C NMR** (CDCl₃, 100 MHz, δ ppm): 177.56, 163.24, 156.30, 153.85, 153.08, 151.47, 151.23, 148.63, 147.01, 146.47, 135.45, 134.58, 130.24, 129.84, 126.50, 125.78, 124.80, 124.43, 124.34, 117.17, 114.97, 111.15, 110.65, 52.54, 31.59, 27.33, 26.68, 22.63, 14.01. **FT-IR (ATR)**, ν cm⁻¹: 2923 (C-H stretch), 1593 (C=C stretch), 1513 (C=N stretch), 1180 (C-O stretch). **Mass (m/z)**: 494.24; Obtained (M+H): 495.47.

4-((E)-(((E)-4-(Hexyl(phenyl)amino)benzylidene)hydrazono)methyl)benzoic acid (D₁₅)

A mixture of (*E*)-*N*-hexyl-4-(hydrazonomethyl)-*N*-phenylaniline, (**6**, 0.25 g, 0.85 mM) and 4-formylbenzoic acid (0.15 g, 1.02 mM) dissolved in methanol (15 mL) was allowed to stir at room temperature for 10-15 minutes. To the reaction mass, two to three drops of glacial acetic acid was added as catalyst and it was refluxed for 7 hours. After completion of the reaction, the reaction mixture was allowed to cool to room temperature, the precipitated solid was filtered and washed with methanol. The pure product was obtained by recrystallization from methanol. Yield: 89%. MP: 130 °C. **¹H NMR** (CDCl₃, 400 MHz, δ ppm): 8.67 (s, 1H), 8.60 (s, 1H), 8.15-8.13 (d, 1H (J=8 Hz)), 7.92-7.90 (1H, d, (J=8 Hz)), 7.67-7.64 (2H, d (J=12 Hz)), 7.46-7.35 (3H, m), 7.22-7.20 (3H, d (J=8 Hz)), 6.81-6.77 (2H, t (J=8 Hz)), 6.70-6.68 (1H, d (J=8 Hz)), 3.74-3.70 (2H, t (J=8 Hz)), 1.73-1.66 (2H, p), 1.31 (6H, s), 0.89-0.86 (3H, t (J=4 Hz)). **¹³C NMR** (DMSO-*d*₆, 100 MHz, δ ppm): 167.22, 161.34, 137.91, 133.49, 130.54, 130.36, 130.22, 128.94, 128.49, 126.55, 115.17, 52.05, 31.44, 27.30, 26.36, 22.48, 14.28. **FTIR (ATR)**, ν cm⁻¹: 2836 (C-H stretch), 1678 (C=O stretch), 1608 (C=C stretch), 1511 (C=N stretch). **Mass (m/z)**: 428.2, M+H observed: 428.1.

(Z)-3-(4((*Z*)-1-Cyano-2-(4-(hexyl (phenyl)amino) phenyl)vinyl)phenyl)-2-(4-nitrophenyl)acrylonitrile (**D₁₆**)

Two drops of piperidine were added to the mixture of 4-nitrophenylacetonitrile (0.22 g, 1.35 mM) and (*E*)-2-(5-formylthiophene-2-yl)-3-(4-(hexyl(phenyl)amino) phenyl)acrylonitrile (**5**, 0.5 g, 1.22 mM) taken in dry ethanol (15 mL) under argon atmosphere. The reaction mixture was refluxed for 3 hours and then cooled to room temperature. The product was extracted using ethyl acetate (50 mL×3). Organic phase was dried using sodium sulphate. The solvent was removed under reduced pressure and the crude product obtained was further purified by column chromatography on silica gel using hexane. The product obtained was red solid. Yield: 75%. MP: 110 °C. ¹H NMR (DMSO-*d*₆, 400 MHz, δ ppm): 8.36-8.33 (2H, d (J=12 Hz)), 8.19 (1H, s), 8.02-7.94 (4H, m), 7.77-7.76 (2H, d (J=4Hz)), 7.61 (1H, s), 7.55-7.43 (4H, m), 7.35-7.33 (1H, d (J=8 Hz)), 7.20-7.18 (2H, d (J=8 Hz)), 7.11-7.07 (2H, q (J=12 Hz)), 3.92-3.89 (2H, t (J=8 Hz)), 1.66-1.62 (2H, p), 1.38-1.23 (6 H, m), 0.86-0.82 (3H, t (J=12 Hz)). ¹³C NMR (DMSO-*d*₆, 100 MHz, δ ppm) : 149.94, 148.28, 147.18, 146.05, 142.50, 141.39, 134.60, 132.19, 131.40, 129.63, 129.36, 128.66, 126.74, 126.01, 125.66, 124.77, 122.91, 119.17, 118.82, 118.58, 108.01, 103.94, 51.91, 31.46, 27.55, 26.35, 22.54, 14.32. FT-IR (ATR), ν cm⁻¹: 2914, 2853 (C-H stretch), 2211 (C≡N Stretch), 1600, 1570 (C=C stretch), 1504 (C=N stretch). Mass (m/z): 552.25, M+H obtained: 553.46.

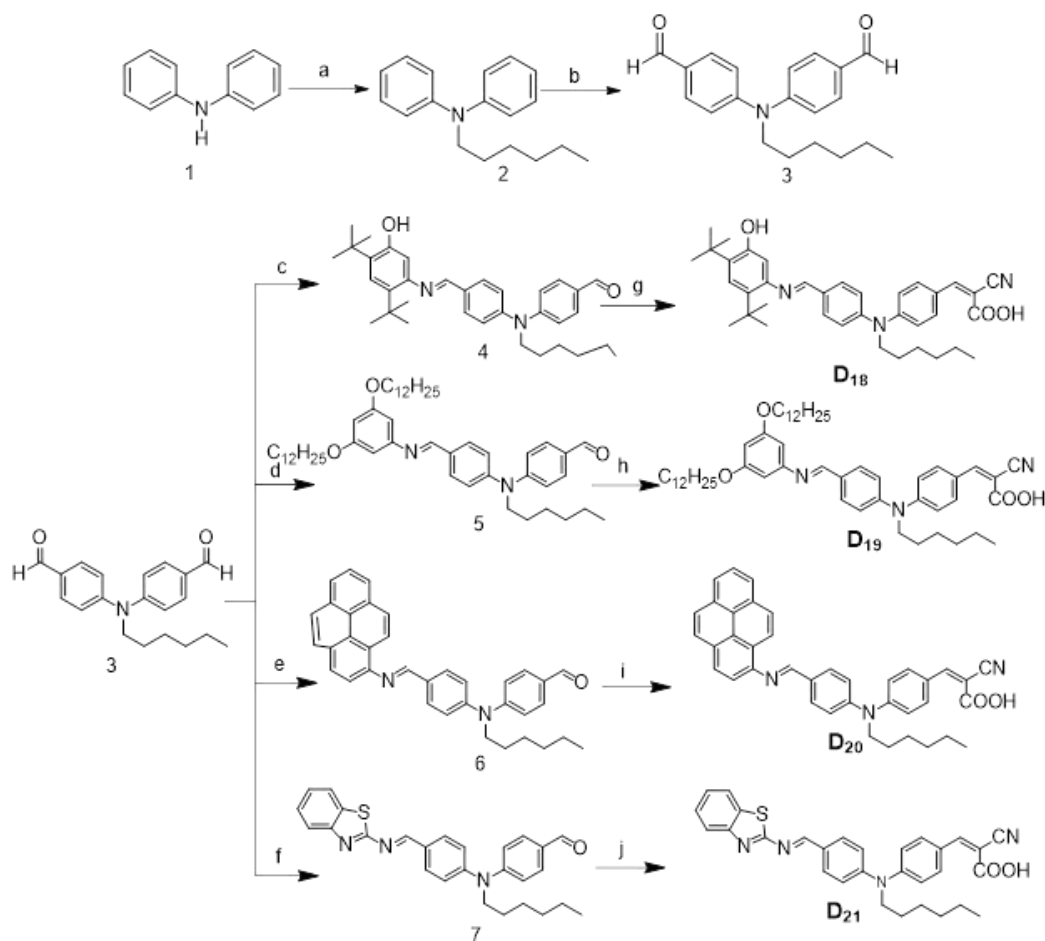
(Z)-3-(4-(Hexyl(phenyl)amino)phenyl)-2-(4-(*E*)-(2-(4-nitrophenyl)hydrazono)methyl)phenyl) acrylonitrile (**D₁₇**)

Compound **5** (0.5g, 1.22 mM) was dissolved in a 100 mL single neck round bottom flask in 10 mL of methanol and stirred at room temperature for about 2 minutes. To this solution (4-nitrophenyl) hydrazine (0.21g, 1.35 mM) was added drop-wise followed by the addition of two drops of acetic acid. The reaction mass was stirred for 5 hours at reflux condition so as to complete the reaction. Upon reaction completion, it was charged with 10 mL of distilled water, followed by 10 mL of dichloromethane and stirred for 10 minutes. Two layers were separated, organic layer was washed with 10 mL of distilled water and then dried over anhydrous sodium sulphate. Organic solvent was distilled off completely, dried at 50 °C under vacuum in rotary evaporator. Red solid was obtained as product. Yield: 95%. MP: 150 °C. ¹H

NMR (DMSO-*d*₆, 400 MHz, δ ppm): 9.78 (2H, s), 8.02 (2H, s), 8.00 (1H, s), 7.95-7.93 (2H, d (J=8 Hz)), 7.78-7.76 (4H, d (J=8 Hz)), 7.54-7.51 (2H, t (J=4 Hz)), 7.46-7.43 (1H, t (J=4 Hz)), 7.38-7.36 (2H, d (J=8 Hz)), 7.09-7.07 (2H, d (J=8 Hz)), 6.61-6.58 (2H, d (J=12 Hz)), 3.89-3.85 (2H, t (J=8 Hz)), 1.63-1.58 (2H, p), 1.36-1.25 (6H, m), 0.86-0.83 (3H, t (J=8 Hz)). **¹³C NMR** (DMSO-*d*₆, 100 MHz, δ ppm): 156.12, 152.42, 148.11, 142.50, 136.13, 134.52, 131.90, 131.43, 129.66, 129.58, 129.49, 128.72, 126.83, 126.10, 124.34, 118.72, 117.64, 112.88, 108.69, 52.00, 31.44, 27.44, 26.32, 22.51, 14.31. **FTIR (ATR)**, ν cm⁻¹: 3365 (N-H stretch), 2923, 2852 (C-H stretch), 2215 (C \equiv N stretch), 1648 (N-H bend), 1585 (C=C stretch), 1510 (C=N stretch). **Mass (m/z)**: 543.26, M+H obtained: 541.39.

3.2.2.5 Synthesis of chromophores *D*₁₈₋₂₁ (Series-5)

Scheme 3.5 shows the synthetic pathway of the newly designed dyes **D**₁₈₋₂₁. Required intermediate *N*-hexyl-*N*-phenylaniline (**2**) was synthesized in the same way as mentioned under **Series-1**. The compound **2** was subjected to formylation using Vilsmeier-Haack reaction for obtaining 4,4'-hexylazanediyldibenzaldehyde (**3**) in good yield. Further, the product **3** was condensed with 5-amino-2,4-di-*tert*-butylphenol, 3,5-bis(dodecyloxy)aniline, pyren-1-amine and benzo[d]thiazol-2-amine to get the penultimate intermediates **4**, **5**, **6**, and **7**, respectively. All the intermediates were obtained in good yield. These intermediates are finally converted to the target dyes **D**₁₈, **D**₁₉, **D**₂₀, **D**₂₁, respectively by condensing with cyanoacetic acid following Knoevenagel condensation protocol, the reaction being carried out at high temperature. Here, a trace of glacial acetic acid acts as a catalyst. In all the dyes, cyanoacetic acid unit acts as a common anchoring agent. These dyes were purified by re-crystallization technique. The procedures used for the synthesis of intermediates **3** to **7** and **D**₁₈₋₂₁ are given in the following paragraphs.



Scheme 3.5. Synthetic routes for target dyes: (a) 1-Bromohexane, NaH, DMF, RT, 10 hours (b) POCl₃, DMF, RT, 12 hours (c) 5-Amino-2,4-di-*tert*-butylphenol (d) 3,5-Bis(dodecyloxy)aniline (e) Pyren-1-amine (f) Benzo[d]thiazol-2-amine, CH₃OH, RT, 5 hours (g, h, i & j) 4/5/6/7, Cyanoacetic acid, ammonium acetate, glacial acetic acid, 110 °C, 10 hours

4,4'-Hexylazanediyl)dibenzaldehyde (3)

A dry two necked round bottomed flask was charged with freshly distilled DMF (12.22 mL, 157.9 mM), to this solution POCl₃ was added drop-wise (14.75 mL, 157.9 mM) at 0 °C under nitrogen. The mixture was stirred for 30-60 minutes and to this *N*-hexyl-*N*-phenylaniline (**2**, 1.0 g, 3.95 mM) dissolved in dichloroethane (15 mL) was added while stirring and stirring was continued at room temperature for 12 hours. The reaction mass was then poured into ice cold water and subsequently basified by using 5 M NaOH solution. The product was extracted using ethyl acetate/water (50 mL×3). Organic phase was dried using sodium sulfate. The solvent was removed under reduced pressure and the crude oily product obtained was further purified by

column chromatography on silica gel using hexane as an eluent. The product was a light brown colour liquid. The crude product was purified by column chromatography on silica gel using ethyl acetate/hexane as mobile phase to give light brown colored liquid. Yield: 90%.

(E)-4-((4-(((2,4-Di-*tert*-butyl-5-hydroxyphenyl)imino)methyl)phenyl)(hexyl)amino)benzaldehyde (**4**)

4-(Hexyl(phenyl)aminobenzaldehyde (**3**, 0.25 g, 0.808 mM) dissolved in 5 mL methanol was taken in single neck round bottom flask. It was added with 5-amino-2,4-di-*tert*-butylphenol (0.18 g, 0.809 mM). To this two drops of glacial acetic acid was added and the mixture was refluxed for 5 hours. After the completion of reaction, the reaction mass was cooled to room temperature. The organic layer was extracted with ethyl acetate (25 mL×2) and washed with water (10 mL×2). Then, the solvent was distilled off completely under vacuum and the resulting product was recrystallized from ethanol to give yellow colored solid. Yield 85%. MP: 90 °C. **Mass (m/z)**: 512.3, M+H obtained: 513.3.

(E)-4-((4-(((3,5-Bis(dodecyloxy)phenyl)imino)methyl)phenyl)(hexyl)amino)benzaldehyde (**5**)

4-(Hexyl(phenyl)aminobenzaldehyde (**3**, 0.25 g, 0.808 mM) and 3,5-bis(dodecyloxy)aniline (0.373 g, 0.809 mM) was dissolved in 5 mL methanol taken in a single necked 100 mL round bottom flask. To this mixture, few drops of glacial acetic acid was added and refluxed for 5 hours. After the completion of reaction, the mixture was cooled to room temperature. The product was extracted with ethyl acetate (25 mL ×2) and finally washed with water (10 mL×2). Ethyl acetate layer was distilled off completely under vacuum and the obtained product was recrystallized from ethanol to give yellow colored solid material. Yield obtained: 88%. MP: 120 °C. **Mass (m/z)**: 752.5, M+H obtained: 753.5.

(E)-4-(Hexyl(4-((pyren-1-ylimino)methyl)phenyl)amino)benzaldehyde (**6**)

A dry round bottom flask was charged with 4-(hexyl(phenyl)aminobenzaldehyde (**3**, 0.25 g, 0.809 mM) and pyren-1-amine (0.176 g, 0.808 mM) dissolved in 5 mL methanol. Two drops of glacial acetic acid was

added and the reaction mass was refluxed for 5 hours. On reaction completion, reaction mass was cooled to room temperature. The product was extracted with ethyl acetate (25 mL×2) and the organic layer was washed with water (10 mL×2). Then, ethyl acetate was distilled off completely under vacuum and the resulting product was recrystallized from ethanol to give dark brown colored solid. Yield: 92%. MP: 105 °C.

(E)-4-((4-((Benzo[d]thiazol-2-ylimino)methyl)phenyl)(hexyl)amino)benzaldehyde (7)

A mixture of 4-(hexyl(phenyl)aminobenzaldehyde (**3**, 0.25 g, 0.808 mM) and benzo[d]thiazol-2-amine (0.12 g, 0.809 mM) was dissolved in 5 mL methanol taken in a clean and dry single neck round bottom flask. To this two drops of glacial acetic acid was added and the reaction mixture was refluxed for 5 hours. Upon completion of reaction, the reaction mass was cooled to room temperature and the product was extracted with ethyl acetate layer (2×25 mL) and the ethyl acetate layers was washed with water (2×10 mL). The solvent was distilled off completely under vacuum and the product was recrystallized from ethanol to give yellow colored solid material. Yield: 90%. MP: 110 °C.

(Z)-2-Cyano-3-(4-((4-((E)-((2,4-di-tert-butyl-5-hydroxyphenyl)imino)methyl)phenyl)(hexyl)amino)phenyl)acrylic acid (D₁₈)

A mixture of (E)-4-(((4-(((2,4-di-tert-butyl-5-hydroxyphenyl) imino)methyl)phenyl)(hexyl)amino)benzaldehyde (**4**, 0.25 g, 0.488 mM), ammonium acetate (0.45 g, 5.85 mM) and cyano acetic acid (0.049 g, 0.586 mM) was taken in glacial acetic acid (5 mL). The reaction mass was refluxed for 10 hours. Upon reaction completion, the reaction mass was cooled to room temperature and filtered to separate the solid. The material was then recrystallized from methanol to obtain bright red colored solid. Yield: 80%. MP: 120 °C. ¹H NMR (DMSO-*d*₆, 400 MHz, δ ppm): 8.10 (1H, s), 7.95-7.92 (2H, d (J=12 Hz)), 7.57 (6H, s), 7.20 (1H, s), 7.14-7.11 (2H, d (J=12 Hz)), 3.87-3.82 (2H, t (J=12 Hz & 8 Hz)), 2.59 (9H, s), 1.70-1.68 (2H, q), 1.42 (2H, s), 1.37 (4H, s), 1.35 (9H, s), 0.90-0.86 (3H, t (J=8 Hz)). ¹³C NMR (DMSO-*d*₆, 100 MHz, δppm): 164.18, 149.04, 147.79, 131.76, 126.70, 120.96, 120.00, 109.60, 51.87, 31.49, 29.85, 27.51, 26.37, 22.57, 14.36. FTIR (ATR), ν cm⁻¹: 3368 (O-H stretch), 2922, 2850 (C-H stretch), 1734 (C=O stretch), 2211 (C≡N stretch), 1582 (C=C stretch),

1506 (C=N stretch). **Elemental analysis** (Theoretical: C=76.65%, H=7.82%, N=7.25%; Observed: C=76.21%, H=7.98%, N=7.5%).

(Z)-3-(4-((4-((*E*)-((3,5-Bis(dodecyloxy)phenyl)imino)methyl)phenyl)(hexyl)amino)phenyl)-2-cyanoacrylic acid (**D19**)

(*E*)-4-((4-(((3,5-Bis(dodecyloxy)phenyl)imino)methyl)phenyl)(hexyl)amino)benzaldehyde (**5**, 0.25 g, 0.332 mM), ammonium acetate (0.31g, 3.98 mM) and cyano acetic acid (0.034 g, 0.398 mM) were dissolved in 5 mL glacial acetic acid. The reaction mass was refluxed for 10 hours. The completion of reaction was monitored and upon completion, the reaction mass was cooled to room temperature. The precipitated solid was filtered. The material was then recrystallized from methanol to obtain bright red colored solid. Yield: 82%. MP: 135 °C. **¹H NMR** (DMSO-*d*₆, 400 MHz, δ ppm): 8.21 (2H, s), 8.04-8.03 (5H, d (J=4 Hz)), 7.29-7.27 (5H, d (J=8 Hz)), 3.93-3.89 (6H, t (J=8 Hz)), 1.63-1.58 (6H, q (J=8 Hz & 4 Hz)), 1.34-1.20 (36H, m), 0.84 (9H, s). **¹³C NMR** (DMSO-*d*₆, 100 MHz, δ ppm): 164.35, 153.52, 150.45, 133.31, 129.93, 128.55, 125.42, 121.22, 117.39, 100.23, 55.89, 51.96, 31.76, 31.40, 29.55, 29.19, 27.51, 26.24, 22.55, 22.50, 14.30. **FTIR (ATR)**, vcm^{-1} : 3187 (O-H stretch), 2911, 2847 (C-H stretch), 2215 (C≡N stretch), 1685 (C=O stretch), 1568 (C=N stretch), 1503 (C=C stretch). **Elemental analysis** (Theoretical: C=77.61%, H=9.46%, N=5.12%; Observed: C=77.25%, H=9.82%, N=5.5%).

(Z)-2-Cyano-3-(4-(hexyl(4-((*E*)-(pyren-1-ylimino)methyl)phenyl)amino)phenyl)acrylic acid (**D20**)

(*E*)-4-(Hexyl(4-((pyren-1-ylimino)methyl)phenyl)amino)benzaldehyde(**6**, 0.25 g, 0.491 mM), ammonium acetate (0.45 g, 5.90 mM) and cyano acetic acid (0.050 g, 0.589 mM) were added together in a single necked round bottom flask and glacial acetic acid (5 mL) was added to it. The reaction mass was heated to reflux for 10 hours. Upon completion of the reaction, the reaction mass was cooled to room temperature and separated solid was filtered, washed with water. The material was then recrystallized from methanol to obtain black colored solid. Yield: 75%. MP: 110 °C. **¹H NMR** (400 MHz, CDCl₃, δ ppm): 8.22-8.19 (1H, t (J=8 Hz & 4 Hz)), 8.16-8.14 (1H, d (J=8 Hz)), 8.09 (2H, s), 8.03-7.99 (4H, t (J=8 Hz)), 7.95-7.91 (4H, m), 7.88-7.86 (2H, d (J=8 Hz)), 7.79-7.74 (2H, t (J=8 Hz & 12 Hz), 3.66 (2H,s), 1.62 (2H,

s), 1.28 (2H, s), 1.25 (4H, s), 0.86 (3H, s). **¹³C NMR** (100 MHz, CDCl₃, δ ppm): 164.58, 140.76, 130.75, 130.58, 128.83, 128.69, 128.59, 127.75, 127.48, 127.33, 127.07, 126.96, 126.85, 126.44, 125.90, 125.85, 125.67, 125.36, 125.07, 124.93, 123.97, 123.61, 123.41, 120.30, 120.17, 120.05, 119.87, 116.79, 113.89, 52.34, 31.38, 27.19, 26.47, 22.51, 13.90. **FTIR (ATR)**, ν cm⁻¹: 3227 (O-H stretch), 3037-2851 (C-H stretch), 2206 (C≡N stretch), 1735 (C=O stretch), 1642 (C=C stretch), 1587 (C=N stretch). **Mass (m/z)**: 575.7, M+H observed: 577.

(Z)-3-(4-((4-((*E*)-(Benzo[*d*]thiazol-2-ylimino)methyl)phenyl)(hexyl)amino)phenyl)-2-cyano-acrylic acid (**D₂₁**)

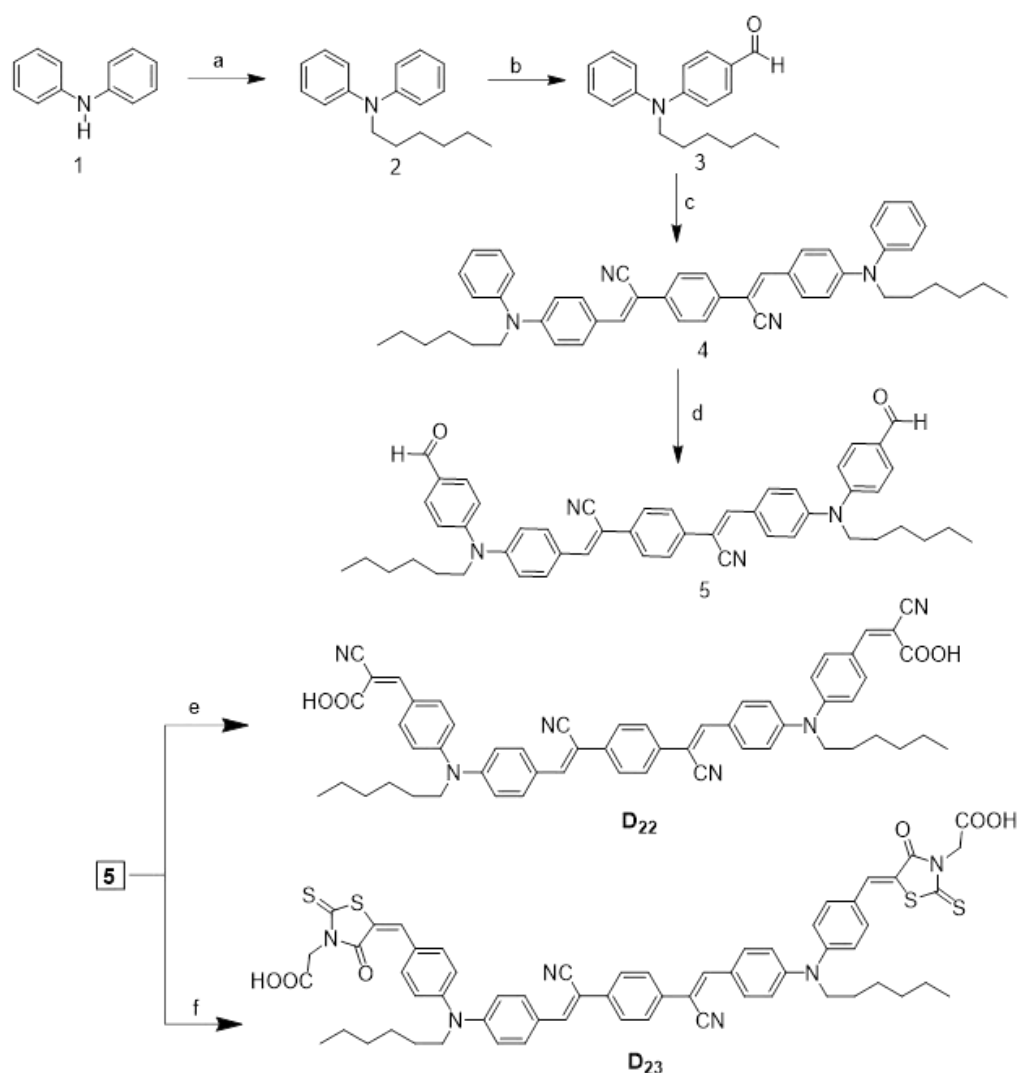
A mixture of (*E*)-4-((4-((benzo[*d*]thiazol-2-ylimino)methyl)phenyl)(hexyl)amino) benzaldehyde (**7**, 0.25 g, 0.566 mM), ammonium acetate (0.52 g, 6.8 mM) and cyano acetic acid (0.058 g, 0.679 mM) was taken in glacial acetic acid (5 mL). The reaction mass was heated to reflux for 10 hours. After the completion of reaction, the reaction mass was cooled to room temperature and separated solid mass was filtered. The material was then recrystallized from methanol to obtain bright red colored solid. Yield: 88%. MP: 124 °C. **¹H NMR** (400 MHz, CDCl₃, δ ppm) : 9.93 (1H, s), 8.21 (1H, s), 8.18 (1H, s), 8.03-8.01 (1H, d (J=8Hz)), 7.99-7.97 (2H, d (J=8Hz)), 7.89-7.87 (2H, d (J=8Hz)), 7.28-7.27 (3H, d (J=4Hz)), 7.19-7.17 (1H, d (J=8Hz)), 7.07-7.04 (2H, d (J=12Hz)), 3.88-3.84 (2H, t (J=8Hz)), 1.75-1.68 (2H, q (J=4Hz & 8Hz)), 1.36-1.29 (6H, m), 0.90-0.87 (3H, t (J=4Hz & 8Hz)). **¹³C NMR** (100 MHz, CDCl₃, δ ppm) : 190.90, 168.33, 167.97, 155.08, 154.80, 151.52, 151.39, 150.86, 133.82, 133.65, 131.75, 125.37, 123.92, 122.92, 121.00, 118.89, 116.33, 116.13, 98.93, 97.52, 52.64, 31.49, 29.74, 27.54, 26.61, 22.60, 14.01. **FTIR (ATR)**, ν cm⁻¹: 3500 (O-H stretch), 3068-2854 (C-H stretch), 2218 (C≡N stretch), 1688 (C=O stretch), 1564 (C=C stretch), 1497 (C=N stretch). **Elemental analysis** (Theoretical: C=70.84%, H=5.55%, N=11.02%; Observed: C=71.10%, H=5.82%, N=11.32%).

3.2.2.6 Synthesis of chromophores **D₂₂₋₂₃** (Series- 6)

Scheme 3.6 outlines the synthetic pathway of the newly designed dyes **D₂₂₋₂₃**. The intermediates N-hexyl-N-phenylaniline (**2**) and 4-(hexyl(phenyl)aminobenzaldehyde (**3**) were synthesized as per the procedures already mentioned under the synthesis of dyes of **Series-1**. Further, compound **3** was treated

with (1,4-phenylene)diacetonitrile in presence of sodium methoxide to yield (2*Z*,2'*Z*)-2,2'-(1,4-phenylene)bis(3-(4-(hexyl(phenyl)amino)phenyl)-acrylonitrile)(**4**).

Compound **4** was further subjected to Vilsmeier-Haack formylation reaction to yield a dialdehyde compound **5** with an excellent yield. This penultimate compound **5** was finally condensed with cyanoacetic acid and rhodanine acetic acid in presence of ammonium acetate to for the target dyes, **D₂₂** and **D₂₃** respectively. Procedures adopted for the synthesis of compounds **4**, **5**, **D₂₂₋₂₃** are given in the following section.



Scheme 3.6. Synthetic routes for target dyes: (a) 1-Bromohexane, NaH, DMF, RT, 10 hours (b) POCl₃, DMF, RT, 12 hours (c) (1,4-Phenylene)diacetonitrile, NaOMe, CH₃OH, reflux, 6 hours (d) POCl₃, DMF, 90 °C, 12 hours (e) Cyanoacetic acid, ammonium acetate, glacial acetic acid, 110 °C, 10 hours (f) Rhodanine acetic acid, ammonium acetate, glacial acetic acid, 110 °C, 10 hours

(2Z,2'Z)-2,2'-(1,4-Phenylene)bis(3-(4-(hexyl(phenyl)amino)phenyl)acrylonitrile) (4)

To a solution of sodium methoxide (0.519 g, 9.6 mM) in methanol (5 mL), 4-(hexyl(phenyl)aminobenzaldehyde (**3**, 1.89 g, 6.72 mM) was slowly added while stirring. 2,2'-(1,4-Phenylene)diacetonitrile (0.5 g, 3.2 mM) was then added to the reaction mass. Stirring was continued for 6 hours at reflux condition. The product was extracted using ethyl acetate (50 mL×3). Organic phase was dried using sodium sulfate. The solvent was removed under reduced pressure and the crude oily product obtained was further purified by column chromatography on silica gel using hexane/ethyl acetate (1%) as an eluent. A yellow solid was the product. Yield:80%. MP: 180 °C. ¹H NMR (CDCl₃, 400 MHz, δ ppm) : 7.80-7.78 (4H, d (J=8 Hz)), 7.65 (4H, s), 7.43-7.39 (5H, t (J=8 Hz & 4 Hz)), 7.23-7.20 (5H, t (J=8 Hz & 4 Hz)), 6.77-6.75 (4H, d (J=8 Hz)), 3.74-3.70 (4H, t (J=8 Hz)), 1.71-1.66 (4H, q (J=4 Hz & 8 Hz)), 1.31 (12H, s), 0.90-0.87 (6H, t (J=8 Hz & 4 Hz)). ¹³C NMR (CDCl₃, 100 MHz, δ ppm): 150.44, 146.17, 142.12, 135.08, 131.23, 129.92, 126.90, 126.83, 125.84, 125.65, 122.99, 119.08, 114.54, 104.44, 52.56, 31.62, 27.37, 26.70, 22.67, 14.05. FTIR (ATR), ν cm⁻¹: 2875 (C-H stretch), 2210 (C≡N stretch), 1660, 1625 (C=C stretch). Mass (m/z): 682.4, M+H obtained: 683.4.

(2Z,2'Z)-2,2'-(1,4-Phenylene)bis(3-(4-((4-formylphenyl)(hexyl)amino)phenyl)acrylonitrile) (5)

A dry two necked round bottomed flask was charged with freshly distilled DMF (2.27 mL, 29.28 mM) and to this, POCl₃ was added drop-wise (2.74 mL, 29.28 mM) at 0 °C under nitrogen. The mixture was stirred for 30 min and to this (2Z,2'Z)-2,2'-(1,4-phenylene)bis(3-(4-(hexyl(phenyl)amino)phenyl)acrylonitrile) (**4**, 0.5 g, 0.732 mM) dissolved in dichloroethane (10 mL) was added while stirring. The stirring was continued at room temperature for 12 hours. The reaction mass was then poured into ice cold water and subsequently basified by using 5 M NaOH solution. The product was extracted using ethyl acetate (50 mL ×3). Organic phase was dried using sodium sulfate. The solvent was removed under reduced pressure and the crude oily product obtained was further purified by column chromatography on silica gel using hexane as an eluent. The product was a light brown colour liquid. The crude product was purified by column chromatography on silica gel using ethyl acetate/hexane (5%) as mobile phase to give light brown colored liquid. Yield: 90%. FTIR (ATR), ν cm⁻¹:

2950-2723 (C-H stretch), 1678 (C=O stretch), 2205 (C≡N stretch), 1580 (C=C stretch).

(2Z,2'Z)-3,3'-((((1Z,1'Z)-1,4-Phenylenebis(2-cyanoethene-2,1-diyl))bis(4,1-phenylene)) bis(hexylazanediy)) bis(4,1-phenylene))bis(2-cyanoacrylic acid) (D₂₂)

A mixture of (2Z,2'Z)-2,2'-(1,4-phenylene)bis(3-(4-((4-formylphenyl)(hexyl)amino)phenyl)acrylonitrile) (**5**) (0.25 g, 0.338 mM), ammonium acetate (0.65 g, 8.45 mM) and cyano acetic acid (0.063g, 0.744 mM) was taken in glacial acetic acid (5mL) and was heated to reflux for 10 hours. After cooling, separated solid was filtered and recrystallized from methanol to obtain bright red color solid. Yield 77%. MP: 190 °C. ¹H NMR (DMSO-*d*₆, 400 MHz, δ ppm): 9.37 (2H, s), 8.05-8.04 (2H, d (J=4 Hz)), 8.00-7.98 (3H, d (J=8 Hz)), 7.91-7.89 (3H, d (J=8 Hz)), 7.87 (4H, s), 7.84 (1H, s), 7.59-7.55 (2H, t (J=8 Hz)), 7.34-7.32 (2H, d (J=8 Hz)), 7.30-7.29 (2H, d (J=4 Hz)), 7.22-7.21 (2H, d (J=8 Hz)), 7.10-7.08 (1H, d (J=8 Hz)), 3.89-3.86 (4H, t (J=8 Hz & 4Hz)), 1.64-1.61 (4H, q (J=8 Hz & 4 Hz)), 1.36-1.33 (4H, q (J=8 Hz, & 4 Hz)), 1.27-1.25 (8H, s), 0.87-0.84 (6H, t (J=8 Hz & 4 Hz)). ¹³C NMR (100 MHz, δ ppm, DMSO-*d*₆): 172.73, 164.63, 148.96, 145.36, 144.94, 132.16, 131.94, 131.71, 126.47, 126.40, 126.22, 125.34, 119.79, 117.42, 117.37, 105.32, 51.85, 31.42, 26.31, 22.51, 21.55, 14.30. FTIR (ATR), cm^{-1} : 3387 (O-H stretch), 2221 (C≡N stretch), 1722, 1703 (C=O stretch), 1576 (C=C stretch). **Elemental analysis** (Theoretical: C=77.04%, H=6.00%, N=9.63%; Observed: C=76.91%, H=5.90%, N=9.75%).

2-(5-((E)-4-(((Z)-2-(4-((Z)-2-(4-((4-((Z)-3-(Carboxymethyl)-4-oxo-2-thioxothiazolidin-5-ylidene)methyl)phenyl)(hexyl)amino)phenyl)-1-cyanovinyl)phenyl)-2-cyanovinyl)phenyl)(hexyl)amino)benzylidene)-4-oxo-2-thioxothiazolidin-3-yl)acetic acid (D₂₃)

(2Z,2'Z)-2,2'-(1,4-Phenylene)bis(3-(4-((4-formylphenyl)(hexyl)amino)phenyl)acrylo-nitrile) (**5**, 0.25 g, 0.338 mM), taken in a single neck round bottom flask was dissolved in glacial acetic acid (10 mL). To this ammonium acetate (0.65 g, 8.45 mM) was added and stirred for 5 minutes. After that, rhodanine acetic acid (0.142 g, 0.744 mM) was added to the mixture and the reaction mixture was refluxed for 10 hours. It was then cooled to room temperature and separated solid was filtered to yield the red solid. It was recrystallized from methanol. Yield: 80%. MP: 193 °C. ¹H NMR

(DMSO- d_6 , 400 MHz, δ ppm): 8.12 (s, 1H), 8.07 (s, 1H), 8.04-8.02 (3H, d (J=8 Hz)), 7.90-7.86 (3H, d (J=16 Hz)), 7.81 (1H, s), 7.77 (1H, s), 7.72 (1H, s), 7.63-7.61 (3H, d (J=8 Hz)), 7.59-7.57 (2H, d (J=8 Hz)), 7.36-7.34 (3H, d (J=8 Hz)), 7.19-7.15 (3H, d (J=16 Hz)), 7.01 (2H, s), 4.71 (4H, s), 3.88 (4H, s), 1.62 (4H, s), 1.35-1.09 (12H, m), 0.85-0.82 (6H, t (J=8 Hz & 4 Hz)). ^{13}C NMR (100 MHz, δ ppm, DMSO- d_6): 193.22 (27), 167.81 (29), 166.95 (26), 149.48 (11), 148.21 (15,18), 142.55 (24), 134.73(3,6), 133.37 (20,22), 131.54 (13,17), 126.52 (12,21), 125.11(4,5,7,8), 122.94 (14,16,23,19), 119.50 (25), 117.71 (1,10), 107.14 (2,9), 51.93 (30), 45.69 (28), 31.34 (33), 27.52 (31), 26.33 (32), 22.54 (34), 14.32 (35). FTIR (ATR), ν cm^{-1} : 3223 (O-H stretch), 2949-2847 (C-H stretch), 2225 ($\text{C}\equiv\text{N}$ stretch), 1751, 1697 (C=O), 1573 (C=C), 1502 (C=S). **Elemental analysis** (Theoretical: C=66.40%, H=5.20%, N=7.74%; Observed: C=66.65%, H=5.42%, N=7.90%).

3.2.2.7 Synthesis of chromophores D_{24-27} (Series-7)

Scheme 3.7 depicts the synthetic pathway of the newly designed dyes D_{24-27} . The required intermediate, 4-(hexyl (phenyl)aminobenzaldehyde (**3**) was synthesized from *N*-hexyl-*N*-phenylaniline (**2**) using the similar procedure, described for other series. Further, compound **3** was condensed with cyanoacetic acid, rhodanine acetic acid, hydrazine benzoic acid and maleimide to form dyes D_{24} , D_{25} , D_{26} and D_{27} , respectively. To synthesize dyes D_{24} and D_{25} Knoevenagel condensation protocol was used, while D_{26} was prepared using simple Schiff base reaction. The dye D_{27} was obtained following Wittig condensation with triphenylphosphine derivative of maleimide. The procedures for the synthesis of D_{24-27} are given below.

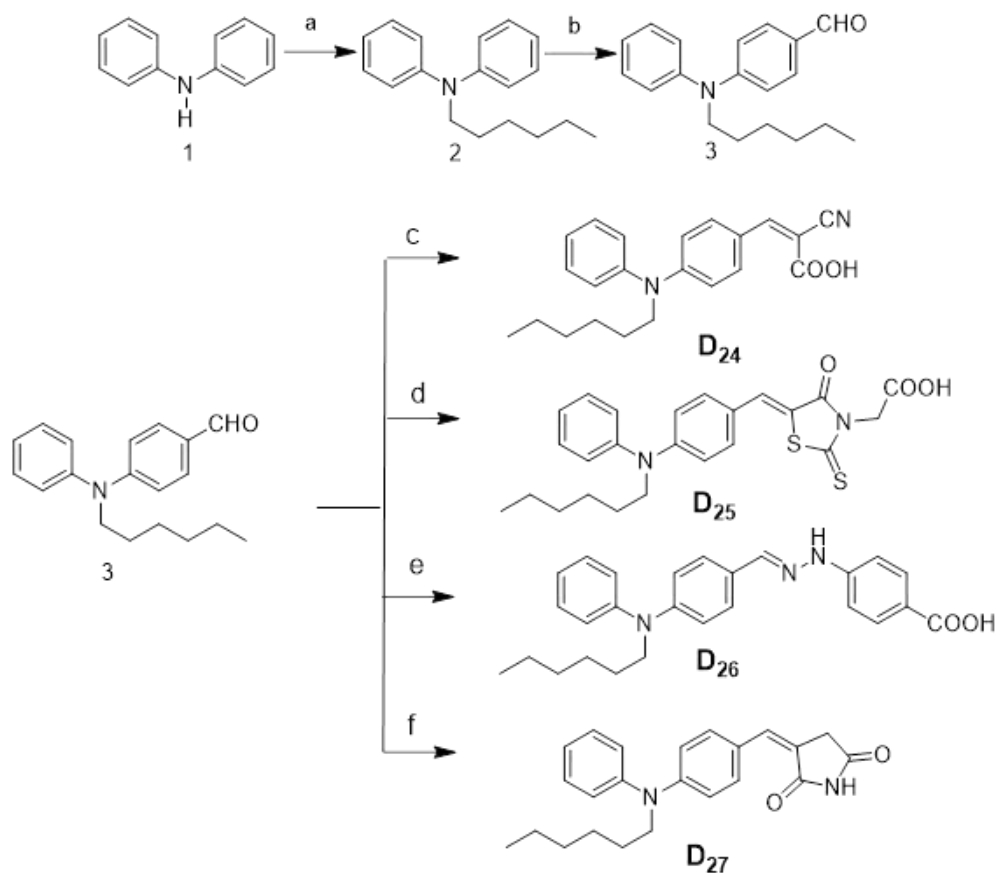
(*Z*)-2-Cyano-3-(4-(hexyl (phenyl) amino) phenyl) acrylic acid (D_{24})

The intermediate, 4-(hexyl-phenyl-amino)-benzaldehyde (**3**, 0.25 g, 0.889 mM) was dissolved in glacial acetic acid (10 mL) taken in single necked round bottom flask. To this solution, ammonium acetate (1.02 g, 13 mM) and cyanoacetic acid (0.091 g, 0.488 mM) g, 1.06 mM) was added and the mixture was stirred at 110 $^{\circ}\text{C}$ overnight. After cooling the reaction mass, the precipitated solid was filtered off. The solid was recrystallized from methanol to obtain bright red coloured solid. Yield 77%. MP 120 $^{\circ}\text{C}$. ^1H NMR (CDCl_3 , 500 MHz, δ ppm): 8.09 (1H, s), 7.89-7.87 (2H, d (J=10 Hz)), 7.48-7.45 (2H, t (J=10 Hz & 5 Hz)), 7.35-7.32 (1H, t (J=10 Hz & 5 Hz)),

7.22-7.21 (2H, d (J=5 Hz)), 6.68-6.66 (2H, d (J=10 Hz)), 3.75-3.72 (2H, t (J=10 Hz & 5 Hz)), 1.73-1.68 (2H, t (J=5 Hz)), 1.35-1.28 (6H, m), 0.90-0.87 (3H, t (J=10 Hz & 5 Hz)). **FTIR (ATR)**, ν cm^{-1} : 1666.49 (C=O stretch), 3320.69 (N-H stretch), 2950-2850 (C-H stretch), 1560.22 (C=C stretch), 1486.09 (C-C stretch). **Mass (m/z)**: 348; Obtained (M+H): 349.

(Z)-2-(5-(4-(Hexyl (phenyl) amino) benzylidene)-4-oxo-2-thioxothiazolidin-3-yl) acetic acid (**D25**)

A dry round bottom flask was charged with 4-(hexyl-phenyl-amino)-benzaldehyde (**3**, 0.25 g, 0.889 mM) dissolved in glacial acetic acid (15 mL). To this ammonium acetate (1.02 g, 13 mM) was added and stirred. After 5 minutes of stirring, rhodanine acetic acid (0.204 g, 1.07 mM) was added to the mixture and was stirred at 110 °C for 10 hours. After cooling the mixture, the separated solid was filtered to yield the orange red solid. The product was re-crystallized from methanol. Yield 70%. **MP**: 156 °C. **¹H NMR** (400 MHz, CDCl_3 , δ ppm): 7.69 (1H, s), 7.46-7.42 (2H, t (J=8Hz)), 7.34-7.31 (2H, d (J=12Hz)), 7.31-7.29 (1H, d (J=8Hz)), 7.22-7.20 (2H, d (J=8Hz)), 6.74-6.71 (2H, d (J=12Hz)), 4.92 (2H, s), 3.74-3.70 (2H, t (J=8Hz)), 1.73-1.66 (2H, q (J=8Hz)), 1.31 (6H, s), 0.90-0.86 (3H, t (J=8Hz)). **¹³C NMR** (CDCl_3 , 100 MHz, δ ppm): 192.83, 171.24, 167.30, 150.93, 145.59, 135.32, 133.13, 130.10, 127.34, 126.42, 121.98, 115.69, 114.39, 52.67, 44.34, 31.55, 27.31, 26.63, 22.61, 13.99. **FTIR (ATR)**, ν cm^{-1} : 3226.20 (O-H stretch), 2950-2850, (C-H stretch), 1757.70 (C=O stretch), 1562.98 (C=C stretch), 1434.48 (C-C stretch), 1176 (C-N stretch). **Mass (m/z)**: 454.14, M+H observed:455.1.



Scheme 3.7. Synthetic routes of target dyes: (a) 1-Bromohexane, NaH, DMF, RT, 10 hours (b) POCl₃, DMF, RT, 12 hours (c) Cyanoacetic acid, ammonium acetate, glacial acetic acid, 110 °C, 10 hours (d) Rhodanine acetic acid, ammonium acetate, glacial acetic acid, 110 °C, 10 hours (e) Hydrazine benzoic acid, methanol, glacial acetic acid, reflux, 3 hours (f) Maleimide, methanol, reflux, 12 hours

(E)-4-(2-(4-(Hexyl (phenyl) amino) benzylidene) hydrazinyl) benzoic acid (**D₂₆**)

4-Hydrazinyl benzoic acid (0.162 g, 1.065 mM) was added to (4-(hexyl-phenyl-amino)-benzaldehyde, (**3**, 0.25 g, 0.889 mM) dissolved in 15 mL of absolute methanol. The reaction mixture was refluxed for 3 hours with three drops of glacial acetic acid as a catalyst. The separated solid was filtered and re-crystallized from methanol to obtain light yellow color solid. Yield: 85%. MP: 180 °C. ¹H NMR (CDCl₃, 400 MHz, δ ppm) : 8.01-7.99 (2H, d (J=8Hz)), 7.73 (1H, s), 7.68 (1H, s), 7.53-7.51 (2H, d (J=8Hz)), 7.36-7.32 (2H, t (J=8Hz)), 7.15-7.13 (2H, d (J=8Hz)), 7.10-7.08 (2H, d (J=8Hz)), 6.86-6.84 (2H, d (J=8Hz)), 3.73-3.69 (2H, t (J=8Hz)), 1.71-1.64 (2H, q (J=4Hz & 8Hz)), 1.31 (6H, s), 0.90-0.86 (3H, t (J=8Hz)). ¹³C NMR (DMSO-*d*₆, 100 MHz, δppm): 167.34, 149.03, 148.15, 146.76, 139.52, 131.16,

129.56, 127.21, 126.22, 123.32, 123.02, 119.61, 117.57, 110.84, 51.42, 30.97, 26.88, 25.92, 22.00, 13.80. **FTIR (ATR)**, ν cm^{-1} : 1682.23 cm^{-1} (C=O stretch), 1591.90 cm^{-1} (C=C stretch), 3319.70 cm^{-1} (N-H stretch), 3320 cm^{-1} (C=C stretch), 2950-2850 cm^{-1} (C-H stretch), 1434.48 cm^{-1} (C-C stretch). **Mass (m/z)**: 415; Obtained (M+H): 416.

3-[4-(Hexyl-phenyl-amino)-benzylidene]-pyrrolidine-2,5-dione (D27)

A mixture of (4-(hexyl-phenyl-amino)-benzaldehyde (**3** 0.25 g, 0.889 mM) and maleimide (0.385g, 1.068 mM) was taken in a dry 100 mL single necked round bottom flask. The mixture was dissolved in 20 mL of absolute methanol and it was refluxed for 12 hours under argon atmosphere. The reaction completion was monitored by TLC technique. After completion of the reaction, the content was allowed to cool to room temperature, the solid obtained was collected by filtration and finally dried. The product was re-crystallized from methanol to yield the pure compound. Yield 85%. Bright yellow solid was resulted. MP: 172 °C. **¹H NMR** (CDCl_3 , 400 MHz, δ ppm) : 7.84 (1H, s), 7.70-7.65 (1H, t (J=8Hz)), 7.50 (1H, s), 7.43-7.39 (2H, t (J=8Hz)), 7.32-7.29 (2H, d (J=12Hz)), 7.20-7.18 (2H, d (J=8Hz)), 6.75-6.73 (2H, d (J=8Hz)), 3.73-3.69 (2H, t (J=8Hz)), 3.56 (2H, s), 1.72-1.65 (2H, q (J=8Hz & 4Hz)), 1.31 (6H, s), 0.89-0.86 (3H, t (J=4Hz & 8Hz)). **¹³C NMR** (CDCl_3 , 100 MHz, δ ppm): 174.70, 171.72, 150.19, 146.14, 135.43, 132.06, 129.95, 126.85, 125.72, 123.08, 118.54, 114.75, 52.51, 35.32, 31.58, 27.32, 26.66, 22.62, 14.00. **FTIR (ATR)**, ν cm^{-1} : 3140.80 (N-H stretch), 2953-2854 (C-H stretch), 1762.20 (C=O stretch), 1581.84 (C=C stretch), 1582.08 (C-C stretch). **Mass (m/z)**: 362.0; Obtained (M+H): 363.0.

3.2.3 Results and discussion

All the designed dyes were synthesized following standard synthetic protocols. Their reaction parameters such as reaction time, selection of solvent, catalyst, temperature and concentration of reactants were optimized to get good yield of the products. Chemical structures of synthesized unknown intermediates as well as target dyes were confirmed by various spectroscopy tools like FTIR, ¹H NMR, ¹³C NMR and Mass spectral techniques. Elemental analysis technique was also used for certain target dyes. Modified synthetic methods were used to prepare known intermediates. Their NMR and FTIR spectra matched with already reported spectral data. In the

following section, structural characterization of a selected representative dye belonging to each series, along with their unknown intermediates have been discussed.

3.2.3.1 Chromophores D_{1-3} (Series-1)

The ^1H NMR spectrum of **D1** is displayed in **Fig 3.1**. Its spectrum shows the appearance of triplet at δ 3.74-3.71 ppm. The fourteen aromatic protons are observed in the region of δ 8.50-6.72 ppm. The ^{13}C NMR spectrum of dye **D1** is displayed in **Fig 3.2**, which shows the characteristic absorption signals obtained at higher frequencies (downfield region). The carbonyl carbon resonates at δ 162.01, whereas the remaining signals appearing in the region of δ 149.92-112.64 ppm are due to other aromatic carbons. Further, the aliphatic carbons have appeared in the region of 8.92-46.76 ppm. Its FTIR spectrum is given in **Fig 3.3**. The spectrum shows a sharp peak at 1677 cm^{-1} indicating the presence of carbonyl group whereas the peak at 3467 cm^{-1} indicates the O-H vibration. Finally its structure has been confirmed by mass spectroscopy analysis. **Fig 3.4** shows the mass spectrum of **D1**. The spectrum displays the $[\text{M}+\text{H}]$ peak at 534.00, which is in agreement with the calculated molecular weight, *i.e.* 533.21 for **D1**. Here, the NMR and FTIR spectral data of all the intermediates **2**, **3**, **4** and **5** are in agreement with reported values.

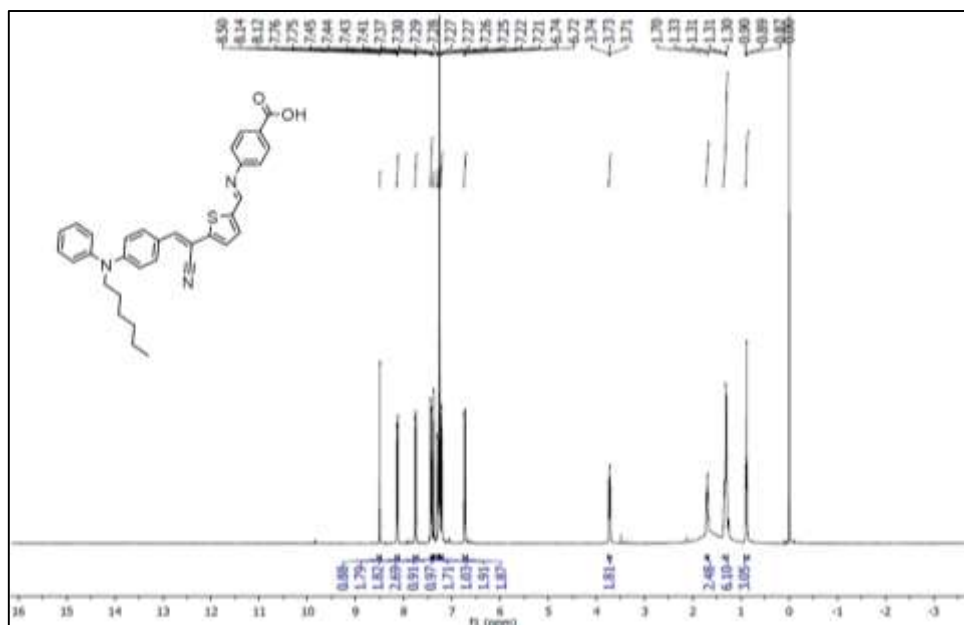


Fig 3.1 ^1H NMR spectrum of dye **D1** recorded in CDCl_3

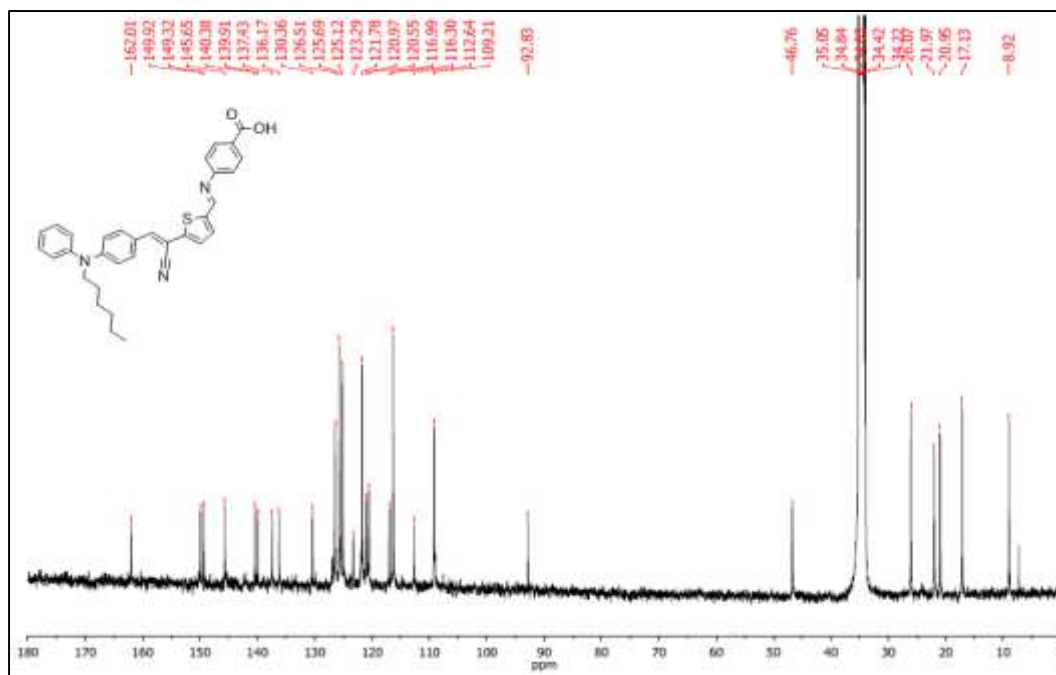


Fig 3.2 ^{13}C NMR spectrum of dye **D**₁ recorded in CDCl_3

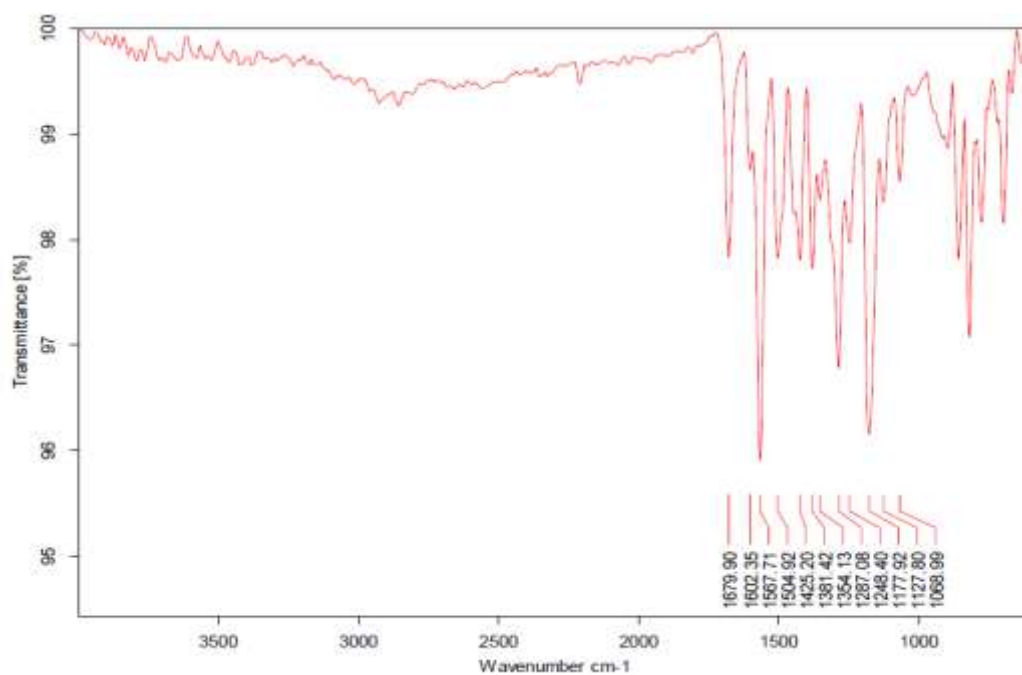


Fig 3.3 FTIR spectrum of dye **D**₁

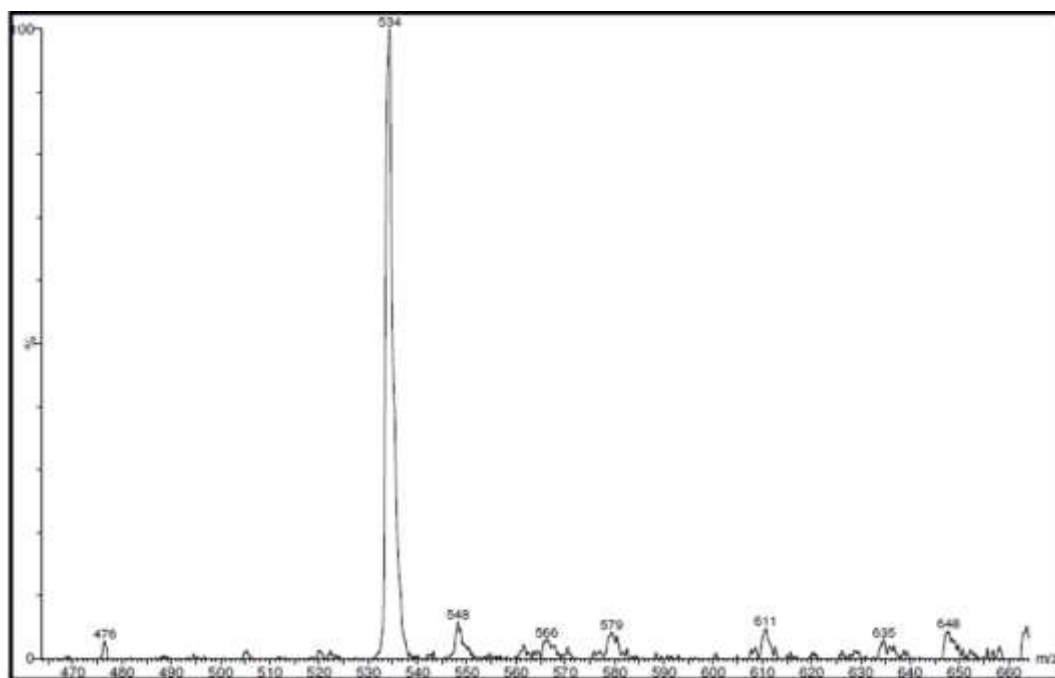


Fig 3.4: Mass spectrum of dye **D1**

3.2.3.2 Chromophores **D4-7** (Series-2)

The chemical structures of all the unknown final compounds of this series were well-characterized by ^1H NMR, ^{13}C NMR spectroscopy and mass spectroscopy techniques. **Fig 3.5** shows the ^1H NMR spectrum of **D4**. All the aromatic protons resonated in between δ 7.96 to 7.12 ppm as multiplet. Further, appearance of a triplet in between δ 3.79 to 3.67 ppm can be assigned to two protons of methylene (CH_2) attached to *N* of the hexyl chain. All the other primary and secondary protons of the hexyl chain have appeared in the region of δ 1.55-0.76 ppm as multiplet. The ^{13}C NMR spectrum of **D4** dye displays the characteristic signals at downfield region (**Fig 3.6**). The carbonyl carbon atoms of cyanoacetic acid resonates at δ 159.12 and 158.36 ppm. The signal appeared at δ 117.00 ppm is due to cyano group of cyanoacetic acid, whereas the signal at δ 119.29 ppm corresponds to the cyanovinylene group. All the aliphatic carbons of hexyl chain appear in the region of δ 8.95-46.56 ppm. Further, the FTIR spectrum (**Fig 3.7**) of **D4** shows carbonyl vibration at 1702 cm^{-1} , whereas broad peak at 3220 cm^{-1} corresponds to hydroxyl group. **Fig 3.7** gives the mass spectrum of **D4**, it exhibits the $[\text{M}+\text{H}]^+$ peak at 576.67, which is in good agreement

with the calculated molecular weight, *i.e.* 575.00, which confirms the chemical structure of the synthesized dye **D4**.

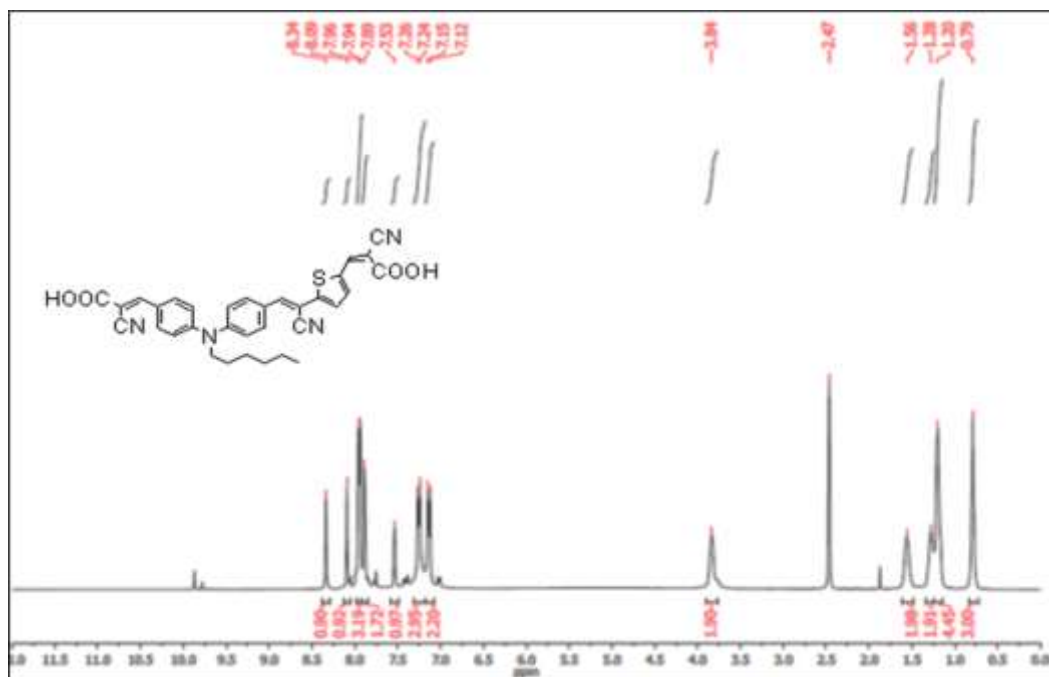


Fig. 3.5 ^1H NMR spectrum of **D4** recorded in $\text{DMSO-}d_6$

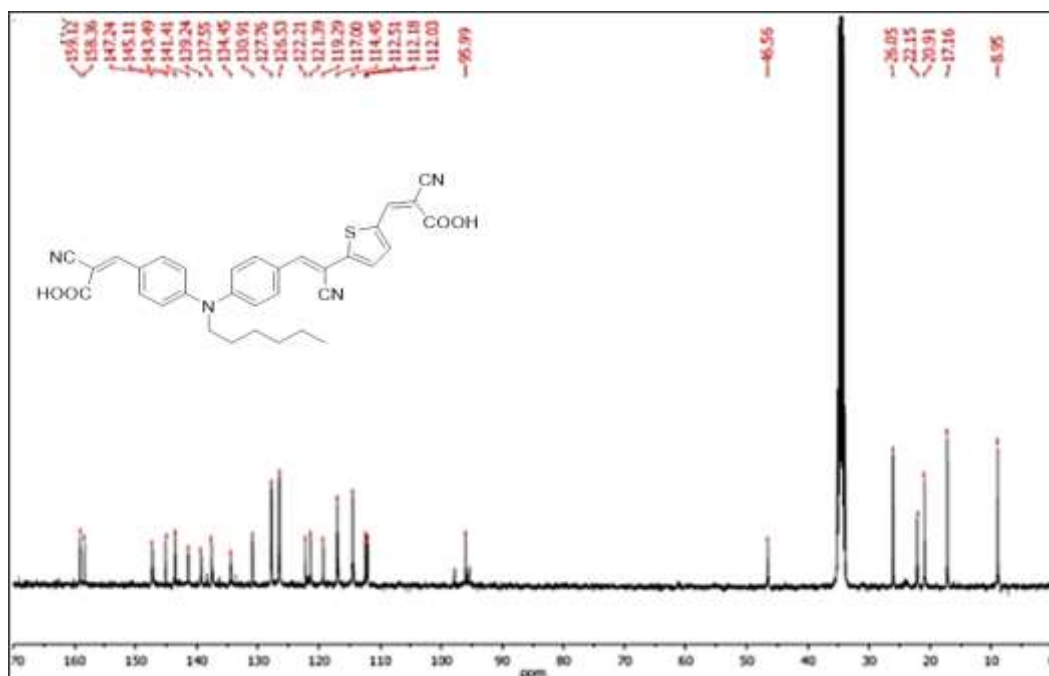


Fig. 3.6 ^{13}C NMR spectrum of **D4** recorded in $\text{DMSO-}d_6$

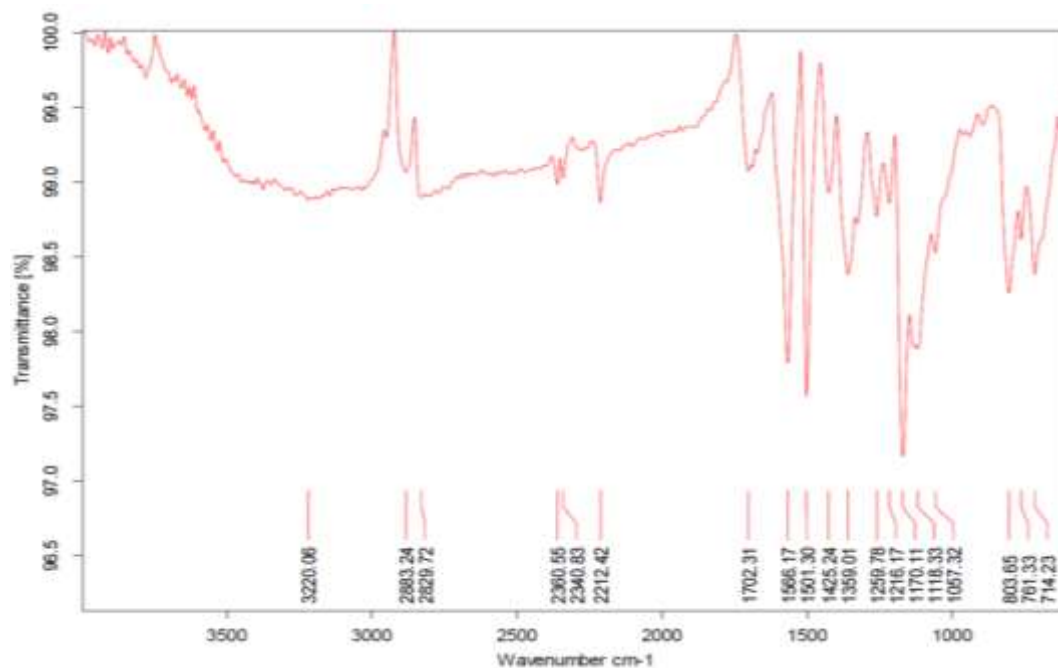


Fig. 3.7 FTIR spectrum of D₄.

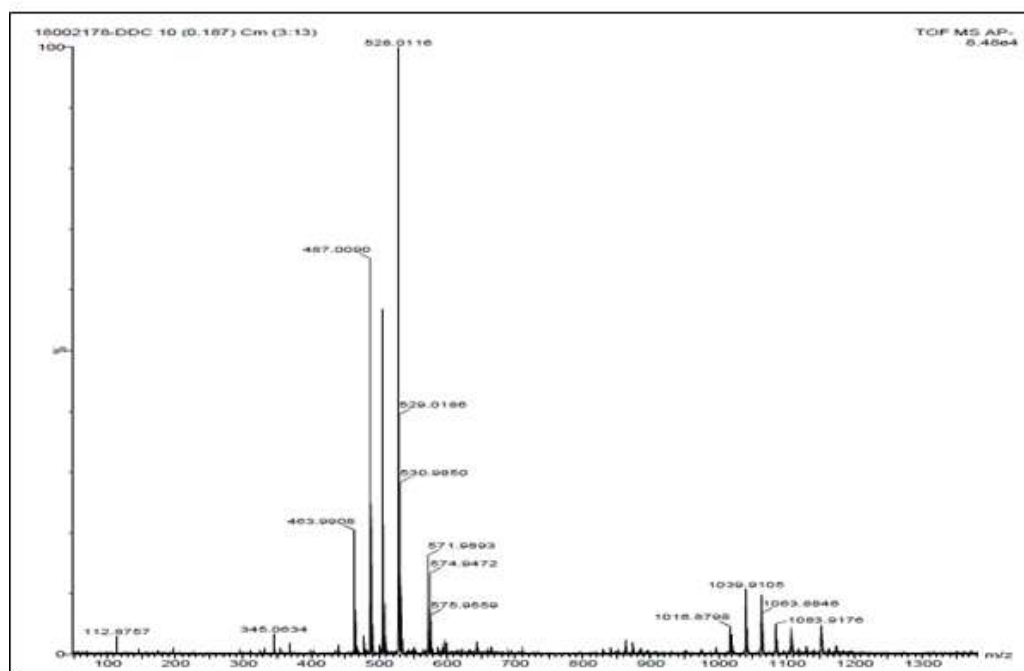


Fig. 3.8 Mass spectrum of D₄

3.2.3.3 Chromophores D₈₋₁₁ (Series-3)

The molecular structures of the dyes **D₈₋₁₁** were elucidated by ¹H NMR, ¹³C NMR, FTIR and mass spectroscopy techniques. The ¹H NMR, ¹³C NMR, FTIR and

mass spectra of the selected dye **D10** are depicted in **Figs 3.9, 3.10, 3.11** and **3.12**, respectively. In its ^1H NMR spectrum, all the aromatic protons of diphenylamine, phenylene ring and thiophene heterocycle have appeared in between δ 8.42 and 6.99 ppm as medium multiplet. Also, the peaks in the region of δ 3.82 to 0.79 ppm correspond to primary and secondary protons of hexyl side chain. The ^{13}C NMR spectrum of **D10** dye displays the characteristic signals, observed at downfield region. The carbonyl carbon atom of acid group resonates at δ 159.09 ppm, while signals due to aromatic carbons are observed in between 102.85 and 158.46 ppm. Further, FTIR spectrum of the dye shows the characteristic C=O vibration band at 1686 cm^{-1} and O-H absorption band at around 3300 cm^{-1} , indicating the presence of COOH group in it. Also, the band obtained at 2209 cm^{-1} is due to presence of C \equiv N functional group in the dye. The structure of **D10** was further confirmed by its mass spectrum, which shows its M+H at 610.01, that matches with the calculated value. The spectral data of intermediates **4, 5, 6**, and **7** totally well with the values reported in the literature.

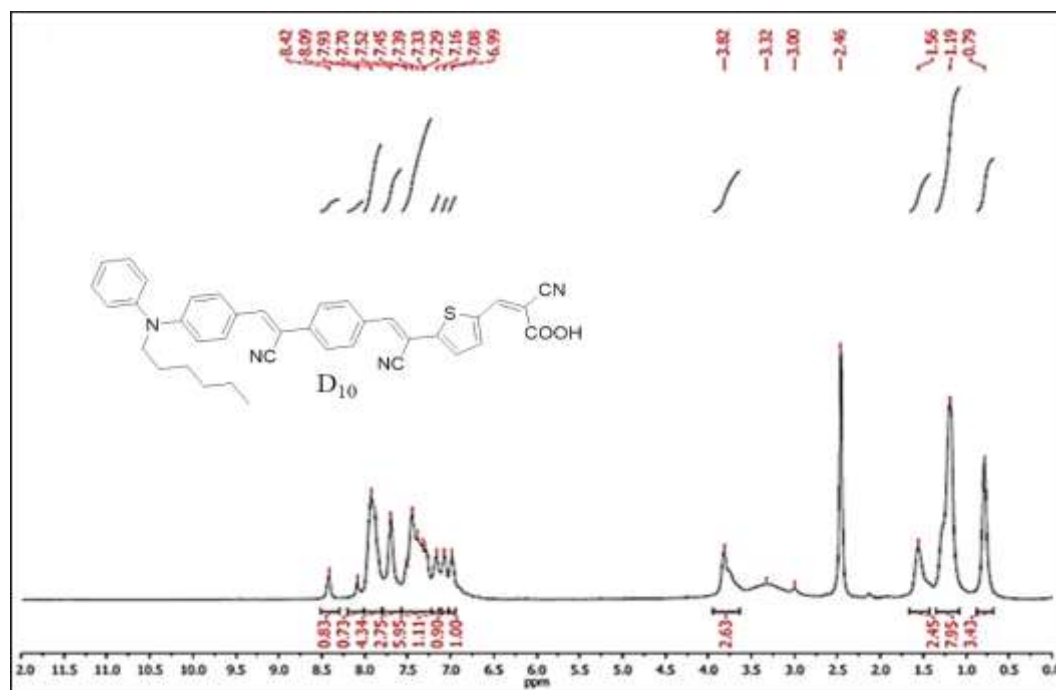


Fig. 3.9 ^1H NMR spectra of **D10** recorded in $\text{DMSO-}d_6$

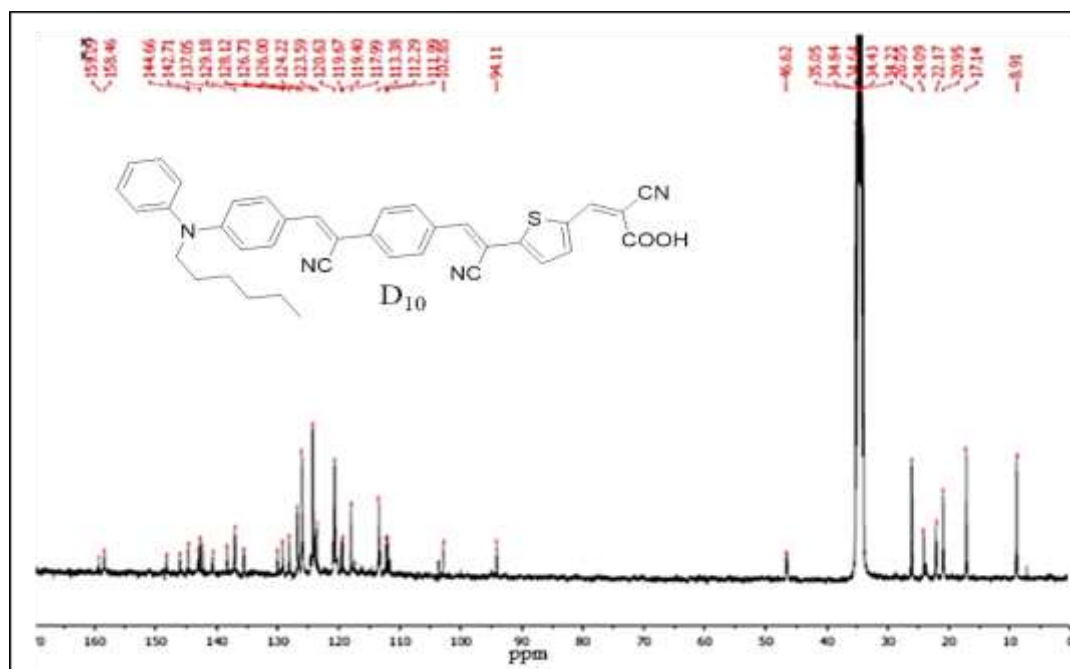


Fig. 3.10 ^{13}C NMR spectra of D_{10} recorded in $\text{DMSO-}d_6$

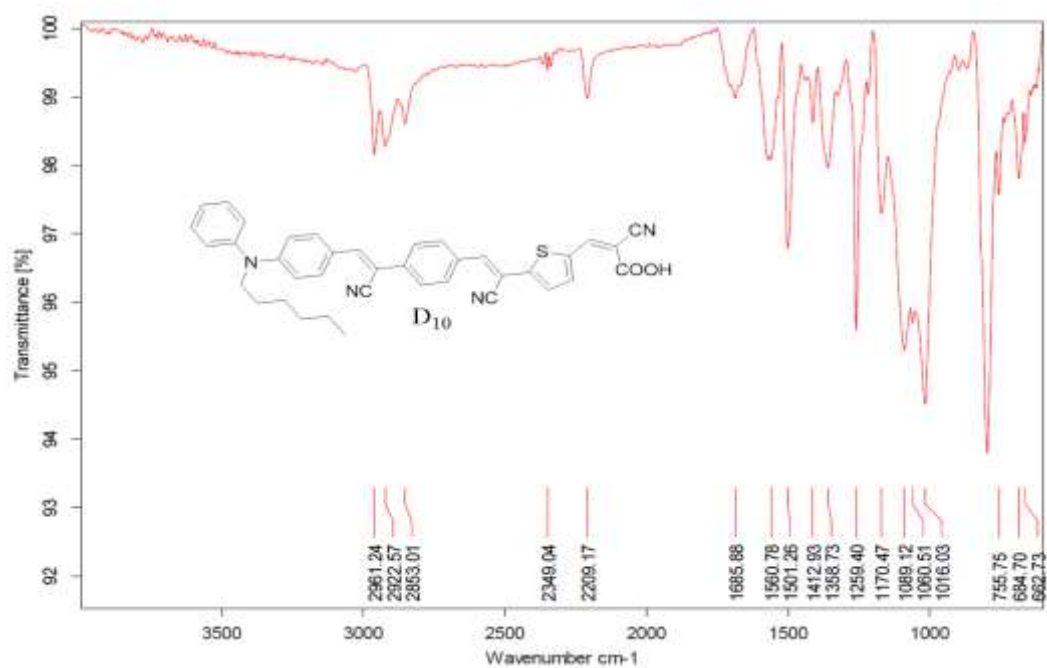


Fig. 3.11 FTIR spectrum of D_{10}

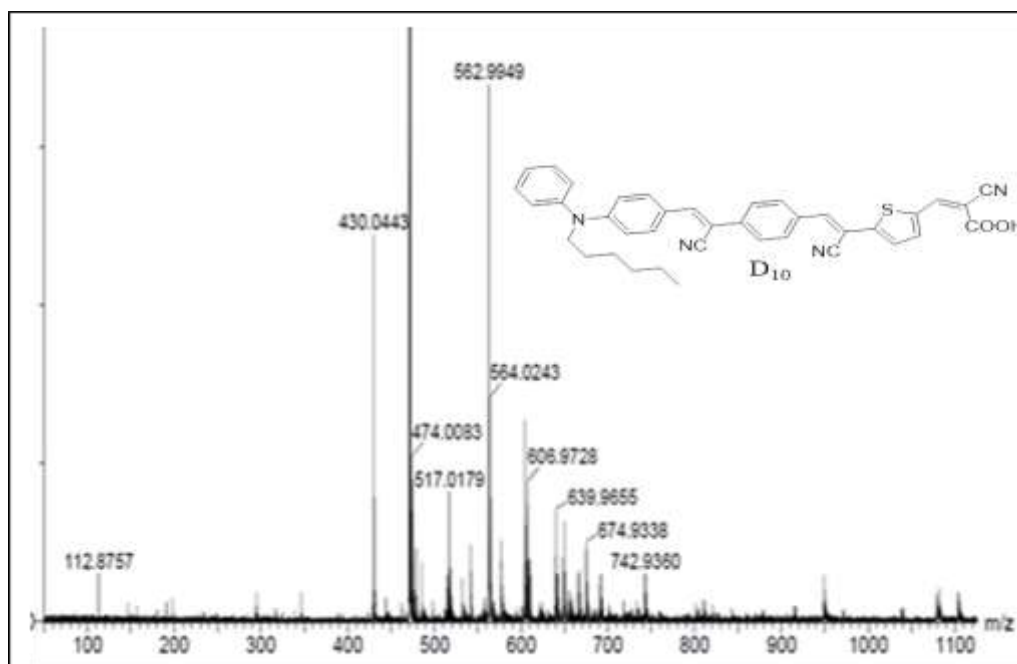


Fig. 3.12 Mass spectrum spectra of **D₁₀**

3.2.3.4 Chromophores **D₁₂₋₁₇** (Series-4)

The chemical structures of final compounds of this series were well-elucidated by ^1H NMR, ^{13}C NMR and Mass spectroscopy techniques. The ^1H NMR, ^{13}C NMR, FTIR and mass spectra of the selected dye **D₁₄** are shown in **Figs 3.13, 3.14, 3.15** and **3.16**, respectively. In its ^1H NMR spectrum, the aromatic protons have resonated in the range δ 8.62-6.77 ppm as multiplet, whereas N-CH₂ protons in the hexyl chain have appeared at δ 3.74-3.71 ppm as triplet. Also, the peaks in the region of δ 1.72 to 0.87 ppm correspond to both primary and secondary protons of hexyl chain. The ^{13}C NMR spectrum of dye **D₁₄** displays the characteristic peaks at downfield region. The carbon of imine (N=C) linkage shows peaks at δ 177.56 and 163.24 ppm. The aliphatic carbons have appeared around δ 52.54 to 14.01 ppm as sharp peaks. Further, its FTIR spectrum displays a characteristic band at 1513 cm^{-1} , corresponding to aliphatic C=N stretching. The C-O bond of the furan ring shows bending vibration at 1180 cm^{-1} . Finally, its mass spectrum exhibits the $[\text{M}+\text{H}]^+$ peak at 495.47, which is in good agreement with the calculated molecular mass, confirming the chemical structure of the synthesized dye **D₁₄**. Intermediates of this series show characteristic spectra, as reported in the literature.

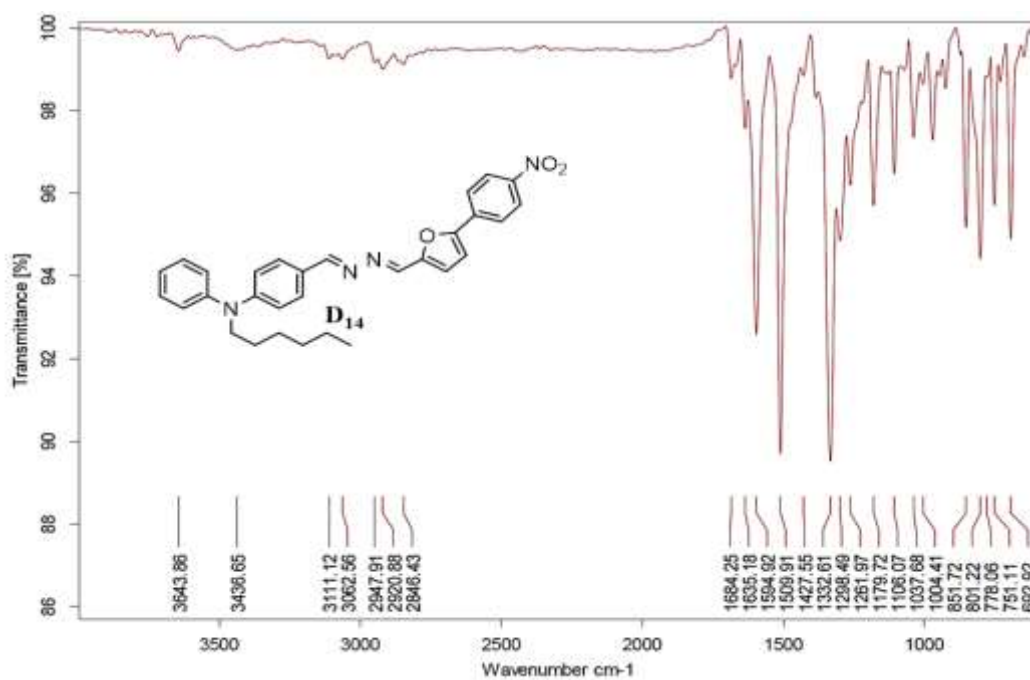


Fig. 3.15 FTIR spectrum of **D14**

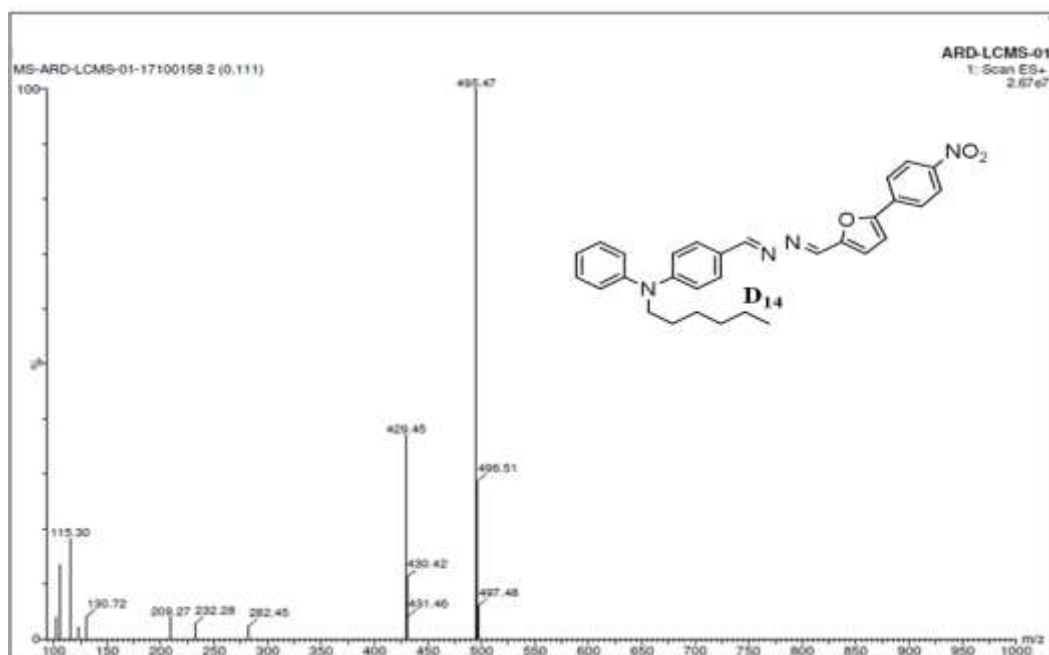


Fig. 3.16 Mass spectrum of **D14**

3.2.3.5 Chromophores **D18-21** (Series-5)

Figs 3.17, 3.18 and **3.19** depict the ¹H NMR, ¹³C NMR and FTIR spectra of **D21** respectively. In its ¹H NMR spectrum, the imine proton has been found at δ 9.93

ppm as a sharp peak and the alkene proton has appeared at δ 8.18 ppm. All the aromatic protons of diphenylamine and benzo[d]thiazol-2-amine have resonated at δ 7.04-8.21 ppm. The ^{13}C NMR spectrum of **D**₂₁ dye displays the characteristic signals which appear at downfield, as shown in the figure. The carbonyl carbon atom of acid group resonates at δ 167.97 ppm, while the carbon of imine bond shows signal at 190.90 and 168.33 ppm. The aliphatic carbon atoms display peaks in the region δ 14.01-52.64 ppm, as in the case of dyes of previous series. Further, FTIR spectrum shows a broad peak at 3500 cm^{-1} due to O-H group of carboxylic acid and a sharp peak at 1688 cm^{-1} , which is attributed to carbonyl group of carboxylic acid. The spectral data of all the intermediates match with reported results.

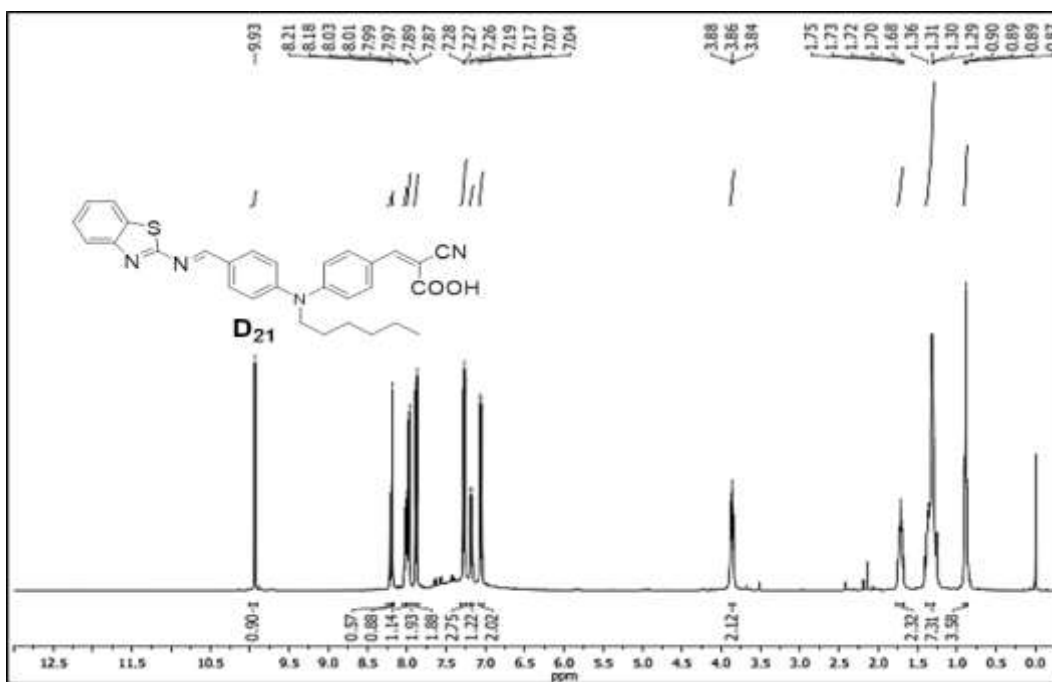


Fig. 3.17 ^1H NMR spectrum of **D**₂₁ recorded in CDCl_3

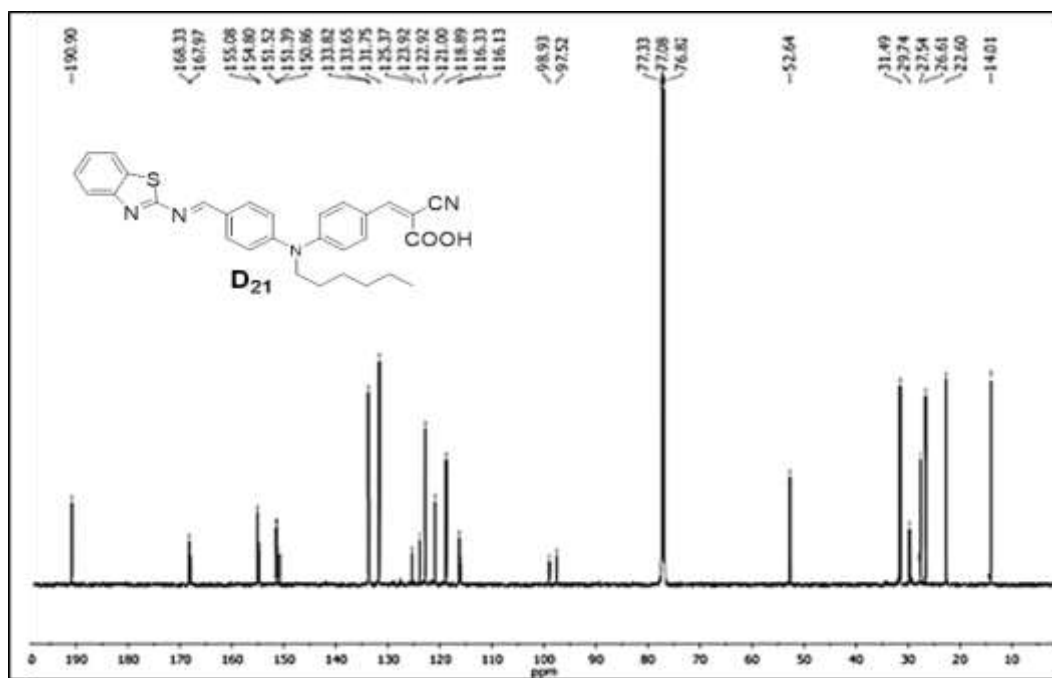


Fig. 3.18 ^{13}C NMR spectrum of D_{21} recorded in CDCl_3

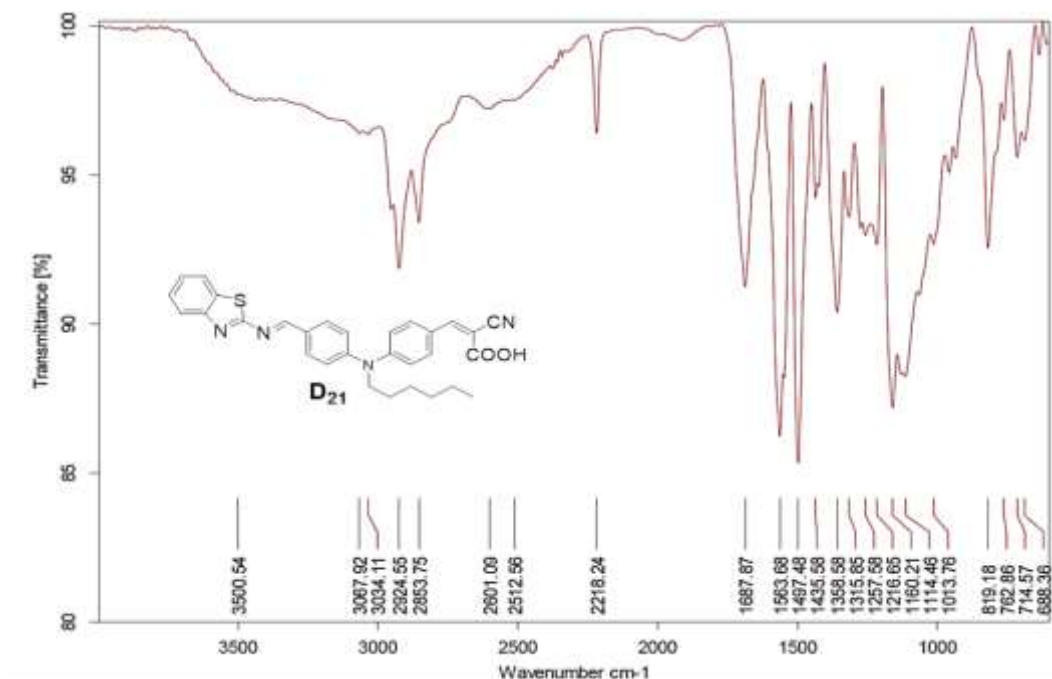


Fig. 3.19 FTIR spectrum of D_{21}

3.2.3.6 Chromophores D_{22-23} (Series-6)

The chemical structures of the new dyes were confirmed by spectroscopy tools. Also, elemental analysis technique was used to establish their final structure.

The representative dye **D₂₃** has been selected for the spectral study. Its ¹H NMR spectrum is depicted in **Fig. 3.20**. In its spectrum, the dye shows two sharp singlets at δ 8.12 and 8.07 ppm corresponding to the two CH groups connecting rhodanine acetic acid and the diphenylamine moiety. Similarly, methylene protons present in the rhodanine acetic acid have been observed at δ 4.71 ppm as singlet. The two singlets seen at δ 7.72 and 7.81 ppm indicate the presence of two CH groups on either side of (1,4-phenylene)diacetonitrile unit. Its ¹³C NMR spectrum is given in **Fig. 3.21**. The dye shows in its spectrum, a strong peak at 167.81 ppm, owing to carbonyl carbon of rhodanine acetic acid. Similarly, the peaks corresponding to C=S and C=O carbons of rhodanine acetic acid are seen at δ 193.22 and 166.95 ppm, respectively. Further, the signal due to the methylene carbon of rhodanine acetic acid is observed at δ 45.69 ppm. The peaks corresponding to carbons belonging to hexyl chain are observed from δ 14.32-51.93 ppm. Finally, its FTIR spectrum (**Fig 3.22**) displays sharp peaks at 3223, 2225 and 1697 cm⁻¹ indicating the presence of the hydroxyl, nitrile and carbonyl groups, respectively. Theoretical: C=66.40%, H=5.20%, N=7.74%; Observed: C=66.65%, H=5.42%, N=7.90%.

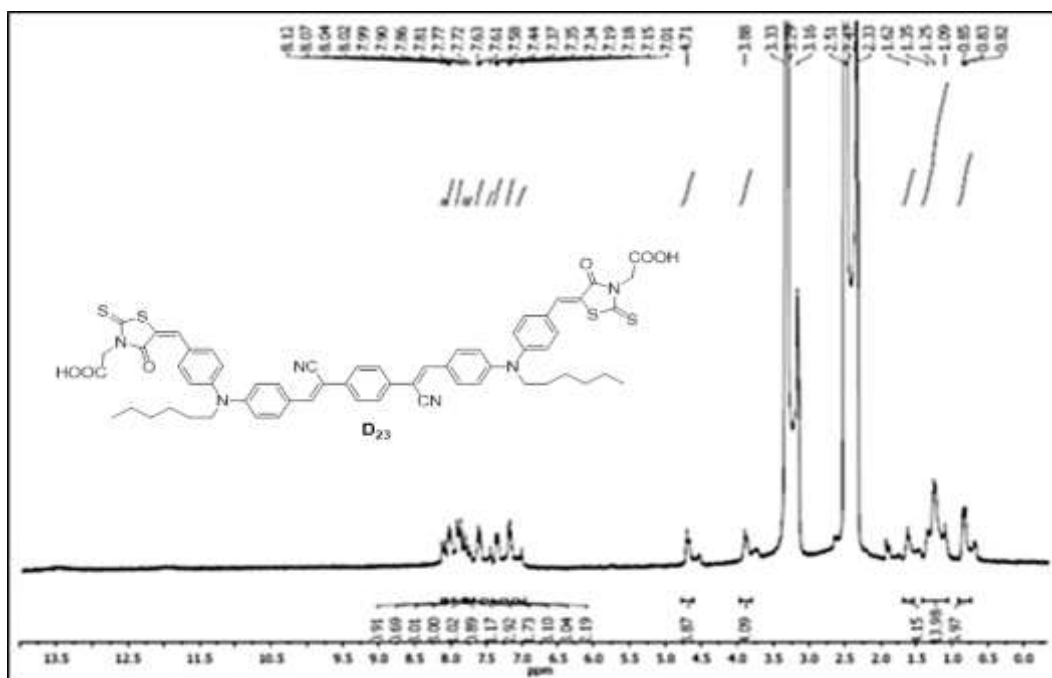


Fig 3.20: ¹H NMR spectrum of **D₂₃** recorded in DMSO-*d*₆

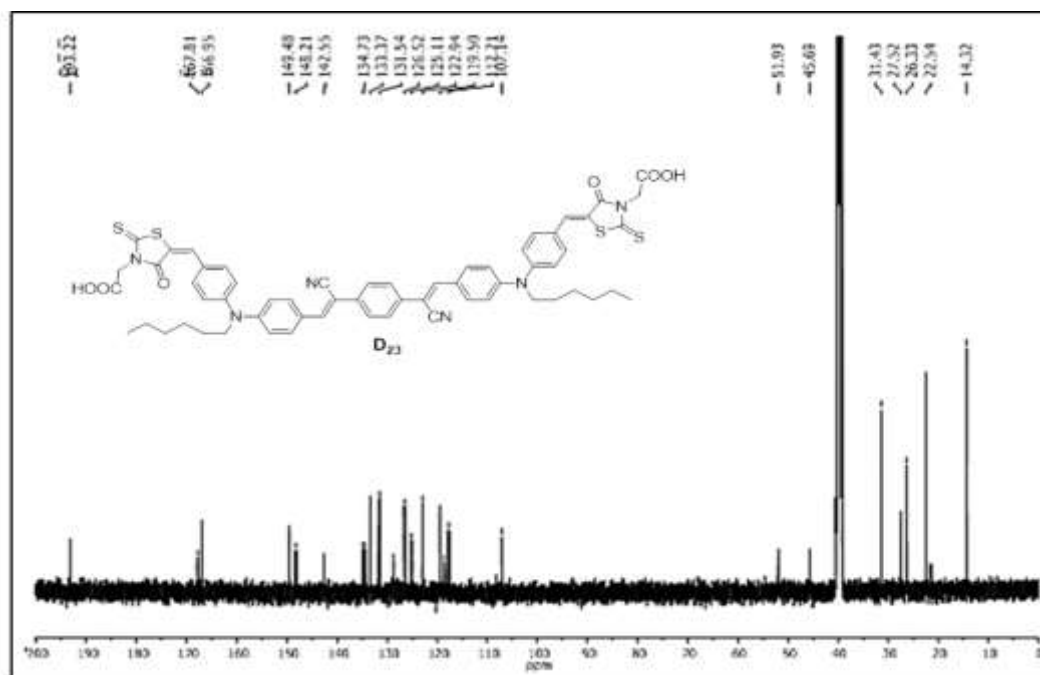


Fig 3.21 ^{13}C NMR spectrum of **D₂₃** recorded in $\text{DMSO-}d_6$

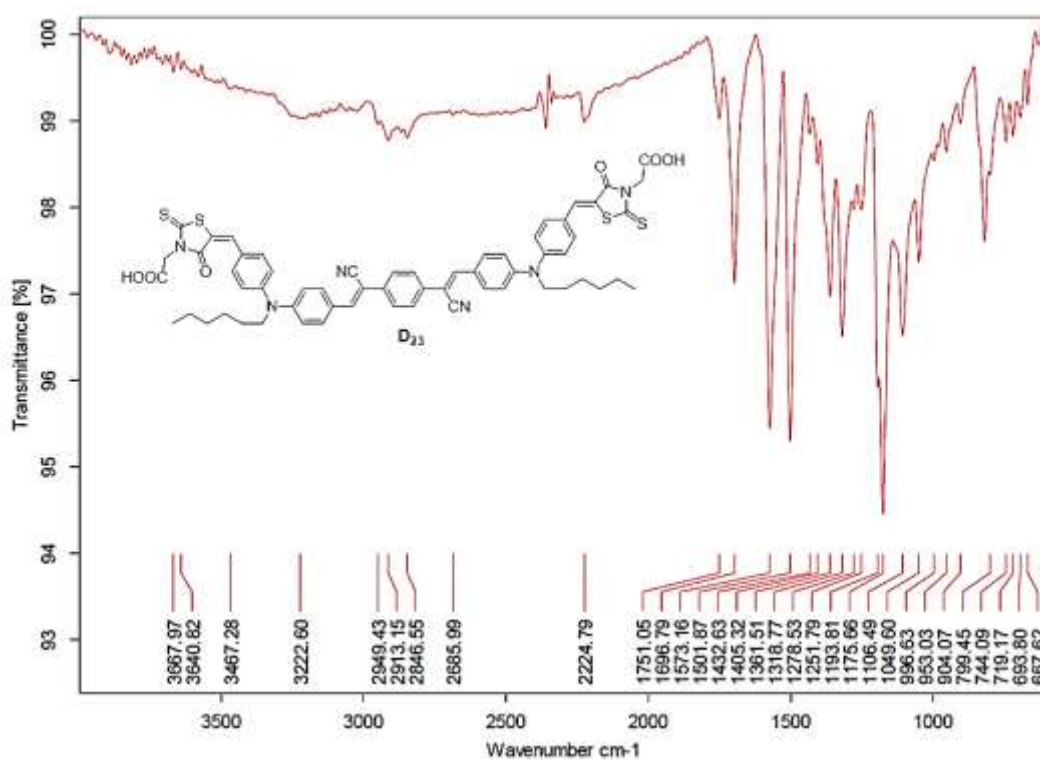


Fig 3.22 FTIR spectrum of **D₂₃**

3.2.3.7 Chromophores D₂₄₋₂₇ (Series-7)

Structures of all final compounds of this series were confirmed by ¹H NMR, ¹³C NMR, FTIR spectroscopy and MS methods. In this particular series, **D₂₆** has been chosen as the representative dye for discussion. **Figs 3.23, 3.24, 3.25** and **3.26** depict the ¹H NMR, ¹³C NMR, FTIR and Mass spectra of **D₂₆**, respectively. In its ¹H NMR spectrum, all the aromatic protons appear in between δ 8.01 and 6.84 ppm as doublet and triplet, whereas aliphatic protons resonate at the region from δ 0.86 to 3.73 ppm. Here, the imine C-H proton appears at δ 7.73 ppm as singlet. Its ¹³C NMR spectrum displays signals at δ 110.84-167.34 ppm due to aromatic carbons and peaks at δ 13.80-51.42 ppm caused by aliphatic carbons. Further, its FTIR spectrum shows a sharp band at 3319.70 and 1682.23 cm⁻¹ owing to presence of N-H and C=O functionalities, respectively. Finally, its mass spectrum exhibits [M+H]⁺ peak at 416.00, which is matching with its calculated mass, *i.e.* 415.00. Thus, the spectral study has confirmed the structures of newly synthesized dyes.

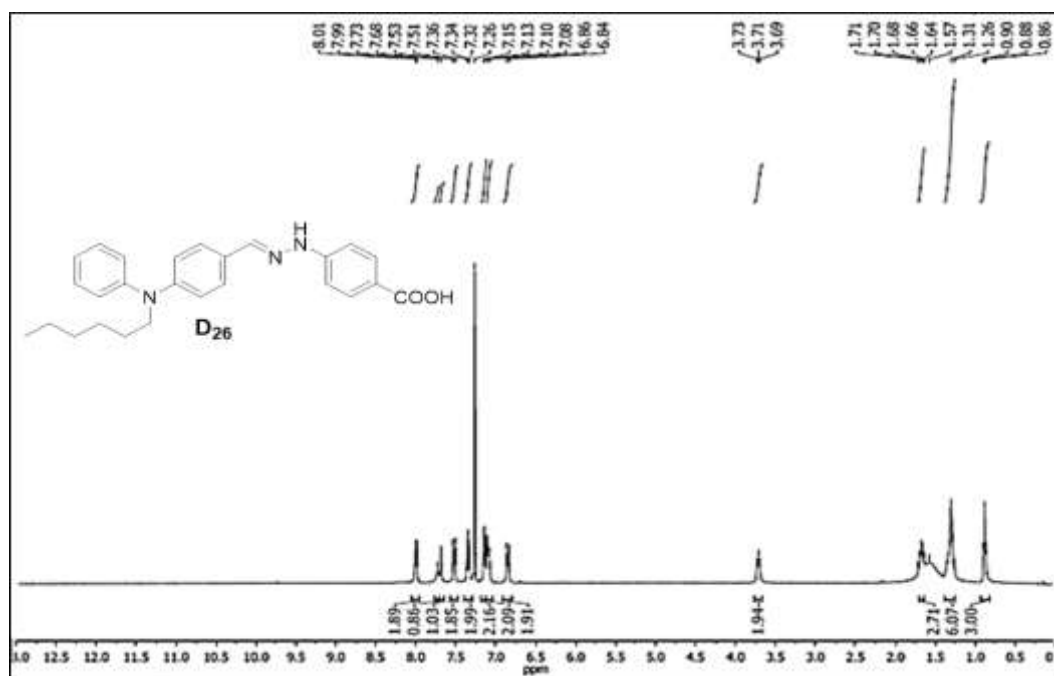


Fig 3.23 ¹H NMR spectrum of **D₂₆** recorded in CDCl₃

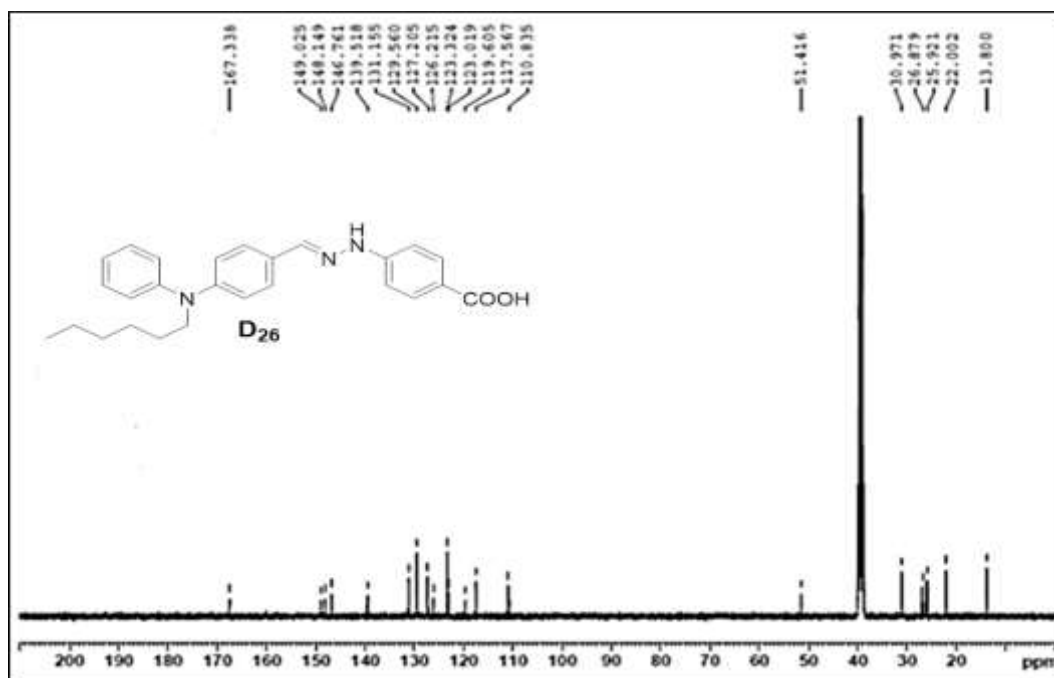


Fig 3.24 ¹³C NMR spectrum of **D₂₆** recorded in DMSO-*d*₆

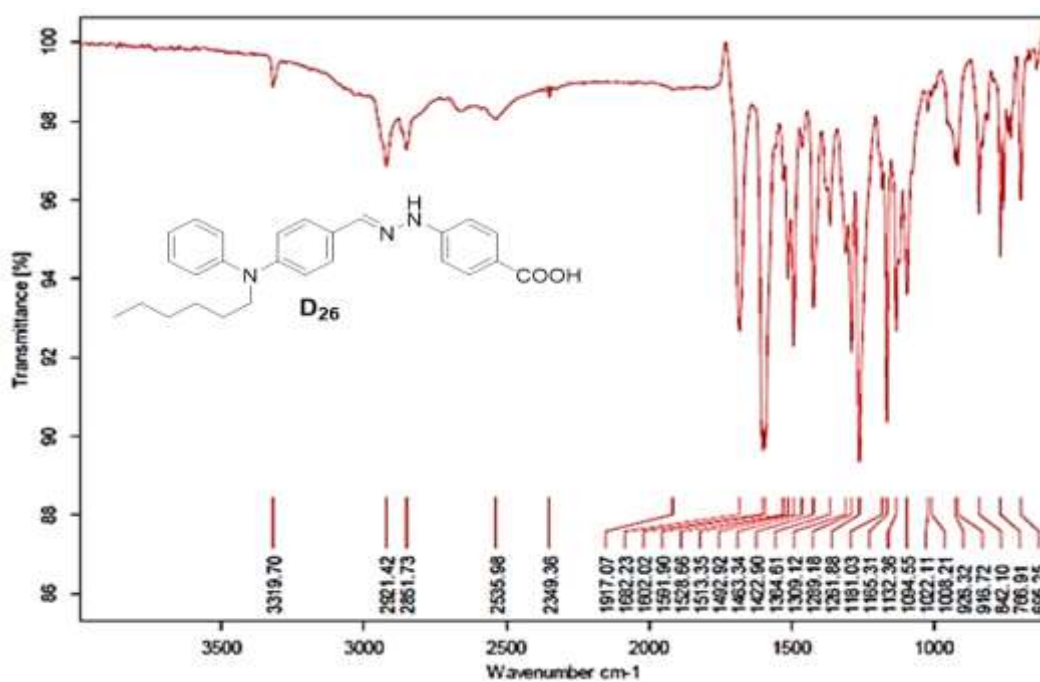


Fig 3.25 FTIR spectrum of **D₂₆**

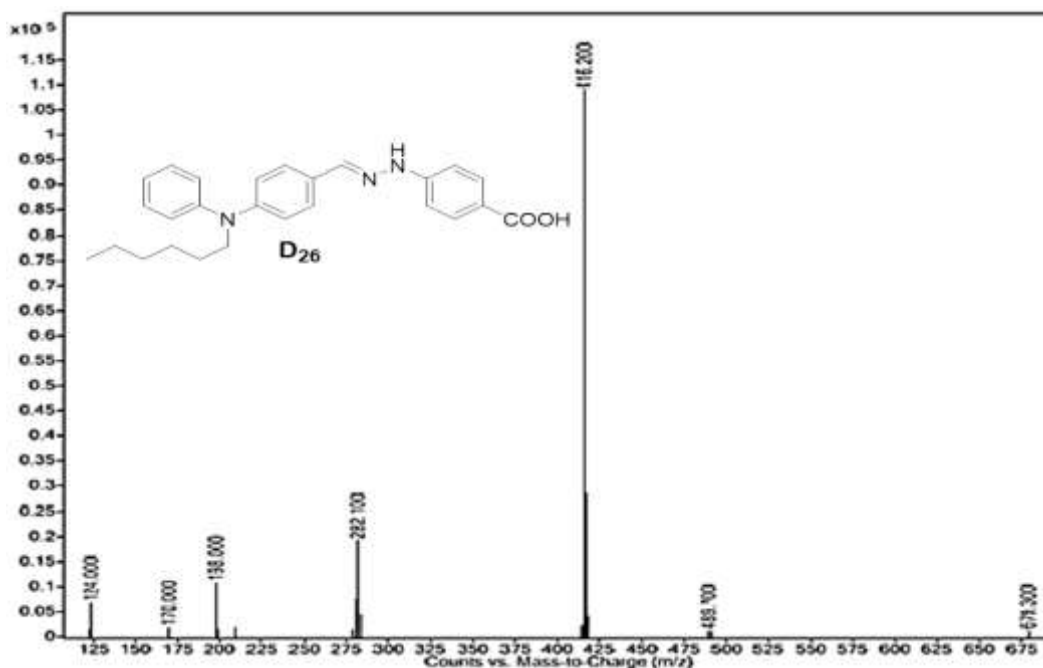


Fig 3.26 Mass spectrum of **D₂₆**

3.3 CONCLUSIONS

In conclusion, seven new series containing twenty seven *n*-type dyes, *i.e.* (i) D- π -A configured **D₁₋₃** (**Series-1**) (ii) A-D- π -A architected **D₄₋₇** (**Series-2**) (iii) D- π - π -A type **D₈₋₁₁** (**Series-3**) (iv) D- π -A configured with nitro anchoring group, **D₁₂₋₁₇** type (**Series-4**) (v) D-D-A type **D₁₈₋₂₁** (**Series-5**) (vi) A-D- π -D-A configured **D₂₂₋₂₃** (**Series-6**) and (vii) simple D-A type **D₂₄₋₂₇** (**Series-7**) were successfully synthesized, following appropriate synthetic routes, as per the **Schemes 3.1-3.7**. The synthetic procedures were optimized with respect to yield, solvent, temperature, reaction time, mole ratio and other reaction conditions. Also, their purification techniques have been developed. The chemical structures of all the final dyes and their unknown intermediates were confirmed by spectroscopy techniques like FTIR, ¹H NMR, ¹³C NMR spectroscopy and Mass spectrophotometry. Also, elemental analysis technique was used for characterization of a few target dyes. In the next chapter, a detailed photophysical, electrochemical, and molecular modeling studies of newly synthesized dyes have been discussed.

PHOTOPHYSICAL, ELECTROCHEMICAL AND THEORETICAL INVESTIGATIONS

Abstract:

This chapter comprises in depth linear optical as well as electrochemical studies of newly synthesized dyes D₁₋₂₇. Further, it involves DFT calculations involving theoretical simulations with regard to geometric optimizations, HOMO-LUMO levels, and electrostatic potential mappings of all the dyes. Also, their structure-property correlation studies have been included.

4.1 PHOTOPHYSICAL INVESTIGATION

Photophysical investigation of newly synthesized molecules mainly includes their UV-Vis absorption and emission studies. This is an important analytical technique employed for both qualitative and quantitative analysis of materials. Generally, UV-Vis absorption spectroscopy involves the measuring of absorbance of light by a compound as a function of wavelength in the UV-visible range. When a dye is subjected to incident light, it absorbs photon and get excited from ground state (HOMO level) to an electronic excited state (LUMO level). Fluorescence is a complementary technique to UV-Vis absorption. It occurs in the same wavelength range, but results from an excited state, emitting a photon of a lower energy than it absorbed. Further, optical studies of any organic material can evaluate the important data like optical band gap, molar extinction coefficient (ϵ) and Stokes shift values. These are valuable parameters used for selecting such materials in organic electronics, particularly in DSSCs as sensitizers/co-sensitizers. Therefore, all the synthesized organic dyes are subjected to UV-Vis and fluorescence spectral studies in order to evaluate their suitability for their applications in DSSCs as sensitizers/co-sensitizers. These generated structure-depending optical data provide valuable information, which are highly useful in designing new sensitizers/co-sensitizers.

4.1.1 Materials and methods

The UV-Vis absorption spectra of the dyes were recorded at room temperature using Analytik Jena SPECORD S 600 spectrophotometer. Further, the fluorescence emission spectra were obtained using Jasco FP 6200 spectrophotometer.

4.1.2 Experimental

The UV-Vis absorption spectra of synthesized dyes, **D**₁₋₂₇ were measured at the concentration of 3×10^{-5} M in chloroform/DMF solutions. Further, their emission spectra were obtained by irradiative excitation at the wavelength of their λ_{abs} , using the same concentration. Their optical band gap, molar extinction coefficient (ϵ) and Stokes shift values were calculated with the help of the spectral data. Also, the UV-Vis absorption studies of **D**₁₋₁₁ adsorbed on semiconductor, TiO₂ surface and that of **D**₁₂₋₂₇ along with **HD-2** adsorbed on TiO₂ were carried out.

4.1.3 Results and discussion

Figs 4.1 to 4.14 depict the absorption as well emission spectra of all the new dyes at concentration 3×10^{-5} M in CHCl₃/DMF and their corresponding photophysical parameters are tabulated in **Table 4.1 to 4.7**. Results of these photophysical studies have been discussed series-wise in the following section.

4.2.3.1 Photophysical studies of chromophores **D**₁₋₃ (Series-1)

The recorded UV-Vis spectra of **D**₁₋₃ of **Series-1** are given in **Fig 4.1(a)** and their calculated optical data are summarized in **Table 4.1**. From the results, it is clear that, all the dyes show two distinctive absorption maxima, the lower maxima lies in the region of 340-380 nm, that corresponds to π - π^* electronic excitations within the structure, whereas the higher maxima is in the range of 440-485 nm, which owes to promotion of electron from HOMO to LUMO and a little promotion from HOMO-1 to LUMO. As per the results, the dyes show λ_{abs} in the decreasing order of **D**₃ > **D**₁ > **D**₂. The observed redshift of **D**₃(483 nm) compared to that of **D**₁(466 nm) and **D**₂(445 nm) is mainly due to the higher electron withdrawing nature of barbituric acid. The recorded and emission spectra are featured in **Fig 4.1(b)** and their corresponding optical parameters tabulated in **Table 4.1**. All the dyes display characteristic λ_{emi} in the region of 545-570 nm. It is seen that the λ_{emi} of **D**₃(546 nm) was blue shifted when compared to the **D**₁(566 nm) and **D**₂(565 nm). The perceived blue shift is attributed to presence of strong electron withdrawing barbituric acid in the dye. Further, their optical band-gap and Stokes shift values were calculated from the intersection between normalized absorption and emission spectra. Their optical band gaps are in the decreasing order as **D**₂(2.32 eV) > **D**₁(2.31 eV) > **D**₃(2.23 eV) and

calculated Stokes shifts are in the increasing order, as $\mathbf{D}_3(2389 \text{ cm}^{-1}) < \mathbf{D}_1(3791 \text{ cm}^{-1}) < \mathbf{D}_2(4772 \text{ cm}^{-1})$. Here, the observed maximum value for \mathbf{D}_2 is mainly due to the presence of highly electron withdrawing 2,(4-nitrophenyl)acetonitrile in its structure, resulting in improved emission characteristic. Further, the molar extinction coefficients (ϵ) for ICT bands were calculated for the dyes. The obtained values for \mathbf{D}_{1-3} are 32790.33, 33587, and 36527.7 $\text{M}^{-1}\text{cm}^{-1}$ respectively, indicating \mathbf{D}_1 as a potential candidate for sensitizer.

To get a realistic picture of light harvesting ability of dyes they were adsorbed on TiO_2 and their UV-Vis spectra in adsorbed state were recorded in separate experiments. These spectra are depicted in **Fig 4.28(a)**. It has been observed that absorption peaks of adsorbed dyes are red shifted and broadened because of the interaction of anchoring group with the titania surface. Generally, when sensitizers anchor onto the mesoporous TiO_2 surface, the resulted de-protonation and aggregation (H and J- aggregation) of dye molecules affect the optical absorption profile. The most common de-protonation and H-aggregation always result in a blue shift in the absorption peak, while J-aggregation mainly leads to the red shift in the absorption peak. All the dyes show redshift, which can also be explained by the fact that the adsorption can lead to more delocalization of dye, thereby decreasing the energy of π^* orbital. $\mathbf{D}_1(531 \text{ nm})$ shows a greater redshift of $\sim 65 \text{ nm}$ than the dyes \mathbf{D}_2 and \mathbf{D}_3 , confirming the better ICT phenomenon to occur. Further, all the absorption spectra show a markedly broad profile, indicating their good light-harvesting ability. Moreover, \mathbf{D}_1 displays more intense bands when compared to other two dyes mainly due to higher anchoring strength of carboxylic group. Conclusively, \mathbf{D}_1 is a potential sensitizer from the point of view of its absorption as well as adsorption behaviour.

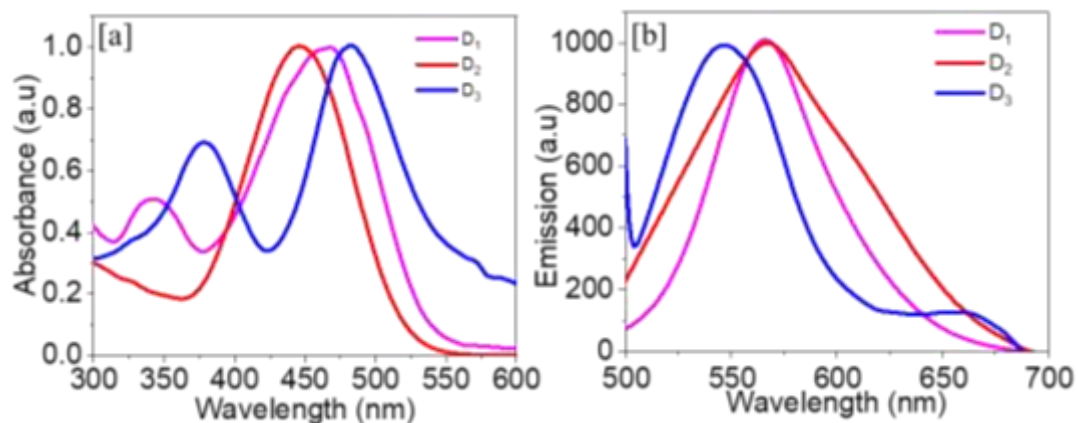


Fig 4.1(a) Normalized absorption spectra of **D**₁₋₃; (b) their emission spectra in CHCl_3 (3×10^{-5} M)

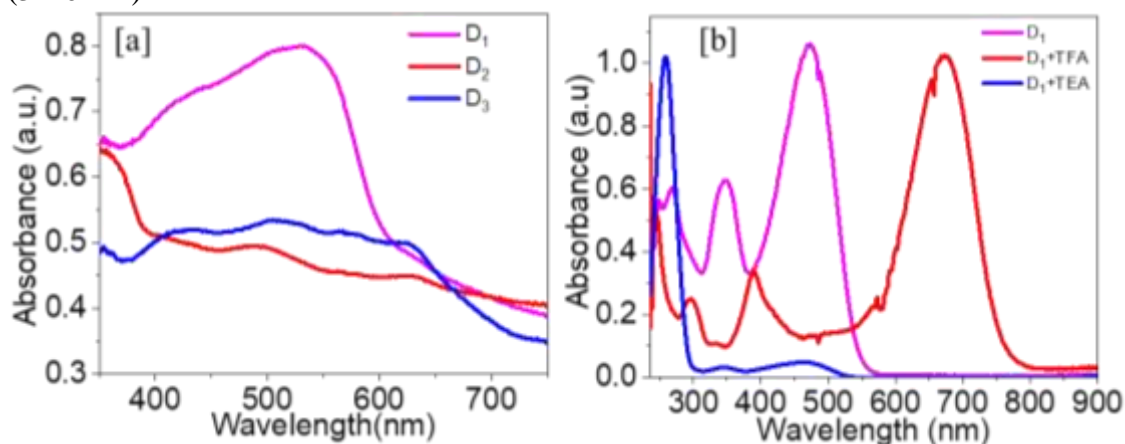


Fig 4.2 Absorption spectra of (a) **D**₁₋₃ adsorbed on TiO_2 ; (b) **D**₁ in acidic and basic medium

In order to study **D**₁'s behaviour in acidic and basic media, its absorption spectra were recorded in presence of little trifluoroacetic acid (TFA) and triethylamine (TEA), separately and their corresponding spectra are depicted in **Fig 4.2(b)**. Usually, the acid group exists in equilibrium with deprotonated and normal form. Here, the dye **D**₁(677 nm) shows a bathochromic shift in presence of TFA. The reason is that the TFA can protonate the carboxylate ion in the deprotonated form which can push the equilibrium towards more neutral form, leading to a bathochromic shift of the dye. But, the addition of TEA results in the blue shift of **D**₁(255 nm) which is due to the de-protonation of dye. From this study, it can be concluded that the charge transfer between donor and acceptor is very much sensitive to the solvent condition.

Table 4.1 Photophysical properties of **D**₁₋₃

Sensitizer/ co-sensitizers	λ_{abs} (nm) ^a	λ_{emi} (nm) ^b	Stokes shift (cm ⁻¹)	E ₀₋₀ , optical (eV) ^c
D ₁	466	566	3791	2.31
D ₂	445	565	4772	2.32
D ₃	483	546	2389	2.23

^a Absorption and emission spectra were recorded in CHCl₃ (3×10⁻⁵M) at room temperature.

^b Dyes were excited at their absorption maximum value.

^c Optical band gap was calculated from the intersection between the absorption and emission spectra.

4.2.3.2 Photophysical studies of chromophores **D**₄₋₇ (Series-2)

Fig 4.3 (a) displays the absorption spectra of **D**₄₋₇ and the observed photophysical properties are tabulated in **Table 4.2**. From the spectra it can be observed that, the higher λ_{abs} was observed for **D**₇(479 nm) than that of **D**₆(472 nm), **D**₄(418 nm) and **D**₅(449 nm), which is majorly due to the powerful electron withdrawing nature of barbituric acid. Further, **D**₆ bearing 4-hydrazinylbenzoic acid, shows a red shift compared to **D**₄ and **D**₅ bearing cyanoacetic acid and rhodanine acetic acid, respectively. The sensitizer **D**₅ that displayed a broad and flat spectrum when compared to other dyes. This dye is expected to absorb more photons than the remaining dyes of the series.

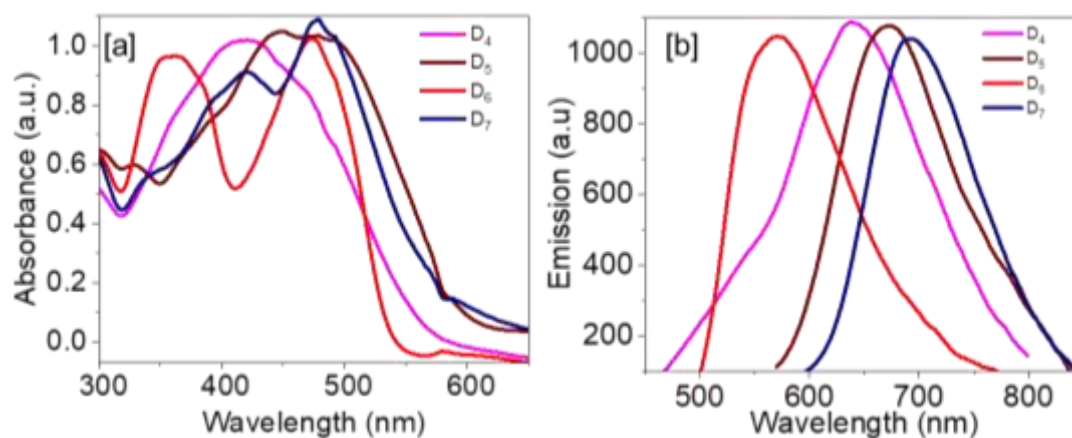


Fig 4.3(a) Normalized absorption spectra of **D**₄₋₇; **(b)** their emission spectra in CHCl₃ (3×10⁻⁵M)

The emission spectra of the dyes are featured in **Fig 4.3(b)** and their corresponding data are summarized in **Table 4.2**. All the dyes display characteristic λ_{emi} in the region of 570-690 nm. The λ_{emi} of sensitizers are in the increasing order of **D₆**(570 nm) < **D₄**(638 nm) < **D₅**(674 nm) < **D₇**(689 nm). Additionally, Stokes shift values of the dyes were also calculated and the obtained values for **D₄₋₇** are 8249, 7435, 3643 and 6363 cm^{-1} , respectively. Among the sensitizers **D₄** shows the highest Stokes shift, which can be accounted for an efficient electron shift from the diphenylamine to the anchoring cyanoacetic acid unit. Further, the optical band gaps of the sensitizers were calculated and they are in the order: **D₆**(2.3 eV) > **D₄**(2.22 eV) > **D₇**(2.2 eV) > **D₅**(2.1 eV). Furthermore, the molar extinction coefficients (ϵ) of the ICT bands were calculated and they were found to be 15000, 29436, 17800 and 15601 $\text{M}^{-1}\text{cm}^{-1}$ for **D₄₋₇**, respectively. Among them, **D₅** shows the highest ' ϵ ' value mainly due to the presence of strongly light absorbing rhodanine acetic acid scaffold.

Table 4.2 Photophysical properties of **D₄₋₇**

Sensitizer/ co-sensitizers	λ_{abs} (nm)	λ_{emi} (nm)	Stokes shift (cm^{-1})	E_{0-0} , optical (eV)
D₄	418	638	8249	2.22
D₅	449	674	7435	2.1
D₆	472	570	3643	2.3
D₇	479	689	6363	2.2

Fig 4.4 shows the UV-Vis spectra of the dyes **D₄₋₇** adsorbed on TiO_2 surface. In the current study, **D₅**(530 nm) shows the highest red shift among the dyes **D₄**(509 nm), **D₆**(455 nm), **D₇**(498 nm). This is attributed to the enhanced delocalization of dye due to presence of conjugated rhodanine acetic acid, thereby decreasing the energy of π^* orbital. Here, **D₇** also shows a red shift but the observed shift is less than that of **D₄** and **D₅**. Amongst the four dyes, **D₆**(455nm) displays a blue shift which is a common trend seen in dyes. Moreover, **D₄** and **D₆** exhibit more intense bands due to strong anchoring strength of carboxylic group. Despite of the fact that, **D₅** anchors through carboxylic group, it shows slightly lower absorption maxima than **D₄** and **D₆**.

It can be inferred from the spectra that, **D7** bearing barbituric acid is poorly anchored to TiO₂ surface. Finally, **D4** is considered to be a potential sensitizer from the view of its strong absorption behaviour.

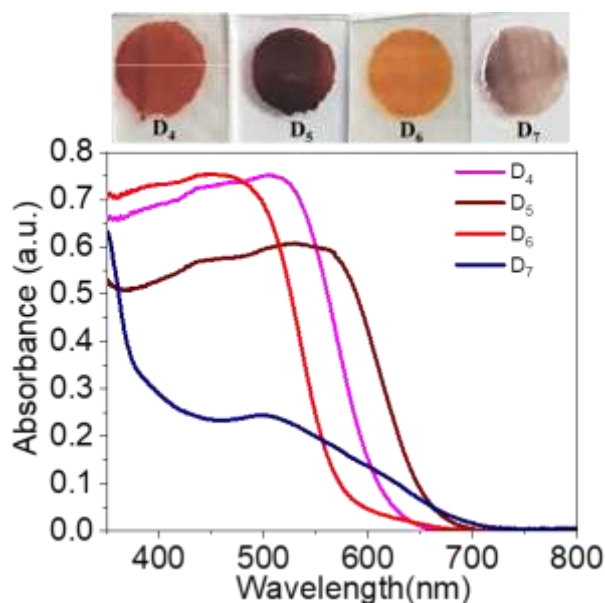


Fig 4.4 Absorption spectra of **D4-7** adsorbed on TiO₂ surface.

4.2.3.3 Photophysical studies of chromophores **D8-11** (Series-3)

The recorded absorption spectra for dyes **D8-11** are shown in **Fig 4.5(a)** and the corresponding optical data are given in **Table 4.3**. The observed absorbance values are in the order **D11**(560 nm) > **D9**(477 nm) > **D8**(438 nm) > **D10**(431 nm). As expected, **D11** dye carrying an additional spacer unit with barbituric acid as anchoring group showed the highest red shift compared to other dyes. The red shift of **D11** can be explained by the fact that, the extension of spacer unit has broadened the absorption spectrum of the dye along with an additional absorbance peak in the higher wavelength region. Also, the higher λ_{abs} of **D11** and **D9** bearing barbituric acid when compared to **D10** and **D8** carrying cyanoacetic acid can be a result of the higher electron withdrawing nature of barbituric acid. The presence of an additional spacer unit has increased the conjugation of **D11** when compared to its counterpart **D9**. In contrary, **D10** with an extended conjugation unit is not showing any red shift when compared to its counterpart **D8**. This behaviour can be a result of aggregation with in the dye **D10**. Additionally, the molar extinction coefficients (ϵ) of the ICT bands were

calculated and the obtained values for **D**₈₋₁₁ are 32790.33, 33587, 36527.7 and 35387 M⁻¹cm⁻¹, respectively.

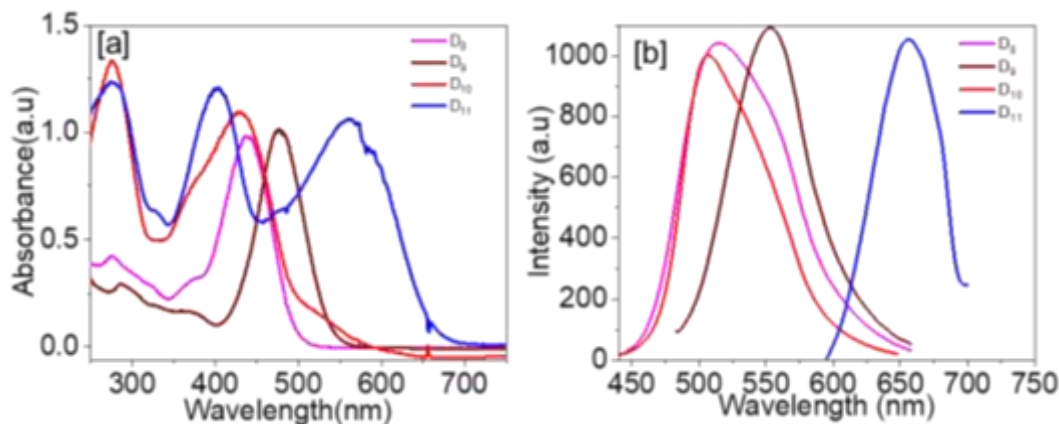


Fig 4.5(a) Normalized absorption spectra of **D**₈₋₁₁; **(b)** their emission spectra in CHCl₃ (3×10^{-5} M)

Fig 4.5(b) shows the emission spectra of dyes **D**₈₋₁₁ (**Series-3**) The obtained λ_{emi} is in the descending order as: **D**₁₁(654 nm) > **D**₉(554 nm) > **D**₈(518 nm) > **D**₁₀(507 nm). The order of λ_{emi} values of dyes are in the same order as their absorbance values. Further, the Stokes shifts calculated are in the ascending order, **D**₁₁(2567 cm⁻¹) < **D**₉(2914 cm⁻¹) < **D**₈(3414 cm⁻¹) < **D**₁₀(3478 cm⁻¹). It is interesting to note that, the order of Stokes shift is opposite to that of the order of absorbance and emissive values. Thus, the highest Stokes shift value of **D**₁₀ may be owing to its proper ICT transfer of electrons. Further, the expansion of the π conjugation has also altered the HOMO and LUMO levels of the sensitizers, thereby tuning the bandgap of the dyes. Furthermore, the band gaps of the dyes were calculated and the obtained values for **D**₈₋₁₁ are 2.47, 2.27, 2.46 and 1.9 eV, respectively. The lower band gap of **D**₁₁ is attributed to lowering of LUMO levels through the extended conjugation.

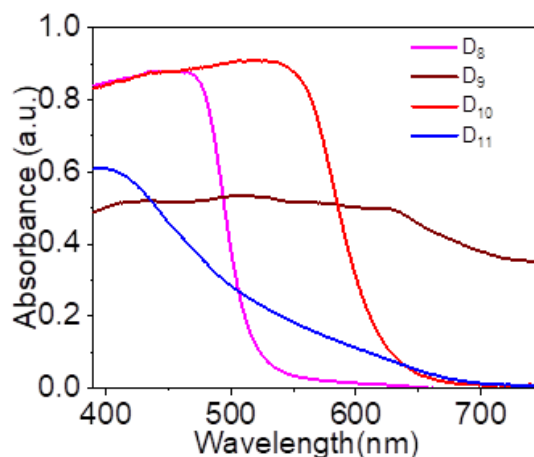


Fig 4.6 Absorption spectra of **D8-11** adsorbed on TiO_2 surface.

Fig 4.6 shows the UV- Visible spectrum of dyes adsorbed on TiO_2 semiconductor surface. It is observed that, absorption peaks of adsorbed dyes are red shifted and broadened because of the interaction of anchoring group with the titania surface. As it can be seen from the spectra, **D8**(465 nm) and **D10**(536 nm) are showing a quite good adsorption onto the TiO_2 surface due the anchoring carboxylic group. But **D9**(570 nm) and **D11**(411 nm) show a weak spectrum due to the poor adsorption onto the TiO_2 surface through the barbituric acid. Conclusively, **D8** and **D11** can behave as potential sensitizers from the point of view of their adsorption behaviour.

Table 4.3 Photophysical properties of **D8-11**

Sensitizer/ co-sensitizers	λ_{abs} (nm)	λ_{emi} (nm)	Stokes shift (cm^{-1})	E_{0-0} , optical (eV)
D8	438	515	3414	2.47
D9	477	554	2914	2.27
D10	431	507	3478	2.46
D11	560	654	2567	1.90

4.2.3.4 Photophysical studies of chromophores D_{12-17} (Series-4)

The UV-Vis absorption and fluorescence emission spectra of the synthesized chromogens **D12-17**, recorded in $\text{CHCl}_3(3 \times 10^{-5} \text{ M})$ solutions are depicted in **Figs 4.7(a)** and **(b)**, respectively and their corresponding results are summarized in **Table 4.4**. The **Fig 4.7(a)** shows that, the absorption maxima obtained for dyes **D12-17** are in the ascending order: **D13**(373 nm) < **D15**(402 nm) < **D12**(433 nm) < **D14**(434 nm) <

$\mathbf{D}_{16}(462 \text{ nm}) < \mathbf{D}_{17}(476 \text{ nm})$. From the spectra, it is noteworthy that \mathbf{D}_{13} and \mathbf{D}_{15} show only single maxima whereas all other dyes display two peaks. The absence of low wavelength peak in \mathbf{D}_{13} and \mathbf{D}_{15} is due to the presence of less electron withdrawing substituted furan and benzoic acid motifs, respectively. \mathbf{D}_{12} bearing 4-nitrobenzaldehyde unit shows distinct two peaks because of the presence of electron withdrawing nitrobenzene unit. The presence of an additional benzene moiety in the structural unit of \mathbf{D}_{14} has caused a bathochromic shift of 61 nm when compared to that of \mathbf{D}_{13} . The increase of conjugation in the structures of \mathbf{D}_{16} and \mathbf{D}_{17} has been reflected in their quite red shifted absorbance values. Further, the “ ϵ ” of \mathbf{D}_{12-17} were calculated and found to be 21,370, 23,000, 16,230, 24,800, 30,000, and 21,333 $\text{M}^{-1}\text{cm}^{-1}$ respectively, indicating their good light harvesting capability.

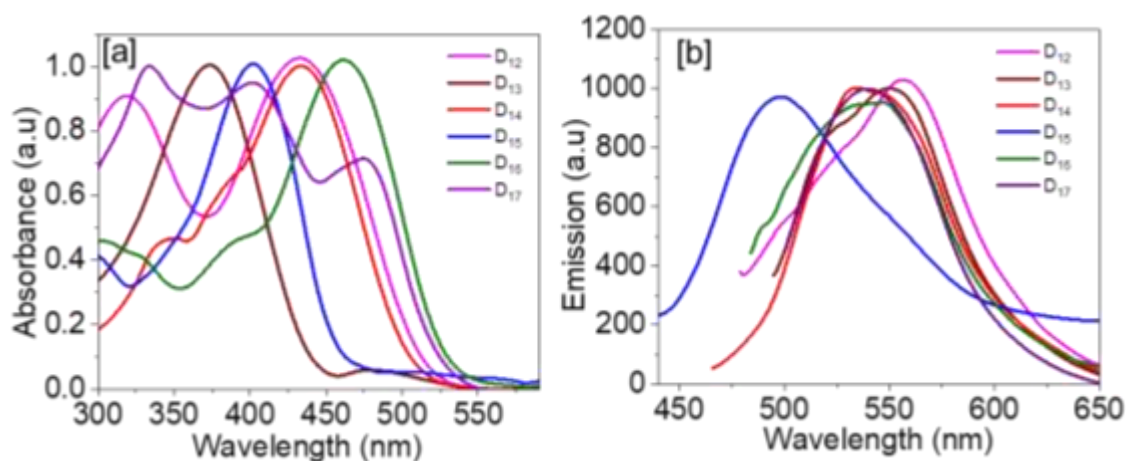


Fig 4.7(a) Normalized absorption spectra of \mathbf{D}_{12-17} ; **(b)** their emission spectra in CHCl_3 ($3 \times 10^{-5} \text{ M}$)

Fig 4.7(b) shows the fluorescence emission spectra of \mathbf{D}_{12-17} upon their excitation at this absorption wavelength (λ_{abs}). The emission values obtained for the sensitizers are in the order $\mathbf{D}_{12}(556 \text{ nm}) > \mathbf{D}_{13}(552 \text{ nm}) > \mathbf{D}_{16}(547 \text{ nm}) > \mathbf{D}_{17}(540 \text{ nm}) > \mathbf{D}_{14}(535 \text{ nm}) > \mathbf{D}_{15}(499 \text{ nm})$. Further, their Stokes shift values were calculated from these normalized UV-Vis absorption and fluorescence emission spectral data (**Table 4.4**). It has been observed that, \mathbf{D}_{12-17} , show a maximum shift of 134 nm when compared to other three dyes of the series. The observed large value of Stokes shift confirms the effective ICT property of the dye \mathbf{D}_{12-17} . Further, the optical band gaps of \mathbf{D}_{12-17} were determined from the intersection between the UV-Vis absorption and

fluorescence emission curves and the corresponding data are summarized in **Table 4.4**.

Fig 4.8 depicts absorption spectra of co-sensitizer **D₁₂₋₁₇** adsorbed on TiO₂ surface, along with **HD-2** sensitizer. Since these dyes have shown good co-sensitization behaviour when used with Ru-based **HD-2**, their absorption studies along with **HD-2** have been undertaken. Moreover, they did not show good device performance when used them as sensitizers. In the present work, the absorption spectra of **D₁₈₋₂₁** with **HD-2** adsorbed on TiO₂ surface were run and the λ_{abs} values obtained for **D_{13+HD-2}**, **D_{15+HD-2}**, **D_{12+HD-2}**, **D_{14+HD-2}**, **D_{16+HD-2}**, **D_{17+HD-2}**, and **HD-2**, are 559, 575, 568, 568, 545, 542, and 571 nm, respectively. It has been noticed that, the intensities of adsorbed dye mixture are more than that of **HD-2** dye alone.

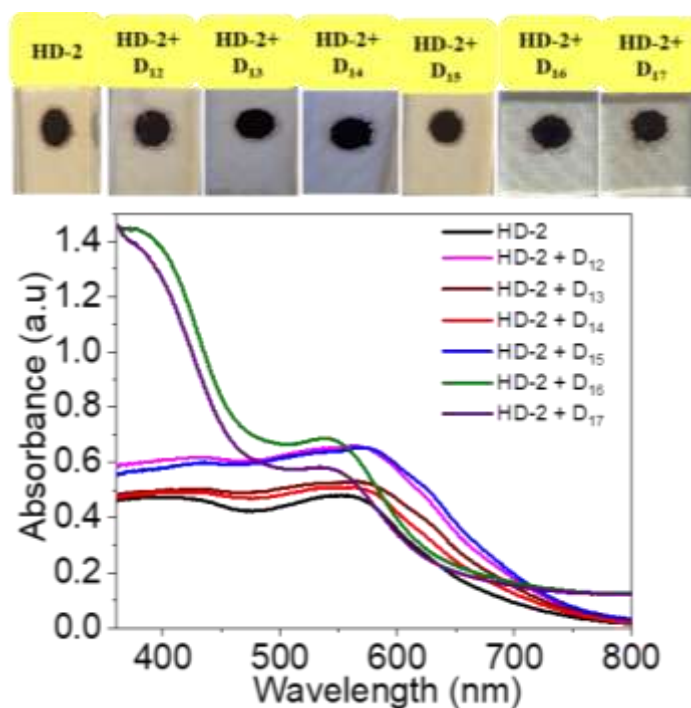


Fig 4.8 Absorption spectra of **D₁₈₋₂₁** with **HD-2** adsorbed on TiO₂ surface

Table 4.4 Photophysical properties of **D12-17**

Sensitizer/ co-sensitizers	λ_{abs} (nm)	λ_{emi} (nm)	Stokes shift (cm^{-1})	E_{0-0} , optical (eV)
D12	433	556	5109	2.40
D13	373	552	8694	2.82
D14	434	535	4350	2.46
D15	402	499	4836	2.70
D16	462	547	6594	2.35
D17	476	540	2490	2.38

4.2.3.5 Photophysical studies of chromophores **D18-21** (Series-5)

The UV-Vis absorption and fluorescence emission spectra of the synthesized dyes **D18-21**, recorded in DMF (3×10^{-5} M) solutions are depicted in **Fig 4.9** and their corresponding results are summarized in **Table 4.5**. As shown in **Fig 4.9(a)**, the absorbance maxima of dyes are in the decreasing order: **D18**(405 nm) > **D19**(404 nm) > **D20**(349 nm) > **D21**(394 nm). Except **D20**, all the other dyes show similar pattern of spectra, whereas **D20** alone displays a blue shift. The observed difference in the pattern may be due to the electron donating ability of attached pyrene moiety to **D20**. The “ ϵ ” values of **D18-21**, were found to be 42,000, 33,333, 52,000 and 49,666 $\text{M}^{-1}\text{cm}^{-1}$, respectively, indicating their good light harvesting capability.

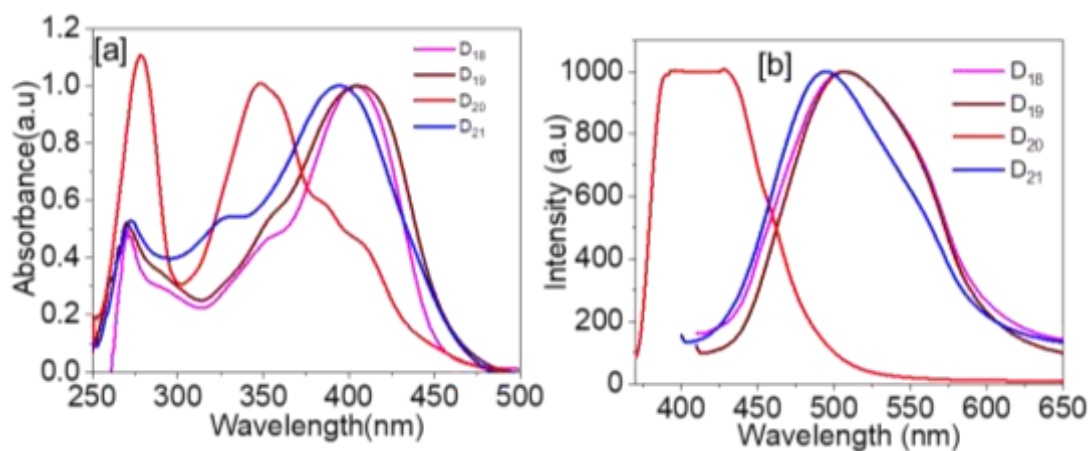


Fig 4.9(a) Normalized absorption spectra of **D18-21**; **(b)** their emission spectra in DMF(3×10^{-5} M)

The absorption spectra of **D**₁₈₋₂₁ along with **HD-2** dye adsorbed on TiO₂ are depicted in **Fig 4.10**. Their absorption values are in the increasing order as: **D**₁₈+**HD-2**(540 nm) < **D**₁₉+**HD-2**(543 nm) < **D**₂₀+**HD-2**(546 nm) < **D**₂₁+**HD-2**(563 nm) < **HD-2**(564 nm). For all the mixtures of dyes, the intensities obtained were prominently higher than that of the **HD-2** dye alone. This behaviour of the dye mixture shows that, the dyes **D**₁₈₋₂₁ can act as potential co-sensitizers.

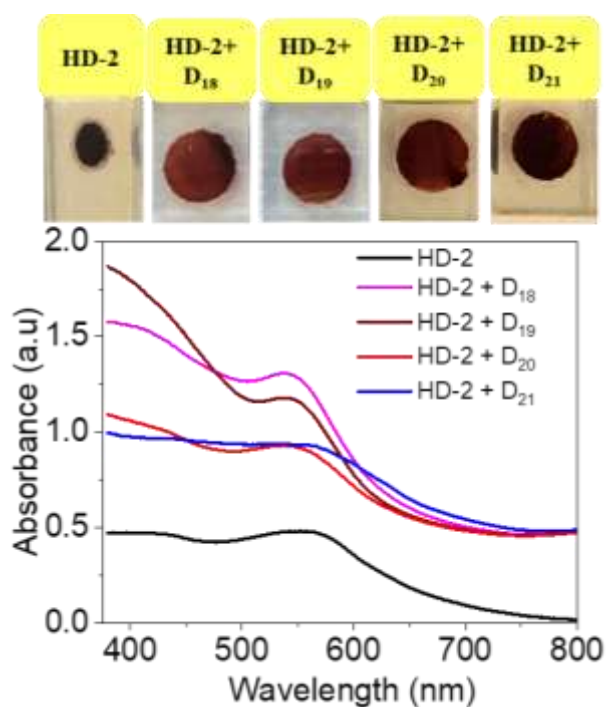


Fig 4.10 Absorption spectra of **D**₁₈₋₂₁ adsorbed on TiO₂ surface

Table 4.5 Photophysical properties of **D**₁₈₋₂₁

Sensitizer/ co-sensitizers	λ_{abs} (nm)	λ_{emi} (nm)	Stokes shift (cm ⁻¹)	E ₀₋₀ , optical (eV)
D ₁₈	405	507	4967	2.75
D ₁₉	404	508	5067	2.70
D ₂₀	349	428	5288	3.09
D ₂₁	394	498	5288	2.71

4.2.3.6 Photophysical studies of chromophores D_{22-23} (Series-6)

The UV-Vis absorption and fluorescence emission spectra of dyes D_{22-23} , recorded in DMF at 3×10^{-5} M, are shown in **Fig 4.11** and their optical data are tabulated in **Table 4.1**. As seen from the spectra given in **Fig 4.11(a)**, a weak peak has been observed in the shorter wavelength region for both the dyes unlike dyes of other series. This may be attributed to the design strategy, *i.e.* A-D- π -D-A configuration used in the dyes. The dye D_{23} (482 nm) shows a red shift compared to that of D_{22} (444 nm), which may be ascribed to the presence of rhodanine acetic acid anchoring unit.

As observed from their emission data, D_{22} shows emission maxima at 546 nm whereas D_{23} displays at 558 nm. Further, their calculated Stokes shift values are 4203 and 2825 cm^{-1} , respectively. Here, D_{23} shows lower value of Stokes shift, even though it possesses better absorbance and emission property. The “ ϵ ” of D_{22-23} , were found to be 30,666 and 38,200 $\text{M}^{-1}\text{cm}^{-1}$ respectively, indicating their good light harvesting capability. Further, the optical band gaps of D_{22-23} were determined to be 2.45 and 2.30 eV, respectively.

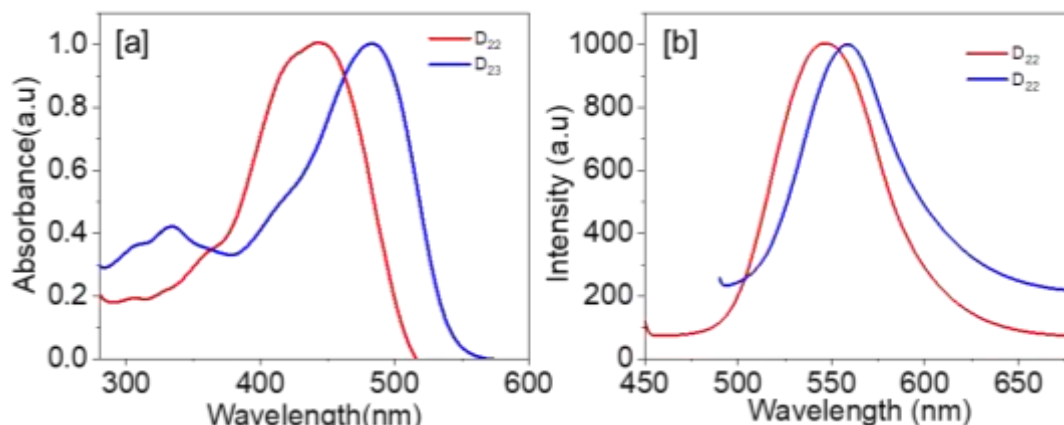


Fig 4.11(a) Normalized absorption spectra of D_{22-23} ; **(b)** their emission spectra in DMF(3×10^{-5} M)

Fig 4.12 portrays the absorption spectra of D_{22-23} along with **HD-2** dye adsorbed on TiO_2 . It is clear from the spectra that, λ_{abs} values are in the order, $D_{22}+\text{HD-2}(508 \text{ nm}) < D_{23}+\text{HD-2}(535 \text{ nm}) < \text{HD-2}(564 \text{ nm})$. Here, the absorption intensity for the dye mixture is more than that of **HD-2** dye alone, indicating the dyes of this series are possessing good co-sensitizing ability.

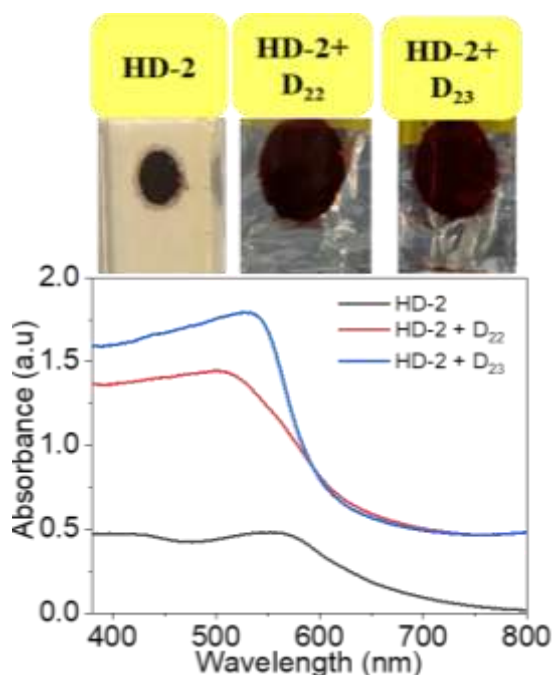


Fig 4.12 Absorption spectra of **D₂₂₋₂₃** adsorbed on TiO₂ surface

Table 4.6 Photophysical properties of **D₂₂₋₂₃**

Sensitizer/ co-sensitizers	λ_{abs} (nm)	λ_{emi} (nm)	Stokes shift (cm ⁻¹)	E ₀₋₀ , optical (eV)
D₂₂	444	546	4208	2.45
D₂₃	546	558	2825	2.30

4.2.3.7 Photophysical studies of chromophores **D₂₄₋₂₇** (Series-7)

Fig 4.13 shows the UV-Vis absorption and emission spectra of dyes **D₂₄₋₂₇**, recorded in CHCl₃ at 3×10^{-5} M and their corresponding results are tabulated in **Table 4.7**. From the **Fig 4.13(a)**, it is evident that, the absorbance values obtained for **D₂₄₋₂₇** are 430, 477, 381 and 388 nm, respectively. The highest λ_{abs} value is obtained for **D₂₅** owing to the presence of electron withdrawing anchor rhodanine acetic acid, as already discussed in the earlier sections. To gain further knowledge on the optical behaviour, molar extinction co-efficient “ ϵ ” values of ICT bands were calculated. The obtained values for dyes **D₂₄₋₂₇** are 71,666, 73,333, 43,333 and 54,5333 M⁻¹cm⁻¹ respectively, indicating their good light capturing ability.

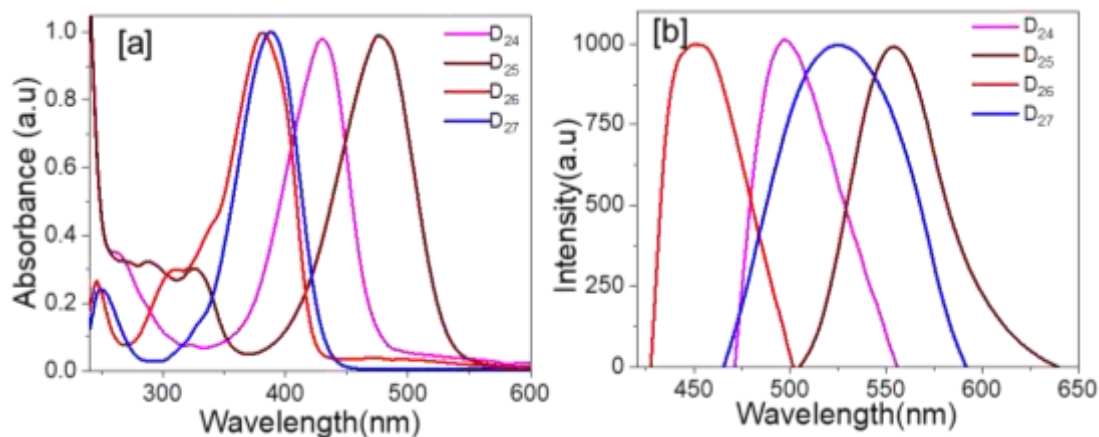


Fig 4.13(a) Normalized absorption spectra of **D₂₄₋₂₇** **(b)** their emission spectra in CHCl₃(3×10⁻⁵ M)

The fluorescence emission spectra of **D₂₄₋₂₇** are portrayed in **Fig 4.13b** and the observed λ_{emi} for the dyes are 497, 554, 452 and 526 nm, respectively. It is noted that, **D₂₇** shows a fairly broad emission behaviour when compared to other dyes of the series. Further, their calculated Stokes shifts values are 3130, 2914, 4122, and 6760 cm⁻¹, respectively. Here, **D₂₇** shows the highest shift among the dyes in the series, indicating good ICT phenomenon in the molecule. Furthermore, their band gaps were found to be in the decreasing order of **D₂₆**(2.92 eV) > **D₂₇**(2.88 eV) > **D₂₄**(2.62 eV) > **D₂₅**(2.35 eV). Because of presence of rhodanine acetic acid, **D₂₅** displays the lowest band gap value in the series.

Fig 4.14 shows the absorbance spectra of dyes along with **HD-2** dye adsorbed on TiO₂ surface. Here, the absorption maxima obtained are in the order: **HD-2**(564 nm) < **D₂₆+HD-2**(558 nm) < **D₂₄+HD-2**(542 nm) < **D₂₅+HD-2**(541 nm) < **D₂₇+HD-2**(540 nm). From the spectra, it is clear that all the pairs show more intense absorption when compared to **HD-2** dye alone, indicating that they are potential co-sensitizers. It is also observed that, the **D₂₆** shows a more flatter absorption spectra in the visible region than that of **D₂₄**, **D₂₅** and **D₂₇**. Eventually, the small molecular size of dyes in this series can help to fill the vacant spaces between the **HD-2** dye molecules effectively.

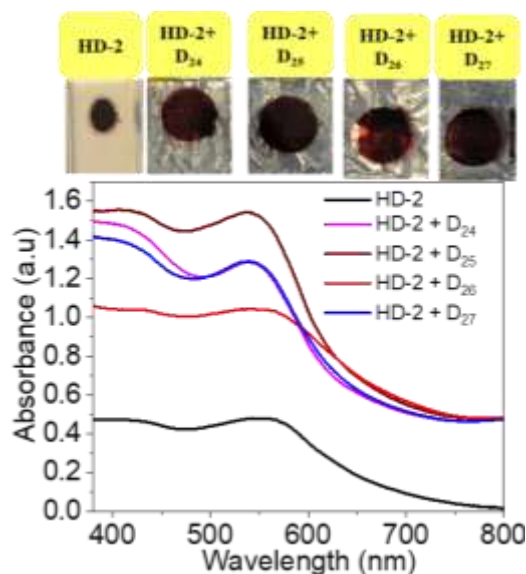


Fig 4.14 Absorption spectra of **D₂₄₋₂₇** along with **HD-2** adsorbed on TiO₂ surface

Table 4.7 Photophysical properties of **D₂₄₋₂₇**

Sensitizer/ co-sensitizers	λ_{abs} (nm)	λ_{emi} (nm)	Stokes shift (cm ⁻¹)	E ₀₋₀ , optical (eV)
D₂₄	430	497	3130	2.62
D₂₅	477	554	2914	2.35
D₂₆	381	452	4122	2.92
D₂₇	388	526	6760	2.88

4.2 ELECTROCHEMICAL STUDIES

Electrochemical studies are highly useful in understanding the redox properties of materials and knowing the stability relations for the radical ions. Particularly, in case of organic sensitizers, the study throws more light upon the thermodynamics of electron movement from the excited states of dyes to the CB of TiO₂ and the dye regeneration from the redox couple in the electrolyte to the oxidised dyes. It describes their oxidation and reduction potentials, which are highly useful in determining their HOMO-LUMO energy levels and charge carrying properties. Cyclic voltammetry (CV) method is largely used for electrochemical studies of organic dyes.

In the present work, CV studies were performed for all the dyes (**D₁₋₂₇**) in order to evaluate their excited state oxidation potential (ESOP/LUMO) and ground

state oxidation potential (GSOP/HOMO) energy levels. Further, the driving forces for the kinetic processes like injection (ΔG_{inj}), regeneration (ΔG_{reg}) and recombination (ΔG_{rec}) involved in the devices, for the sensitizers were determined to get a clear idea about feasibility of the thermodynamic processes.

One of the prerequisites of an ideal *n*-type sensitizer is that, the ESOP/LUMO level of the dye should be more electronegative than the CB edge of TiO₂ to ensure effective charge injection, while the GSOP/HOMO level of the sensitizer should be more positive than the redox potential of the electrolyte to ensure effective dye regeneration. This is one of the key conditions for a dye to act as a potential sensitizer.

4.2.1 Materials and methods

Supporting electrolyte *n*-butyl ammonium hexafluorophosphate (*n*-Bu)₄N⁺(PF₆)⁻ were procured from Sigma Aldrich Company whereas acetonitrile was purchased from Merck. Electrochemical measurements were performed on an IVIUM VERTOSTAT electrochemical workstation.

4.2.2 Experimental

All measurements were carried out at room temperature with a conventional three-electrode configuration consisting of a platinum disc working electrode, a glassy carbon (GC) working electrode, and an Ag/AgCl was used as the reference electrode. The potentials were reported at a scan rate of 100 mV/s using 0.1 M tetra *n*-butyl ammonium hexafluorophosphate (*n*-Bu)₄N⁺(PF₆)⁻ as a supporting electrolyte in acetonitrile under Argon atmosphere.

4.2.3 Results and discussion

The voltammograms obtained for all the dyes **D1-27** are portrayed in **Figs 4.15** to **4.21**. Also, the schematic representation of their HOMO and LUMO levels along with electrochemical band gaps are given in the same figures. Their calculated electrochemical / thermodynamic data, *viz.* E_{ox}, E_{ox}*, ΔG_{inj} , ΔG_{rec} and ΔG_{reg} values are tabulated in **Tables 4.8** to **4.14**. These results are discussed elaborately in the following section.

4.2.3.1 Electrochemical studies of chromophores D_{1-3} (Series-1)

From the voltammograms of the dyes D_{1-3} as depicted in **Fig 4.15(a)**, it is observed that all the dyes display two characteristic peaks, the first irreversible peak in the range 0.6-0.7 V is due the removal of electron from the amine unit, and the spacer unit and the second quasi-reversible peak, at about -1.6 to -1.7 V arises from the reduction of electron withdrawing anchoring group. As seen from **Table 4.8**, the experimental E_{ox} (HOMO) values of the dyes D_1 , D_2 and D_3 are 0.6, 0.64 and 0.7 V, respectively. Their E_{ox}^* (LUMO) values as calculated from equation **4.1** are -1.67 , -1.66 and -1.63 V, respectively.

$$E_{ox}^* = E_{ox} - E_{0-0} \quad (4.1)$$

where, E_{0-0} is the excited state energy of the dye, which is evaluated from the intersection between the normalized absorption and emission spectra.

Further, it is noted that the HOMO levels of dyes are sufficiently lower than the redox energy of I_3^-/I^- (0.4 V vs. NHE), thereby favouring the effective dye regeneration process. On the other hand, the calculated LUMO levels of dyes are higher than the CB of TiO_2 (-0.5 V vs. NHE); this facilitates the electron injection phenomenon. The schematic arrangement of HOMO and LUMO levels as well as calculated band gaps of the dyes D_{1-3} are given in **Fig 4.15(b)**. From the results, it is clear that, D_3 has attained the lowest E_{ox} and E_{ox}^* values, as a consequence of electron withdrawing nature of the barbituric acid. The presence of barbituric acid has lowered LUMO level of dye making it closer to CB of TiO_2 and has pushed the HOMO level close to electrolyte potential.

Additionally, the electrochemical band gaps of D_{1-3} were calculated using experimental E_{0-0} and they are found to be 2.31, 2.36 and 2.23 V, respectively. All the three dyes show a similar band gaps owing to their structural similarity.

To study more precisely about the feasibility of dye injection, recombination and regeneration processes, the thermodynamic driving forces ΔG_{inj} , ΔG_{rec} and ΔG_{reg} were calculated using the equations **4.2** to **4.4**.

$$\Delta G_{\text{inj}} = eE_{\text{ox}}^* - eE_{\text{CB}} \quad (4.2)$$

$$\Delta G_{\text{rec}} = eE_{\text{CB}} - eE_{\text{ox}} \quad (4.3)$$

$$\Delta G_{\text{reg}} = eE_{\text{I}_3/\text{I}^-} - eE_{\text{ox}} \quad (4.4)$$

where E_{CB} is the CB of TiO_2 (-0.5 V vs NHE) and $E_{\text{I}_3/\text{I}^-}$ is the redox potential of electrolyte (0.4 V vs NHE) (Black et al. 2017a; Borgström et al. 2005; Farré et al. 2017). All the calculated ΔG values are negative indicating aforementioned processes are thermodynamically favourable. As the values of ΔG_{inj} and ΔG_{rec} are very close to each other, the feasibility of losing energy through recombination process is high. The dye **D2** with $\Delta G_{\text{inj}} = -1.16$ eV and $\Delta G_{\text{rec}} = -1.2$ eV shows the predominance of injection process. Whereas **D3** is susceptible to lose energy by recombination process because of its higher ΔG_{rec} (-1.17 eV,) and ΔG_{inj} (-1.14 eV) values. Similarly, **D1** with ΔG_{rec} (-1.14 eV) and ΔG_{inj} (-1.1 eV) values follows the same trend. Further, the calculated ΔG_{reg} values for **D1-3** are -0.24 , -0.3 and -0.2 eV, respectively. From the results, it is clear that **D3** has more negative value of ΔG_{reg} showing its spontaneity for dye regeneration. Generally, the dye should have a sufficient driving force for its regeneration in order to prevent recombination between the photo-oxidized dye and injected electrons, thereby causing higher J_{sc} value.

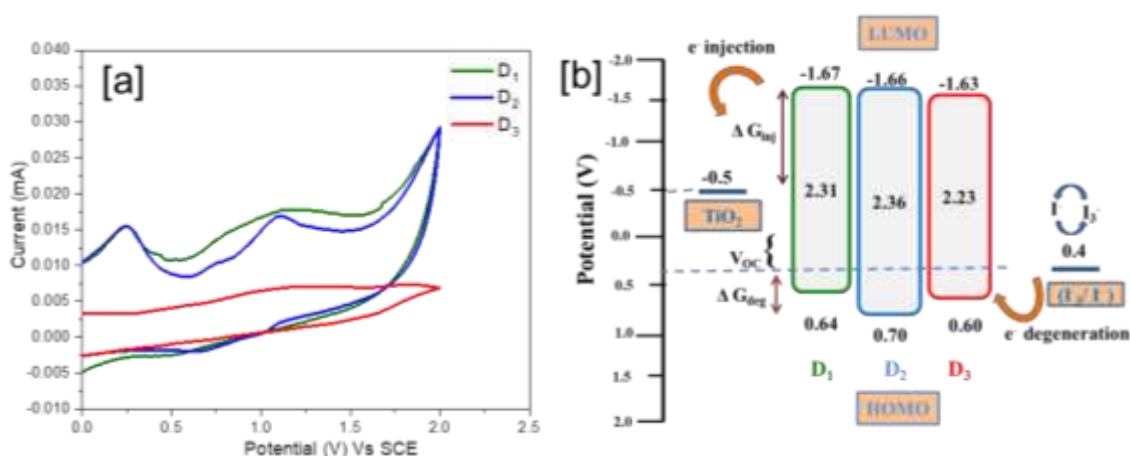


Fig 4.15 (a) Cyclic Voltammograms of **D1-3**; (b) Schematic representation of HOMO and LUMO levels as well as calculated band gaps of the dye.

Table 4.8 Electrochemical data of **D1-3**

Sensitizer/ co-sensitizers	E_{ox} (V vs. NHE)	E_{ox}^* (V vs. NHE)	ΔG_{inj} (eV)	ΔG_{rec} (eV)	ΔG_{reg} (eV)
D1	0.64	-1.67	-1.17	-1.14	-0.24
D2	0.70	-1.66	-1.16	-1.20	-0.30
D3	0.60	-1.63	-1.14	-1.10	-0.20

4.2.3.2 Electrochemical studies of chromophores **D4-7** (Series-2)

The dyes **D4-7** of **Series-2** were subjected to CV studies with a conventional three-electrode configuration system. The obtained voltammograms and the corresponding HOMO-LUMO levels along with the calculated band gaps of all the dyes are depicted in **Fig 4.16**. The generated electrochemical data are tabulated in **Table 4.9**. The experimental E_{ox} (HOMO) values of the dyes **D4-7** were found to be 0.82, 0.93, 1.04 and 1.01 V vs. NHE, respectively. The observed higher E_{ox} values of **D6** and **D7** can be attributed to the presence of higher electron withdrawing hydrazinylbenzoic acid and barbituric acid, respectively in their structures. Further, E_{ox}^* (LUMO) values of **D4-7** were calculated from equation 4.1 and the values obtained are -1.4, -1.17, -1.26 and -1.19 V vs. NHE, respectively. From the E_{ox} and E_{ox}^* values, it can be noted that, the HOMO levels of all the dyes are sufficiently lower than the redox potential of I_3^-/I^- (0.4 V vs. NHE), thereby favouring the dye regeneration process effectively. Furthermore, the calculated LUMO levels of dyes are quite higher than the CB of TiO_2 (-0.5V vs. NHE); this augments the proper electron injection phenomenon in them. The evaluated electrochemical band gaps of the dyes **D4-7** are in the range of 2.1 to 2.3V and their decreasing order is **D6**(2.3 V) > **D4**(2.22 V) > **D7**(2.2 V) > **D5**(2.1 V) (**Fig 4.16(b)**). It is noticed that structurally similar **D4-7** give almost same band gap values. Interestingly, the CV trace of **D4** has covered with more area when compared to other dyes indicating its more current generating capacity. From the thermodynamic driving forces (**Table 4.9**) as calculated from equations 4.2 to 4.4 for the dyes **D4-7**, it is clear that the injection, regeneration as

well as recombination processes are quite spontaneous, as the obtained values are negative. The calculated ΔG_{inj} values for dyes are in the order: **D4**(-0.90 eV) < **D6**(-0.76 eV) < **D7**(-0.69 eV) < **D5**(-0.67 eV). Further, the obtained ΔG_{rec} values are in the increasing order **D6**(-1.54 eV) < **D7**(-1.51 eV) < **D5**(-1.43 eV) < **D4**(-1.32 eV). On comparing ΔG_{inj} and ΔG_{rec} of all the dyes it can be concluded that, the driving force required for recombination process is higher than injection process, resulting in the increased feasibility of injection process.

Further, the ΔG_{reg} values obtained for dyes are **D4**(-0.42 eV), **D5**(-0.53 eV), **D6**(-0.64 eV) and **D7**(-0.61 eV). The observed data reveal that, the driving force is sufficient to prevent the recombination between photo-oxidized state and injected electrons, thereby causing higher J_{SC} value of the cell.

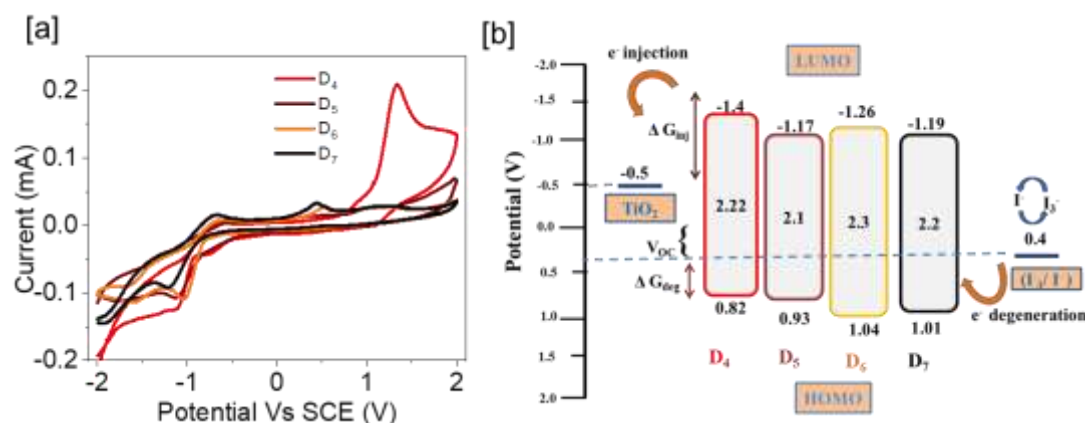


Fig 4.16 (a) Cyclic Voltammograms of **D4-7**; (b) Schematic representation of HOMO and LUMO levels as well as calculated band gaps of the dyes

Table 4.9 Electrochemical data of **D4-7**

Sensitizer/ co-sensitizers	E_{ox} (V vs. NHE)	E_{ox}^* (V vs. NHE)	ΔG_{inj} (eV)	ΔG_{rec} (eV)	ΔG_{reg} (eV)
D4	0.82	-1.40	-0.90	-1.32	-0.42
D5	0.93	-1.17	-0.67	-1.43	-0.53
D6	1.04	-1.26	-0.76	-1.54	-0.64
D7	1.01	-1.19	-0.69	-1.51	-0.61

4.2.3.3 Electrochemical studies of chromophores *D*₈₋₁₁ (Series-3)

The voltammograms along with schematic representation of HOMO and LUMO values of **D**₈₋₁₁ are given in **Fig 4.17**. The pertinent electrochemical data are summarized in **Table 4.10**. The experimental E_{ox} (HOMO) values of the dyes **D**₈₋₁₁ were found to be 0.83, 1.1, 0.59 and 0.50 V vs. NHE, respectively. From the observed E_{ox} values, it is evident that, the **D**₁₀ and **D**₁₁ with extended conjugation show very low E_{ox} values. Their E_{ox}^* (LUMO) values as calculated from equation 4.1 are -1.67, -1.17, -1.87 and -1.40 V vs. NHE, respectively. From the evaluated HOMO and LUMO levels, it is clear that, all the dyes are capable of facilitating proper electron injection to CB of TiO₂ and to regenerate the dye molecule. The electrochemical band gaps of the dyes were calculated to be in the range of 1.64 to 2.50V and they are in the decreasing order: **D**₈(2.50V) > **D**₁₀(2.46 V) > **D**₉ (2.27 V) > **D**₁₁(1.64 V). The lowest band gap value obtained for **D**₁₁ owes to its extended conjugation as well as the presence of barbituric acid in it. **Fig 4.17(b)** shows the schematic representation of HOMO and LUMO levels along with band gap values of dyes **D**₈₋₁₁.

All the the three different thermodynamic driving forces were calculated using the equations 4.2 to 4.4. As observed from the **Table 4.10**, the calculated ΔG_{inj} values for the dyes **D**₈₋₁₁ are -1.17, -0.67, -1.37 and -0.90 eV, whereas the values of ΔG_{rec} are -1.33, -1.60, -1.09 and -1.00 eV, respectively. From the ΔG_{inj} and ΔG_{rec} values it is evident that, **D**₁₀ shows larger ΔG_{inj} force signifying higher possibility of recombination process than other dyes in the series. This undesired behaviour of the dye can be a result of more aggregation because of extended structure and presence of cyanoacetic acid as anchoring group. Further, the ΔG_{reg} values obtained for dyes are in the decreasing order **D**₁₁(-0.10 eV) > **D**₈(-0.43 eV) > **D**₉(-0.70 eV) > **D**₁₀(-1.09 eV). Unlike in the previous series, the ΔG_{reg} values in this series are varying from -0.10 to -1.09 eV, the observed inference is due to the aggregation of the dye molecules having extended conjugation. However, the negative values of ΔG_{reg} signify the feasibility of the regeneration process in the dyes.

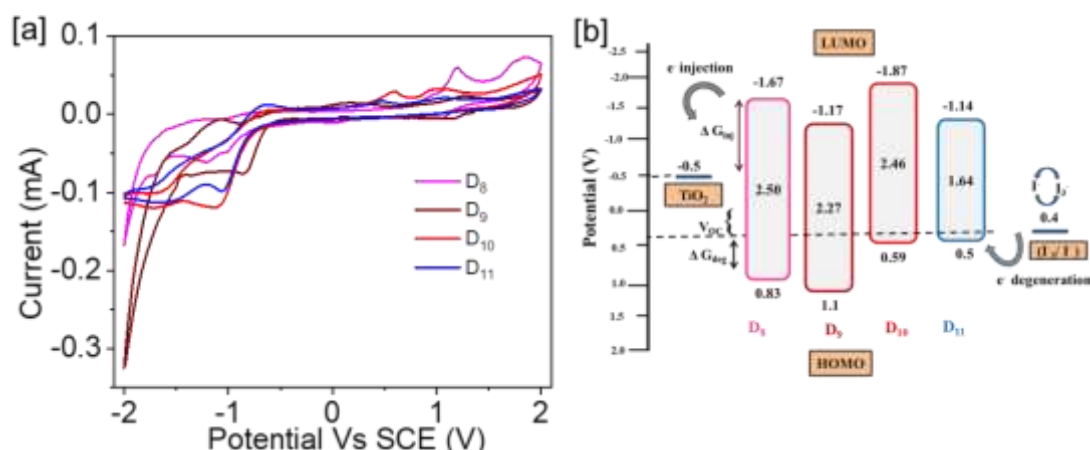


Fig 4.17 (a) Cyclic Voltammograms of **D8-11**; (b) Schematic representation of HOMO and LUMO levels as well as calculated band gaps of the dyes

Table 4.10 Electrochemical data of **D8-11**

Sensitizer/ co-sensitizers	E_{ox} (V vs. NHE)	E_{ox}^* (V vs. NHE)	ΔG_{inj} (eV)	ΔG_{rec} (eV)	ΔG_{reg} (eV)
D8	0.83	-1.67	-1.17	-1.33	-0.43
D9	1.10	-1.17	-0.67	-1.60	-0.70
D10	0.59	-1.87	-1.37	-1.09	-1.09
D11	0.50	-1.40	-0.90	-1.00	-0.10

4.2.3.4 Electrochemical studies of chromophores **D12-17** (Series-4)

Fig 4.18(a) shows the voltammograms of the chromophores **D12-17** and the corresponding electrochemical data are summarized in **Table 4.11**. From the CV traces of the dyes **D12-17**, the E_{ox} (HOMO) values obtained are 0.87, 0.83, 0.80, 0.90, 0.69 and 1.10 V vs. NHE, respectively. The dyes **D12-15** show more or less similar E_{ox} values, owing to their comparable structural features. The dye **D16** demonstrates very low E_{ox} value, due to the fact that, it possesses an extended conjugation through the spacer unit. Further, the E_{ox}^* (LUMO) values of the dyes were calculated using equation 4.1 and were found to be -1.53, -1.99, -1.66, -1.80, -1.66 and -1.28 V vs. NHE, respectively. The obtained HOMO and LUMO values are almost agreeing with

that of standard reported sensitizers in the literature. Furthermore, from the experimental HOMO and LUMO values of dyes, the electrochemical band gaps were determined. The obtained values are in the order of **D**₁₃(2.82 V) > **D**₁₅(2.70 V) > **D**₁₄(2.46 V) > **D**₁₂(2.40 V) > **D**₁₇(2.38 V) > **D**₁₆(2.35 V). The schematic presentation of above mentioned data is given in **Fig 4.18(b)**.

Additionally, the thermodynamic parameters leading to driving forces like ΔG_{inj} , ΔG_{rec} and ΔG_{reg} were calculated from the equations 4.2 to 4.4 to get an insight into the reaction kinetics. **Table 4.11** shows the calculated driving forces and it is found that, all the driving forces are negative demonstrating the thermodynamic feasibility of the processes. As seen from the table, ΔG_{inj} obtained for **D**₁₂₋₁₇ are -1.30, -1.49, -1.16, -1.30, -1.16 and -0.78 eV, respectively. Similarly, the calculated ΔG_{rec} values are -1.37, -1.33, -1.30, -1.40, -1.19 and -1.60 eV, respectively. From the ΔG_{inj} and ΔG_{rec} values, it can be inferred that, **D**₁₇ can have favourable injection process. All other dyes show higher ΔG_{inj} , demonstrating that they experience difficulty in injecting electrons to CB of TiO₂, thereby favouring recombination process. Yet, because of the smaller size, negative values of thermodynamic parameters and attractive photophysical behaviour, these dyes can function as good co-sensitizers along with metal based sensitizers. Convincingly, for all the dyes, the ΔG_{reg} values are sufficiently high to facilitate the regeneration process.

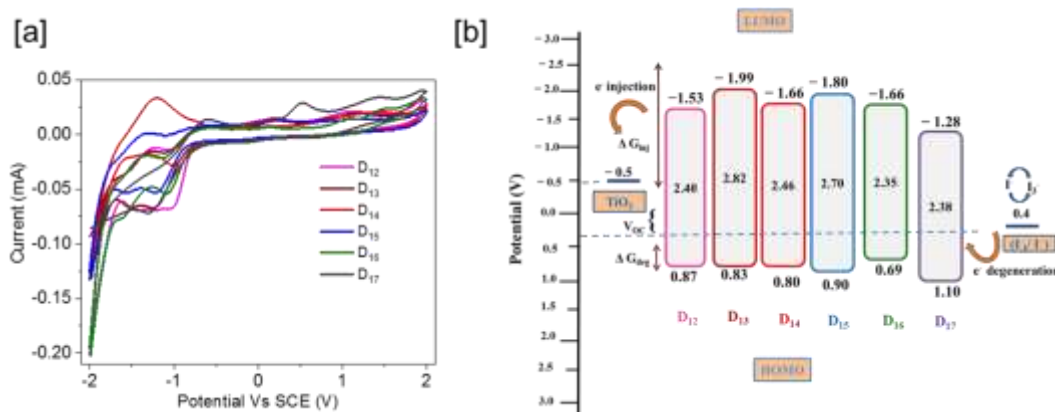


Fig 4.18 (a) Cyclic Voltammograms of **D**₁₂₋₁₇; (b) Schematic representation of HOMO and LUMO levels as well as calculated band gaps of the dyes

Table 4.11 Electrochemical data of **D12-17**

Sensitizer/ co-sensitizers	E_{ox} (V vs. NHE)	E_{ox}^* (V vs. NHE)	ΔG_{inj} (eV)	ΔG_{rec} (eV)	ΔG_{reg} (eV)
D12	0.87	-1.53	-1.30	-1.37	-0.47
D13	0.83	-1.99	-1.49	-1.33	-0.43
D14	0.80	-1.66	-1.16	-1.30	-0.40
D15	0.90	-1.80	-1.30	-1.40	-0.50
D16	0.69	-1.66	-1.16	-1.19	-0.29
D17	1.10	-1.28	-0.78	-1.60	-0.70

4.2.3.5 Electrochemical studies of chromophores **D18-21** (Series-5)

The voltammograms obtained for chromophores **D18-21** are depicted in **Fig 4.17(a)** and the corresponding electrochemical data are tabulated in **Table 4.12**. From the CV results, the E_{ox} (HOMO) values of the dyes **D18-21** are 0.90, 0.88, 1.29 and 1.27 V vs. NHE, respectively. Here, all the dyes demonstrate almost similar HOMO energies. It can be seen from the data that, the **D21** displays an intense oxidation peak unlike other dyes, this behaviour may be attributed to the presence of reactive benzo[d]thiazole core in its structure. From the E_{ox} values of dyes, the respective E_{ox}^* (LUMO) values were calculated using equation **4.1**. The obtained LUMO energy levels of **D18-21** are -1.85, -1.82, -1.80 and -1.45 V vs. NHE, respectively. Interestingly, the E_{ox} and E_{ox}^* values of all the dyes are in agreement with that of reported standard sensitizers. Further, the electrochemical band gaps of the dyes were calculated and they are found to be in the decreasing order: **D20**(3.09 V) > **D18**(2.75 V) > **D21**(2.72 V) > **D19**(2.70 V). These data are schematically represented in **Fig 4.17(b)**.

In addition, the driving forces such as ΔG_{inj} , ΔG_{rec} and ΔG_{reg} were evaluated from the equations **4.2** to **4.4** as before and the data are summarized in **Table 4.12**. The ΔG_{inj} obtained for **D18-21** are -1.35, -1.32, -1.31 and -0.95 eV, respectively and

the calculated ΔG_{rec} values are -1.40 , -1.38 , -1.79 and -1.77eV , respectively. The data indicate that, all the dyes of the series demonstrate feasibility of injection processes. Particularly, in **D**₂₁ the difference in ΔG_{inj} and ΔG_{rec} values is quite high, indicating the least possibility of recombination. Further, the ΔG_{reg} values are evaluated to throw light upon the regeneration process in the dyes. Their calculated values are **D**₁₈(-0.50 eV), **D**₁₉(-0.48 eV), **D**₂₀(-0.89 eV) and **D**₂₁(-0.87 eV). The observed ΔG_{reg} data indicate that the dyes possess ability to drive the regeneration process in the device.

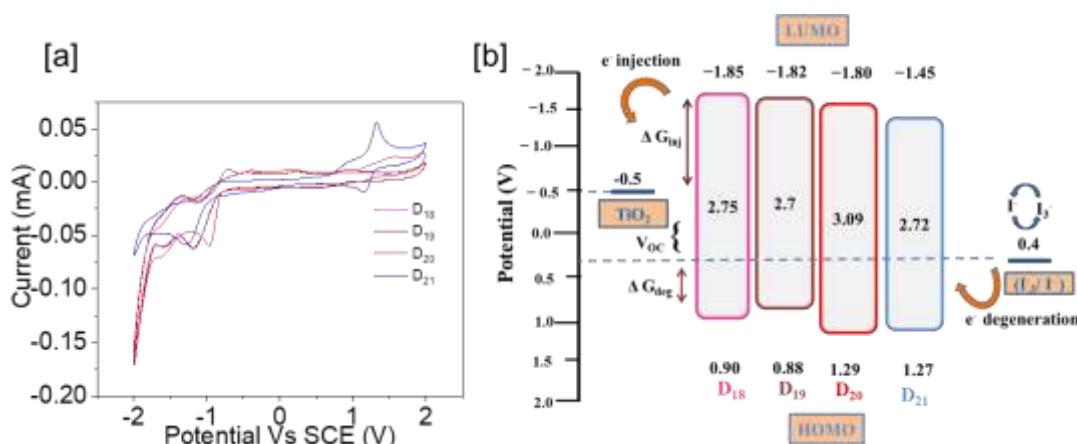


Fig 4.19 (a) Cyclic Voltammograms of **D**₁₈₋₂₁; (b) Schematic representation of HOMO and LUMO levels as well as calculated band gaps of the dyes

Table 4.12 Electrochemical data of **D**₁₈₋₂₁

Sensitizer/ co-sensitizers	E_{ox} (V vs.NHE)	E_{ox}^* (V vs.NHE)	ΔG_{inj} (eV)	ΔG_{rec} (eV)	ΔG_{reg} (eV)
D ₁₈	0.90	-1.85	-1.35	-1.40	-0.50
D ₁₉	0.88	-1.82	-1.32	-1.38	-0.48
D ₂₀	1.29	-1.80	-1.31	-1.79	-0.89
D ₂₁	1.27	-1.45	-0.95	-1.77	-0.87

4.2.3.6 Electrochemical studies of chromophores **D**₂₂₋₂₃ (Series-6)

Fig 4.20 depicts the voltammograms and schematic representation of HOMO-LUMO levels along with the calculated band gaps of dyes **D**₂₂₋₂₃. Their data are summarized in **Table 4.13**. The experimental E_{ox} (HOMO) values of the dyes **D**₂₂₋₂₃

were found to be 0.49V and 0.81V vs. NHE. From the CV plots, it can be conveyed that, **D**₂₂ is having a higher area than **D**₂₃ indicating the more favorable electrochemical behaviour than the latter. Further, the E_{ox}^* (LUMO) values as calculated from equation 4.1, are -1.96 and -1.49 V vs. NHE, respectively. Their HOMO and LUMO levels obtained are almost matching with that of the standard sensitizers. Their calculated electrochemical band gaps are 2.45 and 2.30 V, respectively.

Table 4.13 depicts the thermodynamic parameters ΔG_{inj} , ΔG_{rec} and ΔG_{reg} as calculated from the equations 4.2 to 4.4. The ΔG_{inj} obtained for **D**₂₂₋₂₃ are -1.46 and -0.99 eV and the calculated ΔG_{rec} values are -0.99 and -1.31 eV, respectively. From the results it is clear that, both the dyes have thermodynamic feasibility of injection processes. Further, the ΔG_{reg} values were calculated and the obtained values for **D**₂₂₋₂₃ are -0.09 and -0.81eV, respectively. The results indicate that, both the dyes possess satisfactory forces to drive the regeneration process in the device.

Table 4.13 Electrochemical data of **D**₂₂₋₂₃

Sensitizer/ co-sensitizers	E_{ox} (V vs. NHE)	E_{ox}^* (V vs.NHE)	ΔG_{inj} (eV)	ΔG_{rec} (eV)	ΔG_{reg} (eV)
D ₂₂	0.49	-1.96	-1.46	-0.99	-0.09
D ₂₃	0.81	-1.49	-0.99	-1.31	-0.81

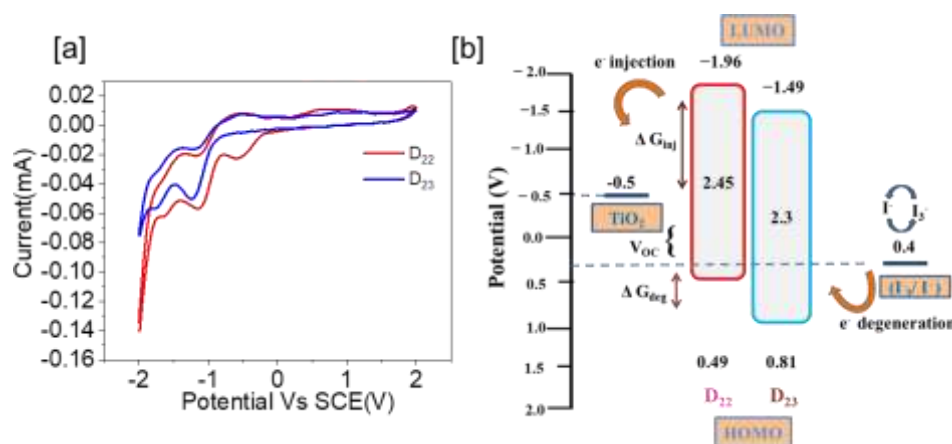


Fig 4.20 (a) Cyclic Voltammograms of **D**₂₂₋₂₃; (b) Schematic representation of HOMO and LUMO levels as well as calculated band gaps of the dyes

4.2.3.7 Electrochemical studies of chromophores D_{24-27} (Series-7)

Fig 4.21(a) displays the cyclic voltammetry plots of chromophores D_{24-27} and the corresponding data are given in **Table 4.14**. The E_{ox} (HOMO) data obtained for the dyes are 0.85, 1.07, 0.97 and 1.07 V vs. NHE, respectively, whereas E_{ox}^* (LUMO) values are -1.77 , -1.29 , -1.95 and -1.81 V vs. NHE, respectively. The redox potentials obtained are in agreement with that of standard sensitizers. Further, the calculated electrochemical band gaps of dyes are in the decreasing order: $D_{26}(2.92\text{ V}) > D_{27}(2.88\text{ V}) > D_{24}(2.62\text{ V}) > D_{25}(2.36\text{ V})$. Schematically, these parameters are shown in **Fig 4.21(b)**.

The thermodynamic parameters, *viz.* ΔG_{inj} , ΔG_{rec} and ΔG_{reg} as calculated from equation 4.2 to 4.4 are given **Table 4.14**. The ΔG_{inj} obtained for D_{24-27} are -1.27 , -0.79 , -1.45 and -1.31 eV, respectively. Also, their ΔG_{rec} values were calculated and the obtained data are -1.35 eV, -1.56 , -1.47 and -1.57 eV, respectively. Based on the results, it can be inferred that, all the dyes of the series can have feasibility towards injection processes. Further, their ΔG_{reg} values were also calculated and the obtained values are -0.45 , -0.66 , -0.57 and -0.67 eV, respectively. These values reveal that, the dyes would possess fairly good forces to drive the regeneration process in the device.

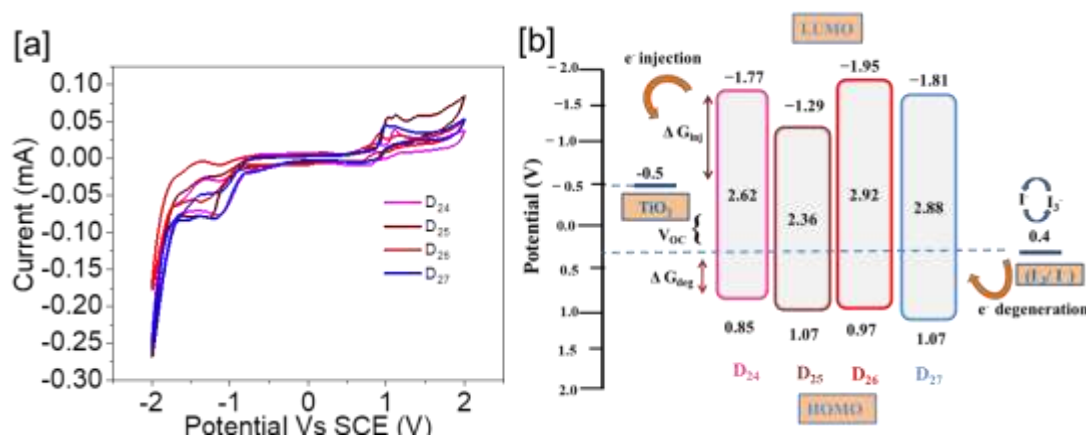


Fig 4.21 (a) Cyclic Voltammograms of D_{24-27} ; (b) Schematic representation of HOMO and LUMO levels as well as calculated band gaps of the dye

Table 4.14 Electrochemical data of **D24-27**

Sensitizer/ co-sensitizers	E_{ox} (V vs. NHE)	E_{ox}^* (V vs. NHE)	ΔG_{inj} (eV)	ΔG_{rec} (eV)	ΔG_{reg} (eV)
D24	0.85	-1.77	-1.27	-1.35	-0.45
D25	1.07	-1.29	-0.79	-1.56	-0.66
D26	0.97	-1.95	-1.45	-1.47	-0.57
D27	1.07	-1.81	-1.31	-1.57	-0.67

4.3 THEORETICAL INVESTIGATION

The development of DSSCs has been accompanied by computational studies that would help to rationalize the relationship between the molecular structure and device performance (Environ et al. 2011). In particular, electronic and optical absorption properties of several dyes, both isolated and adsorbed on the semiconductor (TiO_2) surfaces, were extensively studied using density-functional theory (DFT) and time-dependent DFT. The spectral data of unknown compounds can be generated using the computational data. Moreover, theoretical investigation of the physical properties of sensitizers is very important to disclose the relationship among the molecular geometry and the photovoltaic performance, it is also helpful in designing new dyes as photosensitizers for achieving enhanced photovoltaic performance.

The adiabatic quantum calculations with hybrid functional are considered to be one of the reliable computational methodologies in the field of organic photovoltaics, especially DSSCs to estimate the frontier molecular orbital (FMO) levels of potential *n*- and *p*-type sensitizers.

4.3.1 DFT/TD-DFT simulations

In the present study, the DFT simulations were carried out for isolate **D1-27** in order to evaluate their ground state properties in gas phase. However, the vertical excitation and their response in the excited dye molecules were computed using TD-DFT simulations. The electron delocalization in HOMO/LUMO levels, ESP maps and DOS of dyes were evaluated using Turbomole 7.2V software package. To begin with,

dye's molecular geometry was first optimized using semi-empirical Austin Model 1 (AM1) in 3D molecular builder of T-Mole 4.2. All the DFT simulations were carried out at B3LYP (Becke's three-parameter hybrid functional and Lee-Yang-Parr's gradient-corrected correlation functional) using def TZVPP level (Becke 1993; Peach et al. 2008). Also TD-DFT calculations were performed for all the dyes at B3LYP using def TZVP level to generate optical absorption spectra for few selected dyes (**D24-27**). Computational studies were also carried out for a dye in order to study its binding behaviour on the surface of TiO₂ through anchoring group.

In order to understand the adsorption as well as charge transfer mechanism in the presence of a supporting substrate, the representative example of **D4** was taken and calculations were performed using Vienna Ab initio Simulation Package (VASP) (Kresse and Hafner 1993a). To compute the exchange correlation functional the generalized gradient approximation (GGA) of Perdew-Burke-Ernzerhof (PBE) was used (Perdew et al. 1996). For geometry optimization we adopted an energy cut off of 450 eV. The sampling over the Brillouin zone was done using a gamma centered K mesh of size 5x5x1. The partial occupancy near the Fermi level was treated using a Gaussian smearing scheme (De Vita 1992). An optimized bulk anatase TiO₂ was cleaved along (101) surface and made a super-cell of size 2x2x1. A vacuum separation of 15 Å was provided perpendicular to the surface to eliminate the unphysical periodic image interactions. The van der Waals (vdW) interaction between the **D4** and TiO₂-(101) surface was modelled using the scheme of A. Tkatchenko *et al.* (2012), popularly known as TS-method.

4.3.2 Results and discussion

Figs 4.22 to 4.35 portray the electron cloud delocalization in FMO levels and ESP maps of all the dyes **D1-27**, as obtained from DFT simulation studies. The generated absorption spectra of last series of dyes are depicted in **Figs 4.35** and **4.36**.

4.3.2.1 Theoretical studies of dyes **D1-3** (Series-1)

The optimized geometries and electron density distributions in the HOMOs and LUMOs of **D1-3** are summarized in **Fig 4.22**. The 3-D vision of the molecules shows the clear charge delocalization in ground and excited states, thereby indicating

the effectiveness of ICT. As supported from their HOMO energy levels, the electron density is predominantly delocalized on the diphenylamine ring and the vinyl thiophene system of the dyes. However, at their LUMO levels, the electron cloud is clearly shifted from the electron donor to the electron acceptor units (4-aminobenzoic acid, 2-(4-nitrophenyl)acetonitrile and barbituric acid) to different extent because of their varied electron withdrawing nature. In case of **D**₃ the electron density is concentrated on the spacer unit and the anchoring moiety. Thus, it can be concluded that, all the three dyes show a close proximity of their LUMO levels to the anchoring group facilitating the electronic coupling between the electron cloud at the LUMO level of the dye and the *d* orbitals of TiO₂. The HOMO levels obtained for dyes **D**₁₋₃ are -5.3, -5.2 and -5.5 eV, respectively, which are sufficiently lower than the electrode potential of redox couple, *i.e.* -4.8 eV facilitating the regeneration process. Likewise, obtained LUMO levels of **D**₁₋₃ are -2.6, -3.1 and -3.0 eV, respectively, clearly showing that, electron injection is highly facilitated as the values are higher than the CB of TiO₂, *i.e.* -4.0 eV. The calculated band gaps of dyes are in the order **D**₁(2.7 eV) > **D**₃(2.5 eV) > **D**₂(2.1 eV).

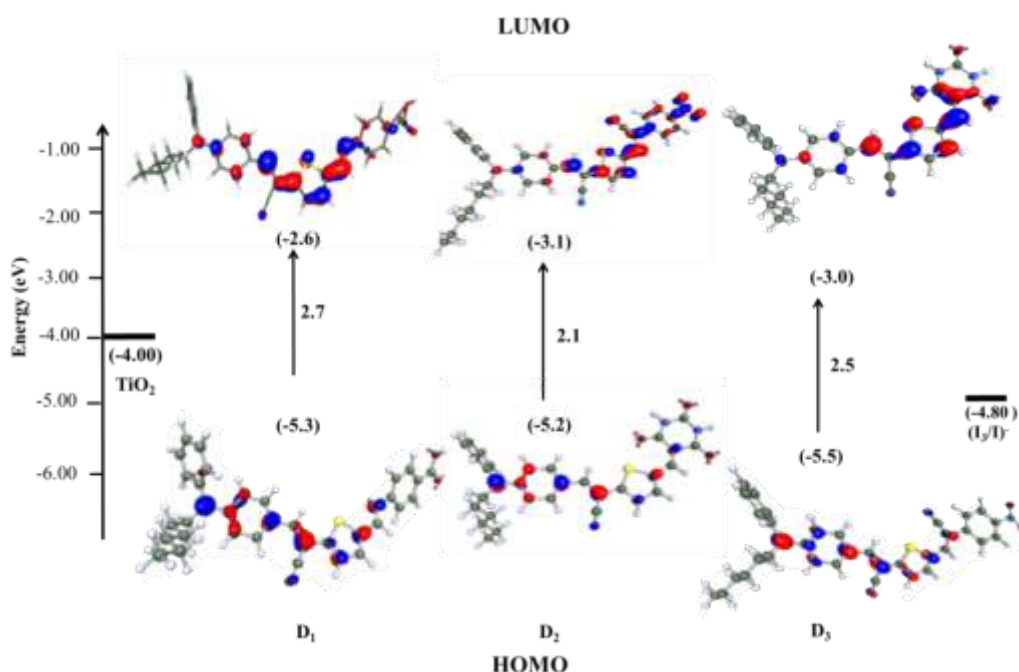


Fig 4.22 HOMO and LUMO levels of dyes **D**₁₋₃

Fig 4.23 depicts the ESP maps of **D₁₋₃** on the iso-surface. Generally, ESP maps give the distribution of total charge of a molecule at a point in space around the molecule which produces net electrostatic effect. Further, ESP involves the total charge distribution possessing dipole moments, partial charges, electronegativity and site of chemical reactivity of a molecule. The varying electrostatic potential values at surface are represented by different colors, and the potential increases in the order blue > green > yellow > orange > red. As shown in ESP maps of the dyes, electron density is concentrated on both CN and the anchoring groups. In **D₁** and **D₃**, it can be seen that the electron density is concentrated on the carbonyl group of anchoring unit. While in case of **D₂**, a clear electron density concentration of nitro group is observed. An obvious shift of the electron density from electro positive donor to electro negative conjugation spacer and then to anchoring group is noted. The ESP maps of the dyes suggest that, the electron distribution is favourable for the electron transfer from the donor to the anchoring units.

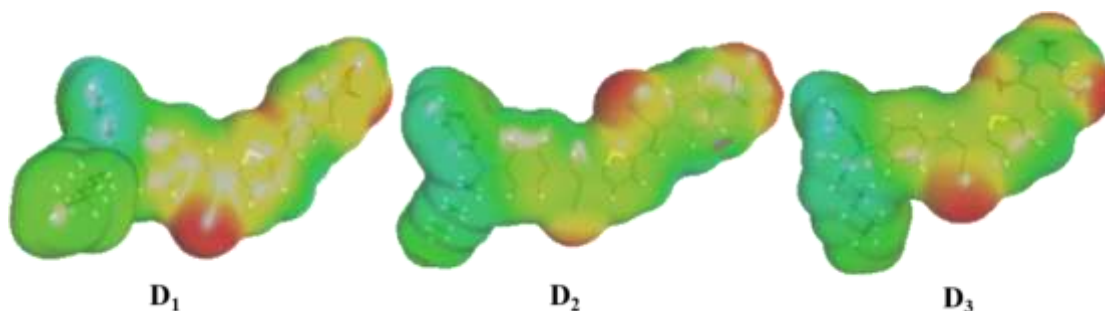


Fig 4.23 Molecular Electrostatic Potential (ESP) maps on the iso-surface of **D₁₋₃**

4.3.2.2 Theoretical studies of dyes **D₄₋₇** (Series-2)

Fig 4.24 gives the HOMO and LUMO levels obtained for dyes **D₄₋₇** of **Series-2**. It is observed that, for all the dyes, the HOMOs are mainly spread over the diphenylamine unit and the π -spacer, 2-(thiophene-2-yl)-acetonitrile moiety in the right wing and it is also spread over the double bond in the left wing. However, their corresponding LUMOs have largely concentrated on the 2-(thiophene-2-yl)-acetonitrile as well as anchoring groups (cyanoacetic acid, rhodanine acetic acid, 4-hydrazinylbenzoic acid and barbituric acid) in the right wing. It is evident that, the extent of electron distribution in the right and left wings are different, which may be

due to the absence of the π -spacer motif in the left wing that has restricted the electron flow to the anchoring group.

From the **Fig 4.24**, it can be noted that, there appears high concentration of electron cloud on the cyanoacetic acid unit in LUMO level of **D4**, whereas the electron cloud is dense mainly on the 2-(thiophene-2-yl)-acetonitrile and rhodanine acetic acid unit in LUMO of **D5**. In case of **D5**, presence of methylene group in the rhodanine acid unit might have interrupted the electron flow to the acid unit and it can further affect the injection of electrons to the TiO₂ surface. Similarly, the electron flow is confined to the thiophene unit and slightly on the anchoring unit (4-hydrazinyl benzoic acid) in **D6**. Interestingly, in **D7** the electron density is high on the 2-(thiophene-2-yl)-acetonitrile unit as well as the anchoring moiety. The HOMO levels obtained for dyes, in the order **D6**(-5.3 eV) > **D5**(-5.9 eV) > **D7**(-5.99 eV) > **D4**(-6.1eV) are significantly lower than the electrode potential of redox couple, *i.e.* -4.8 eV facilitating the effective regeneration process. The obtained LUMO levels of the dyes are **D6**(-2.6 eV) > **D7**(-3.4 eV) > **D4**(-3.5 eV) > **D5**(-3.6 eV) sufficiently higher than the CB (-4.00 eV) of TiO₂. Further, the values of band gap obtained for **D4**, **D6** and **D7** are almost same, that is in the range of 2.6 to 2.7eV, whereas **D5** shows a lower band gap of 2.3 eV. Consequently, it contributes towards enhanced efficiency of the device as the lower band gap leads to wider and stronger absorption region. From the observed data it can be concluded that, all the four dyes have a close proximity of their LUMO levels to the anchoring group, which facilitates the interaction between the electron cloud at the LUMO level of the dye and TiO₂ surface.

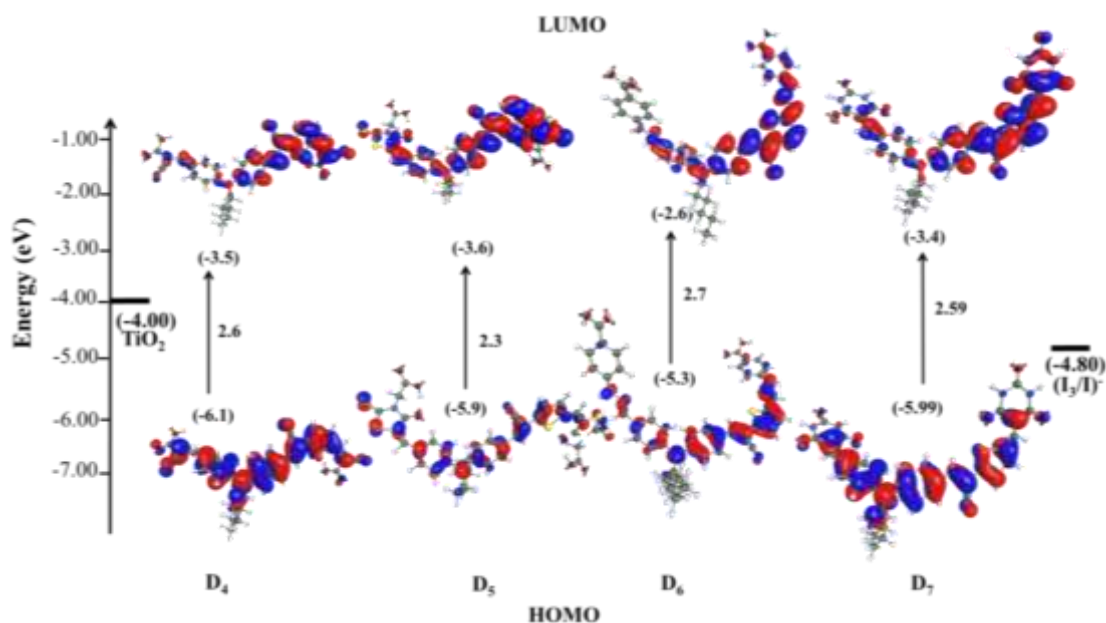


Fig 4.24 HOMO and LUMO levels of dyes **D4-7**

Further, theoretical studies were also carried out in order to assess the binding property of **D4** on the surface of TiO_2 . It is well-known that, one of the stringent characteristics of a sensitizer is the interaction of the anchoring group with TiO_2 so as to provide a strong adsorption on the TiO_2 surface. Generally, the anchoring group promotes the electronic coupling between the donor levels of the excited dye and the delocalized acceptor levels of the TiO_2 , and mediates the electron injection. The widely used anchoring fragment is cyanoacetic acid because it possesses a strong electron withdrawing functional groups, *viz.* CN and COOH. Therefore, **D4** was selected for our computational studies to evaluate its binding property with the TiO_2 cluster.

The assumption that the oxygen in cyanoacetic acid group of **D4** would interact with the unsaturated Ti_{5c} of TiO_2 anatase (101) surface through the lone-pair of electrons, has helped us to estimate the possible adsorption mode by using computational studies. In fact, the mode of adsorption can be determined by the direction of the lone-pair of electrons. In the present simulation study, the bidentate bridging approach has been selected as it is shown to be the most stable adsorption mode for the carboxylic acid anchoring group (Katono et al. 2011a; Prajongtatt et al. 2017; Zhang et al. 2018a). **Fig 4.25** depicts the resulting HOMO and LUMO

geometries of dye-anatase TiO₂ (101) adducts. Typically, the electron transfer from the dye to the TiO₂ depends on the relative symmetry, orientation of the orbitals and electron density localized on the binding atoms. This possibly affects the rate and effectiveness of recombination process. In **Fig 4.25**, the yellowish region depicts the electron rich area whereas the bluish area corresponds to the electron deficit region. The careful observation of the HOMO level of the adduct shows that, the anchored oxygen has electron deficit (blue colour) whereas the linked Ti atom has electron rich (yellow) surroundings, indicating that, the electron transfer takes place from Ti atoms to the dye. In contrast, the LUMO level shows an electron deficit region on Ti atoms, confirming the electron transfer from the dye to the TiO₂ surface. It can also be noticed that, the donor system (hole localized on the dye) was found to be quite away from the TiO₂ surface. This clearly indicates substantial reduction in recombination rates.

Fig 4.26 depicts the ESP maps of **D4-7** on the iso-surface. As described earlier, the obtained ESP maps display the distribution of total charge density of the dye molecule at any point in space around the molecule which produces net electrostatic effect. The colours in the ESP mappings correspond to various electrostatic potentials. The order of potential increases with blue > green > yellow > orange > red. From **Fig 4.26** it is evident that, the electron density is focussed particularly on both nitrile and the anchoring groups. In **D4**, **D5** and **D6**, it can be seen that the electron density is high on the carboxyl group as well as the cyano group, while in case of **D7** electron density concentrates on the carbonyl group of barbituric acid. Conclusively, the ESP maps suggest that, the shift of the electron density is from donor moiety to conjugation spacer, further moving to anchoring group, thereby favouring the electron movement in entire molecule.

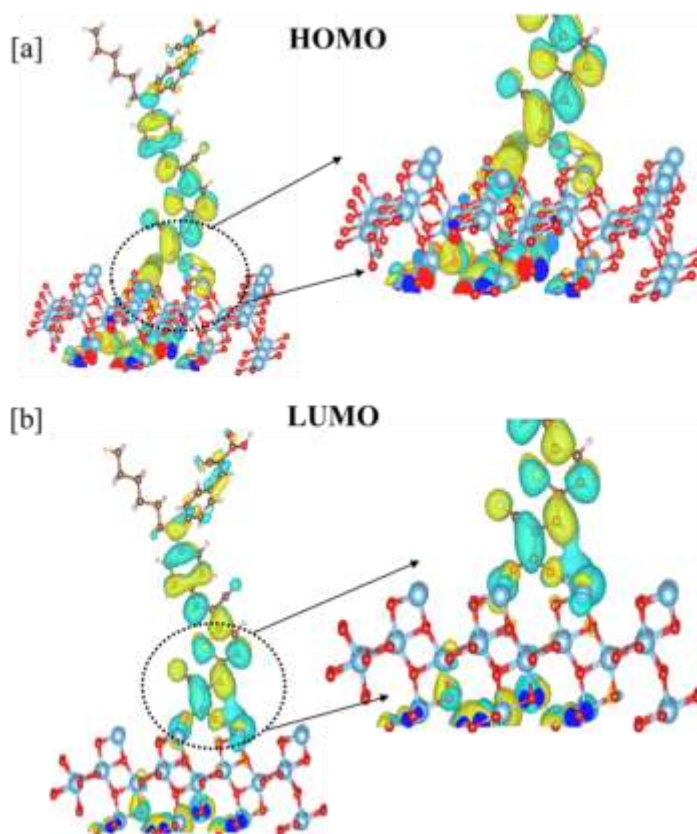


Fig 4.25 (a) HOMO and (b) LUMO levels of dye-TiO₂ (101) adduct

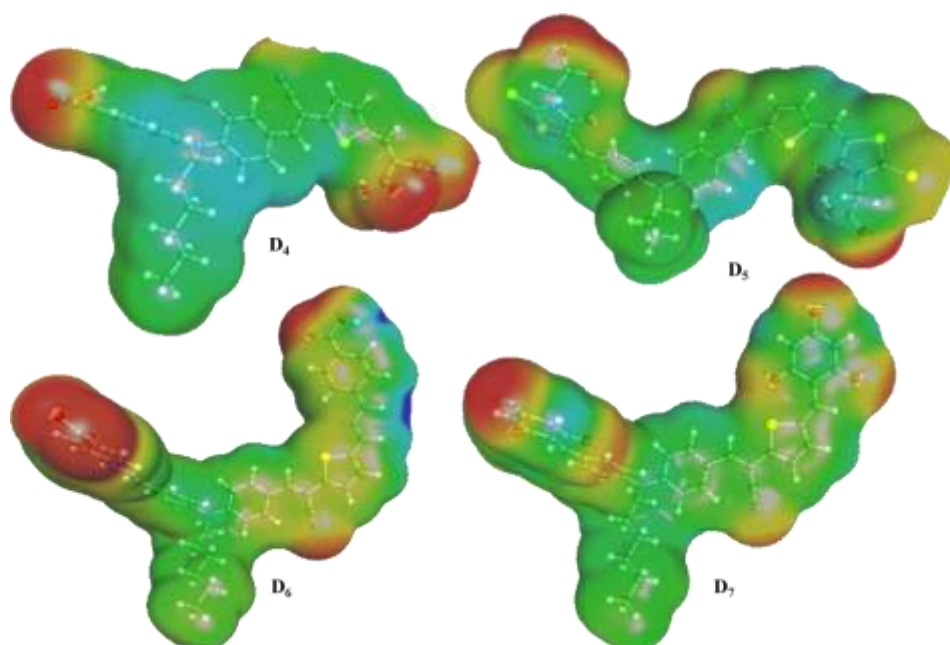


Fig 4.26 Molecular Electrostatic Potential (ESP) maps on the iso-surface of **D4-7**

4.3.2.3 Theoretical studies of dyes **D₈₋₁₁** (Series-3)

The electron density distributions in HOMO and LUMO energy levels of **D₈₋₁₁** visualized using T-mole visualizer are displayed in **Fig 4.27**. From the diagrams it is evident that, the HOMO level is more concentrated with electron density on the diphenyl amine donor, whereas LUMO level on the spacer units ((2-(4-formylphenyl)acetonitrile/2-(thiophene-2-yl)acetonitrile) and anchoring units (cyanoacetic acid/barbituric acid). More precisely, in the HOMO level of **D₈** molecule, electron cloud is observed on the diphenyl amine moiety and slightly on spacer units, whereas in LUMO level the electron cloud is on ((2-(4-formylphenyl)acetonitrile and anchoring cyanoacetic acid unit. The small size of cyanoacetic acid helps to transfer electron from the spacer unit to TiO₂ surface effectively. Analogously, in LUMO level of **D₉** dye, electrons are not found in the vicinity of NH group of barbituric acid (anchoring unit) which can reduce the flow of electrons to semiconductor surface. In continuation, **D₁₀** and **D₁₁** bearing extended conjugation units show similar electron shift in the HOMO and LUMO levels as discussed earlier. But it is noted that, the extended conjugation of **D₁₀₋₁₁** has complimented to the ICT transfer as the distance from donor system to anchoring unit is more than that of **D₈₋₉**. As discussed in case of **D₉**, the dye **D₁₁** bearing barbituric acid also shows distraction of electron flow from the spacer units to the TiO₂ surface. The HOMO levels obtained for dyes, in the order **D₉**(-5.20 eV) > **D₈**(-5.30 eV) > **D₁₀**(-5.50 eV) > **D₁₁**(-5.58 eV) are significantly lower than the electrode potential of redox couple (-4.8 eV), thereby facilitating the effective regeneration process. The obtained LUMO levels of the dyes are **D₈**(-2.60 eV) > **D₁₀**(-3.0 eV) > **D₉**(-3.1eV) > **D₁₁**(-3.36 eV) sufficiently higher than the CB (-4.00 eV) of TiO₂. Further, the values of band gap obtained for **D₈₋₁₁** are 2.7, 2.1, 2.5 and 2.22 eV, respectively.

ESP maps on the iso-surface of **D₈₋₁₁** are displayed in **Fig 4.28**. From the figure, it is clear that the electron cloud is concentrated in C≡N and C=O groups of dyes. Here, the donor system is less concentrated with electron cloud. Thus, the ESP maps of the dyes suggest that, the shift of the electron density is from donor moiety to conjugation spacer, further moving to anchoring group, thereby favouring the electron movement in the entire molecule of it.

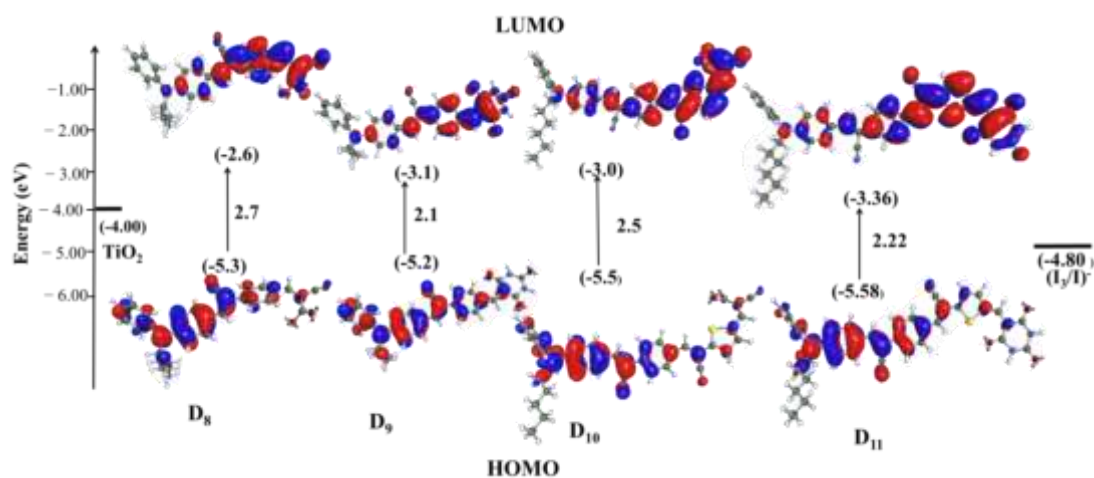


Fig 4.27 HOMO and LUMO levels of dyes **D8-11**

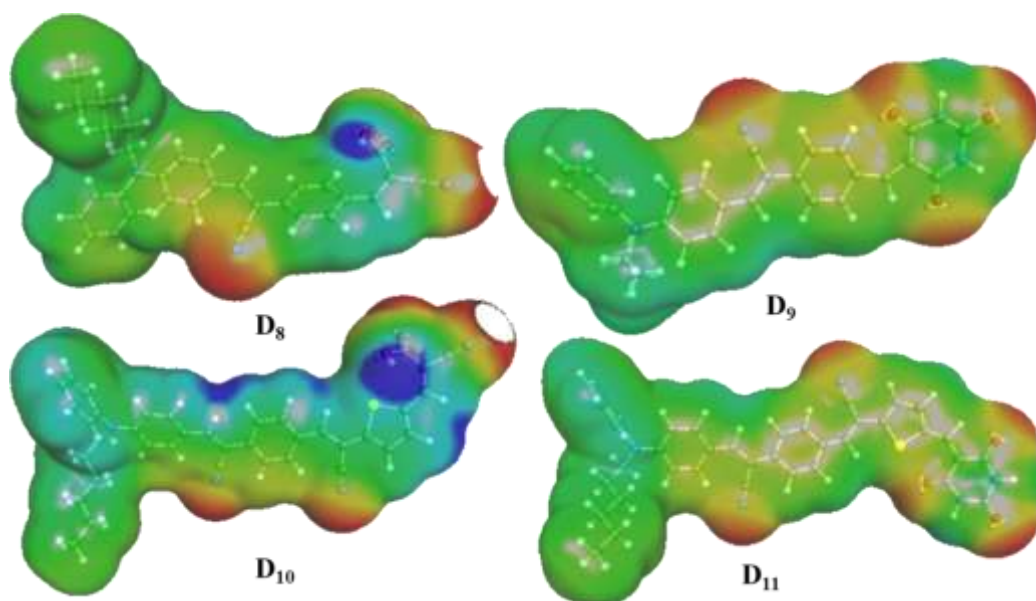


Fig 4.28 Molecular Electrostatic Potential (ESP) maps on iso density of **D8-11**

4.3.2.4 Theoretical studies of dyes **D12-17** (Series-4)

Fig 4.29 shows the distribution of electron in HOMO and LUMO levels of **D12-17**. For all the dyes the HOMOs are mainly spread over the diphenylamine unit and some in spacer unit, as seen in other series. The extent of electron distribution in LUMO levels observed is different for dyes **D12-17**. The last four dyes **D14-17** show a clear shift of electron cloud from HOMO to LUMO level because of extended conjugation, thereby showing ICT phenomenon. In contrary, **D12** and **D13** bearing nitrobenzene, nitrofuran respectively, did not show any ICT behaviour owing to their

small size. In these two molecules, electron distribution in LUMO level is observed on anchoring units as well as on one phenyl ring of diphenyl amine. Even though **D15** is a small molecule, it can manage to display some extent of ICT, because of its favourable structural features. The calculated HOMO levels obtained for dyes are in the order **D14**(-5.33 eV) > **D15**(-5.41 eV) > **D17**(-5.43 eV) > **D13**(-5.49 eV) > **D12**(-5.56 eV) > **D16**(-5.62 eV), whereas the LUMO levels are **D15**(-2.32 eV) > **D17**(-2.52 eV) > **D14**(-2.78 eV) > **D13**(-2.81 eV) > **D12**(-2.87 eV) > **D16**(-3.09 eV). From the HOMO and LUMO energy values the band gaps of **D12-17** were found to be 2.87, 2.68, 2.55, 3.09, 2.53 and 2.92 eV, respectively.

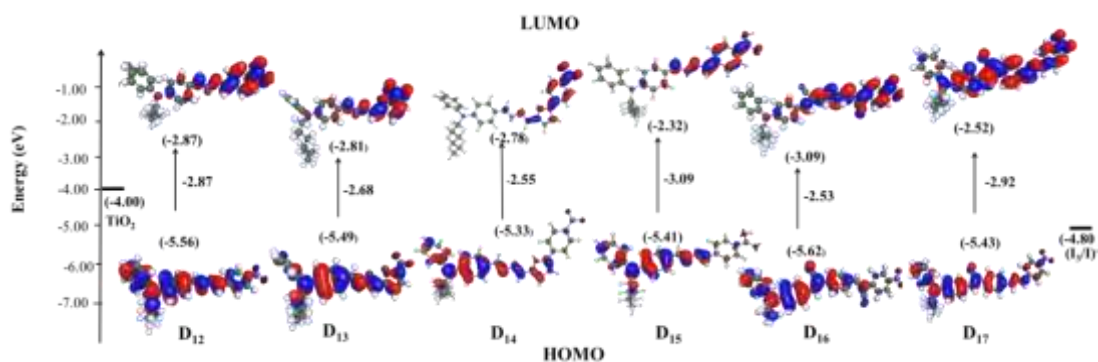


Fig 4.29 HOMO and LUMO levels of dyes **D12-17**

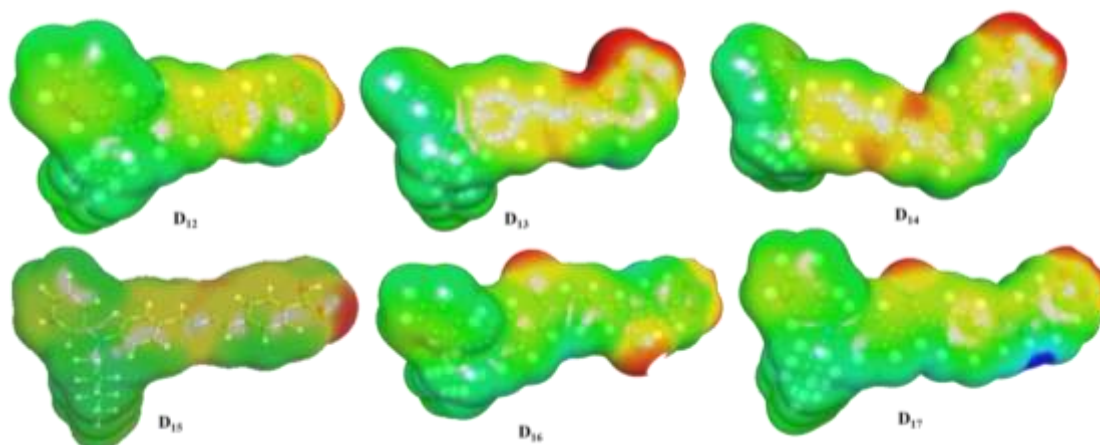


Fig 4.30 Molecular Electrostatic Potential (ESP) maps on the iso density of **D12-17**

ESP maps on the iso-surface of **D12-17** are depicted in **Fig 4.30**. From the figure it is clear that the electron cloud is concentrated on $C\equiv N$, $C=O$ and nitro groups of dyes. In **D12**, electron cloud is observed near nitro group only, whereas in **D13**, the electron density extended to oxygen atom of furan ring also. In this case, a feeble

electron richness is observed near nitrogen atoms of imine bond. In **D14**, electron density observed near imine bond is more than **D13**. Here, **D15** shows negative charge observed solely near C=O group of COOH functionality. The last two dyes **D16-17** containing phenyl acetonitrile derivative as spacer unit show richness of electron near C≡N and C=O groups. Thus, the ESP maps clearly indicate the shifting of electron from electro positive donor moiety to slightly electron rich conjugation spacer and finally to electron rich anchoring group.

4.3.2.5 Theoretical studies of dyes **D18-21** (Series-5)

HOMO and LUMO distributions of the dyes **D18-21** have been given in **Fig 4.31**. Similar to earlier discussions, in these D-D-A configured dyes **D18-21** electron cloud has spread over the auxiliary donor (5-amino-2,4-di-*tert*-butylphenol/3,5-bis(dodecyloxy)aniline /pyren-1-amine/benzo[d]thiazol-2-amine) as well as donor diphenylamine unit in HOMO levels. It is noteworthy that, electron cloud is concentrated more on the auxiliary donor motifs than principal donor moiety. In LUMO state, the cluster of electrons has shifted to the anchoring cyanoacetic acid unit. Further, because of the absence of spacer units, the electron cloud in LUMO level is seen to be extended to one phenyl ring of diphenylamine moiety. It is interesting to note that, in **D19** the electron cloud has concentrated much on cyanoacetic acid unit. This has led to the easy injection of electrons into the CB of TiO₂. Among the dyes, **D21** shows poor ICT owing to the presence of benzothiazole derivative as an additional donor unit.

The HOMO levels obtained for the dyes **D18-21** are in the order **D20**(-5.40 eV) > **D18**(-5.61eV) > **D19**(-5.65 eV) > **D21**(-5.99 eV). These values indicate that, the dyes regenerate efficiently in the devices. Likewise, the LUMO levels of the dyes are **D20** (-2.65 eV) > **D19**(-2.70 eV) > **D18**(-2.72 eV) > **D21**(-2.90 eV) and these value are sufficiently higher to inject the electron to CB of TiO₂. Further, the values of band gap obtained for **D18-21** are 2.89, 2.95, 2.76 and 3.09 eV, respectively.

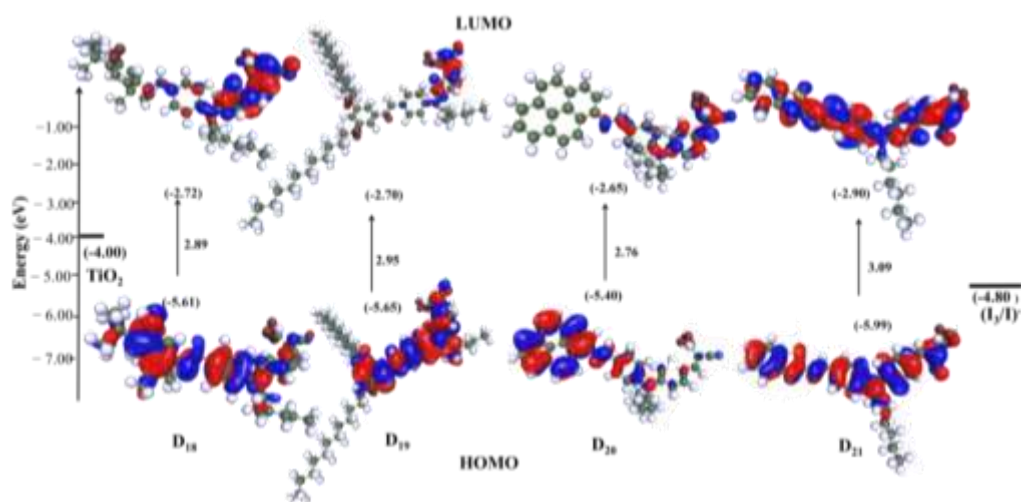


Fig 4.31 HOMO and LUMO levels of dyes **D18-21**

ESP maps on the iso-surface of **D18-21** are depicted in **Fig 4.32**. Here, based on the electronic nature of auxiliary donor units, the electron cloud has distributed differently. In **D18** an electron rich red shade is seen on OH functionality of di-*tert*-butylphenol unit, whereas in **D19** yellow shade is observed on 3,5-bis(dodecyloxy) auxiliary donor unit indicating its less electron negative nature compared to former. But, in case of **D20** bearing pyrene ring the yellow colour is seen on pyrene unit, while in case of **D21** carrying benzothiazol unit intense yellow colour as well as red shade is observed near ring *N* atom. From the results, it is evident that, the electron density is shifting from electron rich additional donor unit to anchoring unit through diphenyl amine moiety.

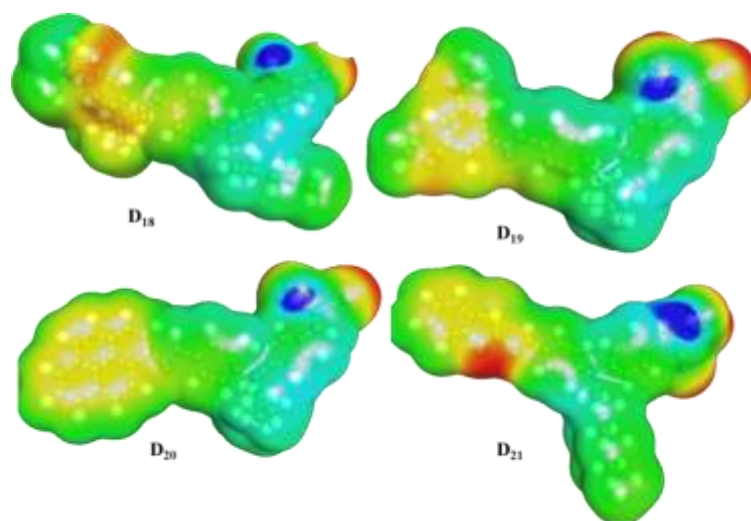


Fig 4.32 Molecular Electrostatic Potential (ESP) maps on the iso density of **D18-21**

4.3.2.6 Theoretical studies of dyes D_{22-23} (Series-6)

The HOMO and LUMO levels of dyes D_{22-23} are shown in **Fig 4.33**. In these new A-D- π -D-A type dyes, the distribution of electrons at HOMO and LUMO levels are in a different fashion compared to the dyes discussed in earlier sections. In spite of the symmetric architecture, the electron distributions in such molecules are not uniform in both HOMO and LUMO levels. The electron shifting is more towards the right wing than the left wing. In dyes D_{22} and D_{23} , HOMO levels are concentrated more on (1,4-phenylene)diacetonitrile unit and donor diphenylamine of the right wing. While in LUMO levels, the electron density has shifted more towards anchoring cyanoacetic acid/rhodanine acetic acid unit. In D_{23} it is also noted that, the methylene group of rhodanine acetic acid group is hindering the flow of electron from rhodanine ring to carboxylic group. The observed HOMO levels of D_{22-23} are -5.53 and -5.82 eV respectively, whereas LUMO values are -2.73 and -3.24 eV respectively. Finally, the values of band gap obtained for D_{22-23} are 2.79 and 2.58 eV, respectively. ESP maps on the iso-surface of D_{22-23} are displayed in **Fig 4.34**. As expected, in both dyes, the electron cloud is seen near the electronegative $C\equiv N$ and $C=O$ functionalities.

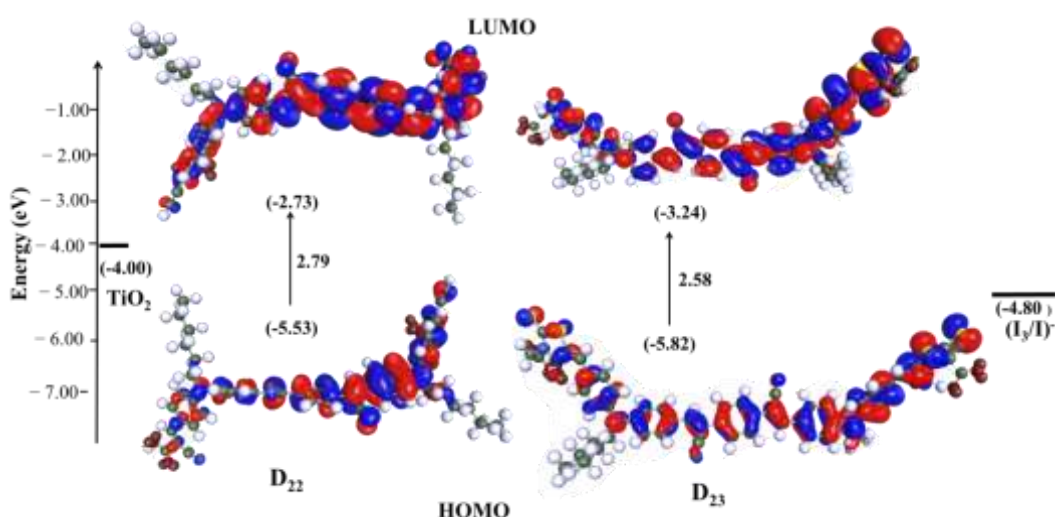


Fig 4.33 HOMO/LUMO levels of dyes D_{22-23}

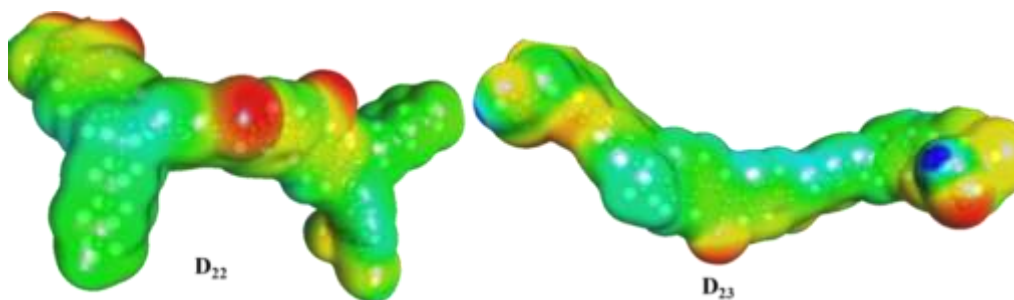


Fig 4.34 Molecular Electrostatic Potential (ESP) maps on the iso density of **D22-23**

4.3.2.7 Theoretical studies of dyes **D24-27** (Series-7)

Fig 4.35 depicts the distribution of electron in HOMO and LUMO levels of dyes **D24-27**. As seen from the figure, in the HOMO level electron density is concentrated on the diphenylamine unit, whereas in LUMO level it is much concentrated on the anchoring units *viz.* cyanoacetic acid, rhodanine acetic acid, hydrazine benzoic acid and maleimide. Here, the electron density on the anchoring unit varies with its electronic structure. The observed HOMO levels of the dyes are **D26**(-5.19 eV) > **D27**(-5.51 eV) > **D25**(-5.67 eV) > **D24**(-5.91 eV) and the observed LUMO levels are **D26**(-1.69 eV) > **D27**(-1.96 eV) > **D24**(-2.47 eV) > **D25**(-2.78 eV). The calculated band gaps for **D24-27** were found to be 3.44, 2.89, 3.51 and 3.56 eV, respectively.

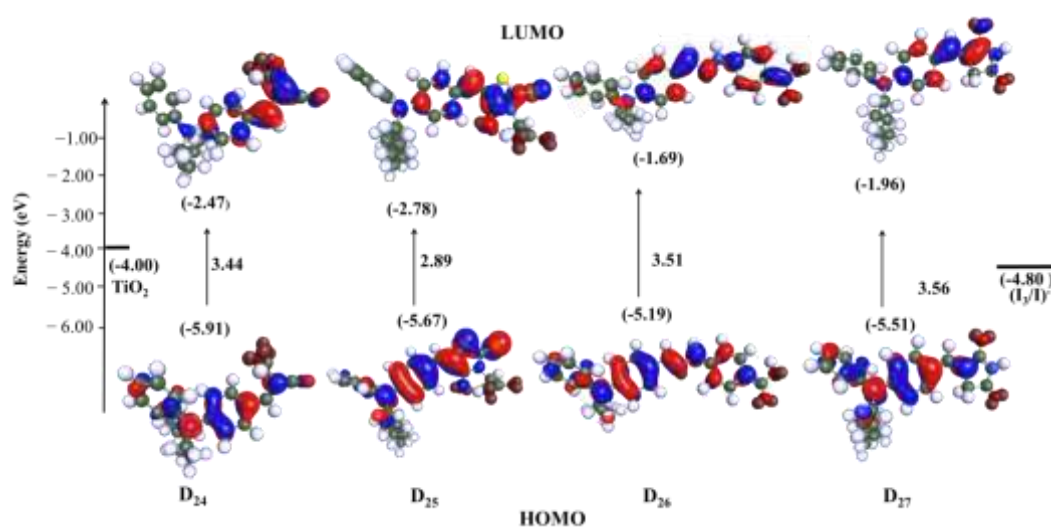


Fig 4.35 HOMO/LUMO levels of dyes **D24-27**

Fig 4.36 shows the ESP of **D**₂₄₋₂₇. From the figures it is clear that, the electron rich red region is around the C≡N and C=O groups in case of all the dyes, as observed in previous chromogens. However, in **D**₂₅ electron cloud is also seen at the vicinity of C=S of rhodanine acetic acid. Thus, it is evident that, the electron density is moving from donor moiety to the anchoring unit effectively.

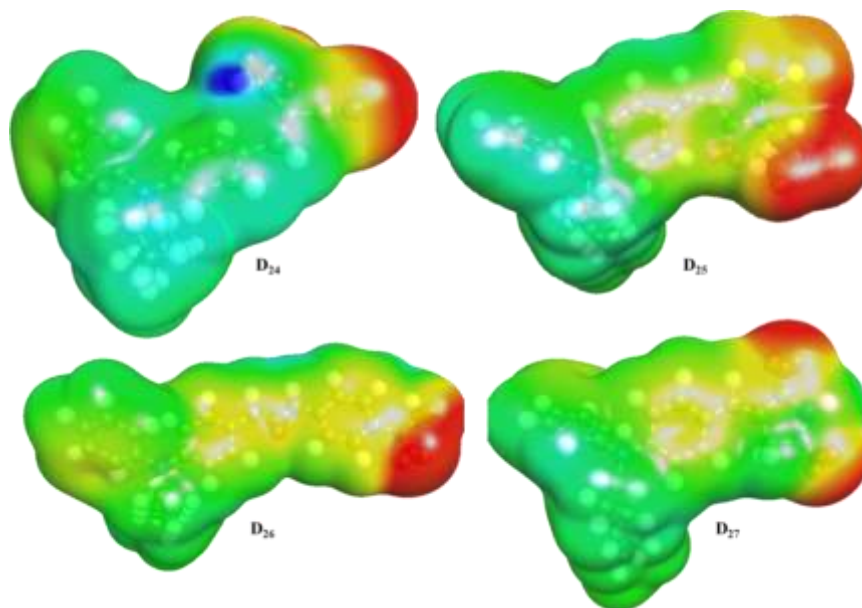


Fig 4.36 Molecular Electrostatic Potential (ESP) mapping on iso density of **D**₂₄₋₂₇

4.3.3 TD-DFT studies

Time-dependent density functional theory (TD-DFT) calculations were performed to predict spectroscopic properties of the selected dyes **D**₂₄₋₂₅. **Fig. 4.37** depicts the simulated absorption spectra of **D**₂₄₋₂₅. These precise and reliable predictions made by TD-DFT studies indicate that, the functional and basis set chosen for TD-DFT studies are quite appropriate. The theoretically obtained spectrum has showed two distinct bands, corresponding to π - π^* and charge transfer phenomenon. Here, the appeared trend is well in agreement with experimental spectral data. It is evident that, the band at higher energy can be attributed to π - π^* transition, whereas the band at lower energy may be assigned to the charge transfer from the donor to the acceptor segment. Similar to the experimental UV observation, **D**₂₅ shows a red shifted absorption value when compared to that of **D**₂₄.

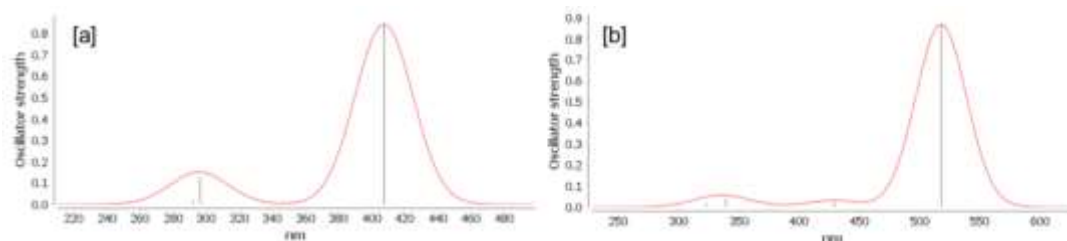
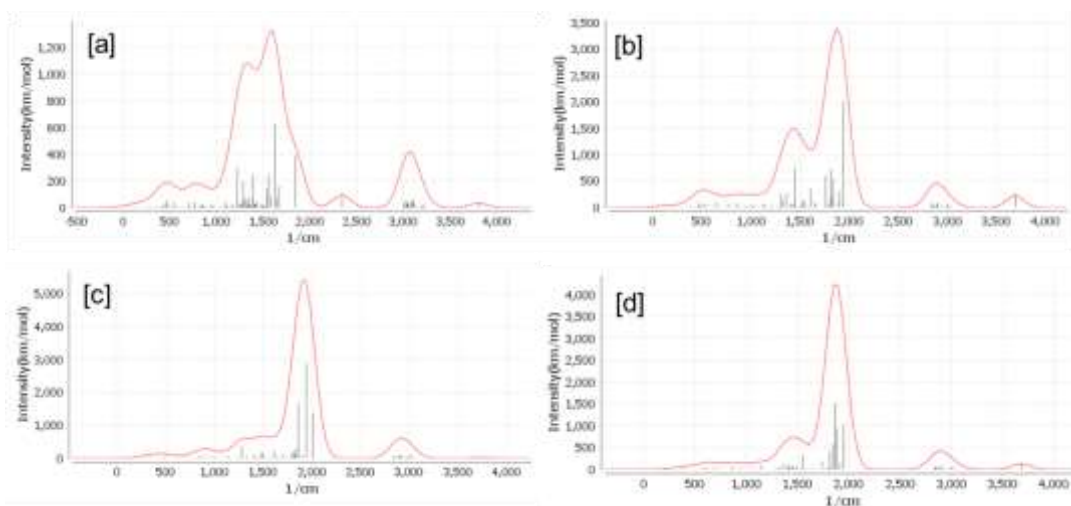


Fig 4.37 (a) Simulated absorption spectrum of **D24** and (b) spectrum of **D25**

Figs. 4.38a-d display the simulated IR spectra for the dyes **D24-27**. The obtained simulated IR spectra are in accordance with the experimentally obtained FTIR spectra. Thus, the observations indicate that the functional basis sets chosen for TD-DFT simulations are quite appropriate.



Figs 4.38a-d Simulated vibrational spectra of **D24**, **D25**, **D26**, and **D27**, respectively

4.4 CONCLUSIONS

In summary, all the synthesized dyes, **D1-27** were subjected to photophysical, electrochemical and molecular modeling studies. Their photophysical characterization reveals that, all the dyes display strong absorption in the range of 349-560 nm and intense emission in the order of 428-689 nm. The calculated optical band gaps are within 1.9-3.3 eV whereas Stoke shifts values are in the range of 2490-8297 cm^{-1} . Amongst the dyes, the **D11** shows the lowest band gap and maximum extent of absorption. Further, the CV study confirms that, all the dyes possess stringent requirements for electron injection and dye regeneration processes. The electrochemical study also shows the least band gap for **D11** dye. The calculated

driving forces reveal that, the thermodynamic processes are spontaneous for all the dyes. Furthermore, DFT calculations confirm clear charge separation between the HOMO and LUMO energy levels of **D1-27**. The obtained electrostatic maps confirm the charge distribution in the molecules. In addition, the binding studies of **D4** with TiO₂ confirm that, the charge transfer takes place from dye molecule to semiconductor surface through anchoring group. Interestingly, the absorption spectra generated by TD-DFT studies are in agreement with the experimental results.

Based on the results of photophysical, electrochemical and theoretical studies, all the well-characterized dyes were employed in the fabrication of DSSCs, as sensitizers. Also, they were used as co-sensitizers in the devices sensitized with Ru (II) based **HD-2** and **N3** dyes. In the next chapter, a detailed account of device fabrication studies as well as their EIS studies is highlighted.

PHOTOVOLTAIC AND ELECTROCHEMICAL IMPEDANCE STUDIES

Abstract:

This chapter deals with the DSSC fabrication studies of newly synthesized n-type (D1-27) dyes used as sensitizers. Also, it covers the investigations of co-sensitization behaviour of new dyes in HD-2/N3 sensitized DSSCs. Further, it includes the EIS studies of the fabricated devices in order to understand various processes involved in the cells. In addition, it involves investigations on mode of adsorption of dyes on TiO₂ surface using FTIR spectroscopy. Furthermore, it comprises the correlation studies between their structure and device performance parameters.

5.1 PHOTOVOLTAIC INVESTIGATION

In the present work, all the synthesized dyes (D1-27) were employed as sensitizers in the fabrication of DSSCs and their photovoltaic parameters were obtained. Also, the dyes were used as co-sensitizers in DSSCs sensitized with HD-2 and N3 dyes and their performances were evaluated. A detailed procedure followed for DSSC fabrication as well as discussion on obtained results is elaborated in the following sections.

5.1.1 Introduction

A typical DSSC consists of a transparent and conductive anode made of fluorine-doped tin dioxide (FTO) deposited on a glass substrate, a thin layer of TiO₂ on the back of the conductive plate, photosensitive dyes covalently bonded to the surface of TiO₂, a thin iodide electrolyte layer, and a conducting counter electrode, *i.e.* Pt. Here, generation of electrical power under illumination is achieved to produce voltage over an external load and current through the load at the same time. This is characterized by the current-voltage (J-V) curve of the cell at certain illumination and temperature. When the cell is short circuited under illumination, the maximum current, the short circuit current (J_{sc}), is generated, while under open circuit conditions no current can flow and the voltage is at its maximum, called the open

circuit voltage (V_{OC}). Another important characteristic of the solar cell performance is the fill factor (FF).

5.1.2 Materials and methods

The J-V (Current-Voltage) characteristics of fabricated *n*-type devices were measured using Oriel SOL3A solar simulator connected to Keithley 2400 source meter. Further, IPCE (Incident photon conversion efficiency) spectra of all the fabricated DSSCs were recorded using QEX10 PV measurement system. Calibration of incident light was performed before measurements using a silicon photodiode (IF035, PV Measurements). All the measurements were carried out without the use of anti-reflecting film.

5.1.3 Experimental

As per the procedure described in the reported literature (El-Shafei et al. 2012, Cheema et al. 2014), DSSCs were fabricated using synthesized dyes **D₁₋₂₇** as sensitizers. Further, all the dyes were exploited as co-sensitizers in the devices sensitized with Ru (II) complex (**HD-2/N3**).

5.1.3.1 Fabrication of DSSCs sensitized with *D₁₋₂₇* (Series-1 to 7)

Etched Fluorine doped tin oxide (2.2 mm thickness, sheet resistance of 8 Ω/cm^2 , TEC, Pilkington)) substrates were cleaned with detergent, water, acetone and ethanol, sequentially. These substrates were then immersed in 40 mM of TiCl_4 solution (Wako Pure Chemical Industries, Ltd) for 30 min at 70 °C, followed by rinsing with water and ethanol. The substrates were held at 500 °C for 30 min to allow formation of TiO_2 crystals to serve as the seed layer. Using a screen-printer, a layer of compact TiO_2 paste (Solaronix, Ti-Nanoxide D/SP) is printed onto the substrate (active area, 0.18 cm^2) using squeegee printing setup. The printed film is allowed for drying at 350 °C for 10 min and curing at 500 °C for 30 min. Next, after drying the electrodes, scattering layer (5 μm thick) TiO_2 particles (Solaronix, Ti-Nanoxide R/SP) were printed onto the already deposited TiO_2 layer. The TiO_2 electrodes were heated under an air flow at 350 °C for 10 min, followed by heating at 500 °C for 30 min. After cooling to room temperature, these substrates were finally immersed in 40 mM of TiCl_4 solution for 30 min at 70 °C to fill up the defective “pin-holes”, followed by

rinsing with water and ethanol. The electrodes were heated again at 500 °C for 30 min and left to cool to 80 °C before dipping them into the dye solution. The dye solutions (0.5 mM) were prepared in 6 mL 1:1:1 acetonitrile, *tert*-butanol and dimethyl sulfoxide. Chenodeoxycholic acid (CDCA) was added at a concentration of 10 mM. The electrodes were immersed in the dye solutions and then kept at 25 °C for 20 hours to adsorb the dye onto the TiO₂ surface.

To prepare the counter electrode, pre-cut TCO glasses were washed with water followed by 0.1 M HCl in EtOH, and sonication in acetone bath for 10 min. These washed TCO were then dried at 400 °C for 15 min. Thin layer of Pt-paste (Solaronix, Platisol T/SP) on TCO was printed and the printed electrodes were then cured at 450 °C for 10 min. The dye sensitized TiO₂ electrodes were sandwiched with Pt counter electrodes and the electrolyte (Solaronix, Iodolyte HI-30) was then injected into the cell, while the two electrodes were held together with the clips.

The generated plots and photoelectrochemical parameters are used for discussion under the section ‘Results and discussion’.

5.1.3.2 Fabrication of DSSCs co-sensitized with D₁₋₂₇ (Series-1 to 7)

Fluorine-doped tin oxide (FTO) coated glasses (2.2 mm thickness, sheet resistance of 8 Ω/cm², TEC, Pilkington) were washed with detergent, water, acetone and ethanol, sequentially. After this FTO glass plates were immersed into a 40 mM aqueous TiCl₄ solution at 70 °C for 30 min and washed with water and ethanol. Thin layer (8-12 μm thick) of TiO₂ (Solaronix, Ti-Nanoxide T/SP) was deposited (active area, 0.18 cm²) on transparent conducting glass by squeegee printing followed by drying at 350 °C for 10 min and curing at 500 °C for 30 min. Next, after drying the electrodes, scattering layer (5 μm thick) TiO₂ particles (Solaronix, Ti-Nanoxide R/SP) were printed onto the already deposited TiO₂ layer. The TiO₂ electrodes were heated under an air flow at 350 °C for 10 min, followed by heating at 500 °C for 30 min. After cooling to room temperature, the TiO₂ electrodes were treated with 40 mM aqueous solution of TiCl₄ at 70 °C for 30 min and then washed with water and ethanol. The electrodes were heated again at 500 °C for 30 min and left to cool to 80 °C before dipping them into the dye solution. The dye solutions (0.2 mM) were

prepared in 6.0 mL 1:1:1 acetonitrile, tert-butyl alcohol and DMSO. Deoxycholic acid was added to the dye solution as a co-adsorbate at a concentration of 20 mM and **HD-2** (0.2 mM) were then dissolved. The electrodes were immersed in the dye solutions and then kept at room temp, 25 °C, for 20 hours in dark to adsorb the dye onto the TiO₂ surface.

For preparing the counter electrode, pre-cut TCO glasses were washed with water followed by 0.1M HCl in ethanol, and sonication in acetone bath for 10 min. These washed TCO were then dried at 400 °C for 15 min. A thin layer of Pt-paste (Solaronix, Platisol T/SP) on TCO was printed and the printed electrodes were then cured at 450 °C for 10 min. The dye sensitized TiO₂ electrodes were sandwiched with Pt counter electrodes and the electrolyte (Solaronix, Iodolyte HI-30) was then injected into the cell, while the two electrodes were held together with the clips.

The obtained photovoltaic parameters are discussed in the sections **5.1.4.1** to **5.1.4.7**.

5.1.4 Results and discussion

The obtained J-V and IPCE curves for the dyes are displayed in **Figs 5.1** to **5.14** and their photovoltaic performance data are summarized in **Tables 5.1-5.10**.

5.1.4.1 Photovoltaic performance of devices sensitized/co-sensitized with D₁₋₃ (Series-1)

DSSCs sensitized with D₁₋₃

Fig 5.1(a) shows J-V characteristic curves of DSSC devices sensitized with dyes **D₁₋₃**. The observed photovoltaic parameters, viz. V_{OC}, J_{SC}, FF and PCE are summarized in **Table 5.1**. Amongst the tested dyes, the dye **D₁** shows the better photovoltaic performance than other dyes. From the results, it is clear that, the dye carrying barbituric acid unit (**D₃**) displays much lower photovoltaic performance than **D₁**, which is mainly due to heavy aggregation of dye molecules on the surface of TiO₂.

The DSSC device with **D₁** shows maximum PCE (η) value of 4.4% (J_{SC}=9.73 mA/cm², V_{OC}=0.68 V, and FF=66.99%) when compared to devices with **D₂**(η =0.16

%, $J_{SC}=0.488 \text{ mA/cm}^2$, $V_{OC}=0.45 \text{ V}$, and $FF=72.35\%$) and **D**₃($\eta=0.22 \%$, $J_{SC}=64 \text{ mA/cm}^2$, $V_{OC}=0.47 \text{ V}$, and $FF=74.40\%$). It is interesting to note that, the anchoring ability of 4-aminobenzoic acid is better than the majorly used cyano acetic acid reported earlier. Its higher J_{SC} value can be attributed to its good anchoring property with TiO_2 ; accordingly, the electron injection to the semiconductor is quite facile when compared to the other **D**₂ and **D**₃. Normally, the lower adsorption of dyes results in poor light harvesting ability which further leads to lowering of J_{SC} value.

Fig 5.1(b) portrays the IPCE spectra and from the spectra, it is clear that **D**₁ shows a broad IPCE spectrum than **D**₂ and **D**₃. This can be attributed to the good adsorption of **D**₁ on TiO_2 through 4-aminobenzoic acid anchor in comparison with **D**₂ and **D**₃.

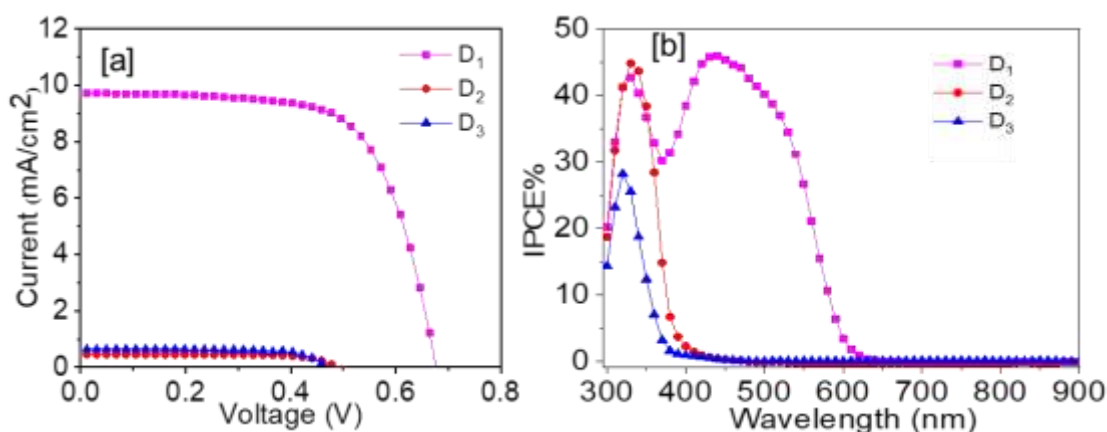


Fig 5.1 (a) Photocurrent density vs. voltage; (b) IPCE characteristics for devices sensitized with **D**₁₋₃ under illumination of simulated solar light (AM 1.5, 100 mW/cm^2)

Table 5.1: Photovoltaic performance data of devices sensitized with **D**₁₋₃

Series	Sensitizers	J_{SC} (mAcm^{-2})	V_{OC} (V)	FF%	$\eta \%$
Series 1	D ₁	9.73	0.68	66.99	4.41
	D ₂	0.488	0.45	72.35	0.16
	D ₃	0.64	0.47	74.40	0.22

DSSCs co-sensitized with D₁₋₃

Fig 5.2 shows the J-V and IPCE characteristic curves for **N3**-based DSSCs co-sensitized with dyes **D₁₋₃** in the presence of CDCA and their detailed photovoltaic data are tabulated in **Table 5.2**. Here, DSSCs were fabricated using **D₁₋₃** as co-sensitizers along with well-known **N3** dye. The co-sensitized devices with **D₁**, *i.e.* **N3+D₁**($\eta=5.44\%$, $J_{SC}=14.25$ mA/cm², $V_{OC}=0.62$ V, and $FF=61.21\%$) and **D₃**, *i.e.* **N3+D₃**($\eta=5.43\%$, $J_{SC}=13.13$ mA/cm², $V_{OC}=0.61$ V, and $FF=67.94\%$) show slightly higher PCE than **N3** dye alone ($\eta=5.39\%$, $J_{SC}=14.39$ mA/cm², $V_{OC}=0.60$ V, and $FF=61.98\%$) whereas with **D₂**, *i.e.* **N3+D₂**($\eta=5.32\%$, $J_{SC}=14.63$ mA/cm², $V_{OC}=0.66$ V, and $FF=54.80\%$) has displayed lower PCE. It is to be noted that, all the co-sensitized devices show an enhanced V_{OC} value, which is due to the efficient filling of co-sensitizer molecules in between bulky **N3** dye molecules, resulting in the minimization of **N3** dye aggregation and prevention of I_3^- ions to penetrate into the TiO₂ surface. But, the IPCE spectrum of the **N3** dye shows a broad spectrum from 300 to 800 nm with a maximum value of 72.966% at 535 nm. Its value dramatically decreases to 40% in the wavelength region of 350-400 nm due to the competitive light absorption between I_3^- and **N3** dye. This competitive absorption can be reduced by a co-sensitization process which will result in a broad and intense IPCE spectrum. Thus, the broad IPCE spectrum shown by **N3+D₁** and **N3+D₃** is a result of the reduction of light absorption of I_3^- . The dye **D₂** along with **N3** displays an IPCE spectrum similar to that of **N3** dye alone which may be due to the improper adsorption of **D₂** in between bulky **N3** dye molecules because of the poor adsorbing property of **D₂**. Also, the low PCE of **N3+D₂** (5.32%) can be explained by the low FF (54.80%) obtained.

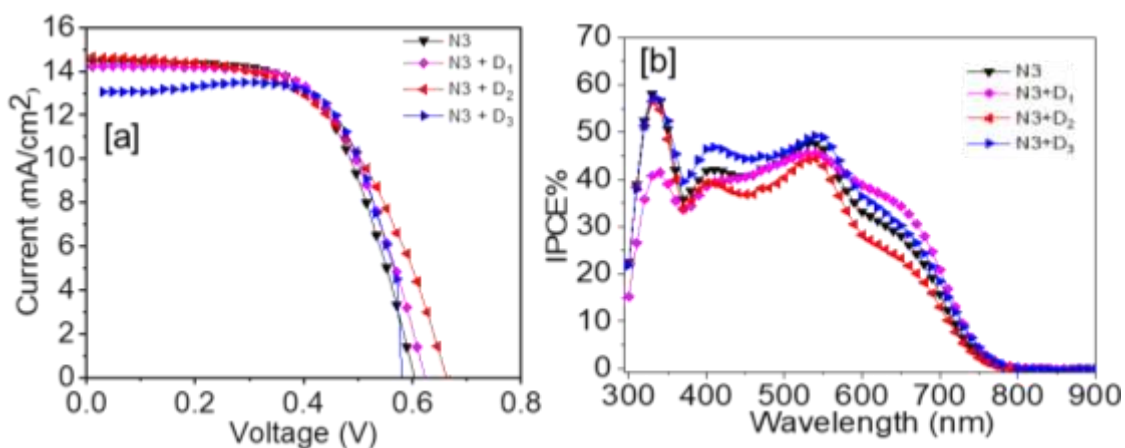


Fig 5.2 (a) Photocurrent density vs voltage; (b) IPCE spectra for **N3** based devices co-sensitized with **D₁₋₃** under illumination of simulated solar light (AM 1.5, 100 mW/cm²)

Table 5.2 : Photovoltaic performance data of devices co-sensitized with **D₁₋₃**

Series	Sensitizer	Co-sensitizer	J _{SC} (mAcm ⁻²)	V _{OC} (V)	FF%	η%
	N3	-	14.39	0.60	61.98	5.39
Series 1	N3	D₁	14.25	0.62	61.21	5.44
		D₂	14.63	0.66	54.80	5.32
		D₃	13.13	0.61	67.94	5.43

5.1.4.2 Photovoltaic performance of devices sensitized/co-sensitized with **D₄₋₇** (Series-2)

DSSCs sensitized with **D₄₋₇**

The J-V characteristic curves of DSSC devices sensitized with dyes **D₄₋₇** are depicted in **Fig 5.3(a)** and the observed photovoltaic parameters, viz. V_{OC}, J_{SC}, FF and PCE are summarized in **Table 5.3**. The fabricated device with synthesized dye **D₄** displays maximum PCE (η) value of 2.53% (J_{SC} = 7.70 mA/cm², V_{OC} = 0.56 V, and FF = 58.4%) when compared to devices with **D₅** (J_{SC} = 0.66 mA/cm², V_{OC} = 0.39 V and FF = 47.14%), **D₆** (J_{SC} = 3.22 mA/cm², V_{OC} = 0.20 V and FF = 33.37%) and **D₇** (J_{SC} = 1.57 mA/cm², V_{OC} = 0.47 V, and FF = 58.32%). The highest value of PCE of **D₄** is due to the

higher J_{SC} value, which can be attributed to its good anchoring property with TiO_2 that facilitated the electron injection to the TiO_2 surface smoothly. The poor performances of other dyes of the series can be ascribed to the reduced adsorption of dye, which has resulted in poor electron injection to TiO_2 surface, further decreasing the J_{SC} value. In addition, experiments were carried out to obtain IPCE spectra of the fabricated devices. **Fig 5.3** portrays the IPCE spectra and from the data, it is clear that, **D4** shows a broader IPCE spectrum than other dyes. This can be attributed to the good adsorption of **D4** on TiO_2 through cyanoacetic acid anchor. In its spectrum, the dip in the region of 360-380 nm is prominent and the maximum value is 38% in the range of 340-360 nm. It's broad range shows a maximum of 34% in the region of 490-510 nm. The enhanced IPCE behaviour of **D4** is reflected in its better J_{SC} value. Further, **D7** and **D5** display poor IPCE spectra, whereas **D6** exhibits slightly better spectrum. It has been observed that, **D7** shows an intense absorption in the range of 360-380 nm compared to the absorption in the range 490-510 nm. The observed weak absorption in the range of 490-510 nm may be attributed to the weak anchoring property of the barbituric acid. The behaviour of **D4** and **D6** is in consistent with the results obtained from UV-Vis absorption spectra of these dyes adsorbed on TiO_2 surface. In contrast, the IPCE results of **D5** and **D7** are quite different from their respective UV-Vis absorption spectra observed. The poor IPCE performance of **D5** can be explained on the basis of its theoretical studies.

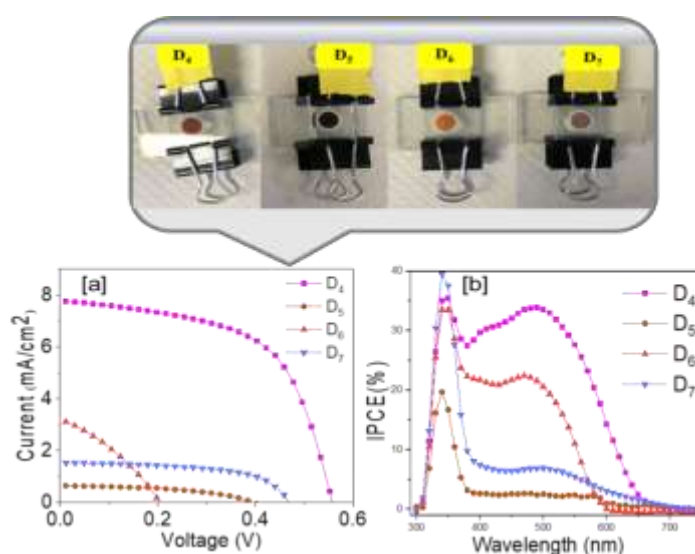


Fig 5.3(a) Photocurrent density vs voltage; **(b)** IPCE characteristics for devices sensitized with **D4-7** under illumination of simulated solar light (AM 1.5, 100 mW/cm²)

Table 5.3 : Photovoltaic performance data of devices sensitized with **D4-7**

Series	Sensitizers	J _{sc} (mAcm ⁻²)	V _{oc} (V)	FF%	η%
Series 2	D4	7.76	0.56	58.41	2.53
	D5	0.66	0.39	47.14	0.12
	D6	3.22	0.20	33.37	0.22
	D7	1.57	0.47	58.32	0.43

DSSCs co-sensitized with D4-7

Fig 5.4(a) shows J-V characteristic curves of DSSC devices co-sensitized with dyes **D4-7** and the observed photovoltaic parameters are summarized in **Table 5.4**. New DSSCs were fabricated employing **D4-7** as co-sensitizers along with well-known Ru (II) based **HD-2** dye. The co-sensitized devices with **D7**, *i.e.* **HD-2+D7** (η=7.69%, J_{sc}=18.34 mA/cm², V_{oc}=0.639 V, and FF=65.61%) shows higher PCE than **HD-2** dye alone (η=7.49%, J_{sc}=19.03 mA/cm², V_{oc}=0.652 V, and FF=60.49%) whereas the fabricated devices using co-sensitizers *i.e.* **D4**, **D5** and **D6** bearing carboxylic acid have displayed lower PCE values. The high PCE of **HD-2+D7** can be attributed to the efficient covering of voids present in bulky **HD-2** dye by small sized co-sensitizer molecules, thereby increasing the surface coverage and reduction in aggregation of **HD-2** dye. Moreover **HD-2+D7** reduces the back reaction of I₃⁻/I⁻ on the TiO₂ surface in the cell.

Interestingly, all the co-sensitized devices show higher FF values than that of **HD-2** alone, which may be due to stronger intermolecular interaction causing better pathway for charge carriers towards the electrodes. However, their V_{oc} values were found to be lower than that of **HD-2** dye alone. This can be attributed to the lowering of the TiO₂ Fermi level. The obtained IPCE spectra of the co-sensitized devices are shown in **Fig 5.4(b)**. The obtained spectrum of device comprised of **HD-2+D7** shows a broad spectrum from 300 to 800 nm with a maximum value of 72.966% at 535 nm, which is similar to that of **HD-2** alone. The observed IPCE results are in consistent with higher PCE value obtained for the device co-sensitized with **D7**. All other

devices display lower IPCE spectra which might be the reason for their lower PCE values. Here, the observed lower IPCE values can be attributed to the presence of dual carboxylic groups, which would have led to the more recombination rate resulting in lower PCEs.

Table 5.4: Photovoltaic performance data of devices co-sensitized with **D4-7**

Series	Sensitizer	Co-sensitizer	J_{SC} (mAcm^{-2})	V_{OC} (V)	FF%	η %
	HD-2	-	19.03	0.652	60.49	7.49
Series 2	HD-2	D4	11.17	0.596	65.99	4.39
		D5	8.49	0.536	64.42	2.93
		D6	13.60	0.604	63.86	5.25
		D7	18.34	0.639	65.61	7.69

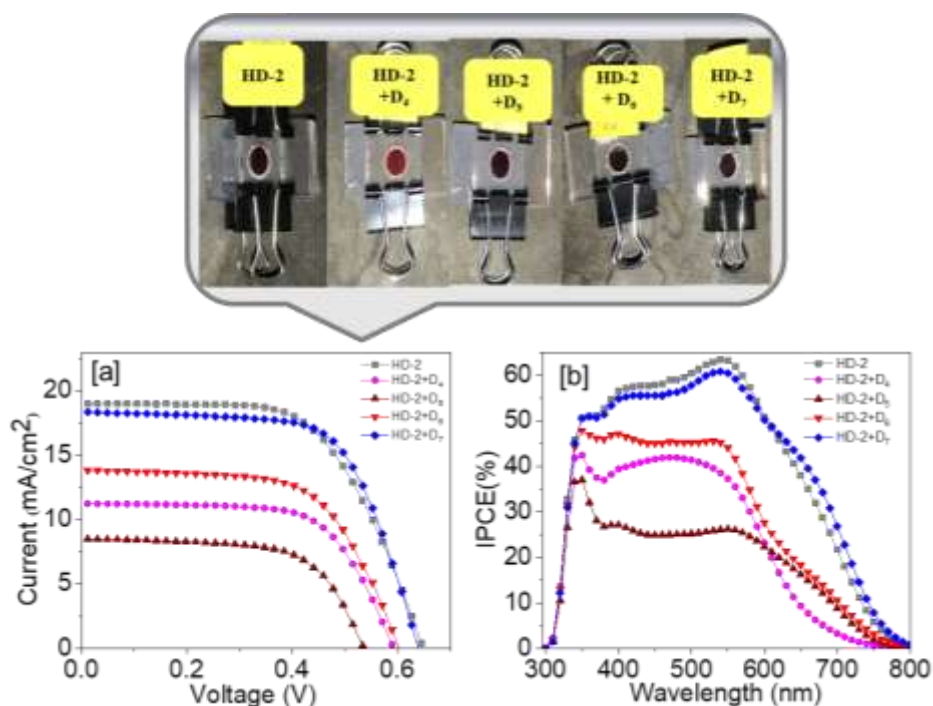


Fig 5.4 (a) Photocurrent density vs. voltage; **(b)** IPCE spectra for **HD-2** based devices co-sensitized with **D4-7** under illumination of simulated solar light (AM 1.5, 100 mW/cm^2)

5.1.4.3 Photovoltaic performance of devices sensitized/co-sensitized with **D₈₋₁₁**

(Series-3)

*DSSCs sensitized with **D₈₋₁₁***

The obtained J-V curves of the devices sensitized with **D₈₋₁₁** are depicted in **Fig 5.5(a)** and the corresponding device parameters are tabulated in **Table 5.5**. The DSSC device sensitized with **D₈** shows a maximum PCE (η) value of **3.48%** ($J_{SC}=8.29$ mA/cm², $V_{OC}=0.62$ V, and FF=67.35%) when compared to devices sensitized with **D₉**($\eta=0.51\%$, $J_{SC}=1.36$ mA/cm², $V_{OC}=0.56$ V, and FF=67.35%), **D₁₀**($\eta=2.58\%$, $J_{SC}=7.01$ mA/cm², $V_{OC}=0.47$ V, and FF=67.29%) and **D₁₁**($\eta=0.36\%$, $J_{SC}=1.06$ mA/cm², $V_{OC}=0.49$ V, and FF=69.0%). From the data it is clear that, the devices sensitized with dyes **D₈** and **D₁₀** carrying cyanoacetic acid as an anchoring unit give a better efficiency than those sensitized with **D₉** and **D₁₁** bearing barbituric acid as an anchor. Their improved performance is due to the good anchoring property of cyanoacetic acid on to the TiO₂ surface. On comparing the performance of devices sensitized with **D₈** and **D₁₀**, it is observed that, the introduction of an additional spacer unit in the **D₁₀** has not contributed to the enhancement of PCE value. This behaviour may be due to the aggregation of elongated **D₁₀** dyes in the device. Additionally, IPCE study of devices was carried out and the obtained spectra are given in **Fig 5.5(b)**. From the figure it is evident that, **D₈** shows a moderate IPCE spectrum with a highest absorption percentage of $\approx 50\%$. Even though, the percentage of light absorbance of device carrying **D₁₀** is less, it is showing a slightly broader spectrum compared to that of device with **D₈**. This behaviour of device with **D₁₀** is due to the presence of additional spacer unit in it. The lower absorbance of **D₁₁** than **D₉** sensitized devices accounts for its achieved lower PCE. Normally, IPCE is directly related to the factors such as absorption properties of the dye, the amount of dye adsorbed on the TiO₂ surface, the quantum yield of electron injection from the excited dye to the CB of the TiO₂ and the efficiency of collection of electrons in the external circuit.

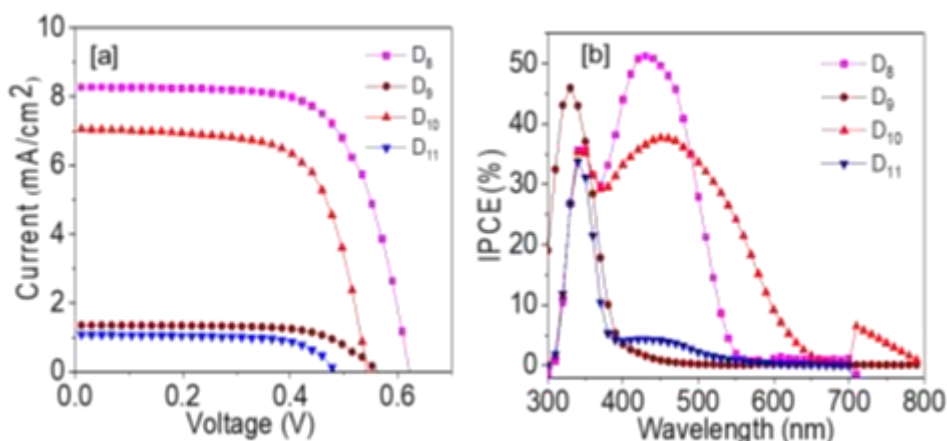


Fig 5.5 (a) Photocurrent density vs voltage; (b) IPCE characteristics for devices sensitized with **D8-11** under illumination of simulated solar light (AM 1.5, 100 mW/cm²)

Table 5.5 : Photovoltaic performance data of devices sensitized with **D8-11**

Series	Sensitizers	J _{SC} (mAcm ⁻²)	V _{OC} (V)	FF%	η%
Series 3	D₈	8.29	0.62	67.35	3.48
	D₉	1.36	0.56	66.81	0.51
	D₁₀	7.01	0.47	67.29	2.58
	D₁₁	1.06	0.49	69.0	0.36

DSSCs co-sensitized with D8-11

DSSCs were fabricated using **D8-11** as co-sensitizers along with well-known **HD-2** sensitizer. The corresponding J-V curves obtained in co-sensitization experiments are shown in **Fig 5.6(a)** and their parameters are summarized in **Table 5.6**. The results reveal that, devices co-sensitized with **D8-10** show enhanced efficiencies compared to that of **HD-2** dye alone. The highest PCE value is observed for the device with **HD-2+D11** ($\eta=8.34\%$, $J_{SC}=20.47$ mA/cm², $V_{OC}=0.641$ V, and $FF=63.44\%$), which can be attributed to the efficient filling of the vacant voids between the molecules of **HD-2** dye. Despite the fact both **D9** and **D11** bear barbituric acid as an anchor, the **HD-2+D9** device shows the lowest PCE ($\eta=7.19\%$, $J_{SC}=17.74$ mA/cm², $V_{OC}=0.622$ V, and $FF=65.18\%$) value. The devices with **HD-2+D8** and **HD-2+D10** bearing cyanoacetic acid group display efficiency of **8.00** and **7.88%**,

respectively. From the results of the IPCE spectra of devices, as shown in **Fig 5.6(b)**, it can be inferred that, the device with **HD-2+D₁₁** displays a much superior IPCE spectrum than **HD-2** dye alone, as reflected in their PCE values. Here, the device with **HD-2+D₁₁** exhibits an absorbance more than 70% whereas cells with **HD-2+D₁₈**, **HD-2+D₁₉** and **HD-2+D₁₀** display a similar absorbance in the range of 60%.

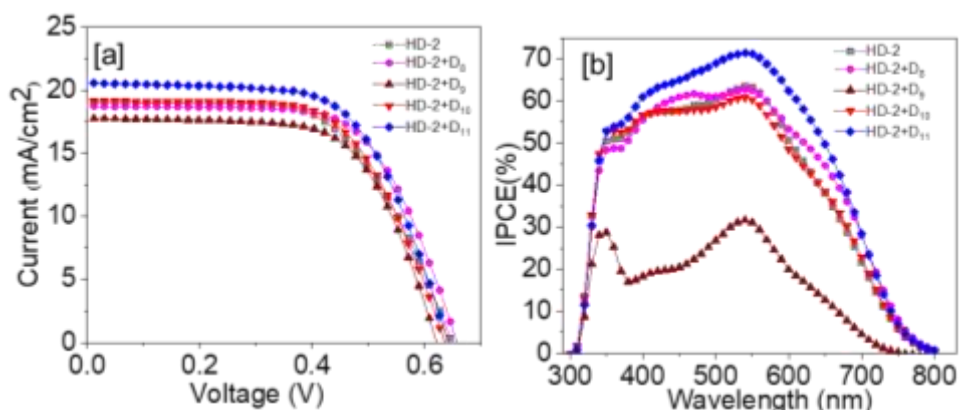


Fig 5.6 (a) Photocurrent density vs voltage; (b) IPCE spectra for **HD-2** based devices co-sensitized with **D₈₋₁₁** under illumination of simulated solar light (AM 1.5, 100 mW/cm²)

Table 5.6: Photovoltaic performance data of devices co-sensitized with **D₈₋₁₁**

Series	Sensitizer	Co-sensitizer	J _{SC} (mAcm ⁻²)	V _{OC} (V)	FF%	η%
Series 3	HD-2	-	19.03	0.652	60.49	7.49
	HD-2	D₈	18.70	0.658	65.00	8.00
		D₉	17.74	0.622	65.18	7.19
		D₁₀	19.15	0.637	63.15	7.88
		D₁₁	20.47	0.641	63.44	8.34

5.1.4.4 Photovoltaic performance of devices sensitized/co-sensitized with **D₁₂₋₁₇** (Series-4)

DSSCs sensitized with **D₁₂₋₁₇**

Fig 5.7 (a) represents J-V curves for DSSCs sensitized with dyes **D₁₂₋₁₇** under AM 1.5G simulated sunlight with a light intensity of 100 mW/cm². The observed

photovoltaic parameters are summarized in **Table 5.7**. In this series, only device sensitized with **D17** shows a moderate performance ($\eta=1.089\%$, $J_{SC}=3.809 \text{ mA/cm}^2$, $V_{OC}=0.545 \text{ V}$ and $FF=52.42 \%$), whereas the devices fabricated with **D12-16** display very poor results. The slight improvement in performance of device sensitized with **D17** may be due to the extension of conjugation and the presence of (4-nitrophenyl)hydrazine anchoring group in it. The obtained IPCE spectra of devices sensitized with the dyes are shown in **Fig 5.7(b)**. The poor performance of the devices can be accounted for the poor absorbance of devices in the visible region. Conclusively, it can be said that, the poor anchoring property of nitro group has brought about the poor IPCE behaviour, resulting in poor PCE of devices.

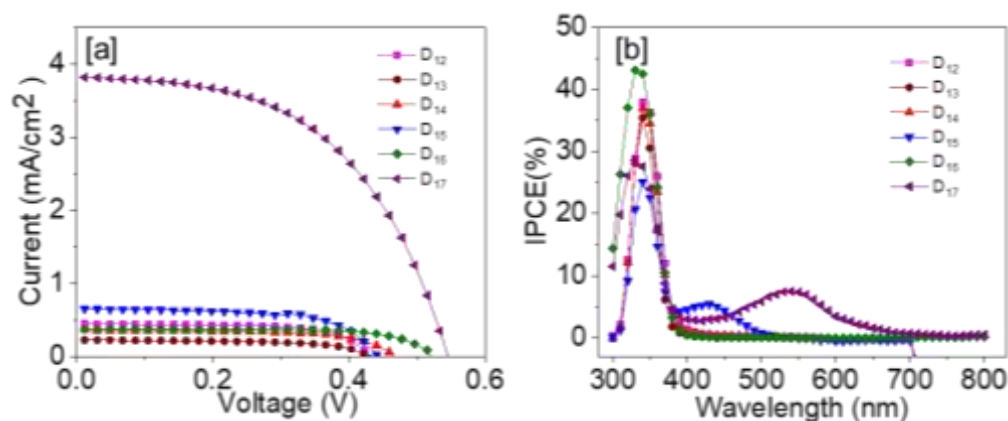


Fig 5.7 (a) Photocurrent density vs voltage; (b) IPCE characteristics for devices sensitized with **D12-17** under illumination of simulated solar light (AM 1.5, 100 mW/cm^2)

Table 5.7: Photovoltaic performance data of devices sensitized with **D12-17**

Series	Sensitizers	J_{SC} (mAcm^{-2})	V_{OC} (V)	FF%	$\eta\%$
Series 4	D12	0.446	0.447	66.72	0.129
	D13	0.433	0.227	61.26	0.060
	D14	0.466	0.360	64.78	0.109
	D15	0.443	0.652	65.53	0.189
	D16	0.373	0.521	71.85	0.140
	D17	3.809	0.545	52.42	1.089

DSSCs co-sensitized with D₁₂₋₁₇

DSSCs were fabricated using **D₁₂₋₁₇** as co-sensitizers along with well-known Ru based **HD-2** dye. The corresponding I-V curves obtained from experiments are shown in **Fig 5.8(a)** and their parameters are summarized in **Table 5.8**. The devices co-sensitized with **D₁₂₋₁₅** exhibit PCE values better than that of device fabricated with **HD-2** dye alone. It is worth to note that, the highest PCE is obtained for device co-sensitized with **HD-2+D₁₄** ($\eta=9.38\%$, $J_{SC}=20.88$ mA/cm², $V_{OC}=0.679$ V, and $FF=66.17\%$) with an enhancement of about 2%. The efficiency obtained for devices with **HD-2+D₁₂**, **HD-2+D₁₃**, and **HD-2+D₁₅** are **8.92 %**, **8.46%** and **8.64%** respectively. The good performance shown by the the devices can be attributed to their small molecular size of the dyes, which can efficiently fit into the vacant spaces between the **HD-2** dye molecules. In addition, the low recombination behaviour of nitro anchoring group also has contributed to its PCE value. On the other hand, the poor performances of devices co-sensitized with **D₁₆** and **D₁₇** may be due to their elongated structure. The IPCE spectra of the co-sensitized devices are presented in **Fig 5.8(b)**. From the spectra it can be derived that, the devices co-sensitized with **D₁₂₋₁₅** show analogous broad spectra in the visible region of absorbance of $\approx 75\%$. The aforementioned devices display enhanced absorbance compared to **HD-2** dye alone.

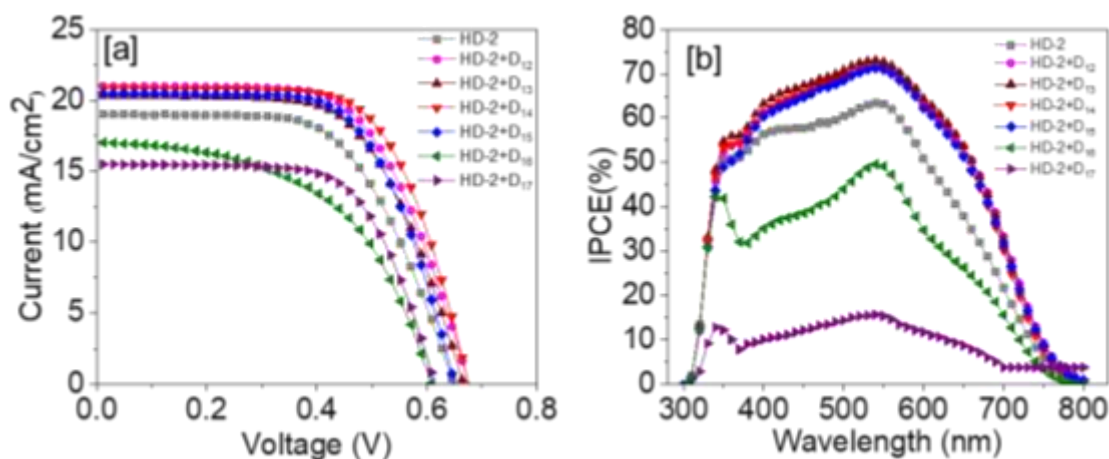


Fig 5.8 (a) Photocurrent density vs voltage; (b) IPCE spectra for **HD-2** based devices co-sensitized with **D₁₂₋₁₇** under illumination of simulated solar light (AM 1.5, 100 mW/cm²)

Table 5.8: Photovoltaic performance data of devices co-sensitized with **D12-17**

Series	Sensitizer	Co-sensitizer	J _{SC} (mAcm ⁻²)	V _{OC} (V)	FF%	η%
	HD-2	-	19.03	0.652	60.49	7.49
Series 4	HD-2	D12	20.98	0.680	62.55	8.92
		D13	20.37	0.672	61.80	8.46
		D14	20.88	0.679	66.17	9.38
		D15	20.61	0.655	64.00	8.64
		D16	17.01	0.615	53.96	5.65
		D17	15.49	0.615	65.78	6.26

5.1.4.5 Photovoltaic performance of devices sensitized/co-sensitized with **D18-21** (Series-5)

*DSSCs sensitized with **D18-21***

The performance of devices sensitized with **D18-21** were evaluated under AM 1.5G simulated sunlight with a light intensity of 100 mW/cm² and the obtained J-V curves are given in **Fig 5.9(a)**. The corresponding photovoltaic parameters are summarized in **Table 5.5**. From the studies, it is noted that, the devices fabricated with the sensitizer **D18**(η=2.44%, J_{SC}=5.751 mA/cm², V_{OC}=0.605 V, and FF=70.07%), **D19** (η=**2.19%**, J_{SC}=5.788 mA/cm², V_{OC}=0.560 V and FF=67.40%) and **D21**(η=**2.86%**, J_{SC}=7.008 mA/cm², V_{OC}=0.651 V, and FF=62.59 %) show almost similar PCE values. The results obtained for the aforementioned devices are attributed to their similar photophysical and electrochemical properties. The device sensitized with **D20**(η=1.20%, J_{SC}=3.026 mA/cm², V_{OC}=0.536 V and FF=67.69%) displays the lowest PCE value. The low performance of this device can be explained by the poor photophysical and electrochemical properties of **D20** bearing pyrene unit. Further, IPCE spectra obtained for the devices sensitized with **D18-21** are depicted in **Fig 5.9(b)**. The device sensitized with **D18** exhibits the highest absorbance of about 60% whereas

the devices with **D₁₉** and **D₂₁** show absorbance in the range of 55%. The poor IPCE shown by the device sensitized with **D₂₀** is lower than 30%. The obtained IPCE results are in well agreement with the device performance data.

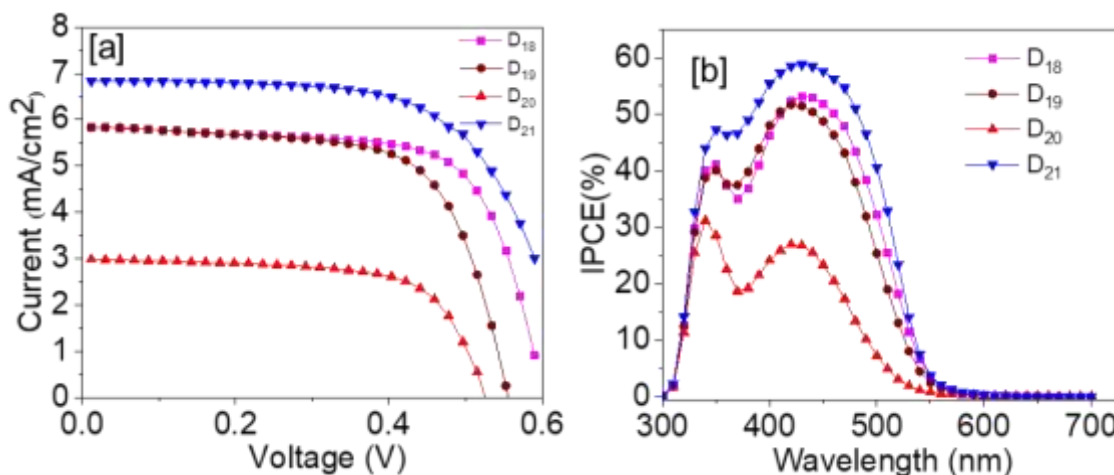


Fig 5.9 (a) Photocurrent density vs voltage; (b) IPCE characteristics for devices sensitized with **D₁₈₋₂₁** under illumination of simulated solar light (AM 1.5, 100 mW/cm²)

Table 5.9: Photovoltaic performance data of devices sensitized with **D₁₈₋₂₁**

Series	Sensitizers	J _{sc} (mAcm ⁻²)	V _{oc} (V)	FF%	η%
Series 5	D₁₈	5.751	0.605	70.07	2.44
	D₁₉	5.788	0.560	67.40	2.19
	D₂₀	3.026	0.536	67.69	1.20
	D₂₁	7.008	0.651	62.59	2.86

*DSSCs co-sensitized with **D₁₈₋₂₁***

The J-V curves obtained for co-sensitization experiments carried out for dyes **D₁₈₋₂₁** along with well-known **HD-2** are presented in **Fig 5.10(a)** and their photovoltaic parameters are summarized in **Table 5.10**. It is interesting to note that, all the devices in this series give a significant enhancement in the efficiency compared to that of **HD-2** dye alone. The device with **HD-2+D₁₈** offers a maximum increment of almost 3%, showing PCE of **10.35%** (J_{sc}=25.76 mA/cm², V_{oc}=0.675 V, and FF=

59.55%). The other devices with **HD-2+D₁₉** ($\eta=8.87\%$ $J_{SC}=24.54\text{ mA/cm}^2$, $V_{OC}=0.657\text{ V}$, and $FF=55.06\%$) and **HD-2+D₂₁** ($\eta=8.77\%$ $J_{SC}=23.32\text{ mA/cm}^2$, $V_{OC}=0.674\text{ V}$, and $FF=55.76\%$) display almost comparable PCEs whereas the device with **HD-2+D₂₀** ($\eta=7.76\%$ $J_{SC}=19.26\text{ mA/cm}^2$, $V_{OC}=0.677\text{ V}$, and $FF=59.57\%$) shows a slightly lower value. The enhanced efficiency of all the co-sensitized devices may be attributed to several causes such as appropriate size, photophysical behaviour and electrochemical properties. These parameters might have synergistically operated for increasing the efficiency. **Fig 5.10(b)** depicts the obtained IPCE spectra of devices. Here, **HD-2+D₁₈** shows a broad absorption in the range from 400-600 nm with a maximum absorption of approximate 60%. This broad absorption is reflected in its enhanced PCE value. Similarly, the devices with **HD-2+D₂₁**, **HD-2+D₁₉**, **HD-2+D₂₀** are showing broad absorption with absorption maxima of 58, 50 and 25 %, respectively. The observed values are well in accordance with the obtained PCE values of the devices.

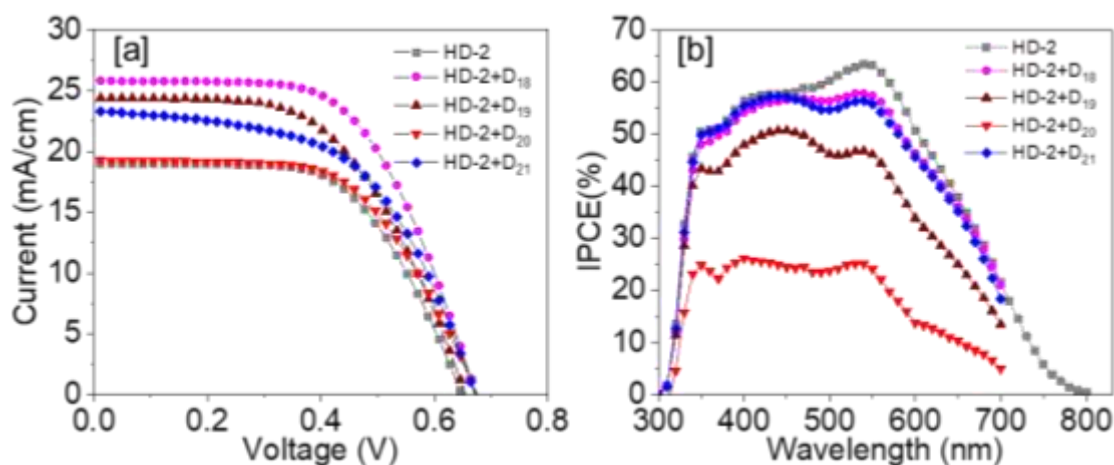


Fig 5.10 (a) Photocurrent density vs voltage; (b) IPCE spectra for **HD-2** based devices co-sensitized with **D₁₈₋₂₁** under illumination of simulated solar light (AM 1.5, 100 mW/cm^2)

Table 5.10 : Photovoltaic performance data of devices co-sensitized with **D18-21**

Series	Sensitizer	Co-sensitizer	J _{SC} (mAcm ⁻²)	V _{OC} (V)	FF%	η%
	HD-2	-	19.03	0.652	60.49	7.49
Series 5	HD-2	D18	25.76	0.675	59.55	10.35
		D19	24.54	0.657	55.06	8.87
		D20	19.26	0.677	59.57	7.76
		D21	23.32	0.674	55.76	8.77

5.1.4.6 Photovoltaic performance of devices sensitized/co-sensitized with **D22-23** (Series-6)

DSSCs sensitized with **D22-23**

Fig 5.11(a) depicts J-V curves for DSSCs sensitized with dyes **D22-23** under AM 1.5G simulated sunlight with a light intensity of 100 mW/cm². The observed photovoltaic parameters are tabulated in **Table 5.11**. According to the results, the devices sensitized with **D22** (η=5.91% J_{SC}=17.12 mA/cm², V_{OC}=0.665 V, and FF=51.897%) shows very good performance when compared to **D23** (η=2.28 % J_{SC}=6.498 mA/cm², V_{OC}=0.622 V, and FF=56.319 %). The A-D-π-D-A design strategy of dyes **D22-23** has facilitated to achieve good device performance. The better performance of devices sensitized with **D22** than **D23** can be attributed to the good anchoring property of cyanoacetic acid to TiO₂ surface. Further, IPCE studies were carried out for the devices and the obtained results are summarized in **Fig 5.11(b)**. The device with **D22** displays a broad spectrum in the range of 400-600nm with a maximum absorption of about 70% whereas **D23** shows two distinct peaks, one in the range of 320-360 nm with a maximum of 30% and the other in the visible range of 400-600 nm with a maximum of 18%. The IPCE spectra are in agreement with the J-V curves of the devices.

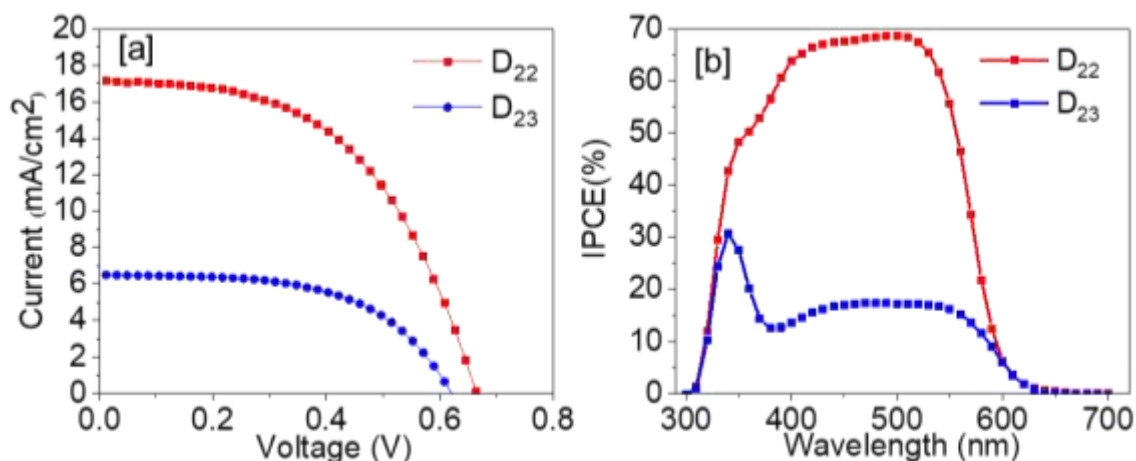


Fig 5.11 (a) Photocurrent density vs voltage; (b) IPCE characteristics for devices sensitized with **D₂₂₋₂₃** under illumination of simulated solar light (AM 1.5, 100 mW/cm²)

Table 5.11: Photovoltaic performance data of devices sensitized with **D₂₂₋₂₃**

Series	Sensitizers	J _{SC} (mAcm ⁻²)	V _{OC} (V)	FF%	η%
Series 6	D₂₂	17.12	0.665	51.897	5.91
	D₂₃	6.498	0.622	56.319	2.28

DSSCs co-sensitized with **D₂₂₋₂₃**

The J-V curves of DSSCs fabricated using **D₈₋₁₁** as co-sensitizers along with well-known **HD-2** dye are shown in **Fig 5.12(a)** and their parameters are summarized in **Table 5.12**. As per results, the co-sensitized device with **D₂₂** ($\eta=8.85\%$ J_{SC}=23.63 mA/cm², V_{OC}=0.669 V, and FF=56.00%) shows an enhancement in the PCE when compared to **HD-2** dye alone, whereas **D₂₃** ($\eta = 6.72\%$ J_{SC}=17.89 mA/cm², V_{OC}=0.666 V, and FF=56.32%) displays a reduction in the efficiency when compared to **HD-2** dye alone. It is noteworthy that, V_{OC} in both cases have increased showing the efficient filling of vacant spaces between the molecules of **HD-2** dye. In order to get an insight into the spectral behaviour of devices, their IPCE studies were carried out and the results are given in **Fig 5.12(b)**. As expected, **HD-2+D₂₂** co-sensitized device displays a broad spectrum in the range of 400-550 nm with a maximum absorption around 68% which is higher than the device with **HD-2** dye alone. Conversely, the

device co-sensitized with **HD-2+D₂₃** exhibits a broad spectrum with a maxima of 55%, which can be the major reason for its low PCE.

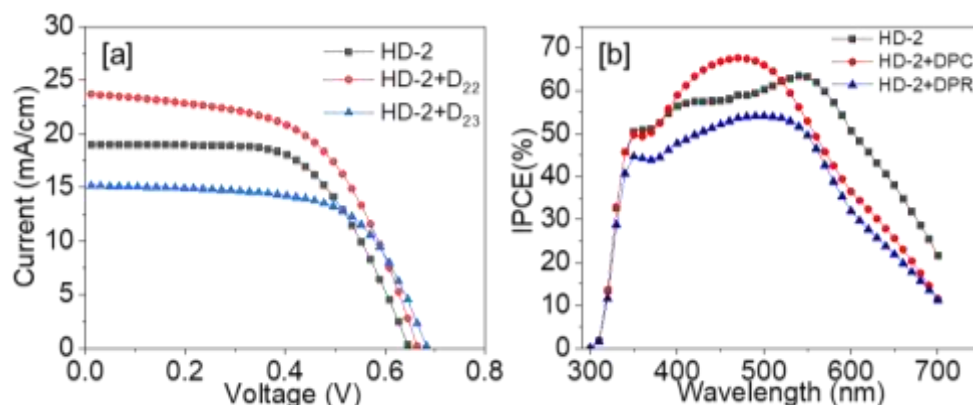


Fig 5.12 (a) Photocurrent density vs voltage; (b) IPCE spectra for **HD-2** based devices co-sensitized with **D₂₂₋₂₃** under illumination of simulated solar light (AM 1.5, 100 mW/cm²)

Table 5.12: Photovoltaic performance data of devices co-sensitized with **D₂₂₋₂₃**

Series	Sensitizer	Co-sensitizer	J _{sc} (mAcm ⁻²)	V _{oc} (V)	FF%	η%
	HD-2	-	19.03	0.652	60.49	7.49
Series 6	HD-2	D₂₂	23.63	0.669	56.00	8.85
		D₂₃	17.89	0.666	56.32	6.72

5.1.4.7 Photovoltaic performance of devices sensitized/co-sensitized with **D₂₄₋₂₇**

(Series-7)

*DSSCs sensitized with **D₂₄₋₂₇***

Fig 5.13(a) represents J-V curves for DSSCs sensitized with dyes **D₂₄₋₂₇** under AM 1.5G simulated sunlight with a light intensity of 100 mW/cm². The observed photovoltaic parameters are summarized in **Table 5.13**. As per the results, the DSSC device fabricated with the sensitizer **D₂₄** (η=2.31%, J_{sc}=5.134 mA/cm², V_{oc}=0.664 V, and FF=67.75%) shows a better photovoltaic parameters compared to devices sensitized with **D₂₅₋₂₇**. The highest PCE shown by **D₂₄** among the series is due to the good adsorption property of cyanoacetic acid on the TiO₂ surface. On the other hand, the devices with **D₂₅** (η=1.18%, J_{sc}=3.284 mA/cm², V_{oc}=0.545 V, and FF=65.87%) and remaining dyes display low PCE because of the lower adsorption ability of

sensitizers. Further, IPCE studies of the devices were carried out and the obtained spectra are given in Fig 5.13(b). The device with dye **D₂₄** shows a maxima of about 61% in the region of 400-500 nm, whereas **D₂₅** displays a broad spectrum at 400-550 nm with a maximum absorption 30%. Both the devices with **D₂₆₋₂₇** show peaks in the lower frequency region other than visible range.

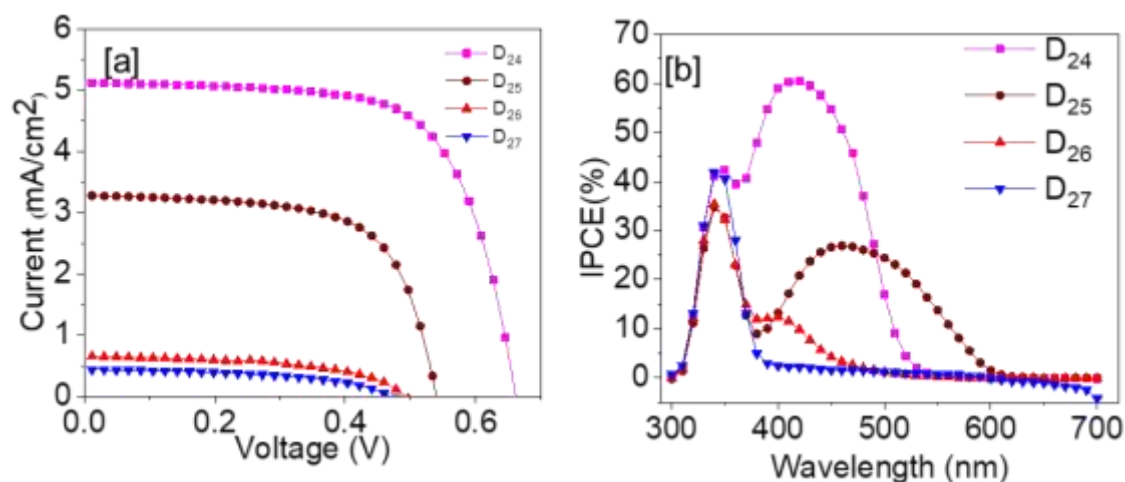


Fig 5.13 (a) Photocurrent density vs voltage; (b) IPCE characteristics for devices sensitized with **D₂₄₋₂₇** under illumination of simulated solar light (AM 1.5, 100 mW/cm²)

Table 5.13: Photovoltaic performance data of devices sensitized with **D₂₄₋₂₇**

Series	Sensitizers	J _{sc} (mAcm ⁻²)	V _{oc} (V)	FF%	η%
Series 7	D₂₄	5.134	0.664	67.75	2.31
	D₂₅	3.284	0.545	65.87	1.18
	D₂₆	0.686	0.499	53.50	0.18
	D₂₇	0.439	0.469	49.55	0.10

*DSSCs co-sensitized with **D₂₄₋₂₇***

DSSCs were fabricated using **D₂₄₋₂₇** as co-sensitizers along with well-known **HD-2** dye. The corresponding J-V curves obtained in co-sensitization experiments are presented in Fig 5.14(a) and the acquired parameters are summarized in Table 5.14. The results reveal that, the devices co-sensitized with **D₂₅₋₂₇** show a substantial

increase in the PCE values. On the other hand, the device sensitized with **HD-2+D₂₄** exhibits lower PCE than **HD-2** dye. It is interesting to note that, device co-sensitized with **D₂₆**($\eta=10.55\%$, $J_{sc}=23.85$ mA/cm², $V_{oc}=0.697$ V and $FF=63.49\%$) and **D₂₇**($\eta=10.25\%$, $J_{sc}=25.27$ mA/cm², $V_{oc}=0.679$ V, and $FF=59.69\%$) show a remarkable increase in PCE values. The obtained IPCE spectra for dyes of this series are depicted in **Fig 5.14(b)**. Here, the procured results are contrary to the J-V data obtained for the devices. This behaviour of the devices may be attributed to the absence of required conjugation in dyes **D₂₄₋₂₇**. All the devices display a broad spectrum of peaks in the visible region with a maxima in the range of 50-60 %, which is lesser than the **HD-2**. Thus, in the device, dye molecules could fill in the vacant voids efficiently in between the **HD-2** dye molecules, thereby increasing the V_{oc} values, and finally leading to enhancement of PCE values. It is interesting to observe that, the **D₂₄** shows lower PCE than **HD-2**, which may be attributed to the higher recombination rate caused by cyanoacetic acid anchor.

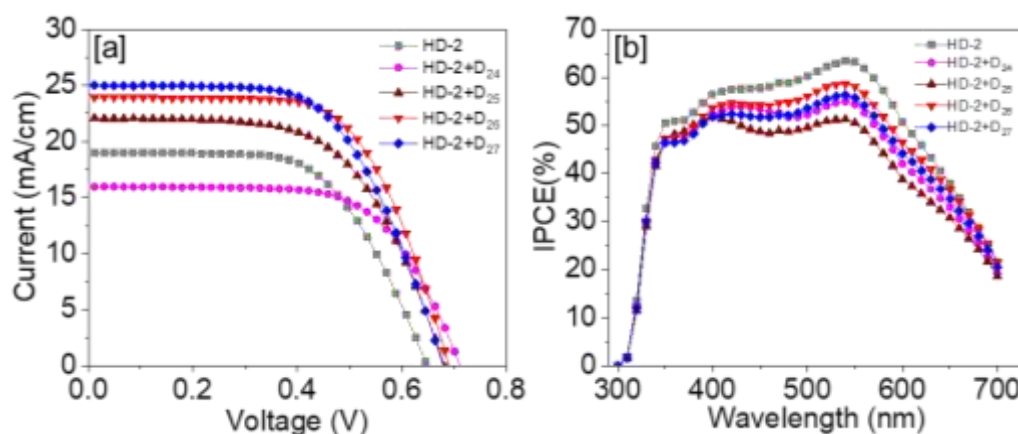


Fig 5.14 (a) Photocurrent density vs voltage; (b) IPCE spectra for **HD-2** based devices co-sensitized with **D₂₄₋₂₇** under illumination of simulated solar light (AM 1.5, 100 mW/cm²)

Table 5.14: Photovoltaic performance data of devices co-sensitized with **D₂₄₋₂₇**

Series	Sensitizer	Co-sensitizer	J _{SC} (mAcm ⁻²)	V _{OC} (V)	FF%	η%
	HD-2	-	19.03	0.652	60.49	7.49
Series 7	HD-2	D₂₄	15.99	0.714	64.56	7.37
		D₂₅	22.02	0.683	59.72	8.98
		D₂₆	23.85	0.697	63.49	10.55
		D₂₇	25.27	0.679	59.69	10.25

5.2 ELECTROCHEMICAL IMPEDANCE SPECTROSCOPY STUDIES

EIS studies were carried out for the devices sensitized with new dyes to get a better understanding of the interfacial charge-transfer processes. Generally, electron flow in DSSC is coupled with electronic and ionic transports. The driving force for the aforementioned transports is obtained due to the internal current generated in the device because of the different processes taking place in the dark and illumination. The Nyquist plot generated from the EIS study depicts the imaginary impedance, which is indicative of the capacitive and inductive character of the cell, versus the real impedance of the cell. Actually, in Nyquist plots activation-controlled processes with distinct time-constants show up as unique impedance curves and the shape of these curves provides an insight into the possible mechanism or important governing phenomena. Further, the observed Bode plot from EIS study deals with the frequency response of a cell simultaneously in terms of phase and magnitude. Such plots are useful for determining device stability as well as system identification from this frequency response.

In the present work, the diphenylamine based sensitizers/co-sensitizers (**D₁₋₂₇**) were subjected to EIS studies in order to evaluate the charge dynamics of operating DSSCs. This study is quite useful in evaluating the interfacial charge recombination

dynamics and redox processes taking place at photoactive anode/electrolyte interface. The equivalent circuit used to fit the data is given in **Fig. 5.15**.

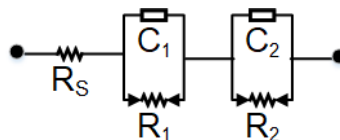


Fig. 5.15 Equivalent circuit diagram

For the sensitization of dyes, the capacitance C_1 and C_2 in the equivalent circuit have been replaced with constant phase element (CPE) since electrodes are having a rough surface. Generally in Nyquist plots, the higher frequency intercept on the real axis of semi-circle corresponds to series ohmic resistance (R_s) whereas the high-frequency region gives the interface capacitance (C_1) and charge transport resistance (R_1) at the counter electrode/electrolyte interface. Similarly, the low-frequency region attributes to chemical capacitance (C_2) and the charge recombination (R_2) resistance at the $\text{TiO}_2/\text{dye}/\text{electrolyte}$ interface. A detailed account of the EIS studies of the devices sensitized/co-sensitized with **D1-27** has been discussed below.

5.2.1 Material and methods

The EIS data, *i.e.* Nyquist and Bode plots for the fabricated devices were obtained from Biologic SP-150 potentiostat using solar simulator under the illumination of standard 1.5 G light source.

5.2.2 Experimental

The EIS studies were performed to analyze the interfacial charge recombination and carrier transport processes in fabricated DSSCs based on **D1-27** sensitizers/co-sensitizers (Bisquert 2003a; Fabregat-Santiago et al. 2005a), using an impedance analyzer potentiostat under solar illumination using a solar stimulator. The applied voltage was set at the V_{OC} of the DSSCs with AC amplitude fixed at 10 mV. The plots were fitted *via* Z-Fit software (Bio-Logic).

5.2.3 Results and discussion

Results of EIS studies of fabricated DSSCs using the dyes **D1-27** as sensitizers and cosensitizers along with **HD-2/N3** are discussed in the following section. The

obtained Nyquist and Bode plots for the devices are shown in **Figs 5.16-5.29** and the corresponding EIS parameters are tabulated in **Tables 5.15-5.21**.

5.2.3.1 *Electrochemical impedance studies of devices sensitized/co-sensitized with D₁₋₃ (Series-1)*

DSSCs sensitized with D₁₋₃

Fig 5.16(a) depicts the Nyquist plot of devices sensitized with **D₁₋₃** and the corresponding EIS parameters are tabulated in **Table 5.15**. For all the devices sensitized with dyes of the series, a single semicircle was obtained. The radii of the circles are in the order of **D₁ < D₃ < D₂**. The obtained order is in reverse with the obtained PCE values. The observed results suggest that, Greischer impedance predominates in these cases. Evidently, the devices with dyes **D₂** and **D₃** give Nyquist plots with larger radii, which can be accounted for the fast electron transport and long lifetime (τ_{eff}) of electron in the film. This happens if the R_r (dark reaction impedance) $\gg R_d$ (diffusion impedance), where Nernst impedance comes into play. In contrast, if $R_d \gg R_r$, Greischer impedance predominates which can be seen in the case of device with **D₁**, where a small semi-circle is observed.

Further, R_s value of devices with **D₁**(20.01 Ω) and **D₂**(20.27 Ω) were found to be almost similar but it is quite high for device with **D₃**(28.39 Ω) due to its high solvent resistance. Usually, larger the R_1 value, more difficult is the transfer of the injected electron from the TiO₂ back to the electrolyte. This indicates the suppression of back recombination in the cell device. Thus, the larger the R_1 leads to enhancement of V_{OC} . Here devices with **D₂**(108.5 Ω) and **D₃**(325.1 Ω) show very high R_1 values, whereas device with **D₁** demonstrates (23.42 Ω) a lower value. Even though, the trend of R_1 values are not in accordance with the obtained V_{oc} values, it is quite agreeing with the observed trend of ΔG_{reg} values. The descending order of R_2 values obtained for the tested devices with dyes is **D₂**(628.1 Ω) > **D₁**(9.53 Ω) > **D₃** (6.48 Ω), which is in accordance with calculated ΔG_{inj} and ΔG_{rec} of dyes. Although the device with **D₂** shows a fairly good resistance, it has exhibited inferior cell performance because of its poor anchoring property.

The obtained Bode phase plots are presented in **Fig 5.16**. An effective life time τ_{eff} of electrons in the CB of TiO_2 is calculated for all the dyes using equation **5.1**. The value of τ_{eff} depends on the density of charge traps which further contributes to V_{OC} value.

$$\tau_{\text{eff}} = \frac{1}{2\pi f} \quad (5.1)$$

Where, f is the frequency of the corresponding peak in the Bode plot. The parameter, τ_{eff} is related to the injection of electron to CB of TiO_2 and can be explained using two widely used theories, (i) Marcus-Greischer theory which states that, rate constants (or life-times) proportional to the energetic overlap between the TiO_2 (e^-) and the electron acceptors. (ii) The theory, which is based on the trap-limited diffusion/recombination applied to explain electron transport and recombination in DSSCs (Wang et al. 2005a). It is observed that, calculated τ_{eff} values for the devices is in the decreasing order of $\mathbf{D}_2(3.18 \text{ ms}) > \mathbf{D}_1(2.87 \text{ ms}) > \mathbf{D}_3(2.00 \text{ ms})$. In principle, longer electron lifetime specifies the better suppression of back reactions between the injected electrons and the electrolyte, which normally leads to improvement of the V_{OC} value. In the present study, the obtained τ_{eff} and V_{OC} values are not in agreement with the theoretical data. Here, the observed higher τ_{eff} can be explained on the basis of greater ΔG_{inj} energy, but the poor adsorption property of \mathbf{D}_3 has resulted in poor performance of the cell. The \mathbf{D}_1 with high τ_{eff} (2.87 ms) has brought about good performance in the device due to its good anchoring property.

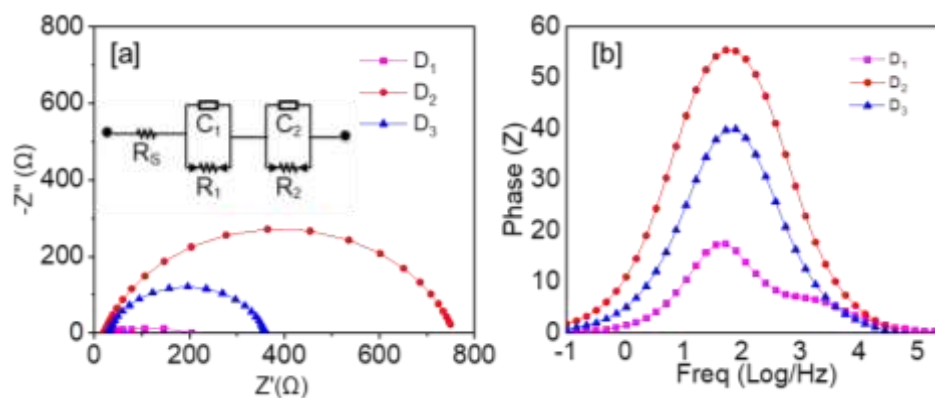


Fig 5.16 (a) Nyquist plots and (b) Bode plots of devices sensitized with \mathbf{D}_{1-3}

DSSCs co-sensitized with D1-3

Fig 5.17(a) depicts the Nyquist plots of devices co-sensitized using **D1-3** with **N3**. From the results, it is clear that, the plots consist of two distinct semicircles and the radii of semicircles obtained for all the devices are almost similar. The device with **N3+D3** shows a higher R_s (29.19 Ω) but lower J_{SC} (13.13 mAcm^{-2}) value than **N3** alone; however, still it shows a higher PCE value. Then, R_2 observed for the device with **N3+D1**(46.89 Ω) is greater than that of **N3** dye, whereas the R_s value (27.1 Ω) is similar to that of **N3**(27.1 Ω). The R_2 trend shown for co-sensitized devices are in the decreasing order as **N3+D2**(348.71 Ω) > **N3+D1**(32.07 Ω) > **N3+D3**(25.14 Ω). The R_1 value for device with **N3+D1** is quite higher (46.89 Ω) than that of **N3**(42.63 Ω) alone, indicating the effective filling of the voids by **D1** in between **N3** molecules. Although **N3+D2** device has shown less R_1 value (7.80 Ω), the V_{OC} has been enhanced to 0.66V.

The EIS Bode phase plots for **N3** based devices co-sensitized with **D1-3** dyes are shown in **Fig 5.17(b)**. All the devices exhibit two characteristic peaks; one at a higher frequency corresponding to the charge transfer at the Pt/electrolyte interface and another at a lower frequency conforming to the charge transfer at the TiO_2 /dye/electrolyte interface. These two peaks are arising due to the difference in local I_3^- concentration in the device. Under illumination, the I_3^- is formed in the device (in situ) due to the dye regeneration at TiO_2 /electrolyte interface. But in the dark condition, I_3^- generates at counter electrode and it penetrates to TiO_2 film by diffusion. The characteristic peak appeared at the lower frequency in the Bode plot is related to the charge recombination rate, and its reciprocal is associated with the electron lifetime. The τ_{eff} values were calculated using the equation 5.1 and they were found to be in the decreasing order, **N3+D2**(6.49 ms) > **N3+D3**(4.39 ms) > **N3+D1**(3.18 ms).

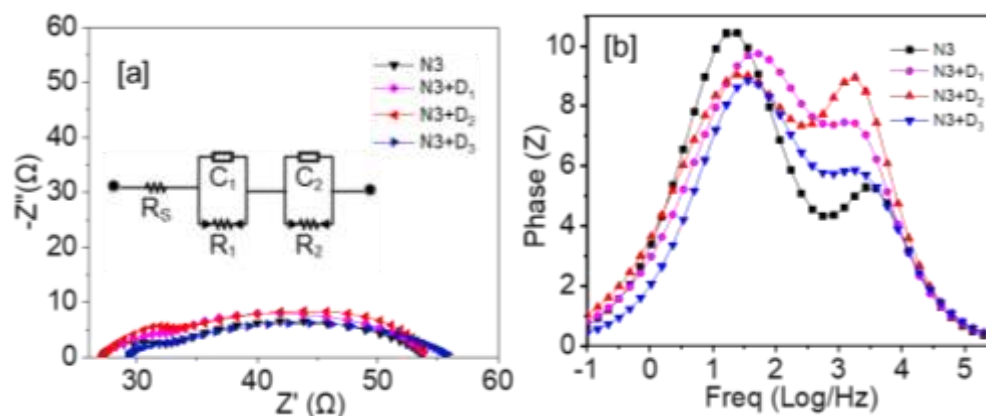


Fig 5.17 (a) Nyquist plots and (b) Bode plots for N3 based devices co-sensitized with D1-3

Table 5.15: EIS parameters of devices sensitized and co-sensitized using D1-3 dyes

Sensitizer/Co-Sensitizer	τ_{eff} (ms)		R_s (Ω)		R_1 (Ω)		R_2 (Ω)	
	Dye	Dye+ N3	Dye	Dye+ N3	Dye	Dye+ N3	Dye	Dye+ N3
N3	7.98	-	27.21	-	22.74	-	42.63	-
D1/ N3 + D1	2.87	3.18	20.01	27.1	9.53	32.07	23.42	46.89
D2/ N3 + D2	3.18	6.49	20.27	28.23	628.1	348.7	108.5	7.80
D3/ N3 + D3	2.00	4.39	28.39	29.19	6.48	25.14	325.1	19.37

5.2.3.2 Electrochemical impedance studies of devices sensitized/co-sensitized with D4-7 (Series-2)

DSSCs sensitized with D4-7

Fig 5.18(a) depicts the Nyquist plots of devices sensitized with D4-7. All the dyes exhibit only single semicircle. In these sketches, the semicircle at the low frequency relating to the diffusion of I_3^- in the cell, is not observed, because of the low viscosity of the electrolyte. Here, the area of the semicircle is equally important. In the present study the radii of Nyquist plots obtained are in the increasing order $D_5 < D_4 < D_6 < D_7$. Thus, the obtained high efficiency of device with D4 is ascribed to its high Greischer impedance. The reason for the lower efficiency of device with D5 has been already discussed under theoretical and photovoltaic studies. All the devices sensitized with dyes show similar R_s values (19-20 Ω) signifying that, the resistance

offered by the solution is almost same. In general, R_1 and V_{OC} values are interrelated. The larger R_1 value suggests that, it is more difficult to transfer the injected electrons from the TiO_2 surface back to the electrolyte and thus, the back recombination process can be suppressed in the device. In the present study, the devices with **D4-7** display R_1 values of 171.2, 77.71, 355.9 and 9.75 Ω , respectively while the descending order of R_2 values obtained for the tested dyes is **D7** (301.3 Ω) > **D6** (210.8 Ω) > **D4** (22.82 Ω) > **D5** (0.15 Ω). Thus, the results indicate that, the recombination process is slow for **D6** and **D7**. However, it is not reflected in their V_{OC} and η values because they possess poor anchoring ability as explained on the basis of photophysical studies.

The Bode phase plots of the devices are depicted in **Fig 5.18(b)**. From the traces, an effective lifetime (τ_{eff}) of electrons in the CB of TiO_2 were calculated, and the obtained values are listed in **Table 5.16**. Generally, τ_{eff} depends on the density of charge traps which further contributes to V_{OC} value of the cell. The values of τ_{eff} were calculated using equation 5.1. Obviously, the longer τ_{eff} value can be an indicative of the less electron recombination rate, thus leading to the improvement of the V_{OC} value. From the results it is evident that, the dye **D7** bearing barbituric acid shows the highest electron lifetime (1.38 ms) among the carboxylic acid based sensitizers, indicating lower recombination process in it. However, the observed lower V_{OC} value might be a result of inferior electron injection and the charge recombination rate.

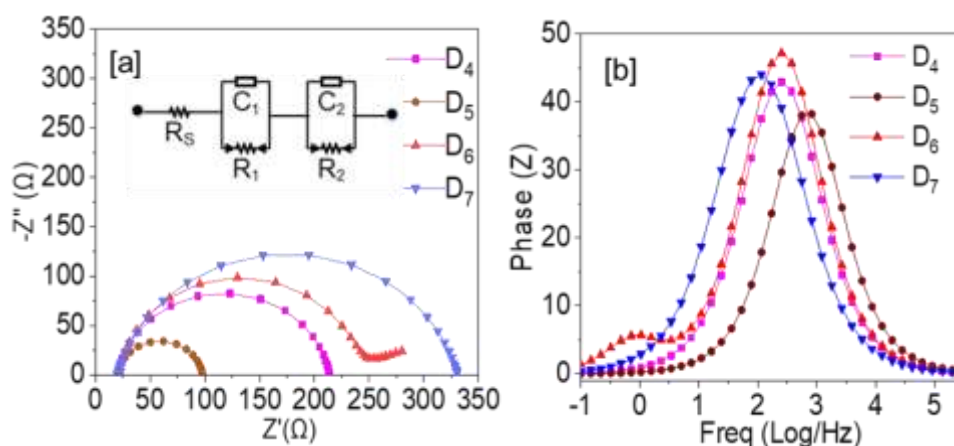


Fig 5.18 (a) Nyquist plots and (b) Bode plots of devices sensitized with **D4-7**

DSSCs co-sensitized with D₄₋₇

Fig 5.19(a) presents the Nyquist plots of **HD-2** based devices co-sensitized with **D₄₋₇** dyes. From the results, it is clear that, the devices fabricated with **HD-2** and **HD-2+D₇** show two semicircles unlike sensitized dyes, whereas **HD-2+D₄**, **HD-2+D₅** and **HD-2+D₆** display one semicircle similar to corresponding sensitized results. All the co-sensitized devices show quite dissimilar R_s values different from the sensitized results. The device with **HD-2+D₄** exhibits R_s (19.82 Ω) value similar to that of **HD-2** alone. Among the devices, the cell with **HD-2+D₅** shows the lowest R_s (12.98 Ω) value, whereas **HD-2+D₇** displays the highest value (22.50 Ω). The R_2 observed for the device with **HD-2+D₄**(18.48 Ω) is quite high compared to all the other devices of the series, but it is comparable to that of **HD-2**(15.31 Ω). The R_2 trend shown by co-sensitized devices are in the decreasing order as: **HD-2+D₄**(18.48 Ω) > **HD-2+D₇**(13.97 Ω) > **HD-2+D₅**(5.83 Ω) > **HD-2+D₆**(2.33 Ω). The R_1 value for the device **HD-2+D₅** was found to be very high (152.6 Ω) when compared to all other devices. Here, devices with **HD-2**(4.093 Ω), **HD-2+D₄**(6.67 Ω) and **HD-2+D₇**(3.88 Ω) display comparable results.

Table 5.16: EIS parameters of devices sensitized and co-sensitized using **D₄₋₇** dyes

Sensitizer/Co-Sensitizer	τ_{eff} (ms)		R_s (Ω)		R_1 (Ω)		R_2 (Ω)	
	Dye	Dye+ HD-2	Dye	Dye+ HD-2	Dye	Dye+ HD-2	Dye	Dye+ HD-2
HD-2	3.01	-	19.35	-	15.31	-	4.09	-
D₄/HD-2+ D₄	0.62	0.42	19.97	19.82	22.82	18.48	171.2	6.67
D₅/HD-2+ D₅	0.19	0.592	19.98	12.98	0.15	5.83	77.71	152.6
D₆/HD-2+ D₆	0.63	0.63	19.56	18.45	210.8	2.33	355.9	23.96
D₇/HD-2+ D₇	1.38	1.99	19.96	22.50	301.3	13.97	9.757	3.88

EIS Bode phase plots of the co-sensitized devices are depicted in **Fig 5.19(b)**. The plot corresponding to **HD-2+D₇** exhibits two characteristic peaks. Usually, the peak at the high frequency corresponds to the charge transfer at the Pt/electrolyte

interface and the another one at low frequency accounts for the charge transfer at the $\text{TiO}_2/\text{dye}/\text{electrolyte}$ interface, similar to the plot of **HD-2** dye alone. The peak appeared at the lower frequency in the Bode plot is related to the charge recombination rate, and its reciprocal is associated with the electron lifetime. Here, obtained Bode phase plots of devices co-sensitized with **D4**, **D5** and **D6** display only a single peak, similar to that of corresponding sensitized devices. The appearance of single peak or in other words, the merging of the high and low frequency peaks in case of **D4**, **D5** and **D6** co-sensitized devices is an indication of large recombination rates of dyes in the devices. Further, the τ_{eff} values were calculated and all the obtained values were found to be less than that of **HD-2** dye (3.01 ms) alone. Among all the co-sensitized devices, the device with **D7** shows the highest τ_{eff} value of 1.992 ms. Conclusively, the results obtained from EIS Bode phase plots are in consistent with the PCE values obtained.

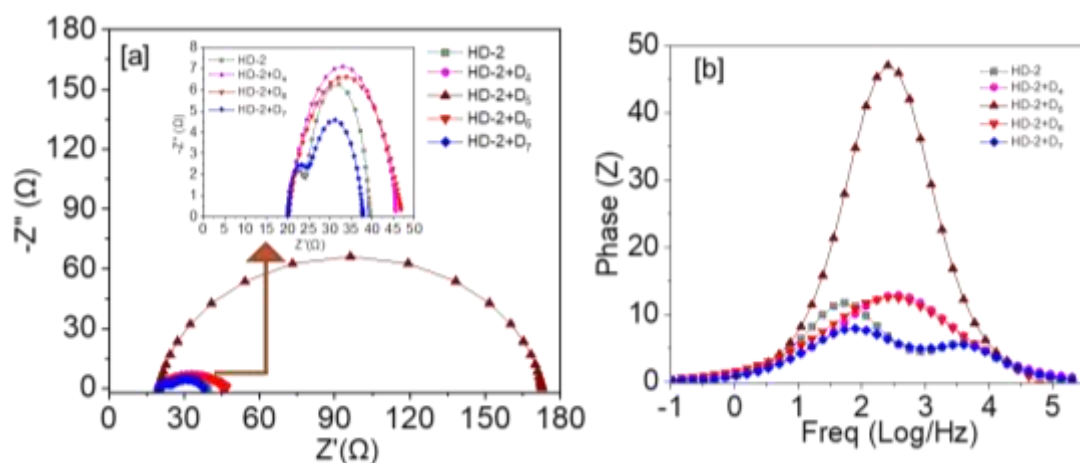


Fig 5.19 (a) Nyquist plots and (b) Bode plots for **HD-2** based devices co-sensitized with **D4-7**

5.2.3.3 Electrochemical impedance studies of devices sensitized/co-sensitized with **D8-11** (Series-3)

*DSSCs sensitized with **D8-11***

Fig 5.20(a) gives the Nyquist plots of devices sensitized with **D8-11**. Further, the obtained EIS data are tabulated in **Table 5.17**. The radii of the Nyquist plots of devices are in the ascending order: **D8** < **D10** < **D9** < **D11**. From the results it is clear that, more resistance has been observed in the device sensitized with **D11**. On

comparing the PCE values with the EIS parameters, it can be noted that the devices follow Greischer impedance. Similar to previous series, characteristic single semicircle is observed in this case also. By fitting the Nyquist data in the circuit, the R_s values were calculated for the devices. They are in the order: $D_8(19.9 \Omega) < D_{10}(19.92 \Omega) < D_{11}(20.27 \Omega) < D_9(28.2 \Omega)$. Except the device with D_9 all the others show similar R_s values. The highest R_s value of D_9 indicates the maximum resistance imparted by the solution. Also, it shows the highest resistance in the interface of counter electrode and the electrolyte. R_1 values obtained are in the increasing order as: $D_{10}(5.67 \Omega) < D_{11}(7.81 \Omega) < D_8(41.62 \Omega) < D_9(211.3 \Omega)$. The generated R_2 values are in the order of $D_8(83610 \Omega) > D_{11}(221.0 \Omega) > D_{10}(39.33 \Omega) > D_9(3.17 \Omega)$.

The Bode phase plots of the devices are depicted in **Fig 5.20(b)**. With the help of Bode phase graphs, τ_{eff} values were calculated following the equation 5.1. The obtained values for the D_{8-11} based devices are 2.7, 13.97, 0.634 and 1.43 ms, respectively. Here, the results of the Bode phase plots are in accordance with Nyquist plots.

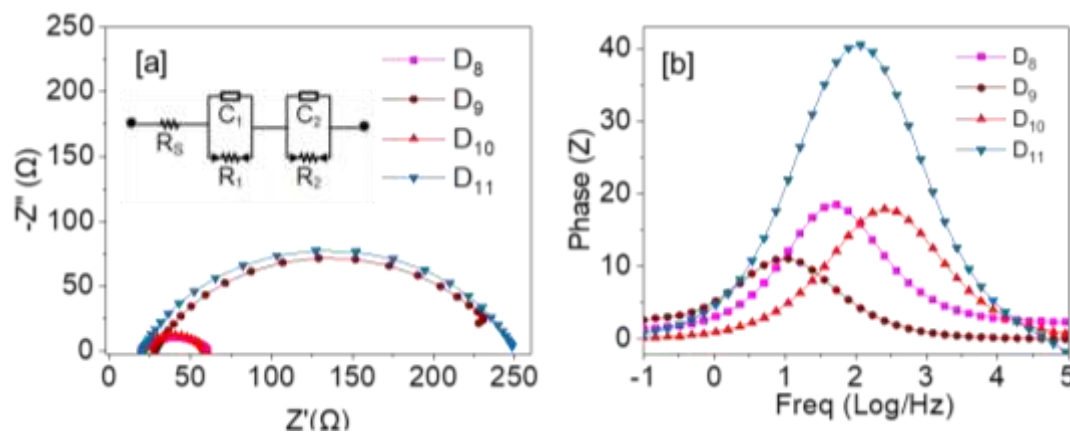


Fig 5.20 (a) Nyquist plots and (b) Bode plots of devices sensitized with D_{8-11}

DSSCs co-sensitized with D_{8-11}

Fig 5.21(a) gives the Nyquist plots of devices sensitized with D_{8-11} . Further, the obtained EIS data are tabulated in **Table 5.17**. The radii of the Nyquist plots of devices are in the order: $HD-2+D_{11} = HD-2+D_{10} < HD-2+D_8 < HD-2+D_9$. From the plots, it is observed that device with D_9 shows the highest resistance and it is reflected in its PCE value. Further, the R_s values obtained for the D_{8-11} based devices are 16.78, 32.97, 29.65 and 20.27 Ω , respectively. Further their R_1 values are 5.29, 15.41, 16.47

and 13.81 Ω , respectively. The calculated R_1 values for the devices with **D₉₋₁₁** indicate that, the resistance in counter electrode-electrolyte is almost same. R_2 data also follow the same order as 13.81, 4.67, 3.70, 5.49 Ω , respectively. The highest charge transfer resistance of the device co-sensitized with **D₈** has reflected in its efficiency.

Table 5.17: EIS parameters of devices sensitized and co-sensitized using **D₈₋₁₁** dyes

Sensitizer/ Co-Sensitizer	τ_{eff} (ms)		R_s (Ω)		R_1 (Ω)		R_2 (Ω)	
	Dye	Dye+ HD-2	Dye	Dye+ HD-2	Dye	Dye+ HD-2	Dye	Dye+ HD-2
HD-2	3.01	-	19.35	-	15.31	-	4.09	-
D₈ /HD-2+D₈	2.73	2.99	19.9	16.78	41.62	5.29	83610	13.81
D₉ / HD-2+D₉	13.97	2.90	28.2	32.97	211.3	15.41	3.17	4.67
D₁₀/HD-2+D₁₀	0.634	0.89	19.92	29.65	5.671	16.47	39.33	3.70
D₁₁/HD-2+D₁₁	1.43	0.97	20.27	27.97	7.814	13.81	221.0	5.49

The Bode plots of the devices co-sensitized with **D₈₋₁₁** are displayed in **Fig 5.21(b)**. These plots follow the same trend as Nyquist graphs. Except with **D₁₀₋₁₁**, all other devices display two peaks in the Bode plots. Further, τ_{eff} values were calculated from the Bode plots for **D₈₋₁₁** and the values obtained are 2.99, 2.90, 0.887 and 0.972 ms respectively.

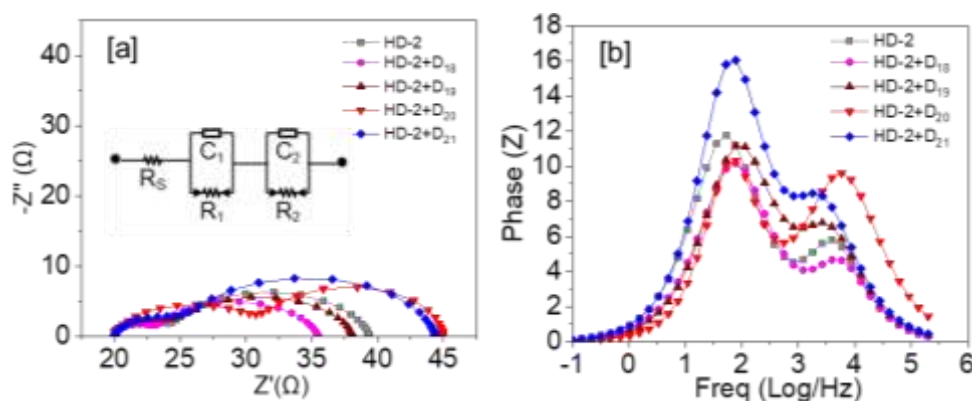


Fig 5.21 (a) Nyquist plots and (b) Bode plots for **HD-2** based devices co-sensitized with **D₈₋₁₁**

5.2.3.4 Electrochemical impedance studies of devices sensitized/co-sensitized with D_{12-17} (Series-4)

DSSCs sensitized with D_{12-17}

The devices sensitized with D_{12-17} were subjected to EIS studies and the results are summarized in **Table 5.18**. The observed Nyquist plots are presented in **Fig 5.22(a)**. It is evident from the plots, the radii of the semicircles are in the order $D_{17} < D_{16} < D_{12} < D_{14} < D_{13} < << D_{15}$. The obtained results are in accordance with the observed PCE values, indicating the presence of Greischer impedance in the devices. Here, the observed low resistance of device sensitized with D_{17} reveals the moderate performance of the device. In contrast, the very high radius of Nyquist plot of the device with D_{15} indicates the immense resistance experienced in the device. The R_s values of the devices were found to be in the order of D_{17} (0.01 Ω) < D_{12} (19.89 Ω) < D_{13} (19.89 Ω) < D_{14} (0.019 Ω) < D_{15} (19.97 Ω) < D_{16} (28.43 Ω). The values (R_1) of resistance in the interface of the counter electrode and the electrolyte for different devices are in the order: D_{12} (29.32 Ω) < D_{17} (77.54 Ω) < D_{16} (134.6 Ω) < D_{15} (389.6 Ω) < D_{14} (1715 Ω) < D_{13} (2227 Ω). It is observed that, these values are quite high in this particular series. Similarly, the obtained R_2 values for D_{12-17} are 1422, 13.93, 19.93, 13430, 553.3 and 46.88 Ω , respectively. The extremely high R_2 value of device sensitized with D_{15} has reflected in its Nyquist plot. Here, the observed high resistance is mainly due to the high recombination rate of benzoic acid anchor.

Fig 5.22(b) shows the Bode phase plots of the devices sensitized with dyes D_{12-17} . The trend obtained in Bode phase plots is slightly different from their corresponding Nyquist graphs. The τ_{eff} values calculated from Bode plot are in the order: D_{12} (2.78 ms) < D_{15} (4.42 ms) = D_{13} (4.42 ms) < D_{14} (4.43 ms) < D_{17} (9.43 ms) < D_{16} (14.15 ms).

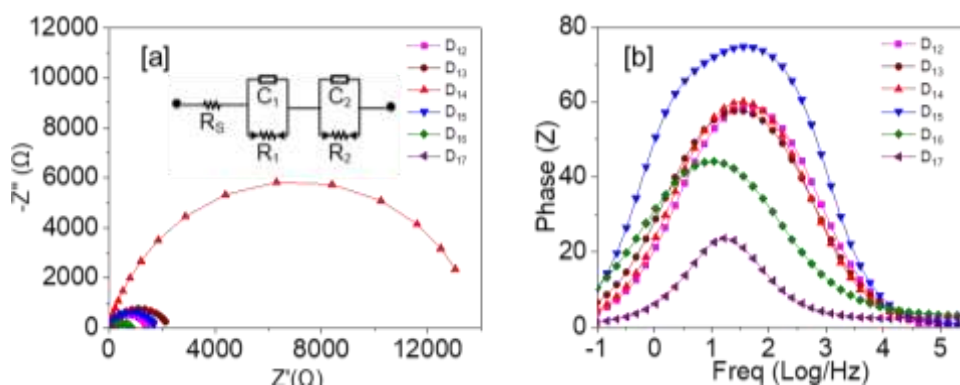


Fig 5.22 (a) Nyquist plots and (b) Bode plots of devices sensitized with **D12-17**

DSSCs co-sensitized with D12-17

The Nyquist plots for the devices co-sensitized with dyes **D12-17** are depicted in **Fig 5.23(a)** and the corresponding EIS parameters are given in **Table 5.18**. All the devices show semicircles with almost similar radii. But the radii of semicircles for the devices with **D16-17** are slightly more than that of the other dyes. This is in accordance with observed PCE values. All the R_s values are obtained in the range of 19.75-20.21 Ω indicating their similar solution resistance. Further, the R_1 values obtained for the devices with **HD-2+D12**, **HD-2+D13**, **HD-2+D14**, **HD-2+D15**, **HD-2+D16**, **HD-2+D17** are 15.43, 5.29, 18.08, 0.13, 18.56 and 17.91 Ω , respectively. Furthermore, R_2 data calculated by fitting in circuit, are in the order: **HD-2+D14**(0.066 Ω) < **HD-2+D12** (3.785 Ω) < **HD-2+D17**(5.196 Ω) < **HD-2+D13**(14.73 Ω) < **HD-2+D15**(17.93 Ω) < **HD-2+D16**(51.96 Ω). It is interesting to note that, both the R_1 and R_2 resistances obtained for the devices are quite less. Thus, variation in the device resistance is clearly depending upon R_1 and R_2 values of the cell.

Bode phase plots of the devices co-sensitized with **D12-17** is given in **Fig 5.23(b)**. As seen in the Bode phase plots, devices with **HD-2+D12** and **HD-2+D15** exhibit single peak whereas rest of the devices display two peaks. The calculated τ_{eff} values using the equation 5.1 were found to be in the range of 1.37-4.35 ms.

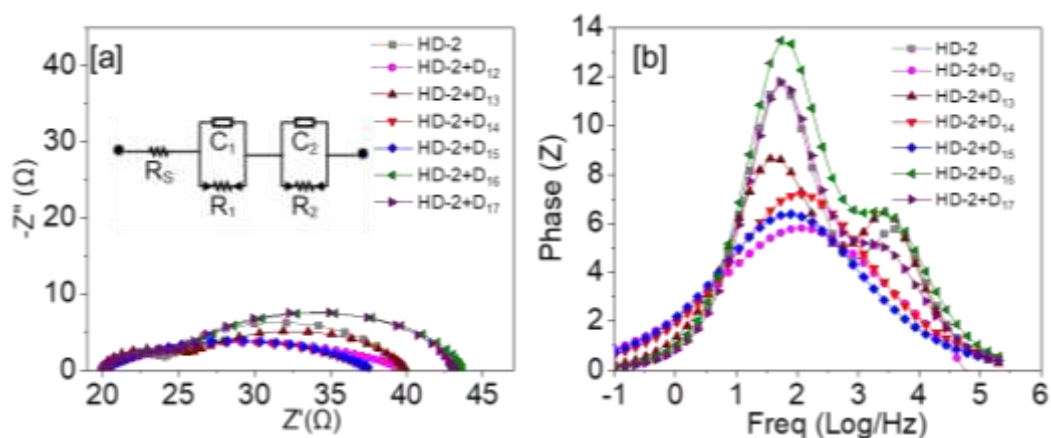


Fig 5.23 (a) Nyquist plots and (b) Bode plots for **HD-2** based devices co-sensitized with **D8-11**

Table 5.18: EIS parameters of devices sensitized and co-sensitized using **D12-17** dyes

Sensitizer/Co-Sensitizer	τ_{eff} (ms)		R_s (Ω)		R_1 (Ω)		R_2 (Ω)	
	Dye	Dye+ HD-2	Dye	Dye+ HD-2	Dye	Dye+ HD-2	Dye	Dye+ HD-2
HD-2	3.01	-	19.35	-	15.31	-	4.09	-
D12/HD-2+D12	2.78	1.37	19.89	20.21	29.32	15.43	1422	3.79
D13/HD-2+D13	4.42	4.35	19.89	19.98	2227	5.29	13.93	14.73
D14/HD-2+D14	4.43	1.37	0.019	19.75	1715	18.08	19.93	0.07
D15/HD-2+D15	4.42	2.06	19.97	19.82	389.6	0.132	13430	17.93
D16/HD-2+D16	14.15	2.99	28.43	19.94	134.6	18.56	553.3	51.96
D17/HD-2+D17	9.43	2.99	0.01	19.94	77.54	17.91	46.88	5.19

5.2.3.5 Electrochemical impedance studies of devices sensitized/co-sensitized with **D18-21** (Series-5)

DSSCs sensitized with D18-21

Nyquist plots for devices sensitized with **D18-21** are given in **Fig 5.24(a)** and the EIS data are tabulated in **Table 5.19**. Similar to other series, single semi circles were obtained in the Nyquist plots and the radii of the semicircles are in the order: **D21** > **D19** > **D18** > **D20**. Unlike other series, the higher radius in this Nyquist plot corresponds to the device that shows the highest PCE. Thus, it can be inferred that, Nernst

impedance is predominating in these devices. Further, the resistances offered in the devices were obtained by fitting the data in appropriate circuit shown in **Fig 5.15**. R_s values for the devices are in the ascending order: **D19** (1.357 Ω) < **D20**(19.98 Ω) < **D21**(19.99 Ω) < **D18**(20.42 Ω). Even though, the solution resistance offered by the device with **D19** is less, it is not reflected in PCE values. Further, R_1 and R_2 values were obtained from circuit fitting; the R_1 values are in the order: **D18**(17.47 Ω) < **D19**(81.3 Ω) < **D20**(1.674 Ω) < **D21**(775900 Ω), while the R_2 values are in the order: **D18**(24.53 Ω) < **D19**(582.9 Ω) < **D20**(62.34 Ω) < **D21**(998.6 Ω).

Fig 5.24(b) shows the Bode phase plots of the devices sensitized with dyes **D18-21**. From the figure it is clear that, in case of devices with **D19** and **D21**, there is shift of peak to the high frequency region. The observed trend of these devices is similar to the Nyquist plots. Further, the lifetime τ_{eff} values obtained are in the order **D21**(6.99 Ω) > **D20**(2.95 Ω) < **D19**(2.807 Ω) < **D18**(0.19 Ω).

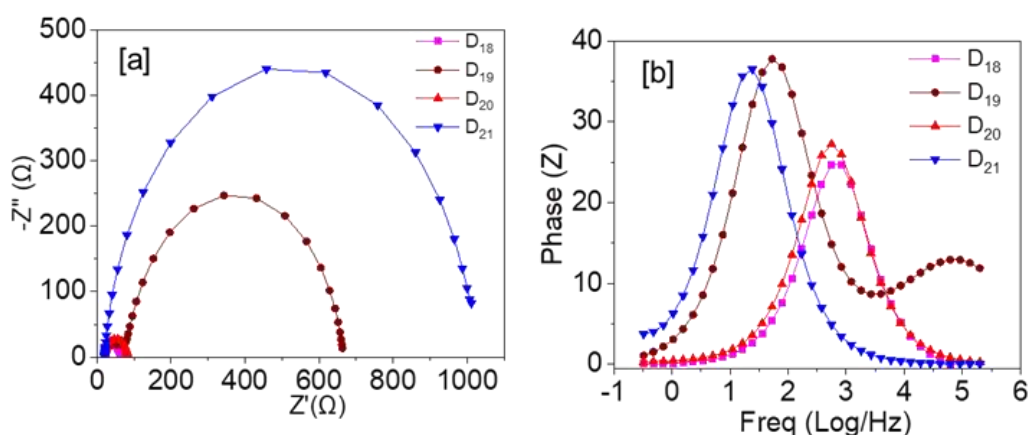


Fig 5.24 (a) Nyquist plots and (b) Bode plots of devices sensitized with **D18-21**

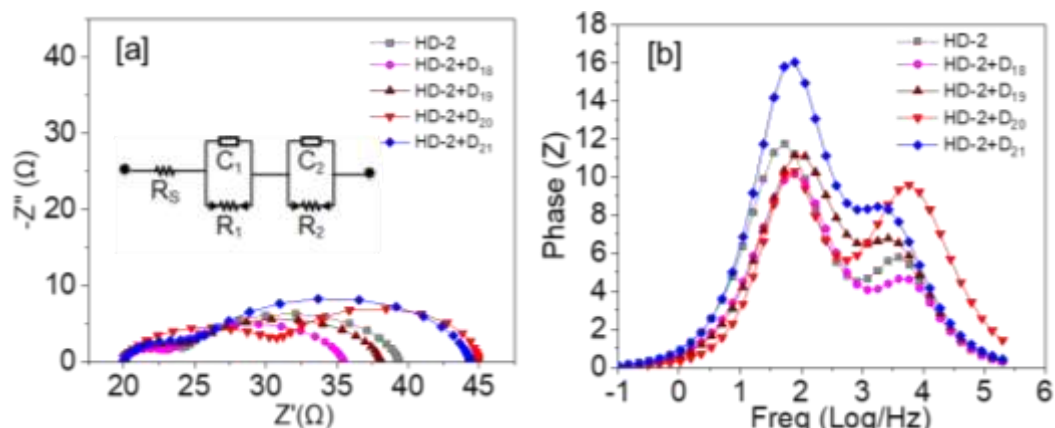


Fig 5.25(a) Nyquist plots and **(b)**Bode plots for **HD-2** based devices co-sensitized with **D18-21**

DSSCs co-sensitized with D18-21

Nyquist plot for devices co-sensitized with **D18-21** along with **HD-2** dye are presented in **Fig 5.25(a)** and the EIS data are tabulated in **Table 5.19**. In this series, all the devices are giving two semicircles having almost same radii, indicating similar performances. The device with **HD-2+D18** shows lower radius of semicircle, demonstrating the highest hike in PCE. Further, the R_s values of devices with **HD-2+D18-21** are 18.76, 17.78, 20.82 and 15.51 Ω , respectively. It is noteworthy that, the R_s values obtained for co-sensitization devices are almost in the same range. The R_1 values calculated for the devices with **HD-2+D18**, **HD-2+D19**, **HD-2+D20** and **HD-2+D21** are 12.55, 13.72, 13.38 and 19.06 Ω , respectively. Similarly, the R_2 values calculated for the devices with **HD-2+D18**, **HD-2+D19**, **HD-2+D20** and **HD-2+D21** are 2.98, 4.46, 11.76 and 5.36 Ω , respectively.

The Bode phase plots of the devices are displayed in **Fig 5.25(b)**. Two distinct peaks are observed for all the co-sensitized devices. The results reveal that, the device with **HD-2+D21** showcases the highest resistance. From the plots τ_{eff} were calculated using the equation 5.1 and the obtained value for **HD-2+D18**, **HD-2+D19**, **HD-2+D18** and **HD-2+D18** are 2.06, 1.99, 1.933 and 2.06 ms, respectively. These values are less than that of **HD-2** (3.01 ms).

Table 5.19: EIS parameters of devices sensitized and co-sensitized using **D18-21** dyes

Sensitizer/Co-Sensitizer	τ_{eff} (ms)		R_s (Ω)		R_1 (Ω)		R_2 (Ω)	
	Dye	Dye+ HD-2	Dye	Dye+ HD-2	Dye	Dye+ HD-2	Dye	Dye+ HD-2
HD-2	3.01	-	19.35	-	15.31	-	4.09	-
D18/HD-2+D18	0.19	2.057	20.42	18.76	17.47	12.55	24.53	2.98
D19/HD-2+D19	2.81	1.997	1.36	17.78	81.3	13.72	582.9	4.46
D20/HD-2+D20	2.95	1.933	19.98	20.82	1.67	13.38	62.34	11.76
D21/HD-2+D21	6.55	2.057	19.99	15.51	77590	19.06	998.6	5.36

5.2.3.6 Electrochemical impedance studies of devices sensitized/co-sensitized with D_{22-23} (Series-6)

DSSCs sensitized with D_{22-23}

Fig 5.26(a) gives the Nyquist plots of the devices sensitized with D_{22-23} dyes and the corresponding data are given in **Table 5.20**. In this particular series, interestingly two semicircles are observed in the Nyquist plots. Here, the device with D_{23} shows semicircles with higher radii indicating high resistance in the cell. Further, the obtained R_s values for the devices with D_{22-23} are 18.10 and 58.48 Ω , respectively. The calculated R_1 values for the devices with D_{22-23} are 18.05 and 18.52 Ω , respectively. In contrary, observed R_2 values show a large variation and the values obtained are 6.49 and 72.77 Ω , respectively.

The Bode phase plots of the devices are displayed in **Fig 5.26(b)** and the graphs show two peaks similar to their Nyquist plots. From the plots τ_{eff} values were calculated and the obtained values are in the increasing order as D_{22} (1.33 ms) < D_{23} (2.96 ms).

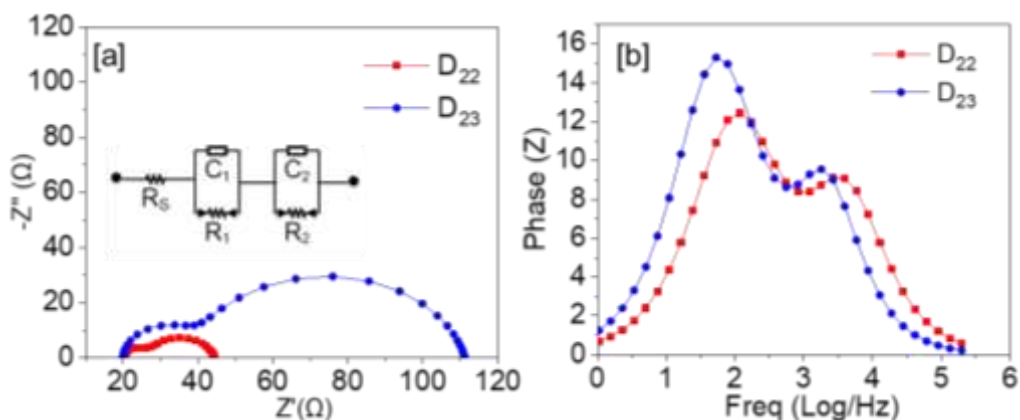


Fig 5.26 (a) Nyquist plots and (b) Bode plots of devices sensitized with **D₂₂₋₂₃** DSSCs co-sensitized with **D₂₂₋₂₃**

Fig 5.27(a) depicts the Nyquist plots of the devices co-sensitized with **D₂₂₋₂₃** along with **HD-2** dye and the generated data are summarized in **Table 5.20**. The graph for the device with **HD-2+D₂₃** ($\eta=6.72\%$) is showing more resistance than that of **HD-2+D₂₂** ($\eta=8.85\%$). The R_s values obtained for the devices with **HD-2+D₂₂** and **HD-2+D₂₃** are 16.2 and 22.44 Ω , respectively. The R_1 values of devices with **HD-2+D₂₂** and **HD-2+D₂₃** are 3.78 and 19.07 Ω , respectively. The R_2 values for **HD-2+D₂₂** and **HD-2+D₂₃** are 14.35, 6.87 Ω , respectively.

Bode phase plots of the devices are shown in **Fig 5.27(b)** and the same trend has been observed as in Nyquist plots. From the curves, the τ_{eff} values were calculated and the obtained values are in the order: **HD-2+D₂₂**(1.93 ms) < **HD-2+D₂₃**(2.06 ms). Thus, all the above mentioned observations may be attributed to the conceptually new A-D- π -D-A design strategy used for dyes **D₂₂₋₂₃**.

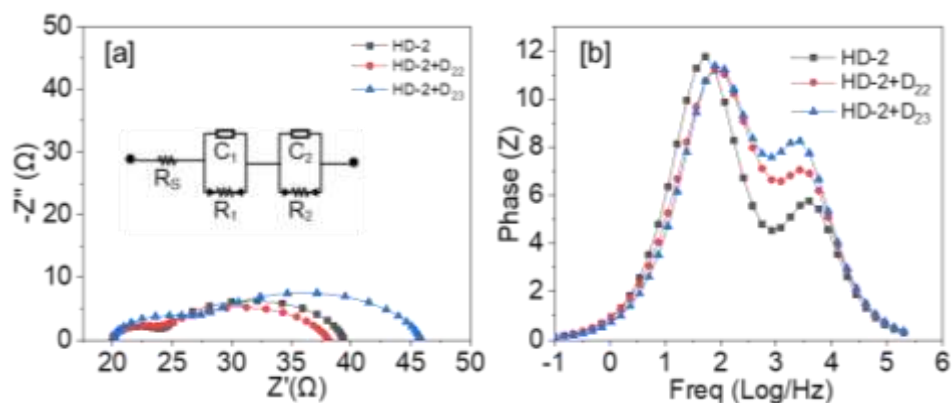


Fig 5.27(a) Nyquist plots and (b) Bode plots for **HD-2** based devices co-sensitized with **D₂₂₋₂₃**

Table 5.20: EIS parameters of devices sensitized and co-sensitized using **D22-23** dyes

Sensitizer/ Co- Sensitizer	τ_{eff} (ms)		R_s (Ω)		R_1 (Ω)		R_2 (Ω)	
	Dye	Dye+ HD-2	Dye	Dye+ HD-2	Dye	Dye+ HD-2	Dye	Dye+ HD-2
HD-2	3.009	-	19.35	-	15.31	-	4.09	-
D22/HD-2+D22	1.33	1.93	18.10	16.20	18.05	3.78	6.49	14.35
D23/HD-2+D23	2.97	2.06	58.48	22.44	18.52	19.07	72.77	6.87

5.2.3.7 Electrochemical impedance studies of devices sensitized/co-sensitized with D_{24-27} (Series-7)

DSSCs sensitized with D_{24-27}

Nyquist curves of the devices sensitized with dyes D_{24-27} are presented in **Fig 5.28(a)** and the corresponding parameters are tabulated in **Table 5.21**. For these dyes, single semicircle are observed in the Nyquist traces and the radii of the semicircles obtained for the devices are in the order: $D_{24} > D_{26} > D_{27} > D_{25}$. From the values fitted as per circuit, the R_s values obtained are ranging from 17.67-19.98 Ω . Similarly, R_1 values obtained are in the order: $D_{26}(0.01 \Omega) < D_{24}(341.5 \Omega) < D_{25}(586.4 \Omega) < D_{27}(11380 \Omega)$ whereas the R_2 values are in the order: $D_{26}(13850 \Omega) > D_{24}(13590 \Omega) > D_{27}(4.01 \Omega) > D_{25}(0.67 \Omega)$.

Fig 5.28(b) gives the Bode plots of the sensitized devices. From the curves, the τ_{eff} values were calculated and the obtained values are in the order: $D_{24}(6.46\text{ms}) < D_{27}(6.696 \text{ ms}) < D_{25}(9.277 \text{ ms}) < D_{26}(10.01 \text{ ms})$. The trend obtained for Bode plots is similar to that of Nyquist traces.

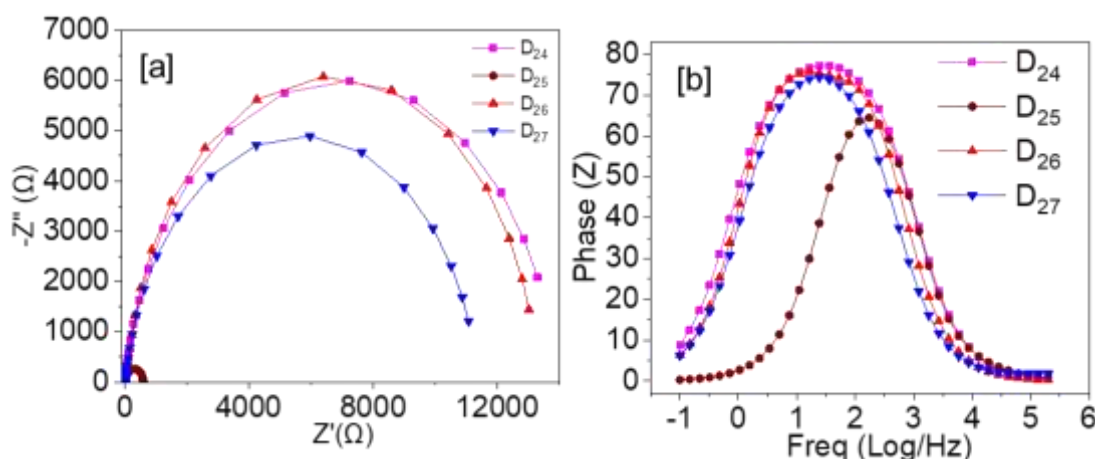


Fig 5.28 (a) Nyquist plots and (b) Bode plots of devices sensitized with **D₂₄₋₂₇**

DSSCs co-sensitized with D₂₄₋₂₇

Fig 5.29(a) depicts the Nyquist plots of the devices co-sensitized with **D₂₄₋₂₇** along with **HD-2**. Their data are summarized in Table 5.21. Two semicircles are obtained for the Nyquist plots of the devices. The radii of semicircles obtained for **HD-2+D₂₄** are more than **HD-2** alone. Rest all the devices show less resistance than that of **HD-2** alone. Here, the observed trend follows the order of their corresponding PCE values. The R_s values obtained for the devices with **HD-2+D₂₄**, **HD-2+D₂₅**, **HD-2+D₂₆** and **HD-2+D₂₇** are 17.64, 17.65, 18.31, and 16.26 Ω , respectively. From the R_s values it is evident that, the resistance experienced from solution is almost same for all the devices and is less than the device with **HD-2**(19.35 Ω) alone. Further, R_1 values obtained are in order: **HD-2+D₂₄** (6.201 Ω) << **HD-2+D₂₆**(12.58 Ω) < **HD-2+D₂₇**(12.75 Ω) < **HD-2+D₂₅**(12.79 Ω) < **HD-2**(15.31 Ω). Similarly, the obtained R_2 values are in the order: **HD-2+D₂₄**(20.43 Ω) >> **HD-2+D₂₇**(4.01 Ω) > **HD-2**(4.09 Ω) > **HD-2+D₂₅**(3.83 Ω) > **HD-2+D₂₆**(2.91 Ω). The order of their resistances in the devices has been clearly reflected in their respective PCE values.

Bode phase plots are depicted in **Fig 5.29(b)** and it is evident from the graphs that, two peaks are obtained for the devices. Further, the τ_{eff} values were calculated and the obtained values are in the decreasing order as **HD-2+D₂₄**(2.99 ms) < **HD-2+D₂₅**(2.06 ms) < **HD-2+D₂₇**(2.99 ms) < **HD-2+D₂₆**(4.35 ms), **HD-2**(3.009 ms).

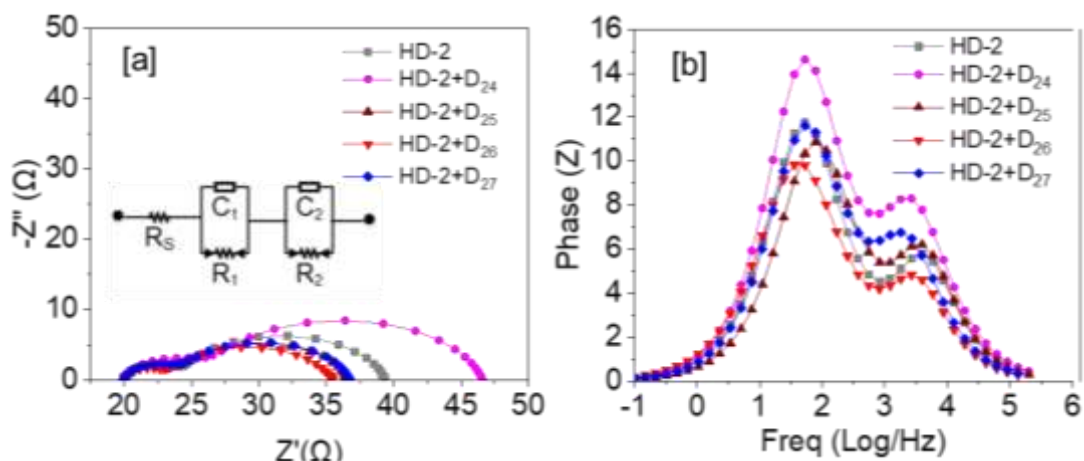


Fig 5.29(a) Nyquist plots and **(b)**Bode plots for **HD-2** based devices co-sensitized with **D₂₄₋₂₇**

Table 5.21: EIS parameters of devices sensitized and co-sensitized using **D₂₄₋₂₇** dyes

Sensitizer/Co-Sensitizer	τ_{eff} (ms)		R_s (Ω)		R_1 (Ω)		R_2 (Ω)	
	Dye	Dye+ HD-2	Dye	Dye+ HD-2	Dye	Dye+ HD-2	Dye	Dye+ HD-2
HD-2	3.009	-	19.35	-	15.31	-	4.09	-
D₂₄/HD-2+D₂₄	6.46	2.99	19.37	17.64	341.5	6.201	13590	20.43
D₂₅/HD-2+D₂₅	9.28	2.06	19.98	17.65	586.4	12.79	0.67	3.83
D₂₆/HD-2+D₂₆	10.01	4.35	19.76	18.31	0.01	12.58	13850	2.907
D₂₇/HD-2+D₂₇	6.70	2.99	17.67	16.26	11380	12.75	4.01	4.01

5.3 FTIR ANALYSIS: ANCHORING STUDIES OF THE DYES ON TiO₂

FTIR spectroscopy technique was used to gain an insight into the behavior of anchoring group and mode of its interaction with TiO₂. For this study, FTIR spectra of **D₁₋₃** adsorbed on TiO₂ surface were recorded. In the present study, the dyes **D₁₋₃** containing carboxylic, nitro and barbituric acid units as anchors, were used. The obtained spectra for **D₁₋₃** are given in **Figs 5.30-5.32**, respectively. From the **Fig 5.30**, it is clear that **D₁** carrying 4-aminobenzoic acid anchor shows good adsorption on TiO₂ whereas **Fig 5.31 (D₂)** and **Fig 5.32 (D₃)** display feeble absorption spectra because of the poor adsorption of nitro and barbituric acid onto the TiO₂ surface,

respectively. As described in the literature, Deacon and Philips had formulated certain rules to deduce the type of adsorption of the carboxylic acid group on the TiO_2 surface. They correlated the difference ($\Delta\nu$) between symmetric ($\Delta\nu_s$) and asymmetric ($\Delta\nu_{as}$) stretching frequencies of a carbonyl bond of carboxylic acid functionality to the corresponding co-ordination type ($\Delta\nu = \Delta\nu_{as(\text{COO}^-)} - \Delta\nu_{s(\text{COO}^-)}$). Evidently, three scenarios are possible; if ($\Delta\nu$) of the dye adsorbed onto TiO_2 ($\Delta\nu_{abs}$) is smaller than that of the free molecule ($\Delta\nu_{free}$), *i.e.* ($\Delta\nu_{abs}$) < ($\Delta\nu_{free}$), then bidentate (either bridging or chelating) adsorption mode would be present; if ($\Delta\nu_{abs}$) <<< ($\Delta\nu_{free}$), in all probability, the strong chelating mode would be present; if ($\Delta\nu_{abs}$) > ($\Delta\nu_{free}$), then dye molecule takes a monodentate binding mode (Deacon and Phillips 1980).

Thus, it is clear that **D₁** shows good adsorption on TiO_2 whereas **D₂** and **D₃** display feeble adsorption on TiO_2 . The dye **D₁** shows prominent bands at 1602 and 2211 cm^{-1} corresponding to the C=O and C \equiv N stretching, respectively. The dye adsorbed on TiO_2 clearly depicts bands at 1654 and 1512 cm^{-1} for the asymmetric and symmetric stretching modes of the C=O group, specifying that the deprotonated carboxylic group is involved in the adsorption on TiO_2 . Further, the appearance of asymmetric and symmetric peaks reveal that, the dye is chemisorbed, thereby ruling out the possibility of physisorption. The dye **D₂** shows a N=O stretching band at around 1503 cm^{-1} and C \equiv N stretching peak at 2200 cm^{-1} . After adsorbing on the TiO_2 surface, $\Delta\nu_{as}$ and $\Delta\nu_s$ of NO₂ group are observed at 1440 and 1320 cm^{-1} respectively, which are almost same as that of unadsorbed dye, confirming very weak interaction. Further, **D₃** demonstrates N-H stretching vibration at 3171 cm^{-1} and C \equiv N stretching peak at 2211 cm^{-1} , while the adsorbed dye displays a weak peak at 2211 cm^{-1} due to C \equiv N stretching with no N-H, and the C=O stretching bands. In the FTIR spectra of all the dyes, the appearance of O-H vibration peak may be due to the residual $\text{Ti}(\text{OH})_2$ present in the powder. Thus, it can be concluded that, the **D₁** has chemisorbed strongly on the TiO_2 surface by means of bidentate chelation or a bridging rather than an ester linkage through the carboxylate unit.

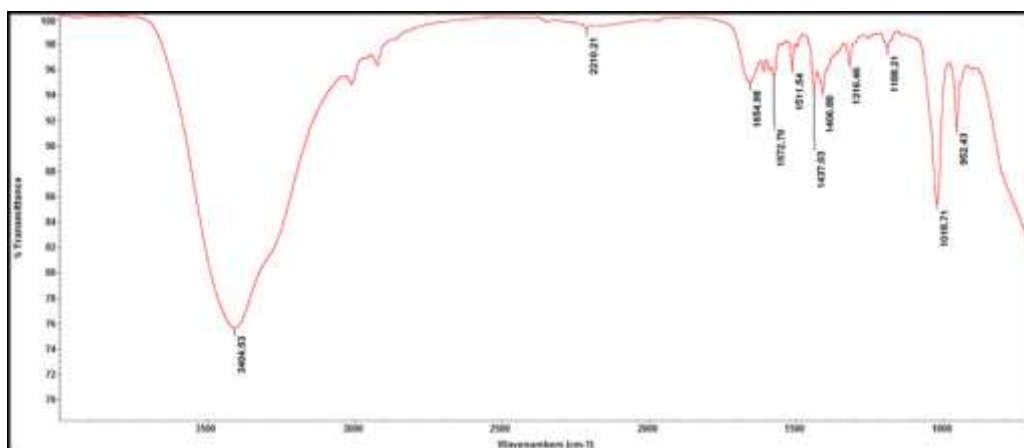


Fig 5.30 FTIR spectrum of **D₁** adsorbed on TiO₂ surface

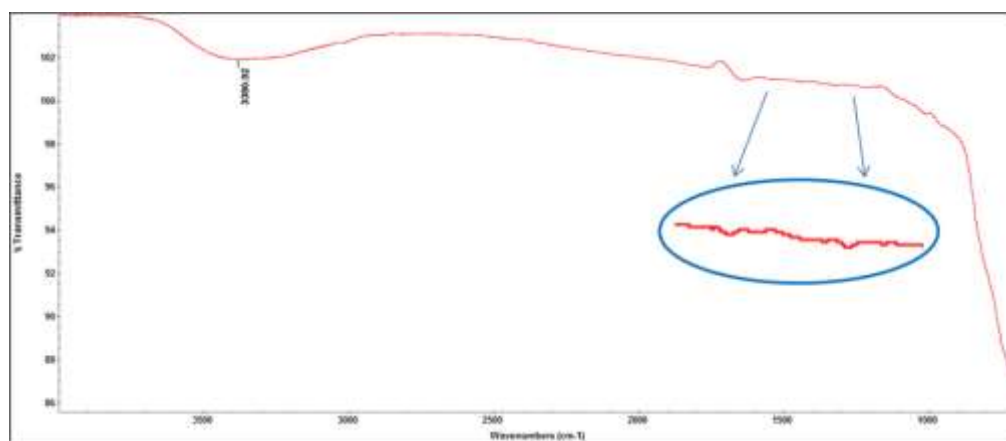


Fig 5.31 FTIR spectrum of **D₂** adsorbed on TiO₂ surface

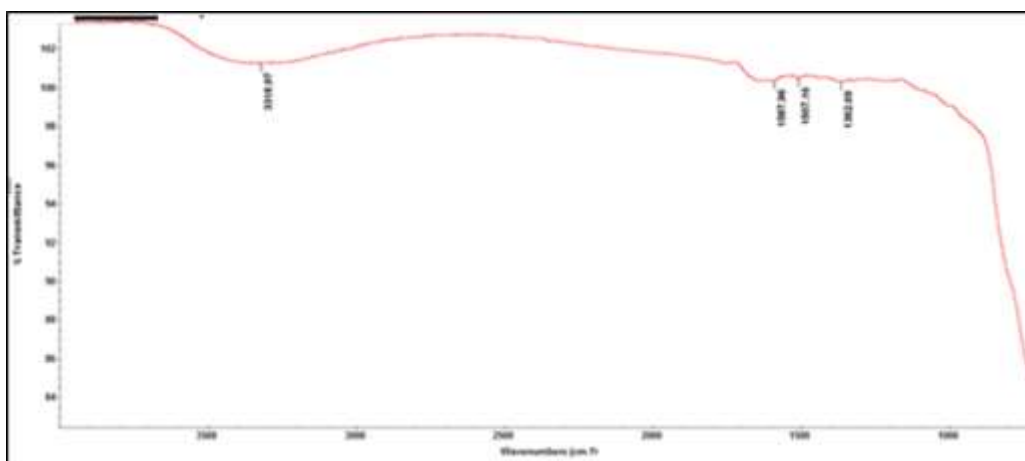


Fig 5.32 FTIR spectrum of **D₃** adsorbed on TiO₂ surface

5.4 CONCLUSIONS

DSSC devices have been fabricated successfully using newly synthesized **D1-27** dyes as sensitizers. The study reveals that, the devices sensitized with dyes **D22** (D-A-D- π -D configured), **D1** (D- π -A) and **D8** (D- π -A) showcase the PCE values 5.91, 4.41 and 3.48 %, respectively. Their higher performance is due to the presence of strong cyanoacetic acid/4-amino benzoic acid as an acceptor/anchoring unit. Further, all the organic dyes were successfully employed as co-sensitizers in DSSCs sensitized with standard Ru (II) dyes (**HD-2/N3**). The studies reveal that, the devices co-sensitized using D-A configured **D26** dye with **HD-2** sensitizer showcases the highest PCE of 10.55 %, J_{sc} of 23.85 V_{oc} of 0.697 V and FF of 63.49 %, enhanced by 3%, while the devices with dyes **D18** (D-D-A) and **D27** (D-A) give the efficiencies of 10.35 and 10.25 % respectively when used as co-sensitizers along with **HD-2** dye. Further, the results obtained from EIS studies are in consistent with the PCE values obtained. Furthermore, anchoring studies of the dyes **D1-3** on TiO_2 confirms the good adsorbing property of carboxylic acid with the TiO_2 . It also confirms the fact that bidentate anchoring is the more stable anchoring mode of carboxylic acid through chemisorption.

SUMMARY AND CONCLUSIONS

Abstract:

This chapter contains summary of the entire work carried out and important conclusions drawn from it. It also includes a brief account on the scope for further work.

6.1 SUMMARY

Solar energy is regarded as one of the most abundant renewable energy sources and it is having the potential to fulfill the global energy demand. The quest for clean and cost-effective energy generation has ended up in the field of organic photovoltaics. Further, DSSCs belongs to the widely investigated area of the organic photovoltaics because of their good performance in converting solar energy to electric energy with low cost of production. The advantages of DSSCs include lightweight, low cost, uncomplicated molecular tuning, intense absorption wavelengths and easy to fabricate with modified colors. Thus, DSSC pioneered by by O'Regan and Grätzel is a credible alternative to conventional inorganic silicon-based solar cells. Among the various components of it, the dye which acts as a photosensitizer plays a crucial role in exerting light harvesting and guiding the electrochemical processes for electricity generation. Several dyes have been investigated as sensitizers as well as co-sensitizers in order to improve the photovoltaic performance of the DSSCs.

Keeping all aforementioned points in mind, the present research work has been mainly focussed on the molecular engineering and synthesis of *n*-type sensitizers/co-sensitizers with favorable photophysical properties as well as thermodynamic feasibility. It has been also aimed at studying their photovoltaic behavior and their structure-performance relationship.

Further, based on the detailed literature survey, seven series of *n*-type organic dyes containing diphenylamine as donor with different π spacer units and electron accepting/anchoring units, were designed. The present design includes D- π -A (**Series-1**), A-D- π -A (**Series-2**), D- π -A/D- π - π -A (**Series-3**), D- π -A(NO₂) (**Series-4**), D-D-A (**Series-5**), A-D- π -D-A (**Series-6**) and D-A (**Series-7**) architectures. The designed molecules were synthesized following standard protocols starting from simple diphenylamine. Their reactions conditions were optimized to get maximum

yield and purification techniques were developed. The chemical structures of newly synthesized dyes and their intermediates were confirmed by various spectroscopy techniques including elemental analysis. Further, their photophysical, electrochemical and theoretical studies were carried out in order to evaluate their suitability for their applications in DSSCs as sensitizers/co-sensitizers. Furthermore, DSSCs were fabricated using synthesized dyes (**D1-27**) as sensitizers and their photovoltaic parameters were evaluated. Also, all the dyes were employed as co-sensitizers in devices sensitized with standard Ru II complex (**HD-2/N3** dye) and their performances were estimated. Finally, the structure-property relationship of **D1-27** was studied with regard to their photophysical, electrochemical, theoretical and EIS parameters; also, their structure-performance correlation study has been undertaken.

6.2 CONCLUSIONS

On the basis of experimental results, following significant conclusions have been drawn from the present research work.

1. Based on detailed literature survey, seven new series of *n*-type organic dyes with various design strategies such as D- π -A (**Series-1**), A-D- π -A (**Series-2**), D- π -A/D- π - π -A (**Series-3**), D- π -A(NO₂) (**Series-4**), D-D-A (**Series-5**), A-D- π -D-A (**Series-6**) and D-A (**Series-7**) have been successfully designed.
2. Twenty seven metal-free organic dyes (**D1-27**) as sensitizers/co-sensitizers have been successfully synthesized, their synthetic protocols and purification techniques were developed, and chemical structures have been established by spectral techniques.
3. From their photophysical studies, it is evident that, all the dyes possess good absorption in the region of UV-visible range and display λ_{abs} in the range of 349 to 560 nm. Also, it establishes the presence of ICT phenomenon in dyes. Further, they exhibit single emission band (λ_{emi}) in the visible region ranging from 428 to 689 nm. Furthermore, the optical band gaps obtained are in the range of 1.9-3.09 eV.
4. From their electrochemical studies, it is clear that, almost all the dyes possess prerequisites to act as good sensitizers. The electrochemical band gap values obtained are in the range of 1.67-3.09 V. Further, the obtained

thermodynamic parameters, viz. ΔG_{inj} , ΔG_{rec} and ΔG_{reg} values were found to be negative showing the feasibility of injection, recombination and regeneration processes.

5. From their theoretical studies, it is concluded that, all the dyes possess good charge separation in their FMO levels confirming the ICT phenomenon. Their ESP maps clearly show extent of charge concentration in various regions of the molecules. Also, it has been shown that, the charge transfer takes place smoothly from **D4** molecule to TiO₂ surface through anchoring group. Further, TD-DFT results are in well agreement with the experimental results.
6. From the results of sensitization studies in devices, it is clear that, among the tested dyes, A-D- π -D-A architected **D22**, exhibits the optimum PCE of **5.91%**. The dyes **D1** (4.41%), **D8** (3.48%), **D24** (2.309%), **D23** (2.275%), **D18** (2.44%), **D19** (2.19%), **D21** (2.86%), **D10** (2.58%) and **D4** (2.53%) as sensitizers, display comparatively moderate photovoltaic performance.
7. Their PCE results clearly indicate that, cyanoacetic acid unit showcases a good anchoring property with TiO₂ and hence causes enhanced PCE values for the devices.
8. FTIR analysis of the device supports the fact that, carboxylic acid is having good anchoring ability with TiO₂ surface and the bidentate anchoring mode is prominent in the dyes.
9. From the co-sensitization studies of dyes (**D1-27**) in DSSC, it can be concluded that, co-sensitizer **D26** with 0.2 mM of **HD-2** sensitizer showcases an improved PCE of **10.55 %**, V_{OC} of 0.697 V and FF of 63.49%, J_{SC} 23.85 mAcm⁻² whereas sensitizer **HD-2** alone displays PCE of **7.49%**, V_{OC} of 0.652V and FF of 60.49%, J_{SC} 19.03 mAcm⁻². Also, the co-sensitizers **D27** (10.25%), **D18** (10.35%), **D14** (9.38%), **D25** (8.98%), **D12** (8.92%), **D19** (8.87%), **D21** (8.77%), **D22** (8.85), **D15** (8.64) and **D13** (8.46%), exhibit quite improved photovoltaic performance when compared to that of **HD-2** alone.
10. Co-sensitizers bearing non-carboxylic anchoring groups (maleimide, nitro derivatives and barbituric acid) display enhanced performance. Further, small

molecular sized dyes function as effective co-sensitizers in **HD-2/N3** sensitized devices.

11. Their EIS studies establish the same trend in the device performance when dyes are employed as sensitizers/co-sensitizers.

Conclusively, in the present work twenty seven *n*-type organic sensitizers/co-sensitizers with various design strategies, have been synthesized and characterized. The dependence of structure on their photophysical, electrochemical and photovoltaic parameters have been discussed. It has been observed that, the chemical structure and position of acceptor/anchoring groups play a vital role in determining the overall PCE of the DSSCs.

6.3 SCOPE FOR FUTURE WORK

As concluded, the sensitizer **D22** with A-D- π -D-A architecture, bearing (1,4-phenylene)diacetonitrile, displays the highest photovoltaic performance. For the first time, the authors reported this architecture carrying new spacer units. Evidently, the photovoltaic efficiency of these dyes can be improved by further modifying the structure of **D22** as well as optimizing the other components such as semiconductor, electrolyte and counter electrolyte of the device.

In the present work, for the first time, nitro group was introduced as anchoring group for co-sensitizers. Thus, nitro group can be explored further as anchoring functionality for new co-sensitizers in future studies. Further in-depth studies can be carried out for the co-sensitizers **D26** and **D27**. In future, these investigated dyes and their intermediates may find applications in various other fields including medicinal chemistry.

REFERENCES

- Ambrosio, F., Martsinovich, N., and Troisi, A. (2012a). "Effect of the anchoring group on electron injection: theoretical study of phosphonated dyes for dye-sensitized solar cells." *J. Phys. Chem. C*, 116(3), 2622–2629.
- Ambrosio, F., Martsinovich, N., and Troisi, A. (2012b). "What is the best anchoring group for a dye in a dye-sensitized solar cell?" *J. Phys. Chem. Lett.*, 3(11), 1531–1535.
- Anderson, A. Y., Barnes, P. R., Durrant, J. R., and O'Regan, B. C. (2011). "Quantifying regeneration in dye-sensitized solar cells." *J. Phys. Chem. C*, 115(5), 2439–2447.
- Anselmi, C., Mosconi, E., Pastore, M., Ronca, E., and De Angelis, F. (2012). "Adsorption of organic dyes on TiO₂ surfaces in dye-sensitized solar cells: interplay of theory and experiment." *Phys. Chem. Chem. Phys.*, 14(46), 15963–15974.
- Babu, D. D., Elsherbiny, D., Cheema, H., El-Shafei, A., and Adhikari, A. V. (2016a). "Highly efficient panchromatic dye-sensitized solar cells: Synergistic interaction of ruthenium sensitizer with novel co-sensitizers carrying different acceptor units." *Dyes Pigments*, 132, 316–328.
- Babu, D. D., Gachumale, S. R., Anandan, S., and Adhikari, A. V. (2015). "New D- π -A type indole based chromogens for DSSC: Design, synthesis and performance studies." *Dyes Pigments*, 112, 183–191.
- Babu, D. D., Su, R., El-Shafei, A., and Adhikari, A. V. (2016b). "From Molecular Design to Co-sensitization; High performance indole based photosensitizers for dye-sensitized solar cells." *Electrochimica Acta*, 198, 10–21.
- Bae, S. H., Seo, K. D., Choi, W. S., Hong, J. Y., and Kim, H. K. (2015). "Near-IR organic sensitizers containing squaraine and phenothiazine units for dye-sensitized solar cells." *Dyes Pigments*, 113, 18–26.
- Becke, A. D. (1988). "Density-functional exchange-energy approximation with correct asymptotic behavior." *Phys. Rev. A*, 38(6), 3098.
- Becke, A. D. (1993). "A new mixing of Hartree–Fock and local density-functional theories." *J. Chem. Phys.*, 98(2), 1372–1377.

- Bisquert, J. (2003b). “Chemical capacitance of nanostructured semiconductors: its origin and significance for nanocomposite solar cells.” *Phys. Chem. Chem. Phys.*, 5(24), 5360–5364.
- Bisquert, J., Cahen, D., Hodes, G., Rühle, S., and Zaban, A. (2004). “Physical chemical principles of photovoltaic conversion with nanoparticulate, mesoporous dye-sensitized solar cells.” *J. Phys. Chem. B*, 108(24), 8106–8118.
- Black, F. A., Clark, C. A., Summers, G. H., Clark, I. P., Towrie, M., Penfold, T., George, M. W., and Gibson, E. A. (2017). “Investigating interfacial electron transfer in dye-sensitized NiO using vibrational spectroscopy.” *Phys. Chem. Chem. Phys.*, 19(11), 7877–7885.
- Borgström, M., Blart, E., Boschloo, G., Mukhtar, E., Hagfeldt, A., Hammarström, L., and Odobel, F. (2005). “Sensitized hole injection of phosphorus porphyrin into NiO: toward new photovoltaic devices.” *J. Phys. Chem. B*, 109(48), 22928–22934.
- Boschloo, G., and Hagfeldt, A. (2009). “Characteristics of the iodide/triiodide redox mediator in dye-sensitized solar cells.” *Acc. Chem. Res.*, 42(11), 1819–1826.
- Chapin, D. M., Fuller, C. S., and Pearson, G. L. (1954). “A new silicon *p-n* junction photocell for converting solar radiation into electrical power.” *J. Appl. Phys.*, 25(5), 676–677.
- Cheema, H., Islam, A., Han, L., and El-Shafei, A. (2014a). “Influence of number of benzodioxan-stilbazole-based ancillary ligands on dye packing, photovoltage and photocurrent in dye-sensitized solar cells.” *ACS Appl. Mater. Interfaces*, 6(14), 11617–11624.
- Cheema, H., Islam, A., Younts, R., Gautam, B., Bedja, I., Gupta, R. K., Han, L., Gundogdu, K., and El-Shafei, A. (2014b). “More stable and more efficient alternatives of Z-907: carbazole-based amphiphilic Ru (II) sensitizers for dye-sensitized solar cells.” *Phys. Chem. Chem. Phys.*, 16(48), 27078–27087.
- Chiba, Y., Islam, A., Watanabe, Y., Komiya, R., Koide, N., and Han, L. (2006). “Dye-sensitized solar cells with conversion efficiency of 11.1%.” *Jpn. J. Appl. Phys.*, 45(7L), L638.
- Clifford, J. N., Martínez-Ferrero, E., Viterisi, A., and Palomares, E. (2011). “Sensitizer molecular structure-device efficiency relationship in dye sensitized solar

- cells.” *Chem. Soc. Rev.*, 40(3), 1635–1646.
- Click, K. A., Beauchamp, D. R., Garrett, B. R., Huang, Z., Hadad, C. M., and Wu, Y. (2014). “A double-acceptor as a superior organic dye design for *p*-type DSSCs: high photocurrents and the observed light soaking effect.” *Phys. Chem. Chem. Phys.*, 16(47), 26103–26111.
- Cui, J., Lu, J., Xu, X., Cao, K., Wang, Z., Alemu, G., Yuang, H., Shen, Y., Xu, J., and Cheng, Y. (2014). “Organic sensitizers with pyridine ring anchoring group for *p*-type dye-sensitized solar cells.” *J. Phys. Chem. C*, 118(30), 16433–16440.
- Daeneke, T., Mozer, A. J., Uemura, Y., Makuta, S., Fekete, M., Tachibana, Y., Koumura, N., Bach, U., and Spiccia, L. (2012). “Dye regeneration kinetics in dye-sensitized solar cells.” *J. Am. Chem. Soc.*, 134(41), 16925–16928.
- De Vita, A. (1992). “The energetics of defects and impurities in metals and ionic materials from first principles.” University of Keele.
- Deacon, G. B., and Phillips, R. J. (1980). “Relationships between the carbon-oxygen stretching frequencies of carboxylato complexes and the type of carboxylate coordination.” *Coord. Chem. Rev.*, 33(3), 227–250.
- Edvinsson, T., Li, C., Pschirer, N., Schöneboom, J., Eickemeyer, F., Sens, R., Boschloo, G., Herrmann, A., Müllen, K., and Hagfeldt, A. (2007). “Intramolecular charge-transfer tuning of perylenes: spectroscopic features and performance in dye-sensitized solar cells.” *J. Phys. Chem. C*, 111(42), 15137–15140.
- Eiamprasert, U., Sudchanham, J., Surawatanawong, P., Pakawatpanurut, P., and Kiatisevi, S. (2018). “Additional donor bridge as a design approach for multi-anchoring dyes for highly efficient dye-sensitized solar cells.” *J. Photochem. Photobiol. Chem.*, 352, 86–97.
- El-Shafei, A., Hussain, M., Atiq, A., Islam, A., and Han, L. (2012). “A novel carbazole-based dye outperformed the benchmark dye N719 for high efficiency dye-sensitized solar cells (DSSCs).” *J. Mater. Chem.*, 22(45), 24048–24056.
- Environ, E., Martsinovich, N., and Troisi, A. (2011). “Environmental Science Theoretical studies of dye-sensitised solar cells: from electronic structure to elementary processes.” 4473–4495.

- Etienne, T., Chbib, L., Michaux, C., Perpete, E. A., Assfeld, X., and Monari, A. (2014). "All-organic chromophores for dye-sensitized solar cells: A theoretical study on aggregation." *Dyes Pigments*, 101, 203–211.
- Fabregat-Santiago, F., Bisquert, J., Garcia-Belmonte, G., Boschloo, G., and Hagfeldt, A. (2005). "Influence of electrolyte in transport and recombination in dye-sensitized solar cells studied by impedance spectroscopy." *Sol. Energy Mater. Sol. Cells*, 87(1–4), 117–131.
- Farré, Y., Raissi, M., Fihey, A., Pellegrin, Y., Blart, E., Jacquemin, D., and Odobel, F. (2017). "A Blue Diketopyrrolopyrrole Sensitizer with High Efficiency in Nickel-Oxide-based Dye-Sensitized Solar Cells." *ChemSusChem*, 10(12), 2618–2625.
- Feldt, S. M., Wang, G., Boschloo, G., and Hagfeldt, A. (2011). "Effects of driving forces for recombination and regeneration on the photovoltaic performance of dye-sensitized solar cells using cobalt polypyridine redox couples." *J. Phys. Chem. C*, 115(43), 21500–21507.
- Freitag, M., Teuscher, J., Saygili, Y., Zhang, X., Giordano, F., Liska, P., Hua, J., Zakeeruddin, S. M., Moser, J.-E., and Grätzel, M. (2017). "Dye-sensitized solar cells for efficient power generation under ambient lighting." *Nat. Photonics*, 11(6), 372–378.
- Gibson, E. A., Smeigh, A. L., Le Pleux, L., Fortage, J., Boschloo, G., Blart, E., Pellegrin, Y., Odobel, F., Hagfeldt, A., and Hammarström, L. (2009). "A *p*-type NiO-based dye-sensitized solar cell with an open-circuit voltage of 0.35 V." *Angew. Chem.*, 121(24), 4466–4469.
- Gong, J., Liang, J., and Sumathy, K. (2012). "Review on dye-sensitized solar cells (DSSCs): fundamental concepts and novel materials." *Renew. Sustain. Energy Rev.*, 16(8), 5848–5860.
- Grätzel, M. (2003). "Dye-sensitized solar cells." *J. Photochem. Photobiol. C Photochem. Rev.*, 4(2), 145–153.
- Grätzel, M. (2005). "Solar energy conversion by dye-sensitized photovoltaic cells." *Inorg. Chem.*, 44(20), 6841–6851.
- Gupta, A., Armel, V., Xiang, W., Bilic, A., and Evans, R. A. (2015). "New organic sensitizers using 4-(cyanomethyl) benzoic acid as an acceptor group for dye-

- sensitized solar cell applications.” *Dyes Pigments*, 113, 280–288.
- Gupta, K. S. V., Suresh, T., Singh, S. P., Islam, A., Han, L., and Chandrasekharam, M. (2014). “Carbazole based A- π -D- π -A dyes with double electron acceptor for dye-sensitized solar cell.” *Org. Electron.*, 15(1), 266–275.
- Hagfeldt, A., Boschloo, G., Sun, L., Kloo, L., and Pettersson, H. (2010). “Dye-sensitized solar cells.” *Chem. Rev.*, 110(11), 6595–6663.
- Han, L., Kang, R., Zu, X., Cui, Y., and Gao, J. (2015). “Novel coumarin sensitizers based on 2-(thiophen-2-yl) thiazole π -bridge for dye-sensitized solar cells.” *Photochem. Photobiol. Sci.*, 14(11), 2046–2053.
- Hara, K., Kurashige, M., Ito, S., Shinpo, A., Suga, S., Sayama, K., and Arakawa, H. (2003). “Novel polyene dyes for highly efficient dye-sensitized solar cells.” *Chem. Commun.*, (2), 252–253.
- Hara, K., Sato, T., Katoh, R., Furube, A., Yoshihara, T., Murai, M., Kurashige, M., Ito, S., Shinpo, A., and Suga, S. (2005). “Novel conjugated organic dyes for efficient dye-sensitized solar cells.” *Adv. Funct. Mater.*, 15(2), 246–252.
- Haram, S. K., Quinn, B. M., and Bard, A. J. (2001). “Electrochemistry of CdS nanoparticles: a correlation between optical and electrochemical band gaps.” *J. Am. Chem. Soc.*, 123(36), 8860–8861.
- Hasan, M. A., and Sumathy, K. (2010). “Photovoltaic thermal module concepts and their performance analysis: a review.” *Renew. Sustain. Energy Rev.*, 14(7), 1845–1859.
- He, J., Hua, J., Hu, G., Yin, X. J., Gong, H., and Li, C. (2014). “Organic dyes incorporating a thiophene or furan moiety for efficient dye-sensitized solar cells.” *Dyes Pigments*, 104, 75–82.
- He, J., Lindström, H., Hagfeldt, A., and Lindquist, S.-E. (1999). “Dye-sensitized nanostructured *p*-type nickel oxide film as a photocathode for a solar cell.” *J. Phys. Chem. B*, 103(42), 8940–8943.
- Hong, Y., Liao, J.-Y., Cao, D., Zang, X., Kuang, D.-B., Wang, L., Meier, H., and Su, C.-Y. (2011). “Organic dye bearing asymmetric double donor- π -acceptor chains for dye-sensitized solar cells.” *J. Org. Chem.*, 76(19), 8015–8021.

- Hosseinzadeh, B., Beni, A. S., Azari, M., Zarandi, M., and Karami, M. (2016). "Novel D- π -A type triphenylamine based chromogens for DSSC: design, synthesis and performance studies." *New J. Chem.*, 40(10), 8371–8381.
- Hosseinzadeh, B., Beni, A. S., Chermahini, A. N., Ghahary, R., and Teimouri, A. (2015). "Novel organic dyes with anchoring group of barbituric/thiobarbituric acid and their application in dye-sensitized solar cells." *Synth. Met.*, 209, 1–10.
- Hu, Y., Chen, Z.-C., Le, Z.-G., and Zheng, Q.-G. (2004). "Organic Reactions in Ionic Liquids: Ionic Liquid Promoted Knoevenagel Condensation of Aromatic Aldehydes with (2-Thio) Barbituric Acid." *Synth. Commun.*, 34(24), 4521–4529.
- Ito, S., Zakeeruddin, S. M., Humphry-Baker, R., Liska, P., Charvet, R., Comte, P., Nazeeruddin, M. K., Péchy, P., Takata, M., and Miura, H. (2006). "High-efficiency organic-dye-sensitized solar cells controlled by nanocrystalline-TiO₂ electrode thickness." *Adv. Mater.*, 18(9), 1202–1205.
- Ji, Z., Natu, G., Huang, Z., and Wu, Y. (2011). "Linker effect in organic donor-acceptor dyes for *p*-type NiO dye sensitized solar cells." *Energy Environ. Sci.*, 4(8), 2818–2821.
- Jose, R., Kumar, A., Thavasi, V., and Ramakrishna, S. (2008). "Conversion efficiency versus sensitizer for electrospun TiO₂ nanorod electrodes in dye-sensitized solar cells." *Nanotechnology*, 19(42), 424004.
- Kathiravan, A., Panneerselvam, M., Sundaravel, K., Pavithra, N., Srinivasan, V., Anandan, S., and Jaccob, M. (2016). "Unravelling the effect of anchoring groups on the ground and excited state properties of pyrene using computational and spectroscopic methods." *Phys. Chem. Chem. Phys.*, 18(19), 13332–13345.
- Katoh, R., Furube, A., Yoshihara, T., Hara, K., Fujihashi, G., Takano, S., Murata, S., Arakawa, H., and Tachiya, M. (2004). "Efficiencies of electron injection from excited N3 dye into nanocrystalline semiconductor (ZrO₂, TiO₂, ZnO, Nb₂O₅, SnO₂, In₂O₃) films." *J. Phys. Chem. B*, 108(15), 4818–4822.
- Katono, M., Bessho, T., Meng, S., Humphry-Baker, R., Rothenberger, G., Zakeeruddin, S. M., Kaxiras, E., and Grätzel, M. (2011). "D- π -A dye system containing cyano-benzoic acid as anchoring group for dye-sensitized solar cells." *Langmuir*, 27(23), 14248–14252.

- Khanasa, T., Prachumrak, N., Kochapradist, P., Namuangruk, S., Keawin, T., Jungsuttiwong, S., Sudyoadsuk, T., and Promarak, V. (2014). "The design, synthesis, and characterization of D- π -A- π -A type organic dyes as sensitizers for dye-sensitized solar cells (DSSCs)." *Tetrahedron Lett.*, 55(21), 3244–3248.
- Kim, S. H., Kim, H. W., Sakong, C., Namgoong, J., Park, S. W., Ko, M. J., Lee, C. H., Lee, W. I., and Kim, J. P. (2011). "Effect of five-membered heteroaromatic linkers to the performance of phenothiazine-based dye-sensitized solar cells." *Org. Lett.*, 13(21), 5784–5787.
- Kim, Y. J., Cheon, Y. R., Jang, J.-W., Kim, Y.-H., and Park, C. E. (2015). "A potential naphtho [2, 1-b: 3, 4-b'] dithiophene-based polymer with large open circuit voltage for efficient use in organic solar cells." *J. Mater. Chem. C*, 3(9), 1904–1912.
- Komatsu, M., Nakazaki, J., Uchida, S., Kubo, T., and Segawa, H. (2013). "A donor–acceptor type organic dye connected with a quinoidal thiophene for dye-sensitized solar cells." *Phys. Chem. Chem. Phys.*, 15(9), 3227–3232.
- Koops, S. E., O'Regan, B. C., Barnes, P. R., and Durrant, J. R. (2009). "Parameters influencing the efficiency of electron injection in dye-sensitized solar cells." *J. Am. Chem. Soc.*, 131(13), 4808–4818.
- Koyyada, G., Botla, V., Thogiti, S., Wu, G., Li, J., Fang, X., Kong, F., Dai, S., Surukonti, N., and Kotamarthi, B. (2014). "Novel 4'-functionalized 4, 4''-dicarboxyterpyridine ligands for ruthenium complexes: near-IR sensitization in dye sensitized solar cells." *Dalton Trans.*, 43(40), 14992–15003.
- Kresse, G., and Hafner, J. (1993). "Ab initio molecular dynamics for liquid metals." *Phys. Rev. B*, 47(1), 558.
- Leandri, V., Ruffo, R., Trifiletti, V., and Abboto, A. (2013). "Asymmetric Tribranched Dyes: An Intramolecular Cosensitization Approach for Dye-Sensitized Solar Cells." *Eur. J. Org. Chem.*, 2013(30), 6793–6801.
- Li, S.-L., Jiang, K.-J., Shao, K.-F., and Yang, L.-M. (2006). "Novel organic dyes for efficient dye-sensitized solar cells." *Chem. Commun.*, (26), 2792–2794.
- Listorti, A., O'regan, B., and Durrant, J. R. (2011). "Electron transfer dynamics in dye-sensitized solar cells." *Chem. Mater.*, 23(15), 3381–3399.

- Liu, F., Yang, Y., Wang, H., Liu, J., Hu, C., Huo, F., Bo, S., Zhen, Z., Liu, X., and Qiu, L. (2015). "Comparative studies on structure–nonlinearity relationships in a series of novel second-order nonlinear optical chromophores with different aromatic amine donors." *Dyes Pigments*, 120, 347–356.
- Liu, J., Zhang, J., Xu, M., Zhou, D., Jing, X., and Wang, P. (2011). "Mesoscopic titania solar cells with the tris (1, 10-phenanthroline) cobalt redox shuttle: uniped versus biped organic dyes." *Energy Environ. Sci.*, 4(8), 3021–3029.
- Liu, X., Cao, Z., Huang, H., Liu, X., Tan, Y., Chen, H., Pei, Y., and Tan, S. (2014). "Novel D–D– π -A organic dyes based on triphenylamine and indole-derivatives for high performance dye-sensitized solar cells." *J. Power Sources*, 248, 400–406.
- Luo, J., Wan, Z., Jia, C., Wang, Y., and Wu, X. (2016a). "A co-sensitized approach to efficiently fill the absorption valley, avoid dye aggregation and reduce the charge recombination." *Electrochimica Acta*, 215, 506–514.
- Luo, J., Wan, Z., Jia, C., Wang, Y., Wu, X., and Yao, X. (2016b). "Co-sensitization of dithiafulvenyl-phenothiazine based organic dyes with N719 for efficient dye-sensitized solar cells." *Electrochimica Acta*, 211, 364–374.
- Ma, W., Jiao, Y., and Meng, S. (2013). "Modeling charge recombination in dye-sensitized solar cells using first-principles electron dynamics: effects of structural modification." *Phys. Chem. Chem. Phys.*, 15(40), 17187–17194.
- Manoharan, S., Asiri, A. M., and Anandan, S. (2016). "Impact of anchoring groups for improving the binding nature of organic dyes toward high efficient dye sensitized solar cells." *Sol. Energy*, 126, 22–31.
- Mao, J., Zhang, X., Liu, S.-H., Shen, Z., Li, X., Wu, W., Chou, P.-T., and Hua, J. (2015). "Molecular engineering of D-A- π -A dyes with 2-(1, 1-dicyanomethylene) rhodanine as an electron-accepting and anchoring group for dye-sensitized solar cells." *Electrochimica Acta*, 179, 179–186.
- Martsinovich, N., and Troisi, A. (2011). "Theoretical studies of dye-sensitised solar cells: from electronic structure to elementary processes." *Energy Environ. Sci.*, 4(11), 4473–4495.
- Mathew, S., Yella, A., Gao, P., Humphry-Baker, R., Curchod, B. F., Ashari-Astani, N., Tavernelli, I., Rothlisberger, U., Nazeeruddin, M. K., and Grätzel, M. (2014).

- “Dye-sensitized solar cells with 13% efficiency achieved through the molecular engineering of porphyrin sensitizers.” *Nat. Chem.*, 6(3), 242–247.
- Matsui, M., Shiota, T., Kubota, Y., Funabiki, K., Jin, J., Yoshida, T., Higashijima, S., and Miura, H. (2012). “N-(2-Alkoxyphenyl)-substituted double rhodanine indoline dyes for zinc oxide dye-sensitized solar cell.” *Tetrahedron*, 68(22), 4286–4291.
- Meng, F. S., Yao, Q. H., Shen, J. G., Li, F. L., and Huang, C. H. (2003). “Novel cyanine dyes with multi-carboxyl groups and their sensitization on nanocrystalline TiO₂ electrode.” *Synth. Met.*, 137(1–3), 1543–1544.
- Michinobu, T., Satoh, N., Cai, J., Li, Y., and Han, L. (2014). “Novel design of organic donor–acceptor dyes without carboxylic acid anchoring groups for dye-sensitized solar cells.” *J. Mater. Chem. C*, 2(17), 3367–3372.
- Mikroyannidis, J. A., Suresh, P., Roy, M. S., and Sharma, G. D. (2011). “New photosensitizer with phenylenebisthiophene central unit and cyanovinylene 4-nitrophenyl terminal units for dye-sensitized solar cells.” *Electrochimica Acta*, 56(16), 5616–5623.
- Mishra, A., Fischer, M. K., and Bäuerle, P. (2009). “Metal-free organic dyes for dye-sensitized solar cells: From structure: Property relationships to design rules.” *Angew. Chem. Int. Ed.*, 48(14), 2474–2499.
- Morandeira, A., Fortage, J., Edvinsson, T., Le Pleux, L., Blart, E., Boschloo, G., Hagfeldt, A., Hammarström, L., and Odobel, F. (2008). “Improved photon-to-current conversion efficiency with a nanoporous *p*-type NiO electrode by the use of a sensitizer-acceptor dyad.” *J. Phys. Chem. C*, 112(5), 1721–1728.
- Mori, S., Fukuda, S., Sumikura, S., Takeda, Y., Tamaki, Y., Suzuki, E., and Abe, T. (2008). “Charge-transfer processes in dye-sensitized NiO solar cells.” *J. Phys. Chem. C*, 112(41), 16134–16139.
- Murali, M. G., Wang, X., Wang, Q., and Valiyaveetil, S. (2016). “New banana shaped A–D– π –D–A type organic dyes containing two anchoring groups for high performance dye-sensitized solar cells.” *Dyes Pigments*, 134, 375–381.
- Naik, P., Abdellah, I. M., Abdel-Shakour, M., Su, R., Keremane, K. S., El-Shafei, A., and Adhikari, A. V. (2018a). “Improvement in performance of N3 sensitized DSSCs

- with structurally simple aniline based organic co-sensitizers.” *Sol. Energy*, 174, 999–1007.
- Naik, P., Elmorsy, M. R., Su, R., Babu, D. D., El-Shafei, A., and Adhikari, A. V. (2017). “New carbazole based metal-free organic dyes with D- π -A- π -A architecture for DSSCs: synthesis, theoretical and cell performance studies.” *Sol. Energy*, 153, 600–610.
- Naik, P., Keremane, K. S., Elmorsy, M. R., Su, R., El-Shafei, A., and Adhikari, A. V. (2018b). “Highly efficient carbazole based co-sensitizers carrying electron deficient barbituric acid for NCSU-10 sensitized DSSCs.” *Sol. Energy*, 169, 386–391.
- Naik, P., Su, R., Elmorsy, M. R., El-Shafei, A., and Adhikari, A. V. (2018c). “New di-anchoring A- π -D- π -A configured organic chromophores for DSSC application: sensitization and co-sensitization studies.” *Photochem. Photobiol. Sci.*, 17(3), 302–314.
- Nakasa, A., Usami, H., Sumikura, S., Hasegawa, S., Koyama, T., and Suzuki, E. (2005). “A high voltage dye-sensitized solar cell using a nanoporous NiO photocathode.” *Chem. Lett.*, 34(4), 500–501.
- Nattestad, A., Mozer, A. J., Fischer, M. K., Cheng, Y.-B., Mishra, A., Bäuerle, P., and Bach, U. (2010). “Highly efficient photocathodes for dye-sensitized tandem solar cells.” *Nat. Mater.*, 9(1), 31–35.
- Nazeeruddin, M. K., Kay, A., Rodicio, I., Humphry-Baker, R., Müller, E., Liska, P., Vlachopoulos, N., and Grätzel, M. (1993). “Conversion of light to electricity by cis-X₂bis (2, 2'-bipyridyl-4, 4'-dicarboxylate) ruthenium (II) charge-transfer sensitizers (X= Cl-, Br-, I-, CN-, and SCN-) on nanocrystalline titanium dioxide electrodes.” *J. Am. Chem. Soc.*, 115(14), 6382–6390.
- Nazeeruddin, M. K., Pechy, P., and Grätzel, M. (1997). “Efficient panchromatic sensitization of nanocrystalline TiO₂ films by a black dye based on atrithiocyanato-ruthenium complex.” *Chem. Commun.*, (18), 1705–1706.
- Nazeeruddin, M. K., Zakeeruddin, S. M., Humphry-Baker, R., Jirousek, M., Liska, P., Vlachopoulos, N., Shklover, V., Fischer, C.-H., and Grätzel, M. (1999). “Acid- Base equilibria of (2, 2'-Bipyridyl-4, 4'-dicarboxylic acid) ruthenium (II) complexes and

- the effect of protonation on charge-transfer sensitization of nanocrystalline titania.” *Inorg. Chem.*, 38(26), 6298–6305.
- Ning, Z., Fu, Y., and Tian, H. (2010). “Improvement of dye-sensitized solar cells: what we know and what we need to know.” *Energy Environ. Sci.*, 3(9), 1170–1181.
- Odobel, F., Le Pleux, L., Pellegrin, Y., and Blart, E. (2010). “New photovoltaic devices based on the sensitization of *p*-type semiconductors: challenges and opportunities.” *Acc. Chem. Res.*, 43(8), 1063–1071.
- Ondersma, J. W., and Hamann, T. W. (2009). “Impedance investigation of dye-sensitized solar cells employing outer-sphere redox shuttles.” *J. Phys. Chem. C*, 114(1), 638–645.
- Ooyama, Y., Shimada, Y., Inoue, S., Nagano, T., Fujikawa, Y., Komaguchi, K., Imae, I., and Harima, Y. (2011). “New molecular design of donor- π -acceptor dyes for dye-sensitized solar cells: control of molecular orientation and arrangement on TiO₂ surface.” *New J. Chem.*, 35(1), 111–118.
- Oprea, C. I., Panait, P., Lungu, J., Stamate, D., Dumbravă, A., Cimpoesu, F., and Gîrțu, M. A. (2013). “DFT study of binding and electron transfer from a metal-free dye with carboxyl, hydroxyl, and sulfonic anchors to a titanium dioxide nanocluster.” *Int. J. Photoenergy*, 2013.
- O’regan, B., and Grätzel, M. (1991). “A low-cost, high-efficiency solar cell based on dye-sensitized colloidal TiO₂ films.” *nature*, 353(6346), 737–740.
- Oskam, G., Bergeron, B. V., Meyer, G. J., and Searson, P. C. (2001). “Pseudohalogens for dye-sensitized TiO₂ photoelectrochemical cells.” *J. Phys. Chem. B*, 105(29), 6867–6873.
- Park, J.-H., Cho, N. S., Jung, Y. K., Cho, H.-J., Shim, H.-K., Kim, H., and Lee, Y. S. (2007). “Polymeric light emitting properties and structural relationships of fluorene-based conjugated copolymers containing various hole transporting derivatives.” *Org. Electron.*, 8(2–3), 272–285.
- Peach, M. J., Benfield, P., Helgaker, T., and Tozer, D. J. (2008). “Excitation energies in density functional theory: An evaluation and a diagnostic test.” *J. Chem. Phys.*, 128(4), 044118.

- Perdew, J. P., Burke, K., and Ernzerhof, M. (1996). "Generalized gradient approximation made simple." *Phys. Rev. Lett.*, 77(18), 3865.
- Planells, M., Pellejà, L., Clifford, J. N., Pastore, M., De Angelis, F., López, N., Marder, S. R., and Palomares, E. (2011). "Energy levels, charge injection, charge recombination and dye regeneration dynamics for donor–acceptor π -conjugated organic dyes in mesoscopic TiO₂ sensitized solar cells." *Energy Environ. Sci.*, 4(5), 1820–1829.
- Pond, S. J., Rumi, M., Levin, M. D., Parker, T. C., Beljonne, D., Day, M. W., Brédas, J.-L., Marder, S. R., and Perry, J. W. (2002). "One- and two-photon spectroscopy of donor- acceptor- donor distyrylbenzene derivatives: effect of cyano substitution and distortion from planarity." *J. Phys. Chem. A*, 106(47), 11470–11480.
- Powar, S., Wu, Q., Weidener, M., Nattestad, A., Hu, Z., Mishra, A., Bäuerle, P., Spiccia, L., Cheng, Y.-B., and Bach, U. (2012). "Improved photocurrents for *p*-type dye-sensitized solar cells using nano-structured nickel (II) oxide microballs." *Energy Environ. Sci.*, 5(10), 8896–8900.
- Prajongtat, P., Suramitr, S., Nokbin, S., Nakajima, K., Mitsuke, K., and Hannongbua, S. (2017). "Density functional theory study of adsorption geometries and electronic structures of azo-dye-based molecules on anatase TiO₂ surface for dye-sensitized solar cell applications." *J. Mol. Graph. Model.*, 76, 551–561.
- Qin, P., Linder, M., Brinck, T., Boschloo, G., Hagfeldt, A., and Sun, L. (2009). "High incident photon-to-current conversion efficiency of *p*-type dye-sensitized solar cells based on NiO and organic chromophores." *Adv. Mater.*, 21(29), 2993–2996.
- Qin, P., Zhu, H., Edvinsson, T., Boschloo, G., Hagfeldt, A., and Sun, L. (2008). "Design of an organic chromophore for *p*-type dye-sensitized solar cells." *J. Am. Chem. Soc.*, 130(27), 8570–8571.
- Qu, P., and Meyer, G. J. (2001). "Proton-controlled electron injection from molecular excited states to the empty states in nanocrystalline TiO₂." *Langmuir*, 17(21), 6720–6728.
- Ramkumar, S., and Anandan, S. (2013). "Synthesis of bianchored metal free organic dyes for dye sensitized solar cells." *Dyes Pigments*, 97(3), 397–404.
- Ramkumar, S., Manoharan, S., and Anandan, S. (2012). "Synthesis of D-(π -A) 2

- organic chromophores for dye-sensitized solar cells.” *Dyes Pigments*, 94(3), 503–511.
- Rezende, M. C., Campodonico, P., Abuin, E., and Kossanyi, J. (2001). “Merocyanine-type dyes from barbituric acid derivatives.” *Spectrochim. Acta. A. Mol. Biomol. Spectrosc.*, 57(6), 1183–1190.
- Robertson, N. (2008). “Catching the rainbow: light harvesting in dye-sensitized solar cells.” *Angew. Chem. Int. Ed.*, 47(6), 1012–1014.
- Roy, J. K., Kar, S., and Leszczynski, J. (2018). “Insight into the optoelectronic properties of designed solar cells efficient tetrahydroquinoline dye-sensitizers on TiO₂ (101) surface: first principles approach.” *Sci. Rep.*, 8(1), 1–12.
- Saritha, G., Mangalaraja, R. V., and Anandan, S. (2017). “High-efficiency dye-sensitized solar cells fabricated using D-D- π -A (donor-donor/ π -spacer-acceptor) architecture.” *Sol. Energy*, 146, 150–160.
- Saritha, G., Wu, J. J., and Anandan, S. (2016). “Modified pyrene based organic sensitizers with thiophene-2-acetonitrile as π -spacer for dye sensitized solar cell applications.” *Org. Electron.*, 37, 326–335.
- Seo, K. D., Song, H. M., Lee, M. J., Pastore, M., Anselmi, C., De Angelis, F., Nazeeruddin, M. K., Grätzel, M., and Kim, H. K. (2011). “Coumarin dyes containing low-band-gap chromophores for dye-sensitized solar cells.” *Dyes Pigments*, 90(3), 304–310.
- Sharma, S., Jain, K. K., and Sharma, A. (2015). “Solar cells: in research and applications—a review.” *Mater. Sci. Appl.*, 6(12), 1145.
- Shockley, W., and Queisser, H. J. (1961). “Detailed balance limit of efficiency of p - n junction solar cells.” *J. Appl. Phys.*, 32(3), 510–519.
- Silva, B. P., Florio, D. Z. de, and Brochsztain, S. (2014). “Characterization of a Perylenediimide Self-Assembled Monolayer on Indium Tin Oxide Electrodes Using Electrochemical Impedance Spectroscopy.” *J. Phys. Chem. C*, 118(8), 4103–4112.
- Singh, S. P., Chandrasekharam, M., Gupta, K. S., Islam, A., Han, L., and Sharma, G. D. (2013). “Co-sensitization of amphiphilic ruthenium (II) sensitizer with a metal free organic dye: Improved photovoltaic performance of dye sensitized solar cells.” *Org. Electron.*, 14(5), 1237–1241.

- Sivanadanam, J., Ganesan, P., Madhumitha, R., Nazeeruddin, M. K., and Rajalingam, R. (2015). "Effect of π -spacers on the photovoltaic properties of D- π -A based organic dyes." *J. Photochem. Photobiol. Chem.*, 299, 194–202.
- Soni, S. S., Fadadu, K. B., Vaghasiya, J. V., Solanki, B. G., Sonigara, K. K., Singh, A., Das, D., and Iyer, P. K. (2015). "Improved molecular architecture of D- π -A carbazole dyes: 9% PCE with a cobalt redox shuttle in dye sensitized solar cells." *J. Mater. Chem. A*, 3(43), 21664–21671.
- Subbaiah, M., Sekar, R., Palani, E., and Sambandam, A. (2013). "One-pot synthesis of metal free organic dyes containing different acceptor moieties for fabrication of dye-sensitized solar cells." *Tetrahedron Lett.*, 54(24), 3132–3136.
- Sun, K., Ma, Y., Zhang, W., Wen, Y., Wang, L., and Zhang, J. (2017). "New carbazole-based dyes with asymmetric butterfly structure for dye-sensitized solar cells: design and properties studies." *Dyes Pigments*, 139, 148–156.
- Tang, J., Hua, J., Wu, W., Li, J., Jin, Z., Long, Y., and Tian, H. (2010). "New starburst sensitizer with carbazole antennas for efficient and stable dye-sensitized solar cells." *Energy Environ. Sci.*, 3(11), 1736–1745.
- Thomas, K. J., Venkateswararao, A., Lee, C.-P., and Ho, K.-C. (2015). "Organic dyes containing fluoreneamine donor and carbazole π -linker for dye-sensitized solar cells." *Dyes Pigments*, 123, 154–165.
- Thomas, S., Deepak, T. G., Anjusree, G. S., Arun, T. A., Nair, S. V., and Nair, A. S. (2014). "A review on counter electrode materials in dye-sensitized solar cells." *J. Mater. Chem. A*, 2(13), 4474–4490.
- Tian, H., Yang, X., Chen, R., Pan, Y., Li, L., Hagfeldt, A., and Sun, L. (2007). "Phenothiazine derivatives for efficient organic dye-sensitized solar cells." *Chem. Commun.*, (36), 3741–3743.
- Tian, H., Yang, X., Chen, R., Zhang, R., Hagfeldt, A., and Sun, L. (2008). "Effect of different dye baths and dye-structures on the performance of dye-sensitized solar cells based on triphenylamine dyes." *J. Phys. Chem. C*, 112(29), 11023–11033.
- Tkatchenko, A., DiStasio Jr, R. A., Car, R., and Scheffler, M. (2012). "Accurate and efficient method for many-body van der Waals interactions." *Phys. Rev. Lett.*, 108(23), 236402.

- Tseng, C.-Y., Taufany, F., Nachimuthu, S., Jiang, J.-C., and Liaw, D.-J. (2014). “Design strategies of metal free-organic sensitizers for dye sensitized solar cells: Role of donor and acceptor monomers.” *Org. Electron.*, 15(6), 1205–1214.
- Venkateswararao, A., Thomas, K. J., Lee, C.-P., Li, C.-T., and Ho, K.-C. (2014). “Organic dyes containing carbazole as donor and π -linker: optical, electrochemical, and photovoltaic properties.” *ACS Appl. Mater. Interfaces*, 6(4), 2528–2539.
- Venkateswararao, A., Thomas, K. J., Li, C.-T., and Ho, K.-C. (2015). “Functional tuning of organic dyes containing 2, 7-carbazole and other electron-rich segments in the conjugation pathway.” *RSC Adv.*, 5(23), 17953–17966.
- Viswanathan, A., Prakashaiah, B. G., Subburaj, V., and Shetty, A. N. (2019). “High energy reduced graphene oxide/vanadium pentoxide/polyaniline hybrid supercapacitor for power backup and switched capacitor converters.” *J. Colloid Interface Sci.*, 545, 82–93.
- Wang, G., Wu, Y., Ding, W., Yu, G., Hu, Z., Wang, H., Liu, S., Zou, Y., and Pan, C. (2015). “Photovoltaic performance of long-chain poly (triphenylamine-phenothiazine) dyes with a tunable π -bridge for dye-sensitized solar cells.” *J. Mater. Chem. A*, 3(27), 14217–14227.
- Wang, P., Zakeeruddin, S. M., Moser, J. E., Nazeeruddin, M. K., Sekiguchi, T., and Grätzel, M. (2003). “A stable quasi-solid-state dye-sensitized solar cell with an amphiphilic ruthenium sensitizer and polymer gel electrolyte.” *Nat. Mater.*, 2(6), 402–407.
- Wang, Q., Ito, S., Grätzel, M., Fabregat-Santiago, F., Mora-Sero, I., Bisquert, J., Bessho, T., and Imai, H. (2006). “Characteristics of high efficiency dye-sensitized solar cells.” *J. Phys. Chem. B*, 110(50), 25210–25221.
- Wang, Q., Moser, J.-E., and Grätzel, M. (2005). “Electrochemical impedance spectroscopic analysis of dye-sensitized solar cells.” *J. Phys. Chem. B*, 109(31), 14945–14953.
- Wang, Y., Wan, Z., Jia, C., and Yao, X. (2016). “Indole-based organic dyes with different electron donors for dye-sensitized solar cells.” *Synth. Met.*, 211, 40–48.

- Wang, Z.-S., Cui, Y., Dan-oh, Y., Kasada, C., Shinpo, A., and Hara, K. (2008). "Molecular design of coumarin dyes for stable and efficient organic dye-sensitized solar cells." *J. Phys. Chem. C*, 112(43), 17011–17017.
- Wang, Z.-S., Cui, Y., Hara, K., Dan-oh, Y., Kasada, C., and Shinpo, A. (2007). "A high-light-harvesting-efficiency coumarin dye for stable dye-sensitized solar cells." *Adv. Mater.*, 19(8), 1138–1141.
- Warnan, J., Pellegrin, Y., Blart, E., Zhang, L., Brown, A., Hammarström, L., Jacquemin, D., and Odobel, F. (2014). "Acetylacetonate anchoring group for NiO-based dye-sensitized solar cell." *Dyes Pigments*, 105, 174–179.
- Wu, K.-L., Ho, S.-T., Chou, C.-C., Chang, Y.-C., Pan, H.-A., Chi, Y., and Chou, P.-T. (2012). "Engineering of Osmium (II)-Based Light Absorbers for Dye-Sensitized Solar Cells." *Angew. Chem.*, 124(23), 5740–5744.
- Wu, W., Wang, J., Zheng, Z., Hu, Y., Jin, J., Zhang, Q., and Hua, J. (2015). "A strategy to design novel structure photochromic sensitizers for dye-sensitized solar cells." *Sci. Rep.*, 5(1), 1–4.
- Wu, Y., and Zhu, W. (2013). "Organic sensitizers from D- π -A to D-A- π -A: effect of the internal electron-withdrawing units on molecular absorption, energy levels and photovoltaic performances." *Chem. Soc. Rev.*, 42(5), 2039–2058.
- Wu, Z., Ma, W., Meng, S., Li, X., Li, J., Zou, Q., Hua, J., and Tian, H. (2016). "New sensitizers containing amide moieties as electron-accepting and anchoring groups for dye-sensitized solar cells." *RSC Adv.*, 6(78), 74039–74045.
- Yen, Y.-S., Chou, H.-H., Chen, Y.-C., Hsu, C.-Y., and Lin, J. T. (2012). "Recent developments in molecule-based organic materials for dye-sensitized solar cells." *J. Mater. Chem.*, 22(18), 8734–8747.
- Zarate, X., Claveria-Cadiz, F., Arias-Olivares, D., Rodriguez-Serrano, A., Inostroza, N., and Schott, E. (2016). "Effects of the acceptor unit in dyes with acceptor-bridge-donor architecture on the electron photo-injection mechanism and aggregation in DSSCs." *Phys. Chem. Chem. Phys.*, 18(35), 24239–24251.
- Zeng, K., Lu, Y., Tang, W., Zhao, S., Liu, Q., Zhu, W., Tian, H., and Xie, Y. (2019). "Efficient solar cells sensitized by a promising new type of porphyrin: dye-aggregation suppressed by double strapping." *Chem. Sci.*, 10(7), 2186–2192.

- Zhang, J., Zhu, H.-C., Zhong, R.-L., Wang, L., and Su, Z.-M. (2018). "Promising heterocyclic anchoring groups with superior adsorption stability and improved IPCE for high-efficiency noncarboxyl dye sensitized solar cells: A theoretical study." *Org. Electron.*, 54, 104–113.
- Zhang, L., and Cole, J. M. (2015). "Anchoring groups for dye-sensitized solar cells." *ACS Appl. Mater. Interfaces*, 7(6), 3427–3455.
- Zhang, L., and Cole, J. M. (2016). "Can nitro groups really anchor onto TiO₂? Case study of dye-to-TiO₂ adsorption using azo dyes with NO₂ substituents." *Phys. Chem. Chem. Phys.*, 18(28), 19062–19069.
- Zhang, L., and Cole, J. M. (2017). "Dye aggregation in dye-sensitized solar cells." *J. Mater. Chem. A*, 5(37), 19541–19559.
- Zhang, L.-P., Jiang, K.-J., Li, G., Zhang, Q.-Q., and Yang, L.-M. (2014). "Pyrazino [2, 3-g] quinoxaline dyes for solar cell applications." *J. Mater. Chem. A*, 2(36), 14852–14857.
- Zhang, Q.-Q., Jiang, K.-J., Huang, J.-H., Zhao, C.-W., Zhang, L.-P., Cui, X.-P., Su, M.-J., Yang, L.-M., Song, Y.-L., and Zhou, X.-Q. (2015). "A push-pull thienoquinoidal chromophore for highly efficient p-type dye-sensitized solar cells." *J. Mater. Chem. A*, 3(15), 7695–7698.
- Zhang, S., Islam, A., Yang, X., Qin, C., Zhang, K., Numata, Y., Chen, H., and Han, L. (2013). "Improvement of spectral response by co-sensitizers for high efficiency dye-sensitized solar cells." *J. Mater. Chem. A*, 1(15), 4812–4819.
- Zheng, D., Ye, M., Wen, X., Zhang, N., and Lin, C. (2015a). "Electrochemical methods for the characterization and interfacial study of dye-sensitized solar cell." *Sci. Bull.*, 60(9), 850–863.
- Zheng, J., Zhang, K., Fang, Y., Zuo, Y., Duan, Y., Zhuo, Z., Chen, X., Yang, W., Lin, Y., and Wong, M. S. (2015b). "How to optimize the interface between photosensitizers and TiO₂ nanocrystals with molecular engineering to enhance performances of dye-sensitized solar cells?" *ACS Appl. Mater. Interfaces*, 7(45), 25341–25351.

Zhu, B., Wu, L., Ye, Q., Gao, J., and Han, L. (2017). "Asymmetric double donor- π -acceptor dyes based on phenothiazine and carbazole donors for dye-sensitized solar cells." *Tetrahedron*, 73(44), 6307–6315.

Zhu, L., Yang, H. B., Zhong, C., and Li, C. M. (2014). "Rational design of triphenylamine dyes for highly efficient *p*-type dye sensitized solar cells." *Dyes Pigments*, 105, 97–104.

LIST OF PUBLICATIONS

1. **Kesavan, R.**, Abdellah, I. M., Singh, S. P., El-Shafei, A. and Adhikari, A. V. (2019). "Simple diphenylamine based D- π -A type sensitizers/co-sensitizers for DSSCs: a comprehensive study on the impact of anchoring groups." *Physical Chemistry Chemical Physics*, 21(20), 10603-10613.
2. **Kesavan, R.**, Attia, F., Su, R., Anees, P., El-Shafei, A. and Adhikari, A. V. (2019). "Asymmetric Dual Anchoring Sensitizers/Co-Sensitizers for DSSC Application: An Insight into Various Fundamental Processes inside the Cell." *The Journal of Physical Chemistry*, 123(40), 24383-24395.
3. **Kesavan, R.**, Attia, F., Abdellah, I. M., El-Shafei, A. and Adhikari, A. V. (2019). "Effect of extended π -conjugation of the D- π -A type diphenyl amine based sensitizers/co-sensitizers on the photovoltaic performance of DSSC." (Manuscript draft is ready).
4. **Kesavan, R.**, Attia, F., Abdellah, I. M., El-Shafei, A. and Adhikari, A. V. (2019). "Highly efficient diphenyl based co-sensitizers bearing nitro group as anchors for DSSC application." (Manuscript under preparation).
5. **Kesavan, R.**, Attia, F., El-Shafei, A. and Adhikari, A. V. (2019). "Role of additional donor units in diphenylamine based D-A type sensitizers/co-sensitizers for DSSCs." (Manuscript under preparation).
6. **Kesavan, R.**, Attia, F., El-Shafei, A. and Adhikari, A. V. (2019). "Highly efficient conceptually new A-D- π -D-A type sensitizers/co-sensitizers for DSSCs." (Manuscript under preparation).
7. **Kesavan, R.**, Attia, F., Anees, P., El-Shafei, A. and Adhikari, A. V. (2019). "Diphenylamine based structurally small co-sensitizers with PCE exceeding 10%." (Manuscript under preparation).

PAPER PRESENTED IN NATIONAL/INTERNATIONAL CONFERENCES

1. **Kesavan, R.**, Attia, F., Abdellah, I. M., El-Shafei, A. and Adhikari, A. V. (2019). "New D- π - π -A type diphenylamine based sensitizers/co-sensitizers for DSSCs: Photophysical, electrochemical, theoretical and photoelectrochemical studies", 3rd

-
- International Conference on Advanced Materials (ICAM) 2019, IUMSE, School of Chemical Sciences, Aug. 09-11, Mahatma Gandhi University, Kottayam, Kerala.
2. **Kesavan. R.**, Abdellah. I. M., El-Shafei. A. and Adhikari. A. V. (2019). “Design, synthesis and characterization of A-D- π -A type diphenylamine based metal-free sensitizers for DSSCS”, International Conference on Material for Millennium (MATCON 2019), Mar 14-16, 2019 at Cochin University of Science and Technology, Kerala.
 3. **Kesavan. R.**, Abdellah. I. M., El-Shafei. A. and Adhikari. A. V. (2018). “Study of simple diphenyl amine based D- π -A metal-free dyes containing nitro group as anchoring unit for DSSC application.”, International conference on Chemistry and Physics of Materials (ICCPM-2018), Dec 19-21, 2018 at St. Thomas College (Autonomous), Thrissur-680001, Kerala.
 4. **Kesavan. R.**, Priyadarshi. A., Mhaisalkar. S. and Adhikari. A. V. (2018). “Role of different additives used in precursor solution for printable perovskite solar cells”, Annual Conference Indian Council of Chemists (ICC-2018), Dec 12-14, 2018 at National Institute of Technology Karnataka, Surathkal, Karnataka.
 5. **Kesavan. R.**, Abdellah. I. M., El-Shafei. A. and Adhikari. A. V. (2018). “Comparison of anchoring properties of acid and nitro groups on the photovoltaic performance of diphenylamine based dyes for dye sensitized solar cells”, International Conference on Recent Trends in Material Science and Technology (ICMST 2018), Oct 10-13, 2018 at Indian Institute of Space Science and Technology (IIST), Veli, Thiruvananthapuram, Kerala.
 6. **Kesavan. R.**, Priyadarshi. A., Mhaisalkar. S. and Adhikari. A. V. (2018). “Study on the effect of different additives used in printable perovskite solar cells”, International Conference on Sustainable Chemistry for Health, Environment and Materials (SU-CHEM 2018), Aug 05-08, 2018 at CSIR- Indian Institute of Chemical Technology, Hyderabad, Telangana (**Best Poster award**).
 7. **Kesavan. R.** and Adhikari. A. V. (2017). “Design and synthesis of an asymmetric bi-anchored metal-free dye for dye sensitized solar cells”, International Conference on Advances in Materials Science and Technology (ICAMST), Oct 09-11, 2017 at VIT University, Vellore, Tamil Nadu.

-
8. **Kesavan. R.** and Adhikari. A. V. (2017). “Molecular design and synthesis of metal-free diphenylamine based sensitizer for dye sensitized solar cells”, International Conference on Emerging Trends in Chemical Sciences (ICETCS-2017), Sept 14-16, 2017 at Manipal Institute of Technology, Manipal, Karnataka.

BIO-DATA

Rajalakshmi K

PRESENT ADDRESS

Department of Chemistry
National Institute of Technology Karnataka
Suratkal, Srinivasanagar -575 025
Mangaluru, Karnataka, India

PERMANENT ADDRESS

16/338 , “Chitra Bhavan”
Vadakkumuri, Kalmandapam ,
Palakkad-678001
Kerala, India

CONTACT DETAILS

Email id: rajalakshmik7@gmail.com

Mobile: +91 9995989262

RESEARCH EXPERIENCE

- Since Jan 2015 Doctoral student in Dept. of Chemistry, National Institute of Technology Karnataka (NITK), Suratkal, Karnataka, India.
- Jan-Jun 2018 Intern in School of Material Science and Engineering Nanyang Technological Institute, Singapore.(6 months)
- Dec 2016-Jun 2017 Visiting researcher in Inorganic and Physical Chemistry Division, CSIR- Indian Institute of Chemical Technology, Hyderabad, Telangana, India (6 months).
- Jan-April 2014 Post Graduate project student in CSIR- Central Electrochemical Research, Institute (CECRI), Karaikudi, Tamil Nadu, India (4 months).
- May-July 2013 Summer Internship fellow in NMR Centre, Indian Institute of Science, Bengaluru, Karnataka, India (2 months).

EDUCATIONAL BACKGROUND

2015-Present **Doctor of Philosophy (Ph.D.)** in Molecular design and synthesis of diphenylamine based metal-free chromophores for Dye sensitized solar cells(DSSCs).

Supervisor- Prof. A Vasudeva Adhikari

-
- 2012-2014 **Master of Science** (M.Sc.) in Hydrochemistry, with CGPA: 8.29/10 (First Class with distinction) from Department of Chemical Oceanography, Cochin University of Science and Technology (CUSAT), Cochin, Kerala, India.
- 2009-2012 **Bachelor of Science** (B.Sc.) in Chemistry, 2009-2012 With 94% (Distinction) from Government Victoria College, Palakkad, under University of Calicut, Kerala, India.
- 2007-2009 **Higher Secondary**, 2007-2009 With 87.3% (First Class with Distinction) from GMMGHSS, Palakkad, Kerala Higher Secondary Board, Kerala, India.
- 2007 **Secondary School**, 2007 With 94 % (Distinction) from GMMGHSS, Palakkad, Board of Public Examinations, Kerala, India.

PERSONAL DATA

- Date of Birth : 10/ 09/ 1991
- Gender : Female
- Nationality: Indian
- Languages Known: English, Malayalam, Hindi and Tamil.

* * *